Timing, Rates, and Styles of Cenozoic Tectonism in the Basin and Range and Lesser Caucasus: Linking Observations of Intracontinental Deformation to Geodynamic Processes

by

Nikolas Midttun

A dissertation submitted in partial fulfillment
of the requirements for the degree of
Doctor of Philosophy
(Earth and Environmental Sciences)
in the University of Michigan
2022

Doctoral Committee:

Professor Nathan A. Niemi, Chair
Professor Catherine Badgley
Professor Marin K. Clark
Associate Professor Eric A. Hetland
Associate Professor Naomi E. Levin



Sunset in the northern Basin and Range.

Nikolas Midttun

nmidttun@umich.edu

ORCID iD: 0000-0001-7729-8851

© Nikolas Midttun 2022

For Becca

Acknowledgements

It has been an extraordinary privilege to spend the past five years learning about the Earth, developing my skills as a scientist and scholar, and discovering so many long-term collaborations and friendships. During my time at the University of Michigan, I benefited from an outstanding community of people who guided and supported me intellectually and emotionally. I only hope that in the future, I can pass on to others the same level of goodwill and kindness that I received from the people below.

First and foremost, I want to thank my advisor, Nathan Niemi. Continuously since I first met Nathan, he demonstrated superhuman patience, good humor, and thoughtfulness that together made him an exceptional academic advisor. Through all the challenges I faced during my degree, Nathan steadfastly believed in me, and for that I am immensely thankful. The next time Nathan and I are in Beatty together, the first round of chili and beer at the Happy Burro will be on me!

I received a huge amount of support from my dissertation committee. Marin Clark, despite being a very busy department chair, was always generous with her time and advice, especially when it came to working on scientific writing. Naomi Levin not only advised me on my research, but also helped me become a much better instructor. Eric Hetland instilled in me a deep appreciation of (and dare I say, love for?) statistics and modeling. Catherine Badgley continuously inspired me with the effortless way she orchestrated interdisciplinary scientific collaborations (including working with Nathan and me!).

During my studies, I had the good fortune to work with scientists from around the world. I want to thank our hosts and collaborators in the Caucasus, Orhan Karsli, Arkady Karakhanian, Hayk Igityan, Hektor Babayan, and Mikayel Gevorgyan. Thank you to Stuart Thomson at the University of Arizona, and Eric Cowgill at University of California, Davis thoughtful discussions about my data. A heartfelt thanks to Alison Duvall, Darrel Cowan, and Jody Bourgeois, the three scientists who first got me interested in tectonics, structural geology, and stratigraphy during my bachelor's degree at the University of

Washington. Thank you also to Kate Scharer at the USGS for inspiring me early in my scientific career.

Thank you to the many graduate students who joined me on this amazing (but also sometimes harrowing!) journey. There are far too many people to list here, but I am honored to call all of you colleagues and friends, and nothing excites me more than being able to follow all your successes in the future.

The SCALE lab at the University of Michigan was my academic home, and there are so many people to thank there. I learned so much from the lab "elders," Kendra Murray, Eric Portenga, Tim Stahl, Alyssa Abbey, and Alex Tye. A huge thank you to our former lab manager, Amanda Maslyn (now at University of Rochester), who taught me a great deal about mineral separation and thermochronology analysis. Of course, where would I be without the support and friendship of my lab mates, Kirk Townsend, Maddie Hille, Bianca Gallina, and especially Billy Medwedeff.

Thank you to my family, especially my parents. This dissertation reflects the decades of love, support, and sense of adventure my parents always gave me.

Finally, thank you to Becca, my constant inspiration, and the only person on Earth I could imagine ever navigating the high seas of life with.

Table of Contents

Dedication ..... **ii**
Acknowledgements ..... **iii**
List of Tables ..... **viii**
List of Figures ..... **ix**
List of Appendices ..... **xi**
Abstract ..... **xii**
Chapter 1 Introduction **1**

1.1 Thesis Motivation 1
1.2 Study areas and outstanding questions 2
1.3 References 5

Chapter 2 Stratigraphy of the Eocene–Oligocene Titus Canyon Formation, Death Valley, California, and Eocene Extensional Tectonism in the Basin and Range **9**

2.1 Abstract 9
2.2 Introduction 10
2.3 Paleogene Stratigraphy of the Death Valley Region—Correlations and Controversies 13

2.3.1 Previous Work Describing the Titus Canyon Formation 15
2.3.2 Controversies on the Age and Definition of the Titus Canyon Formation 16
2.3.3 Resolving the Early Extensional and Basin Development History of the Death Valley Region 18

2.4 Methods 22

2.4.1 Geologic Mapping and Measured Sections 22
2.4.2 Geochronology 23

2.5 Revised Stratigraphy and Age of Paleogene Strata in Eastern Death Valley 27

2.5.1 Titus Canyon Formation 27
2.5.2 Rocks of Porter Mine 38

2.6 Tectono-Stratigraphy and Formation of the Titus Canyon Basin 42

2.6.1 Extensional Basin Initiation and Fluvial Phase 43
2.6.2 Acceleration of Extension and Fluvial-Lacustrine Phase 45
2.6.3 Extent of the Titus Canyon Basin and Regional Correlations of the Titus Canyon Formation 47

2.7 Structure of the Titus Canyon Basin 48

2.7.1 Fall Canyon Fault 49

2.7.2 Titus Canyon Fault 50
2.7.3 Boundary Canyon Detachment 52
2.7.4 Implications of Titus Canyon Basin Structures for Regional Palinspastic Reconstructions of Basin and Range Extension 53
2.8 Tectonic and Topographic Implications for the Evolution and Collapse of the Sevier Orogenic Belt 55
2.8.1 Stratigraphic Record of Crustal Extension along the Axis of the Sevier Orogenic Belt 55
2.8.2 Spatial Extent of an Early Eocene Nevadaplano 59
2.9 Conclusions 60
2.10 Acknowledgments 61
2.11 References 61
Chapter 3 Multi-thermochronometer Analysis Reveals Strain Heterogeneity in the Northern Basin and Range Extensional Province, Utah and Nevada 79
3.1 Abstract 79
3.2 Introduction 80
3.3 Methods 90
3.3.1 Sampling approach 91
3.3.2 Thermochronologic analyses 92
3.3.3 QTQt Thermal modeling: Criteria for selecting modeling inputs and additional constraints on allowable time-temperature paths 95
3.4 Results 97
3.4.1 Northern Nevada 98
3.4.2 I-80 Corridor 100
3.4.3 Southern Transect and House Range 102
3.4.4 Patterns of thermochronologically constrained cooling histories 106
3.4.5 Mesozoic contractional exhumation 107
3.4.6 Protracted Mesozoic and Cenozoic cooling 108
3.4.7 Miocene exhumation 108
3.5 Discussion 110
3.5.1 Pre-extensional and early-extensional tectonic history 110
3.5.2 Miocene to present extensional tectonism 113
3.6 Conclusions 117
3.7 Acknowledgments 118
3.8 References 118
Chapter 4 Low-temperature Thermochronology Limits Recent Uplift in the Lesser Caucasus and Eastern Pontides During the Initiation of Continent-continent Collision 130
4.1 Abstract 130
4.2 Introduction 131

4.2.1 Discontinuities in the Arabia-Eurasia Collision Zone 133
4.2.2 Geology and Topography of the Lesser Caucasus and Eastern Pontides .. 136
4.3 Geomorphic Observations of an Elevated Low-relief Surface 139
4.3.1 Characteristics of the Elevated Low-Relief Surface 141
4.3.2 Age and Origin of Elevated Low-relief Topography in the Lesser Caucasus and Eastern Pontides 143
4.4 (U-Th)/He Thermochronology Methods 144
4.4.1 Sampling 144
4.4.2 Apatite and Zircon (U-Th)/He Analytical Procedure 148
4.4.3 Inverse Thermal Modeling in QTQt 149
4.5 (U-Th)/He Thermochronology Results 150
4.5.2 Potential Helium Implantation and Quality of the Apatite (U-Th)/He Thermochronology 153
4.5.3 Thermal Histories Produced by Inverse Modeling of Thermochronology .155
4.5.4 Sensitivity of Thermochronology Modeling to Geothermal Gradient 158
4.5.5 Interpretations from Thermochronology Modeling 159
4.6 Discussion 160
4.6.1 Strike-slip Faulting Accommodates Arabia-Eurasia Convergence in the LCEP 161
4.6.2 Middle Miocene Erosional Event and the Support of Topography in the LCEP 162
4.7 Conclusions 163
4.8 Acknowledgements 164
4.9 References 164
Chapter 5 Conclusions 175
5.1 References 177
Appendix A Supplementary Information for Chapter 2 178
A.1 Titus Canyon $^{40}Ar/^{39}Ar$ data recalculations 178
Appendix A References 214
Appendix B Analytical Data for Chapter 3 216
Appendix C Analytical Data for Chapter 4 224

List of Tables

Table 2.1: Summary of geochronology samples, sources, and ages. 20

Table 3.1: Sample locations and pluton names. 85

Table 3.2: Compiled estimates of pluton emplacement-depths. 86

Table 3.3: Compiled Ar geochronology. 87

Table 3.4: Compiled pluton emplacement ages. 88

Table 3.5: Apatite and zircon (U-Th)/He ages, apatite fission-track ages, and apatite fission-track track length distributions. 89

Table 4.1: Summary of (U-Th)/He samples and ages analyzed in this study. 146

Table 4.2: Summary of compiled apatite fission-track samples and ages. 147

Table A.1:Analytical data for Titus Canyon detrital zircon U-Pb analyses. 183

Table A.2: Analytical data for Titus Canyon zircon (U-Th)/He analyses.....209

Table A.3: Analytical data for 40Ar/39Ar ages of Gutenkunst (2006) 210

Table B.1: Apatite fission-track analytical data. 217

Table B.2: Apatite (U-Th)/He analytical data. 218

Table B.3: Zircon (U-Th)/He analytical data. 222

Table C.1: Zircon and apatite (U-Th)/He analytical data. 225

List of Figures

Figure 2.1: Overview maps of the Basin and Range and Death Valley. 10
Figure 2.2: Cenozoic chronostratigraphy of Death Valley. 14
Figure 2.3: Location names in the Grapevine and Funeral mountains. 16
Figure 2.4: Location map of samples and measured sections. 24
Figure 2.5: Radial plots and histograms for detrital zircon MDA calculations. 25
Figure 2.6: Images of faults in the Grapevine Mountains. 28
Figure 2.7: Images of the Redbed member of the Titus Canyon Formation. 30
Figure 2.8: Images of the Variegated member of the Titus Canyon Formation. 32
Figure 2.9: Detrital zircon spectra for the Titus Canyon Formation. 34
Figure 2.10: Images of the Rocks of Porter Mine. 40
Figure 2.11:Simplified Cenozoic chronostratigraphy of the Nevadaplano. 43
Figure 2.12: Simplified structural map of the Grapevine and Funeral Mountains. 49
Figure 2.13: Oblique view of the Titus Canyon Anticline and Titus Canyon Fault. 51
Figure 2.14: Geography of the Nevadaplano and Sevier hinterland basins. 57
Figure 3.1: Overview map of the northern Basin and Range. 81
Figure 3.2: Detailed map of thermochronology in the northern Basin and Range. 91
Figure 3.3: Histograms of apatite fission-track length distributions. 94
Figure 3.4: Selected geographic names in the northern Basin and Range. 98
Figure 3.5: Modeled time-temperature histories for the northern Basin and Range. 105
Figure 3.6: Categorized cooling histories in the northern Basin and Range. 106
Figure 3.7: Comparison of cooling histories to geologic context data. 109

Figure 3.8: Phase diagram of extensional styles.....115

Figure 3.9: Simplified model for the evolution of Basin and Range extension. 117

Figure 4.1: Overview of the Arabia-Eurasia collision zone.....132

Figure 4.2: Regional geology of the Caucasus collision.....135

Figure 4.3: Lesser Caucasus and Pontides topography and thermochronology.....137

Figure 4.4: Low-relief surface in the Lesser Caucasus and Eastern Pontides. 140

Figure 4.5: Elevation swath profiles in the Lesser Caucasus and Eastern Pontides.....141

Figure 4.6: Thermochronologic cooling age versus elevation plots.....145

Figure 4.7: Modeled thermal histories in the Lesser Caucasus and Eastern Pontides...155

Figure 4.8: Age versus eU relationships in the apatite thermochronology.....157

Figure 4.9: Tests of thermal model sensitivity to geothermal gradient. 158

Figure A.1: Measured sections of the Titus Canyon Formation. 180

Figure A.2: Geologic map of the southern Grapevine Mountains and northern Funeral Mountains, with an emphasis on Cenozoic stratigraphy. 181

Figure A.3: Supplementary plots of $^{40}Ar/^{39}Ar$ analytical data (Gutenkunst, 2006)..... 182

List of Appendices

Appendix A: Supplementary Information for Chapter 2 178
Appendix B: Analytical Data for Chapter 3 216
Appendix C: Analytical Data for Chapter 4 224

Abstract

Continental lithosphere exhibits complex deformation across broad regions, challenging simplistic tectonic models of how plate boundaries behave. As geologists develop models to explain observed patterns of deformation, they have proposed a wide array of geodynamic mechanisms and material properties that may control the rates, styles, and magnitudes of continental deformation. In most study areas, we now have an excess of hypothesized controls and a dearth of data with which to test competing models of deformation. This dissertation presents three field studies of continental deformation that apply a diverse set of investigative approaches to characterize deformation, then link that deformation to the most likely geodynamic causes.

Two studies are from the Basin and Range extensional province, addressing debates around the relative role of plate boundary stresses and internal gravitational potential energy gradients in driving extensional tectonism over the Cenozoic. In Chapter 2, I use field mapping, stratigraphy, detrital zircon geochronology, and structural observations to build a basin history for the Titus Canyon Formation, one of the earliest syn-extensional deposits in the central Basin and Range. Our results from the Titus Canyon Formation suggest that it records extension related to a ~40 Ma slowdown in plate convergence along western North America. In Chapter 3, I apply multiple low-temperature thermochronometers to a suite of Jurassic plutons in the northern Basin and Range to decipher their exhumational histories. My data support a major phase of extension in the Miocene, and also reveal changes in Cretaceous-Paleogene exhumation that may be related to contractional tectonism of the Sevier orogeny and construction of the Nevadaplano. Chapter 4 examines the recent tectonic history of the down-going plate in the Caucasus collisional orogen. I apply low-temperature thermochronology to measure the tectonic response to the initiation of collision at 5 Ma with the goal of understanding the partitioning of strain between the two colliding plates. The results indicate that the collision is highly asymmetric, with the majority of shortening in the

down-going plate being accommodated by strike-slip faulting, in contrast with deformation in the overriding plate which is accommodated primarily by reverse faulting and folding. Together these studies illustrate the rich complexity of continental deformation and the wide variety of geodynamic mechanisms that must be considered when building models of how deformation evolves in old continental lithosphere.

Chapter 1
Introduction

1.1 Thesis Motivation

The sudden and widespread acceptance of plate tectonic theory transformed our understanding of the Earth system (Wilson, 1969; Dickinson, 1971; Hammond, 1971). Simply stated, plate tectonics describes the lithosphere as broken into a number of internally rigid plates that float (i.e., are isostatically compensated) in a fluid-like asthenosphere. These plates move relative to one another, concentrating deformation into narrow zones along the plate boundaries. Once fully realized in the 1960s, the plate tectonic framework proved revolutionary for explaining many puzzling aspects of the structure, geometry, and history of the Earth, including enigmas within biological evolution (e.g., McKenna, 1972), the distribution of hazards like volcanos and earthquakes (e.g., Coats, 1962; Wilson, 1963; Anderson, 1975), and the ultimate origin of mountainous regions (e.g., Atwater, 1970; Smith, 1976).

Early in the development of plate tectonics, it was recognized that while the theory quite accurately predicts the morphology, motion, and deformation of oceanic lithosphere, the inherent heterogeneity and complexity of continental lithosphere defies many of the theory's simplistic assumptions (Molnar, 1988). For example, instead of only deforming along narrow zones near plate boundaries, continental lithosphere deforms across vast regions that stretch 100s to 1000s of kilometers inboard from continental margins. Furthermore, within these broad zones of continental deformation, strain is not evenly distributed. This complexity arises because continental lithosphere consists of a heterogeneous amalgam of accreted terranes, cratonic fragments, failed rifts, and extinct orogenic belts, thus creating a complex composite material riddled with discontinuities and rheological contrasts that can produce highly unpredictable patterns of deformation.

To account for this observed complexity, tectonicists have spent much of the past 70 years attempting to augment plate tectonic theory with models for orogenesis

developed through detailed studies in deforming regions that fail to conform to simple predictions of plate tectonics (Molnar and Lyon-Caen, 1988). This work has produced a tremendous body of literature detailing the nuances and complexity within the East African Rift, the Himalaya and Tibetan plateau, the Andes and Altiplano, and the North American Cordillera. These studies have also produced a sizeable list of geodynamic mechanisms and material properties hypothesized to potentially control the rates, magnitudes, and distribution of continental deformation within these complexly deforming continental regions.

This dissertation continues in this tradition of elucidating the proximal causes of unusual patterns of deformation. To this end, I apply a variety of tools that measure continental deformation including low-temperature thermochronology, geologic and geomorphic mapping (both in the field and remotely), and basin analysis. The objective of each of these analyses is to constrain the timing, rates, and styles of continental deformation, enabling precise comparison to established timelines of potential geodynamic causes. In my studies, these causes included changes in plate boundary conditions, changes to the structure of the lithosphere, and changes to the state of stress during deformation. The datasets I present constrain the deformation histories of the western U.S. and Lesser Caucasus, moving us closer to understanding how topography evolves on orogenic timescales, how inherited lithospheric structure can influence later deformation, and what geodynamic factors are most important to consider when reconstructing the tectonic history of a region.

1.2 Study areas and outstanding questions

Chapters 2 and 3 examine the Basin and Range province of western North America, a type-locality for long-lived continental extension (Dickinson, 2002; 2006). Named for its iconic horst-and-graben topography, the modern Basin and Range is the result of at least 40 Myr of extension, a tectonic history that reflects potentially three separate processes: the post-orogenic collapse of an ancient mountain range (i.e. the Nevadaplano; Ernst, 2009), the transition of the western plate boundary of North America from convergent to transform (Atwater, 1970; Dickinson, 2002), and the delamination of the Farallon subducted slab from beneath the continent (Humphreys, 1995; Cassel et al., 2018). The relative contribution of topographic stresses, changing plate boundary

stresses, and slab removal to the multi-phase extensional history of the Basin and Range remains a topic of significant debate (cf. Wells et al., 2012; Long, 2018; Lund Snee and Miller, 2022).

Chapter 2 explores these debates by examining the Eocene-Oligocene Titus Canyon Formation in Death Valley, central Basin and Range. Most of the extension in Death Valley occurred since the middle Miocene, overprinting and deforming structural and sedimentary evidence for earlier (Eocene-Oligocene) phases of extensional tectonism. These earlier phases may be genetically related to well-documented Eocene-Oligocene extension in the northern Basin and Range (e.g., Evans et al., 2015; Canada et al., 2019; 2020), making their timing, magnitude, and style critical for understanding the extent of early phases of extension across the Basin and Range. Prior to our study, the Titus Canyon Formation was understood to be the earliest Cenozoic sedimentary deposit in the Death Valley region, but it remained poorly dated and only partially mapped due to the complexity of its exposure and general lack of easily datable tuffs. We employed geologic mapping, stratigraphic correlation, and detrital zircon U-Pb dating to reconstruct the history of the basin and correlate observed changes in detrital zircon provenance to extension triggered by plate boundary reorganization at ~40 Ma.

Chapter 3 examines the Cenozoic tectonic evolution of the northern Basin and Range, a region marked by complex and overlapping phases of extension that vary spatially and temporally (Dickinson, 2002). Much of the debate around the tectonic history of the northern Basin and Range revolves around the significance of a belt of metamorphic core complexes: surface exposures of mid-crustal metamorphic rocks that record both ductile and brittle extensional exhumation from 15-25 km depths. The belt of core complexes has been hypothesized as marking the location of a once tall mountain range built during the Sevier orogeny, and which produced steep gravitational potential energy gradients that localized later extension during post-orogenic collapse (Coney and Harms, 1984; DeCelles, 2004). However, alternatives to this hypothesis have grown in popularity as additional mechanisms for accommodating extension beyond topographically modulated collapse have been proposed, including flow of a low-viscosity lower crust (Block and Royden, 1990), syn-extensional magmatic underplating (Catchings et al., 1992), and diapiric models for core complex exhumation (Konstantinou et al., 2012). Today, significant debates continue regarding the importance of magmatic

addition, lower crustal flow, and diapirism as opposed to older models of slip along deeply rooted low-angle detachments (e.g., Wernicke and Burchfiel, 1982), but a critical lack of data constraining the timing and magnitude of tectonism outside of the well-studied core-complexes continues to prevent effective testing of these competing hypotheses.

In our study, we expanded our understanding of the tectonic history of the northern Basin and Range to the less-studied regions outside of the metamorphic core complexes. We applied three thermochronometers to individual samples collected from small plutons exposed outside of the metamorphic core complexes. The broad range of closure temperatures of our three thermochronometers (apatite and zircon (U-Th)/He and apatite fission-track systems) enabled us to track the progressive cooling of our samples as they were extensionally exhumed to the surface. Our data indicate that the magnitude of Miocene extensional exhumation (the Miocene being the largest single phase of extension in the Basin and Range) varies significantly across the province, not clearly reflecting the influence of inherited regional contractional structures or pre-extensional crustal thickness. We speculate that such spatially quasi-periodic variability in extensional strain is similar to modeled patterns of extension controlled by periodic necking instability (i.e. lithospheric scale boudinage) during extension (e.g., Fletcher and Hallet, 1983). Additionally, our data show no evidence of major exhumation in the Eocene-Oligocene, when gravitationally driven topographic collapse was hypothesized to be occurring most rapidly (McQuarrie and Wernicke, 2005; Chapman et al., 2015; Bahadori et al., 2018). Tectonic quiescence during orogenic collapse in the Eocene-Oligocene points towards the importance of mechanisms that can produce broadly distributed crustal thinning without widespread upper-crustal extension (e.g., lower crustal flow, magmatic addition, or diapirism), especially in the early stages of Basin and Range extension.

Chapter 4 pivots away from the extensional setting of the Basin and Range to explore the geodynamic controls on the collisional tectonics of the Lesser Caucasus and Pontides mountains of Armenia and Turkey. The Lesser Caucasus and Pontides share a similar structural position within the broad Arabia-Eurasia collision zone, together forming the lower plate of the nascent Caucasus continent-continent collision (Cowgill et al., 2016). Regional observations of fault networks (Allen et al., 2011), rock exhumation (Avdeev and Niemi, 2011), sediment provenance (Tye et al., 2021), and foreland basin

deposition (Cavazza et al., 2018) all show evidence for a regional tectonic reorganization following the initiation of continental collision between the Greater Caucasus and Lesser Caucasus-Pontides mountain belts at ~5 Ma. Thermochronology and structural observations of the Greater Caucasus mountains indicate that they experienced significant rock exhumation, folding, and reverse faulting in response to the onset of continental collision. In contrast, the magnitude and style of deformation within the Lesser Caucasus-Pontides mountains during the initiation of collision remains an open question due to a paucity of tectonic data from the region. To reconstruct the recent deformation history of these ranges, we applied low-temperature thermochronology to samples from the Armenian Lesser Caucasus and eastern Pontides, and performed remote geomorphic analyses of the mountainous topography. Our data indicate that the ranges appear to have not experienced significant rock exhumation over the past 10 Myr, precluding significant reverse faulting during the initiation of collision. Instead, the shortening across the ranges appears to have been accommodated primarily on continental scale strike-slip faults that reactivate a Cretaceous ophiolitic suture zone. The difference between the tectonic response to the initiation of continental collision in the Greater Caucasus (reverse faulting, rock uplift) and the Lesser Caucasus-Pontides (strike slip faulting, surface uplift) provides a specific example of how pre-existing optimally oriented faults can control the style deformation within a collision zone.

1.3 References

Allen, M.B., Kheirkhah, M., Emami, M.H., and Jones, S.J., 2011, Right-lateral shear across Iran and kinematic change in the Arabia-Eurasia collision zone: Geophysical Journal International, v. 184, p. 555–574, doi:10.1111/j.1365-246X.2010.04874.x.

Anderson, D.L., 1975, Accelerated plate tectonics: Science, v. 187, p. 1077–1079, doi:10.1126/science.187.4181.1077.

Anderson, D.L., 2006, Plate tectonics; the general theory: Complex Earth is simpler than you think, *in* Manduca, C.A. and Mogk, D.W. eds., Earth and Mind: How Geologists Think and Learn about the Earth, Geological Society of America, p. 29–38, doi:10.1130/2006.2413(03).

Atwater, T., 1970, Implications of plate tectonics for the Cenozoic tectonic evolution of western North America: Geological Society of America Bulletin, v. 81, p. 3513–3536.

Avdeev, B., and Niemi, N.A., 2011, Rapid Pliocene exhumation of the central Greater Caucasus constrained by low-temperature thermochronometry: Tectonics, v. 30, p. 1–16, doi:10.1029/2010TC002808.

Block, L., and Royden, L.H., 1990, Core complex geometries and regional scale flow in the lower crust: Tectonics, v. 9, p. 557–567, doi:10.1029/TC009i004p00557.

Canada, A.S., Cassel, E.J., McGrew, A.J., Smith, M.E., Stockli, D.F., Foland, K.A., Jicha, B.R., and Singer, B.S., 2019, Eocene exhumation and extensional basin formation in the Copper Mountains, Nevada, USA: Geosphere, v. 15, p. 1577–1597, doi:10.1130/GES02101.1.

Canada, A.S., Cassel, E.J., Stockli, D.F., Smith, M.E., Jicha, B.R., and Singer, B.S., 2020, Accelerating exhumation in the Eocene North American Cordilleran hinterland: Implications from detrital zircon (U-Th)/(He-Pb) double dating: Geological Society of America Bulletin, v. 132, p. 198–214, doi:10.1130/B35160.1.

Cassel, E.J., Smith, M.E., and Jicha, B.R., 2018, The impact of slab rollback on earth's surface: Uplift and extension in the hinterland of the North American Cordillera: Geophysical Research Letters, v. 45, p. 10966–11004, doi:10.1029/2018GL079887.

Catchings, R.D., 1992, A relation among geology, tectonics, and velocity structure, western to central Nevada Basin and Range: Geological Society of America Bulletin, v. 104, p. 1178–1192.

Chapman, J.B., Ducea, M.N., DeCelles, P.G., and Profeta, L., 2015, Tracking changes in crustal thickness during orogenic evolution with Sr/Y: An example from the North American Cordillera: Geology, v. 43, p. 919–922, doi:10.1130/G36996.1.

Coats, R.R., 1962, Magma Type and Crustal Structure in the Aleutian Arc, *in* Macdonald, G.A. and Kuno, H. eds., Geophysical Monograph Series, Washington, D. C., American Geophysical Union, p. 92–109, doi:10.1029/GM006p0092.

Cowgill, E., Forte, A.M., Niemi, N., Avdeev, B., Tye, A., Trexler, C., Javakhishvili, Z., Elashvili, M., and Godoladze, T., 2016, Relict basin closure and crustal shortening budgets during continental collision: An example from Caucasus sediment provenance: Tectonics, v. 35, p. 2918–2947, doi:10.1002/2016TC004295.

DeCelles, P.G., 2004, Late Jurassic to Eocene evolution of the cordilleran thrust belt and foreland basin system, western U.S.A.: American Journal of Science, v. 304, p. 105–168, doi:10.2475/ajs.304.2.105.

Dickinson, W.R., 1972, Evidence for plate-tectonic regimes in the rock record: American Journal of Science, v. 272, p. 551–576, doi:10.2475/ajs.272.7.551.

Dickinson, W.R., 2006, Geotectonic evolution of the Great Basin: Geosphere, v. 2, p. 353–368, doi:10.1130/GES00054.1.

Dickinson, W.R., 1971, Plate Tectonics in Geologic History: New global tectonic theory leads to revised concepts of geosynclinal deposition and orogenic deformation.: Science, v. 174, p. 107–113, doi:10.1126/science.174.4005.107.

Dickinson, W.R., 2002, The Basin and Range Province as a composite extensional domain: International Geology Review, v. 44, p. 1–38, doi:10.2747/0020-6814.44.1.1.

Ernst, W.G., 2009, Rise and fall of the Nevadaplano: International Geology Review, v. 51, p. 583–588, doi:10.1080/00206810903063315.

Evans, S.L., Styron, R.H., van Soest, M.C., Hodges, K.V., and Hanson, A.D., 2015, Zircon and apatite (U-Th)/He evidence for Paleogene and Neogene extension in the Southern Snake Range, Nevada, USA: Tectonics, v. 34, p. 2142–2164, doi:10.1002/2015TC003913.

Fletcher, R.C., and Hallet, B., 1983, Unstable extension of the lithosphere: A mechanical model for basin-and-range structure: Journal of Geophysical Research: Solid Earth, v. 88, p. 7457–7466, doi:10.1029/JB088iB09p07457.

Gillooly, T., Coltice, N., and Wolf, C., 2019, An anticipation experiment for plate tectonics: Tectonics, v. 38, p. 3916–3938, doi:10.1029/2018TC005427.

Hammond, A.L., 1971, Plate Tectonics: The Geophysics of the Earth's Surface: Science, v. 173, p. 40–41, doi:10.1126/science.173.3991.40.

Humphreys, E.D., 1995, Post-Laramide removal of the Farallon slab, western United States: Geology, v. 23, p. 987–990, doi:10.1130/0091-7613(1995)023<0987:PLROTF>2.3.CO;2.

Konstantinou, A., Strickland, A., Miller, E.L., and Wooden, J.P., 2012, Multistage Cenozoic extension of the Albion-Raft River-Grouse Creek metamorphic core complex: Geochronologic and stratigraphic constraints: Geosphere, v. 8, p. 1429–1466, doi:10.1130/GES00778.1.

Liesa, C.L., and Simón, J.L., 2007, A Probabilistic Approach for Identifying Independent Remote Compressions in an Intraplate Region: The Iberian Chain (Spain): Mathematical Geology, v. 39, p. 337–348, doi:10.1007/s11004-007-9084-x.

Lund Snee, J.-E., and Miller, E.L., 2022, Magmatism, migrating topography, and the transition from Sevier shortening to Basin and Range extension, western United States, *in* Craddock, J.P., Malone, D.H., Foreman, B.Z., and Konstantinou, A. eds., Tectonic Evolution of the Sevier-Laramide Hinterland, Thrust Belt, and Foreland, and Postorogenic Slab Rollback (180–20 Ma), Boulder, Colorado, Geological Society of America, Geological Society of America Special Paper 555, doi:10.1130/2021.2555(13).

McKenna, M.C., 1972, Possible Biological Consequences of Plate Tectonics: BioScience, v. 22, p. 519–525, doi:10.2307/1296311.

Molnar, P., 1988, Continental tectonics in the aftermath of plate tectonics: Nature, v. 335, p. 131–137, doi:10.1038/335131a0.

Molnar, P., and Lyon-Caen, H., 1988, Some simple physical aspects of the support, structure, and evolution of mountain belts, *in* Geological Society of America Special Papers, Geological Society of America, v. 218, p. 179–208, doi:10.1130/SPE218-p179.

Smith, A.G., 1976, Plate tectonics and orogeny: A review: Tectonophysics, v. 33, p. 215–285, doi:10.1016/0040-1951(76)90148-7.

Turcotte, D.L., 2006, Modeling geocomplexity: "A new kind of science," *in* Manduca, C.A. and Mogk, D.W. eds., Earth and Mind: How Geologists Think and Learn about the Earth, Geological Society of America, p. 39–50, doi:10.1130/2006.2413(04).

Tye, A.R., Niemi, N.A., Safarov, R.T., Kadirov, F.A., and Babayev, G.R., 2021, Sedimentary response to a collision orogeny recorded in detrital zircon provenance of Greater Caucasus foreland basin sediments: Basin Research, v. 33, p. 933–967, doi:10.1111/bre.12499.

Wells, M.L., Hoisch, T.D., Cruz-Uribe, A.M., and Vervoort, J.D., 2012, Geodynamics of synconvergent extension and tectonic mode switching: Constraints from the Sevier-Laramide orogen: Tectonics, v. 31, TC1002, doi:10.1029/2011TC002913.

Wernicke, B., and Burchfiel, B.C., 1982, Modes of extensional tectonics: Journal of Structural Geology, v. 4, p. 105–115, doi:10.1016/0191-8141(82)90021-9.

Wilson, J.T., 1963, A possible origin of the Hawaiian islands: Canadian Journal of Physics, v. 41, p. 8.

Wilson, J.T., 1969, Static or mobile earth: The current scientific revolution: Tectonophysics, v. 7, p. 600–601, doi:10.1016/0040-1951(69)90033-X.

Chapter 2
Stratigraphy of the Eocene–Oligocene Titus Canyon Formation, Death Valley, California, and Eocene Extensional Tectonism in the Basin and Range

2.1 Abstract

Geologic mapping, measured sections, and geochronologic data elucidate the tectono-stratigraphic development of the Titus Canyon extensional basin in Death Valley, California, and provide new constraints on the age of the Titus Canyon Formation, one of the earliest syn-extensional deposits in the central Basin and Range. Detrital zircon maximum depositional ages (MDAs) and compiled $^{40}Ar/^{39}Ar$ ages indicate that the Titus Canyon Formation spans 40(?)–30 Ma, consistent with an inferred Duchesnean age for a unique assemblage of mammalian fossils in the lower part of the formation. The Titus Canyon Formation preserves a shift in depositional environment from fluvial to lacustrine at ca. 35 Ma, which along with a change in detrital zircon provenance may reflect both the onset of local extensional tectonism and climatic changes at the Eocene–Oligocene boundary. Our data establish the Titus Canyon basin as the southernmost basin in a system of late Eocene extensional basins that formed along the axis of the Sevier orogenic belt. The distribution of lacustrine deposits in these Eocene basins defines the extent of a low-relief orogenic plateau (Nevadaplano) that occupied eastern Nevada at least through Eocene time. As such, the age and character of Titus Canyon Formation implies that the Nevadaplano extended into the central Basin and Range, ~200 km farther south than previously recognized. Development of the Titus Canyon extensional basin precedes local Farallon slab removal by ca. 20 Ma, implying that other mechanisms, such as plate boundary stress changes due to decreased convergence rates in Eocene time, are a more likely trigger for early extension in the central Basin and Range.

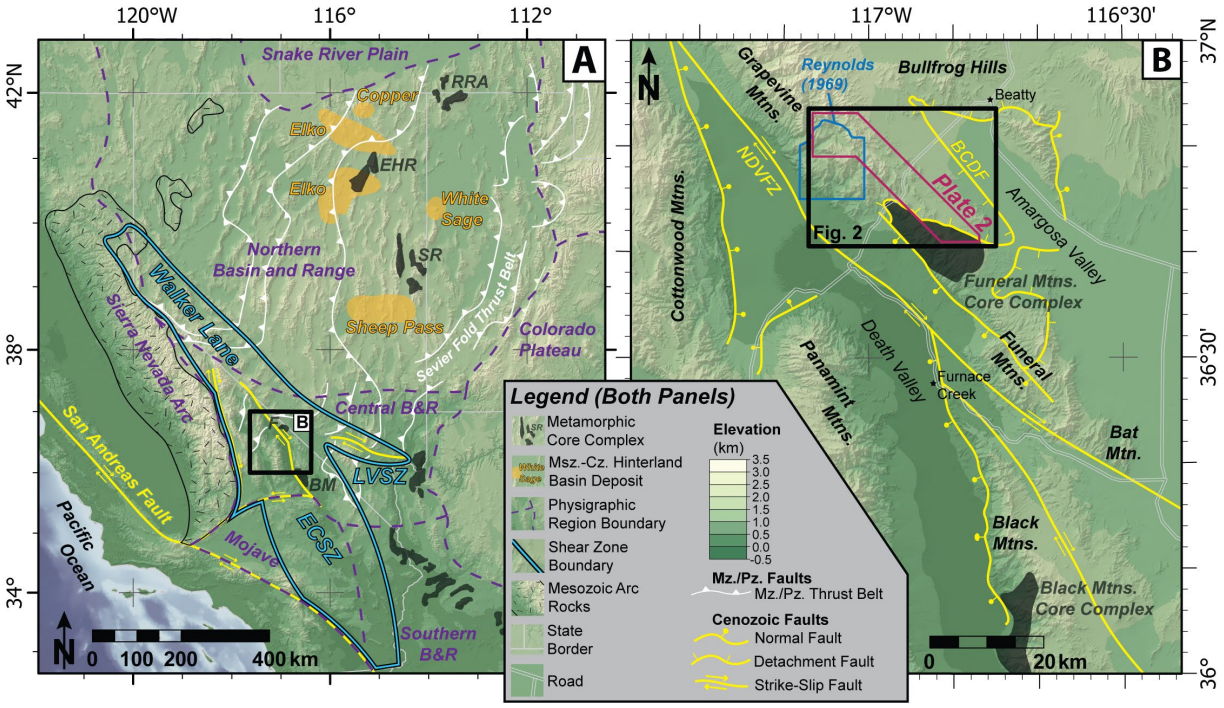


Figure 2.1: Overview maps of the Basin and Range and Death Valley.
Shaded elevation maps of Western North America and the Grapevine and Funeral Mountains of northern Death Valley. Elevation data are from ETOPO and SRTM. Panel A: Shaded relief map of western North America showing physiographic regions, major thrust belts, metamorphic core complexes, the Sierra Nevada arc, the San Andreas fault, major shear zones, and the extent of panel B. Panel B: Shaded relief map of northern Death Valley with key place names, Cenozoic faults, highways, the extent of the map in Reynolds (1969), the extent of the geologic map on Fig. A.2, and the extent of Figure 2.2. Abbreviations: RRA—Raft River–Albion metamorphic core complex, EHR—East Humboldt–Ruby metamorphic core complex; SR—Snake Range metamorphic core complex; F—Funeral Mountains metamorphic core complex; BM—Black Mountains metamorphic core complex; ECSZ—Eastern California shear zone; LVSZ—Las Vegas shear zone; NDVFZ—Northern Death Valley fault zone; BCDF—Boundary Canyon detachment fault.

2.2 Introduction

During the Cenozoic, the Basin and Range extensional province of western North America (Fig. 2.1) underwent distributed continental extension driven by a combination of external stresses (i.e., changing plate boundary stresses) and internal stresses (i.e., topographically induced gravitational potential energy gradients and buoyancy forces) (e.g., Sonder and Jones, 1999). Our ability to separate the relative influence of these geodynamic drivers relies on estimates of the initial state of topography and lithospheric structure prior to extension (e.g., Jones et al., 1996; Molnar et al., 2015; Levandowski et al., 2017; Ghosh et al., 2019; Zhou and Liu, 2019; Lund Snee and Zoback, 2020). Internal

stresses are thought to have been a major driver of pre-Miocene extension in the Basin and Range, when significant gravitational potential energy gradients may have existed along the margins of the Nevadaplano, an inferred region of over-thickened crust constructed across western North America during the Cretaceous Sevier orogeny. External stress changes caused by plate boundary reorganization may also have played a role in continuing extension after initial orogenic collapse. Separating the roles of external stress changes and internal driving stresses on extension in the Basin and Range depends on knowing the location and rate of extension across the Basin and Range throughout the Cenozoic.

Early extension in the Basin and Range is thought to have started with a Cretaceous and Paleogene phase of relatively small magnitude syn-convergent upper-crustal extension, followed by a later phase of larger-magnitude extensional collapse (Dickinson, 2002). Late Cretaceous and early Paleogene low-magnitude, syn-convergent extension is primarily inferred from a sparse stratigraphic record (e.g., Potter et al., 1995; Dubiel et al., 1996; Druschke et al., 2009; Lund Snee et al., 2016), and to a lesser degree from thermochronologic and geochronologic evidence (e.g., Wells et al., 1990; Applegate and Hodges, 1995; Camilleri and Chamberlain, 1997; Sullivan and Snoke, 2007). The record of Eocene to Miocene extension is both more widespread and indicative of larger magnitude extension that likely resulted in significant crustal thinning and topographic collapse, as recorded in thermochronologic data from metamorphic core complexes (e.g., Holm and Dokka, 1991; Lee, 1995; Foster and Raza, 2002; Vogl et al., 2012; Evans et al., 2015; Lee et al., 2017) and stratigraphic sequences deposited in hanging-wall sedimentary basins (Satarugsa and Johnson, 2000; Wagner and Johnson, 2006; Smith et al., 2017; Canada et al., 2020).

The importance of internal stresses in localizing early extension in the Basin and Range is reasoned from the narrow north-south–oriented belt of Cordilleran metamorphic core complexes that lie to the west of the Sevier fold-thrust belt (Fig. 2.1; e.g., Coney and Harms, 1984). Localization of extension along this north-south belt is inferred to have been driven by enhanced topographic and buoyancy stresses in a continental lithosphere that was over-thickened by late Cretaceous shortening during the Sevier orogeny (Coney and Harms, 1984; Sonder et al., 1987; Jones et al., 1998). The presence of thickened crust in the Cordillera prior to extension is supported by multiple

lines of evidence, including palinspastic reconstructions of extension (e.g., Coney and Harms, 1984; Bahadori et al., 2018), stable isotope proxy estimates of paleotopography (e.g., Chamberlain et al., 2012; Lechler et al., 2013; Cassel et al., 2014; Snell et al., 2014), and petrologic estimates of crustal thickness (Best et al., 2009; Chapman et al., 2015).

Despite compelling evidence of crustal thicken-ing in the Sevier hinterland, the lag between the attainment of maximum crustal thickness and subsequent extensional collapse and crustal thinning (~60 m.y.; Chapman et al., 2015) suggests that the onset of extension may also require an external forcing. Two main mechanisms are proposed to have initiated early Basin and Range extension: the first is the time-transgressive, north-south removal of the Farallon slab and subsequent heating and weakening of the over-thickened crust (e.g., McQuarrie and Oskin, 2010); the second is a reduction in plate convergence rates resulting in plate boundary stress changes (e.g., Schellart et al., 2010). A particular challenge in disentangling the roles of these two external drivers is that a wealth of information regarding early Basin and Range extension is derived from studies in the northern Basin and Range (e.g., Potter et al., 1995; Druschke et al., 2009; Cassel et al., 2014; Lund Snee et al., 2016; Smith et al., 2017; Cassel et al., 2018; Long, 2018; Canada et al., 2019; Canada et al., 2020), where Eocene removal of the Farallon slab is contemporaneous with the ca. 40 Ma change in the rate of plate convergence and initiation of trench retreat along the plate boundary (Jurdy, 1984; Humphreys, 1995; McQuarrie and Oskin, 2010; Schellart et al., 2010). Farther south, in the central Basin and Range, Farallon slab removal occurred in the middle Miocene, at ca. 15 Ma, significantly later than the Eocene reduction in plate convergence, thus presenting a potential opportunity to examine the extensional response of the Basin and Range to slab removal and plate boundary reorganization separately. To leverage such an opportunity, however, requires the preservation of thermochronologic or stratigraphic evidence of Eocene extensional tectonism.

The Titus Canyon Formation, in eastern Death Valley (Fig. 2.1), is recognized as one of the earliest syn-extensional basin deposits in the central Basin and Range (Reynolds, 1969; Saylor, 1991; Snow and Lux, 1999; Fridrich and Thompson, 2011; Niemi, 2012). Previous detailed studies of the Titus Canyon Formation primarily focused on mapping its extent (Reynolds, 1969; Niemi, 2012) and describing its lithostratigraphy (Stock and Bode, 1935; Saylor, 1991; Gutenkunst, 2006), collectively providing limited

geochronology and biostratigraphy to constrain the depositional age of the formation and thus the evolution of the Titus Canyon basin. We present ten new measured sections (Fig. A.1) and a detailed geologic map (Fig. A.2) of the Titus Canyon Formation in eastern Death Valley National Park. The stratigraphic sections and geologic mapping are accompanied by newly determined stratigraphic positions of paleontologic sites, detrital zircon U-Pb analyses used to inform both basin provenance and provide maximum depositional age (MDA) constraints, and compiled and recalculated $^{40}Ar/^{39}Ar$ geochronologic age data. We develop both an age model for the Titus Canyon Formation and a basin evolution model for the Titus Canyon basin in response to tectonic drivers. These models yield revisions to both the internal stratigraphy and stratigraphic continuity of the Titus Canyon Formation, as well as a reassessment of regional correlations of early Cenozoic stratigraphy in the Death Valley region. The age model and basin evolution model are considered in the context of Farallon slab removal and Eocene plate boundary reorganization to connect the development of the Titus Canyon basin to the initiation of extension across the entire Basin and Range province.

2.3 Paleogene Stratigraphy of the Death Valley Region—Correlations and Controversies

Paleogene strata in northern Death Valley that may record the earliest phases of extensional tectonism in the western Basin and Range are thin, discontinuous, and difficult to date. These challenges have inhibited the development of lithostratigraphic and chronostratigraphic models of these strata, resulting in a lack of consensus around regional correlation and temporal range of Paleogene rocks (2; e.g., Snow and Lux, 1999; Fridrich and Thompson, 2011). We outline below several of the controversies surrounding these strata to illustrate the challenges associated with correlating these strata across the highly extended Death Valley region.

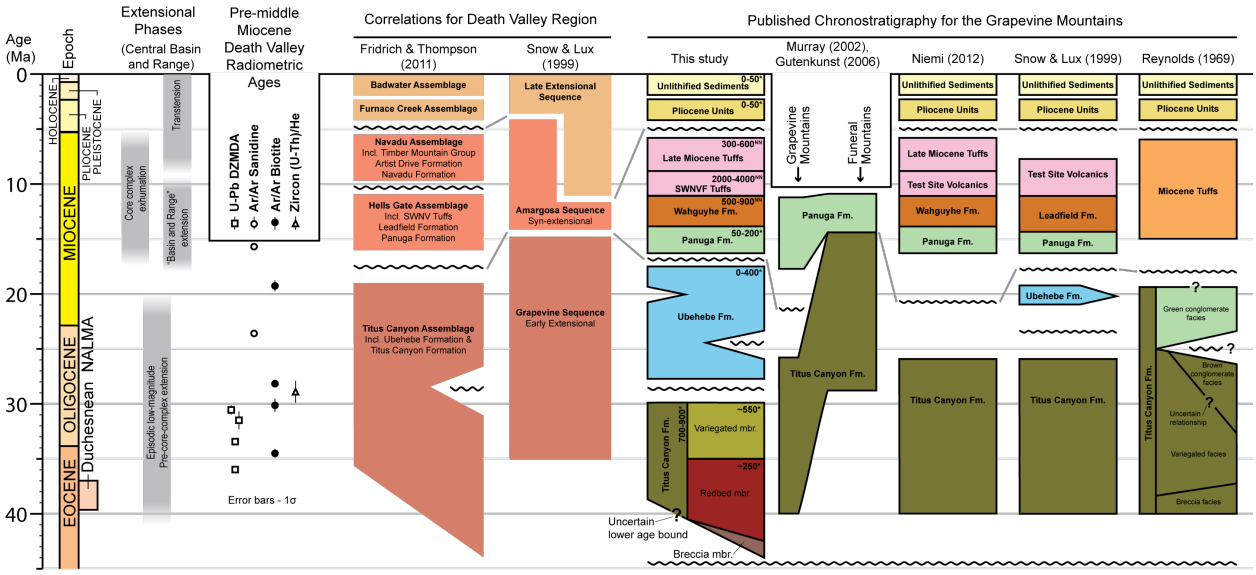


Figure 2.2: Cenozoic chronostratigraphy of Death Valley.
*Stratigraphic correlation chart for the past 45 m.y. showing extensional phases in the central Basin and Range, pre-middle Miocene radiometric ages, Death Valley stratigraphic assemblages, and stratigraphy of the Grapevine and Funeral Mountains (study area). Post- middle Miocene radiometric ages (e.g., Bindeman et al., 2006) were excluded from this chart for visual clarity. All geochronologic ages plotted on this figure are listed in Table 2.1. Numbers in upper-right corner of units in This Study column are compiled and measured stratigraphic thicknesses (meters) where NN—Niemi (2012); *—this study. DZMDA—detrital zircon maximum depositional ages; SWNVF—Southwest Nevada volcanic field.*

Cenozoic strata in the Death Valley region were deposited in rapidly evolving extensional basins, resulting in significant lateral variability, time-transgressive deposition, and complex interplay between deposition and active faulting (e.g., Çemen et al., 1999; Snow and Lux, 1999; Snyder and Hodges, 2000; Niemi, 2002; Fridrich and Thompson, 2011). Early efforts to map and define stratigraphic units within Death Valley were restricted to isolated study areas, resulting in nomenclature that varied from mountain range to mountain range for units that may in fact be lithologically or temporally correlative. Snow and Lux (1999) presented a tectono-stratigraphic framework that coherently placed these individual formations into allostratigraphic packages that they correlated across the entire Death Valley region, and in doing so defined three distinct episodes of basin development (Fig. 2.2). They termed these three phases the pre-extensional, syn-extensional, and post-extensional basin development stages, and although the phases are time-transgressive across the Death Valley region, the phases are identified by the development of regional unconformities, variations in

depositional rates and styles, and variations in volcanic input. This tectono-stratigraphic framework was further expanded by Fridrich and Thompson (2011), who correlated seven tectono-stratigraphic assemblages across the Death Valley region (five of these seven assemblages that are geographically relevant to northern Death Valley are shown on Fig. 2.2). The oldest tectonostratigraphic package, referred to as the Titus Canyon Assemblage (Fridrich and Thompson, 2011) or the Grapevine Sequence (Snow and Lux, 1999), contains two early-extensional units, the Titus Canyon Formation and the Ubehebe Formation; however, the depositional age, formational boundaries, and stratigraphic relationships between these two units remain unresolved (cf. Snow and Lux, 1999; Fridrich and Thompson, 2011).

2.3.1 Previous Work Describing the Titus Canyon Formation

The Titus Canyon Formation was first defined by Stock and Bode (1935), who were excavating fossil land mammal remains in the southern Grapevine Mountains (Fig. 2.1), including a Titanothere skull (Stock, 1936). Stock and Bode performed preliminary stratigraphic measurements and descriptions of the fossiliferous beds and defined the Titus Canyon Formation as an ~1000-m-thick sequence of brightly colored conglomerates, sandstones, limestones, and tuffs, but they did not provide detailed mapping of the areal extent of the unit or of its relationship to adjacent geologic units. The Titus Canyon Formation was originally assigned an Oligocene age based on the mammalian fossils found within it (Stock and Bode, 1935; Mason, 1988). Reynolds (1969) significantly refined the stratigraphy of the Titus Canyon Formation with the detailed geologic mapping in Titanothere and Titus canyons (Fig. 2.3) and also defined a type section for the formation in upper Titus Canyon (Fig. 2.3). Reynolds (1969) internally divided the Titus Canyon Formation into four units, from stratigraphically lowest to highest: (1) the sedimentary breccia facies; (2) the variegated facies; (3) the brown conglomerate facies; and (4) the green conglomerate facies, and provided an interpretation of the Titus Canyon basin as an extensional basin.

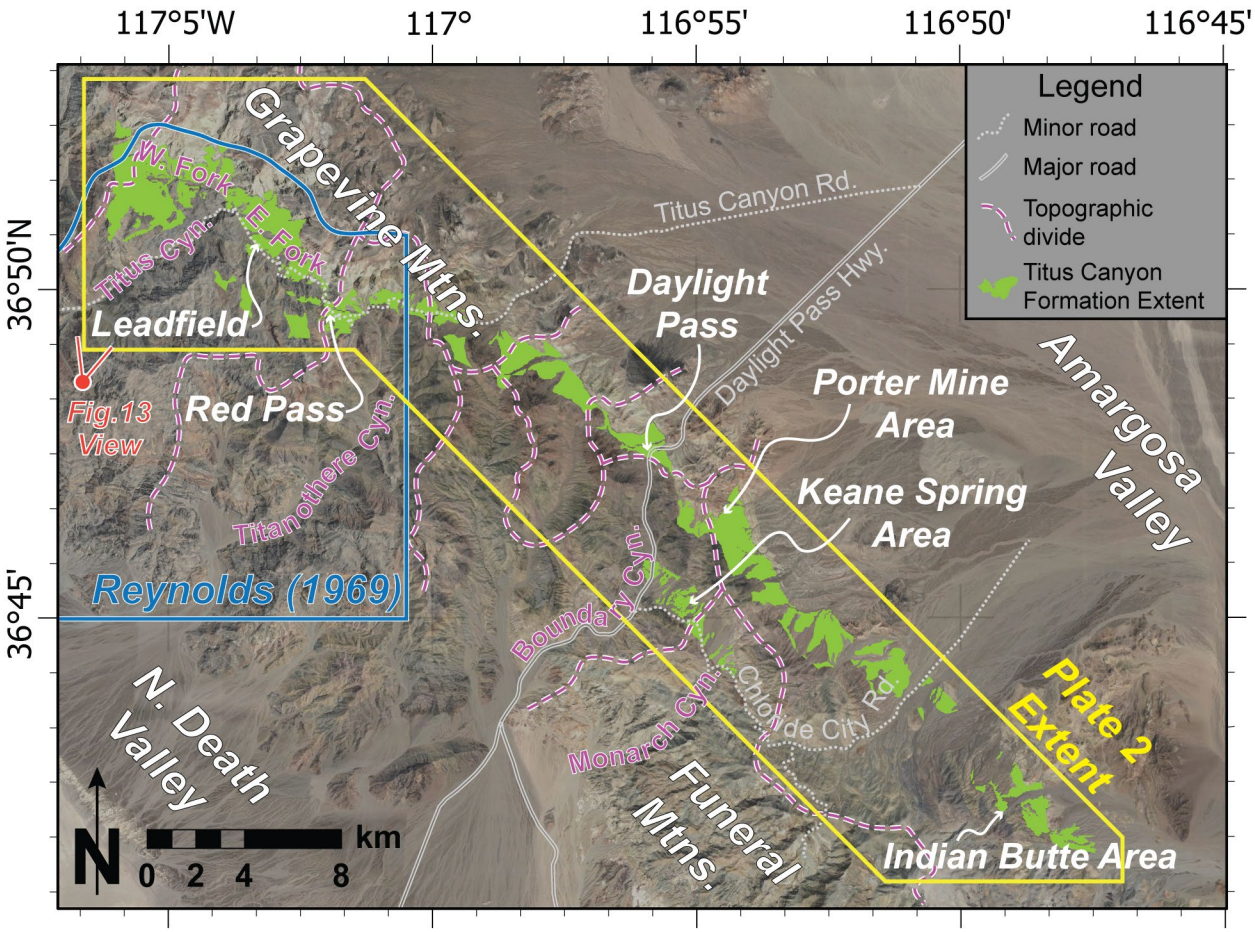


Figure 2.3: Location names in the Grapevine and Funeral mountains.
Aerial imagery of the study area in the southern Grapevine and northern Funeral Mountains showing place names, roads, topographic divides, the extent of the Titus Canyon Formation, the extent of the geologic map of Reynolds (1969), and the extent of the geologic map in Fig. A.2. Imagery is © 2021 Google Earth and Maxar Technologies.

2.3.2 Controversies on the Age and Definition of the Titus Canyon Formation

The stratigraphic definition of the Titus Canyon Formation by Reynolds (1969) was revisited with the expanded availability of geochronologic age control (Snow and Lux, 1999). In particular, $^{40}Ar/^{39}Ar$ ages bracketing an angular unconformity between the green conglomerate facies and the underlying variegated facies revealed a 15 m.y. hiatus in deposition, with an Oligocene depositional age for the variegated facies and a middle Miocene age for the green conglomerate facies (Saylor and Hodges, 1994; Snow and Lux, 1999). This discovery led to a revised stratigraphic definition of the Titus Canyon

Formation that reassigned the green conglomerate facies to the Miocene Panuga Formation (Snow and Lux, 1999).

Geochronologic analyses throughout the Death Valley region led to the revised definition and regional correlation of multiple other early Cenozoic deposits. Early Cenozoic sedimentary strata from Bat Mountain (Fig. 2.1), in the southern Funeral Mountains (Fig. 2.1; McAllister, 1971; Çemen et al., 1982, 1985; Çemen and Wright, 1990) and the Cottonwood Mountains (Fig. 2.1; McAllister, 1952; Snow, 1990; Snow and White, 1990; Snow, 1993) were demonstrated to share latest Oligocene to early Miocene depositional ages, on the basis of intercalated tuffs (Çemen et al., 1999; Snow and Lux, 1999). These strata were defined as the Ubehebe Formation and consist of a fining-upwards sequence of conglomerates, sandstones, marls, and tuffs exposed in the Cottonwood and southern Funeral Mountains (Fig. 2.1; Çemen et al., 1982; Çemen et al., 1999; Snow and Lux, 1999). In both the Cottonwood Mountains and the Funeral Mountains (Fig. 2.1), the Ubehebe Formation is deposited directly on the sub-Tertiary unconformity (i.e., the regional unconformity across the Basin and Range defined by the deposition of Cenozoic strata on deformed Paleozoic or Mesozoic strata), and it is separated by a distinct angular unconformity from the overlying Panuga Formation (Snow and Lux, 1999).

In the southern Grapevine Mountains (Fig. 2.1), where the Titus Canyon Formation is defined, no strata demonstrably equivalent in age to the Ubehebe Formation have been previously recognized (Reynolds, 1969; Niemi, 2012). Snow and Lux (1999) considered the possibility that the Titus Canyon Formation might be an older, time-transgressive equivalent to the Ubehebe Formation, since Ubehebe Formation strata were not definitively observed stratigraphically above the Titus Canyon Formation anywhere, and the two units share some lithologic similarities. They concluded, however, that the Titus Canyon Formation is most likely distinct in age from, and thus not correlative with, the Ubehebe Formation. This conclusion hinged on reports that the Titus Canyon Formation is overlain by 20–24 Ma strata, equivalent in age to the Ubehebe Formation, at two isolated and relatively small, exposures (Reynolds, 1974; Wright and Troxel, 1993).

Strata broadly similar in lithology to the Titus Canyon and Ubehebe Formations have subsequently been reported along the eastern flank of Funeral Mountains (Fig. 2.1; Murray, 2002; Gutenkunst, 2006; Ridgway et al., 2011). Sections along the eastern

Funeral Mountains were correlated by Gutenkunst (2006) to the Titus Canyon Formation on the basis of their similar lithofacies. However, geochronologic analyses from these sections ranged from latest Oligocene to early Miocene (Gutenkunst, 2006), which would suggest temporal equivalence to the Ubehebe Formation, not the Titus Canyon Formation. The continuum of exposures of early Cenozoic strata from the Grapevine Mountains southward along the eastern margin of the Funeral Mountains to Bat Mountain, at the southern end of the Funeral Mountains (Fig. 2.1), led Fridrich and Thompson (2011) to challenge the distinction of Snow and Lux (1999) and to propose that the Titus Canyon and Ubehebe Formations reflect a single, time-transgressive continuum of deposition. Support for this interpretation, in part, arises from a lack of definitive absolute age control that differentiates the depositional age of the Titus Canyon Formation from the Ubehebe Formation.

2.3.3 Resolving the Early Extensional and Basin Development History of the Death Valley Region

The challenge of resolving and understanding the early extensional history of the Death Valley region arises from two specific issues. First is the lack of absolute age control on the deposition of the Titus Canyon Formation, as discussed above. The age of the Titus Canyon Formation is primarily derived from paleontologic evidence and has been reported as Eocene to Oligocene (Stock and Bode, 1935; Mason, 1988; Lander, 2019), presenting difficulties in comparing the age of the Titus Canyon Formation to other lithologic units. The second issue is a lack of detailed mapping of the extent, continuity, and regional correlation of the Titus Canyon Formation, which had the added effect of preventing extrapolation of the limited biostratigraphic and geochronologic age constraints that do exist for the formation. Geologic maps at 1:48,000 scale in the Grapevine and Funeral Mountains (Cornwall and Kleinhampl, 1964; Wright and Troxel, 1993; Niemi, 2012) expanded the recognized areal extent of the Titus Canyon Formation beyond Titus Canyon to a northwest-southeast strip along the eastern Grapevine and Funeral Mountains (Fig. 2.3). However, these maps omit the internal stratigraphy of the Titus Canyon Formation as defined by Reynolds (1969), and, in areas particularly relevant

to discriminating the Titus Canyon and Ubehebe Formations, pre-date the recognition of these two formations (e.g., Cornwall and Kleinhampl, 1964; Wright and Troxel, 1993).

Below, we present detailed measured sections (Fig. A.1) and geologic mapping (Fig. A.2) in the southern Grapevine Mountains and northern and central Funeral Mountains (Fig. 2.1) that inform the above-described controversies. The internal stratigraphy of the Titus Canyon Formation is mapped throughout the study region, with recognition of the possibility that the Ubehebe Formation can be differentiated from the Titus Canyon Formation. Robust geochronologic age constraints (Table 2.1) are provided for the type section of the Titus Canyon Formation and are integrated with previously unpublished age constraints from other sections to develop a coherent early Cenozoic chronostratigraphy for eastern Death Valley and resolve the age, stratigraphic definition of, and regional tectonic significance of, the Titus Canyon Formation.

Table 2.1: Summary of geochronology samples, sources, and ages.

Sample	Latitude (ºN)	Longitude (ºW)	Age ± 1S.E. (Ma)	Age ± 1σ (Ma)	Method	Grains	Source	Analytical data	Location certainty	Stratigraphic position
Unit 38 Tuff	36.84675	117.04754	-	30.6±0.3	DZMDA	106	This study	Table A.1	GPS	Unit 38 Tuff, Variegated Mbr., Titus Canyon Fm.
TC-09-04	36.84037	117.04137	-	31.5±0.8	DZMDA	87	This study	Table A.1	GPS	Variegated Mbr., Titus Canyon Fm.
TC19-9	36.84424	117.05414	-	33.4±0.2	DZMDA	105	This study	Table A.1	GPS	Unit 8 Tuff, Variegated Mbr., Titus Canyon Fm.
TC19-2	36.82998	117.01923	-	36.0±0.2	DZMDA	105	This study	Table A.1	GPS	Variegated Mbr., Titus Canyon Fm.
TC19-5	36.83873	117.03860	-	N.D. **	DZ	110	This study	Table A.1	GPS	Redbed Mbr., Titus Canyon Fm.
TC19-01NN	36.85915	117.09045	-	N.D. **	DZ	103	This study	Table A.1	GPS	Redbed Mbr., Titus Canyon Fm.
TC19-02NN	36.86059	117.08305	-	N.D. **	DZ	110	This study	Table A.1	GPS	Redbed Mbr., Titus Canyon Fm.
17TCTF04	36.86301	117.06580	28.9±1.0	-	(U-Th)/He zircon	3	This study	Table A.2	GPS	Unit 38 Tuff, Variegated Mbr., Titus Canyon Fm.
17TCTF01	36.83907	117.03937	15.2±1.4 #	-	(U-Th)/He zircon	3	This study	Table A.2	GPS	Unit 8 Tuff, Variegated Mbr., Titus Canyon Fm.
17TCTF03	36.85942	117.06672	25.7±4.0 #	-	(U-Th)/He zircon	3	This study	Table A.2	GPS	Unit 8 Tuff, Variegated Mbr., Titus Canyon Fm.
17CH03	36.73715	116.85796	24.4±2.1	-	(U-Th)/He zircon	3	This study	Table A.2	GPS	Rocks of Porter Mine (Ubehebe Fm.)
FM-2_16.5 Biotite2	36.69517	116.79875	-	19.3±0.5	Ar/Ar biotite	-	Murray (2002), Gutenkunst (2006)	Table A.3, Fig. A.3	Estimated*	Rocks of Porter Mine (Ubehebe Fm.)
FM-3_102.5 Sanidine1	36.69304	116.79596	-	23.6±0.1	Ar/Ar sanidine	-	Murray (2002), Gutenkunst (2006)	Table A.3, Fig. A.3	Estimated*	Rocks of Porter Mine (Ubehebe Fm.)
FM-3_2.1 Biotite1	36.69159	116.79298	-	28.2±0.2	Ar/Ar biotite	-	Murray (2002), Gutenkunst (2006)	Table A.3, Fig. A.3	Estimated*	Rocks of Porter Mine (Ubehebe Fm.)

TC-4	NL	NL	-	30.2±0.6	Ar/Ar biotite	-	Saylor and Hodges (1994)	††	NL	Unit 38 Tuff, Variegated Mbr., Titus Canyon Fm.
T1	NL	NL	-	34.5±0.4	Ar/Ar biotite	-	Saylor and Hodges (1994)	††	NL	Unit 8 Tuff, Variegated Mbr., Titus Canyon Fm.
592-GV1 K1	36.8650	117.0778	-	15.7±0.2	Ar/Ar sanidine	-	Snow and Lux (1999)	††	Estimated§	Panuga Fm.

* Location uncertainty ~200 meters. Position of sample within a measured stratigraphic section is known, but location of measured section is uncertain.

NL No sample location information provided in Saylor and Hodges (1994)

§ Sample coordinates reported in Snow and Lux are incorrect. Coordinates given here are estimated from bearing, distance, and stratigraphic position described in Snow and Lux (1999).

Age inconsistent with stratigraphic constraints.

** No Cenozoic zircons for MDA.

†† Original analytical data no longer available (K. Hodges, personal commun., 2020).

2.4 Methods

To refine the internal stratigraphy and determine an age model for the Titus Canyon Formation, we measured stratigraphic sections, undertook largescale field mapping, and completed zircon U-Pb geochronology. These efforts resulted in ten detailed measured stratigraphic sections (Fig. A.1), a 1:24,000 scale geologic map (Fig. A.2), and maximum depositional ages (MDAs) for the Titus Canyon Formation. These data were correlated with published and unpublished $^{40}Ar/^{39}Ar$ age determinations to develop a new basin evolution and regional stratigraphic model for the early-extensional sequences in Death Valley.

2.4.1 Geologic Mapping and Measured Sections

Geologic mapping included field and remote components. Fieldwork was conducted over two field seasons in 2019. We measured and described the internal stratigraphy of the Titus Canyon Formation using a Jacob's staff at ten locations, comprising a total of 2600 m of strata. During geologic mapping in the field, the locations of faults and contacts were recorded directly onto high-resolution, ortho-rectified aerial imagery using a GPS-enabled tablet running Esri Collector for ArcGIS. Field mapping was principally focused on detailed analysis of Eocene to early Miocene stratigraphic units, with older and younger units mapped remotely (see index map on Fig. A.2). The locations and contacts of Proterozoic and Paleozoic units were principally derived from previous 1:48,000 and 1:100,000 geologic maps (Cornwall and Kleinhampl, 1964; Reynolds, 1969; Wright and Troxel, 1993; Carr et al., 1996; Niemi, 2012). Geologic contacts on those maps, which were originally on topographic base maps, were digitally refined to 1:24,000 scale by tracing color changes visible on high-resolution aerial imagery. In addition to ground truthing, some contacts between early Cenozoic sedimentary strata (including the Titus Canyon Formation) and overlying Miocene units were mapped by referencing the geologic mapping of Niemi (2012) and unpublished mapping by C. Fridrich (1999, personal commun.) and tracing contacts onto high-resolution aerial imagery. All field and remote mapping was compiled on a 1:24,000 U.S. Geological Survey topographic map base composed of digital line graphs (DLGs; 1980–1990 vintage), which were simplified for visual clarity (Fig. A.2).

We precisely located Caltech and the Los Angeles County Museum paleontological localities excavated in the 1930s (Stock and Bode, 1935; Mason, 1988; Lander, 2019) by the visual matching of distinctive outcrops visible in original glass slide images of excavations to their modern exposures. We have purposefully obfuscated the exact geographic locations of fossil localities to protect the sites, although the stratigraphic position of such sites in reported measured sections (Fig. A.1) is representative of their observed positions within the Titus Canyon Formation.

2.4.2 Geochronology

New geochronologic analyses were undertaken by multiple methods; these new data were combined with previously unpublished $^{40}Ar/^{39}Ar$ ages to obtain an age model for deposition of the Titus Canyon Formation. All ages are summarized in Table 2.1.

Detrital Zircon U-Pb Geochronology

Seven samples of tuffs and tuffaceous sandstones were collected from a range of stratigraphic levels within the Titus Canyon Formation for geochronologic analysis (Fig. 2.4 and Table 2.1). Selected samples appeared tuffaceous as assessed in the field with a hand lens. Zircon separates were produced at the University of Michigan following standard mineral separation techniques for rock crushing, sieving, and heavy liquids separation. U-Pb geochronology on detrital zircons (analytical data are available in Table A.1) was performed using laser ablation–inductively coupled plasma mass spectrometry (LA-ICPMS) at the University of Arizona LaserChron Center following the analytical methods of Gehrels et al. (2008).

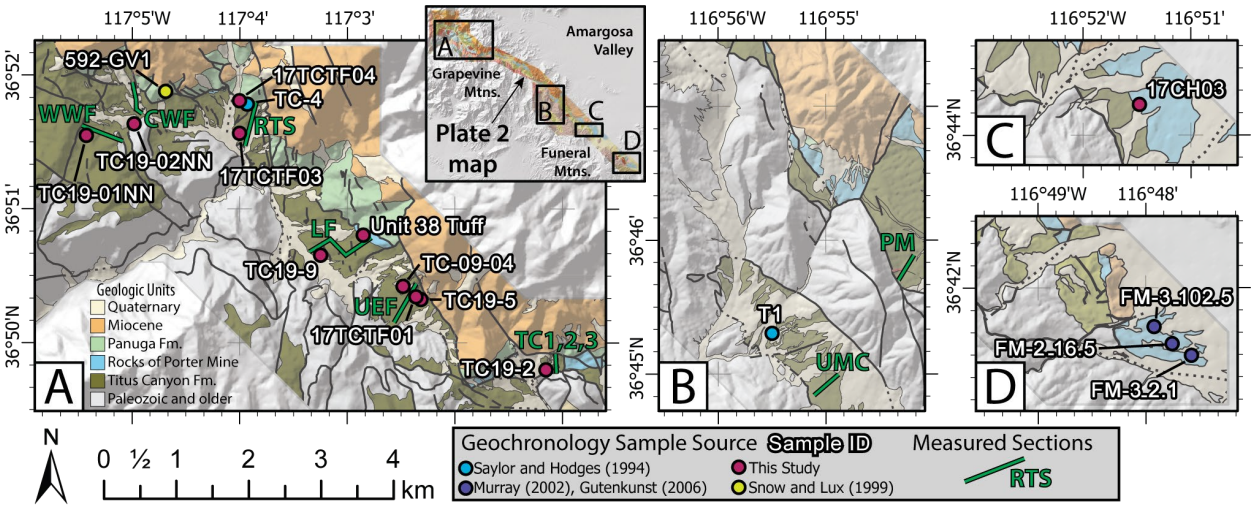


Figure 2.4: Location map of samples and measured sections.
Location maps of measured sections (green and black; Fig. A.1) and geochronology samples (various colors with black outlines; Table 2.1). Geologic base map is simplified from Fig. A.2 with hillshade overlay. Abbreviated measured section names from Fig. A.1: WWF—Western West Fork; CWF—Canyon West Fork; RTS—Reynolds Type Section; LF—Leadfield; UEF—Upper East Fork; TC1,2,3—Titanothere Canyon 1, 2, and 3; UMC—Upper Monarch Canyon; PM—Porter Mine. Latitude-longitude coordinates for of the base of each measured section are on Fig. A.1.

Maximum Depositional Age Analysis from U-Pb Detrital Zircon Geochronology

Maximum depositional ages were calculated from the zircon U-Pb ages for detrital zircon samples that contained Cenozoic zircons (four out of seven samples). There are a variety of published methods for MDA determination (e.g., Dickinson and Gehrels, 2009; Coutts et al., 2019), many of which are recognized to bias MDA estimates to young values when seeking the youngest zircon age or population (e.g., Coutts et al., 2019; Vermeesch, 2021). We present MDAs based on the Maximum Likelihood Age (MLA) algorithm, which is designed to minimize MDA bias (Galbraith and Laslett, 1993; Vermeesch, 2021). Application of the MLA method (Fig. 2.5) yielded consistent age determinations for a single tuffaceous unit dated by U-Pb detrital zircon MDA, $^{40}Ar/^{39}Ar$, and zircon (U-Th)/He methods (Unit 38 tuff; Table 2.1), and consistent U-Pb detrital zircon MDA and $^{40}Ar/^{39}Ar$ ages determined on samples from two localities that were inferred to be the same geologic unit based on field mapping and stratigraphic relationships.

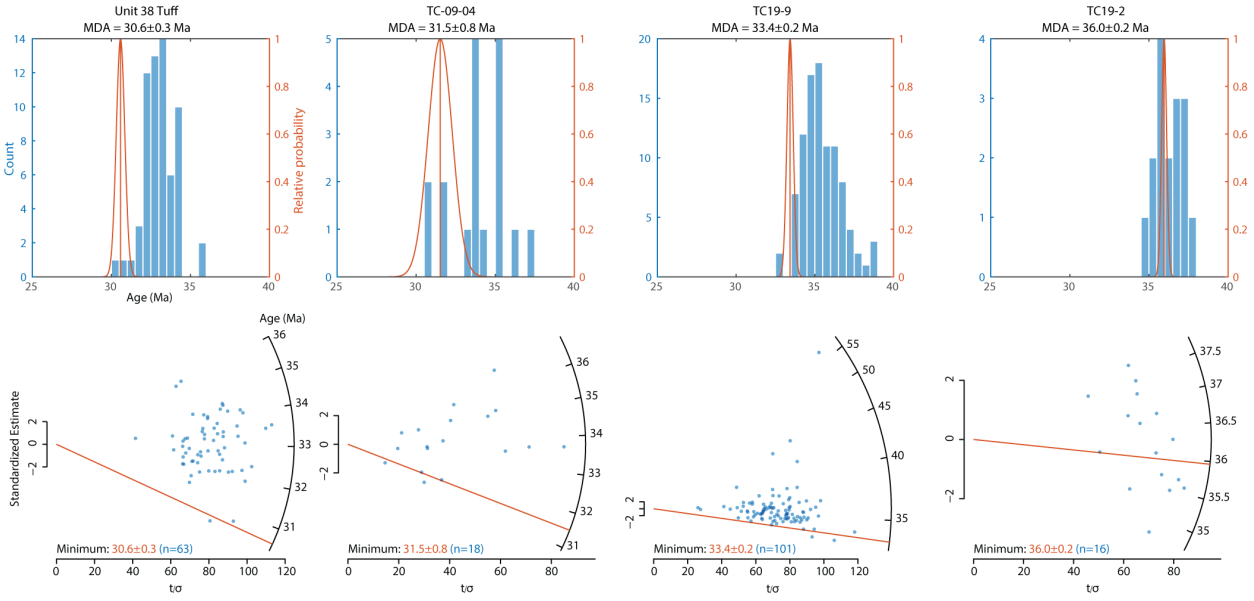


Figure 2.5: Radial plots and histograms for detrital zircon MDA calculations. *Detrital zircon U-Pb age distributions, radial plots, and estimated maximum depositional ages (MDA) based on the Maximum Likelihood Estimation (MLE) algorithm of Vermeesch (2021) for four samples that contained Cenozoic zircons. Lower panels show radial plots (Galbraith and Laslett, 1993; Vermeesch, 2021) along with an orange line indicating the estimated MDA. The maximum likelihood MDA is reported with ±1σ errors. The upper plots show histograms of individual grain ages (blue) overlaid with the normal probability distribution (orange) of the MDA age based on the MLE analysis. Each sample uses all of its Cenozoic grains for the MDA calculation (n given in radial plots) with the exception of the Unit 38 Tuff which has a single 24 Ma outlier removed. The 24 Ma grain had 6675 ppm U—6× the U concentration of the other grains in the sample—and contradicted independent stratigraphic constraints on the age of the Unit 38 Tuff.*

All Cenozoic zircon U-Pb ages from each detrital zircon sample were included in each MLA analysis, with the exception of a single 24 Ma zircon grain from the Unit 38 Tuff. This age was excluded because it could be demonstrated independently that the age disagreed with stratigraphic constraints on the depositional age of the unit sampled. Additionally, the measured U concentration from this grain (6675 ppm) was a factor of 6 higher than for any other grain analyzed, suggesting that the young age may be the result of diffusional lead loss due to radiation damage (Lee et al., 1997).

Zircon (U-Th)/He Thermochronology

Four tuffaceous sandstones were dated with the (U-Th)/He method at the University of Michigan Thermochronology lab following the standard methods of Niemi and Clark (2018). Three grains were analyzed per sample and reported uncertainties are

±1 standard error of the mean age of each sample. Ages are summarized in Table 2.1, and full analytical data are in Table A.2.

$^{40}Ar/^{39}Ar$ Geochronology

No new $^{40}Ar/^{39}Ar$ analyses were performed for this study; however, six previously analyzed $^{40}Ar/^{39}Ar$ ages from tuffs within the Titus Canyon Formation and other Cenozoic strata in eastern Death Valley were recalculated and updated to the K decay constant of Renne et al. (2010, 2011) and the MMhb-1 monitor mineral age of Spell and McDougall (2003). Three unpublished $^{40}Ar/^{39}Ar$ ages from Cenozoic strata in the eastern Funeral Mountains (Gutenkunst, 2006) were recalculated from original analytical data using IsoplotR (Vermeesch, 2018) to determine plateau, isochron, weighted, and integrated ages (Fig. A.2 and Table A.3). Two additional unpublished $^{40}Ar/^{39}Ar$ ages collected from the Titus Canyon Formation (Saylor and Hodges, 1994) were recalculated using the ArAR program (Mercer and Hodges, 2016). Original analytical data are not available for the samples from Saylor and Hodges (K. Hodges, personal commun., 2020). A single published $^{40}Ar/^{39}Ar$ age from the Panuga Formation in the southern Grapevine Mountains (Snow and Lux, 1999) was recalculated using ArAR (Mercer and Hodges, 2016). All $^{40}Ar/^{39}Ar$ ages are summarized in Table 2.1.

The accuracy of the geographic and stratigraphic positions of the $^{40}Ar/^{39}Ar$ samples is variable (location uncertainties are summarized in Table 2.1). Three sample locations from Gutenkunst (2006) were reported as stratigraphic position within a measured stratigraphic section from the eastern Funeral Mountains (section FM of Murray, 2002). The location of the FM measured section is approximated from a small-scale figure; so we employed field observations of the orientation and younging direction of strata in the field area of Murray (2002) to assess the location of the measured section and to estimate the geographic position of the samples in the field (Fig. 2.4). The two sample locations from Saylor and Hodges (1994) are unknown, but their approximate location within the stratigraphy was reported. An $^{40}Ar/^{39}Ar$ age from the Panuga Formation in the southern Grapevine Mountains (Fig. 2.1) is well defined stratigraphically (Snow and Lux, 1999). The written description of the sample locality within the Panuga Formation is consistent with the known distribution of this formation (Snow and Lux, 1999); however, reported geographic coordinates for this sample are

inconsistent with both the written description and the distribution of the Panuga Formation. We therefore estimated the sample coordinates from the written description (Sample 592-GV1 K1; Fig. 2.4 and Table 2.1).

2.5 Revised Stratigraphy and Age of Paleogene Strata in Eastern Death Valley

Our mapping supports the division of Paleogene strata in eastern Death Valley into the 40(?)–30 Ma Titus Canyon Formation, and the ca. 18–28 Ma Rocks of Porter Mine, units that can be differentiated based on their lithologic content, differing volcanic content, distinct depositional timing based on radiometric ages, and consistent superposed stratigraphic relationship throughout the map area. Based on its distinctive lithology and our revised geochronology, the Rocks of Porter Mine may correlate with the Ubehebe Formation of Snow and Lux (1999). We describe both units below, with emphasis on the characteristics that distinguish them, both in the field and in terms of depositional age.

2.5.1 Titus Canyon Formation

Our geologic mapping identifies exposures of the Titus Canyon Formation in a 35-km-long strip along the northeastern margin of the southern Grapevine and northern Funeral Mountains (Fig. 2.3 and Fig. A.2). The thickness of the formation varies from 500 m to ~1 km, with an overall trend of thickening to the northwest (Fig. A.2). Compared to previous studies (Stock and Bode, 1935; Cornwall and Kleinhampl, 1964; Wright and Troxel, 1993), our mapping extends the recognized distribution of the Titus Canyon Formation farther to the southeast. A small number of exposures originally mapped as the Titus Canyon Formation ~10 km northwest of the area mapped on Fig. A.2 (Stock and Bode, 1935; Saylor, 1991) have been previously refined as correlating with younger stratigraphic units (Niemi, 2012).

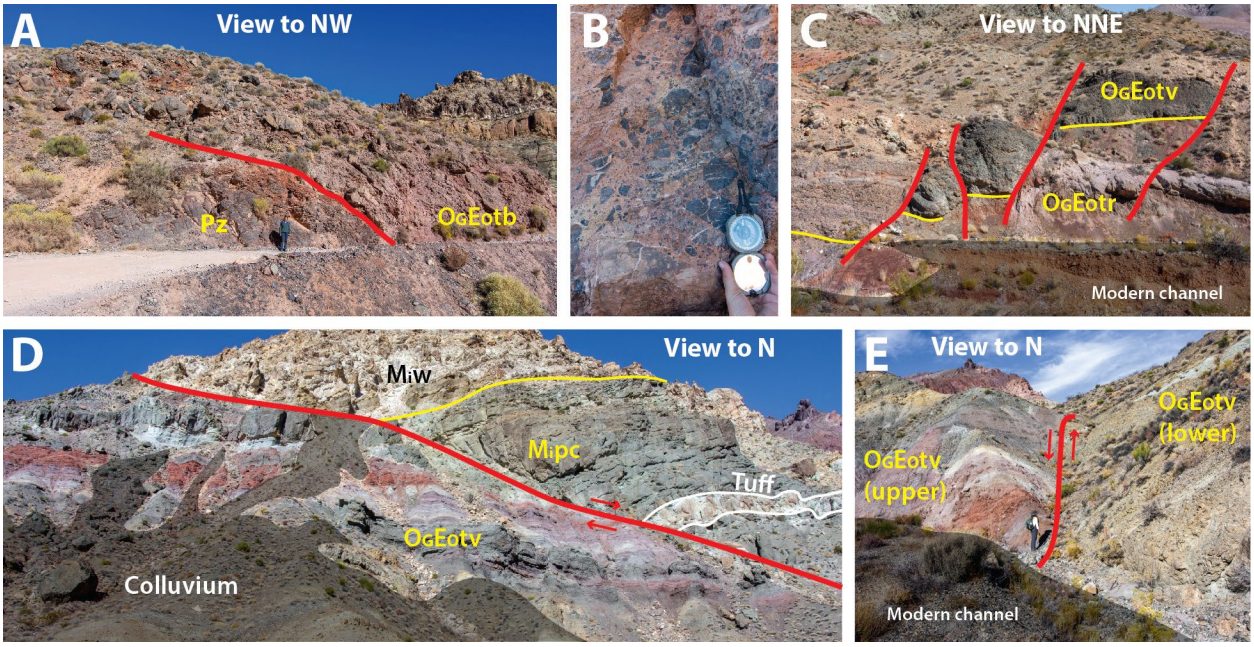


Figure 2.6: Images of faults in the Grapevine Mountains.
Field photos of different expressions of normal faulting in the study area. (A) Shallowly dipping normal fault exposed ~0.5 km east of Red Pass on Titus Canyon road (Fig. 2) separating the Breccia member of the Titus Canyon Formation (OGEOtb) from Paleozoic rocks (Pz) below. (B) Typical matrix supported angular to subangular breccia of the Basal breccia member of the Titus Canyon Formation. The Titus Canyon Formation is faulted along much of its basal contact; so some exposures of limestone breccia near the base of the formation may be products of fault-zone brecciation as opposed to sedimentary deposition. (C) Characteristic small offset, closely spaced, and steeply dipping normal faults that pervade the study area, here seen offsetting the contact between the Variegated (OGEOtv) and Redbed (OGEOtr) members of the Titus Canyon Formation. (D) A major shallowly dipping normal fault placing Miocene Panuga Formation (Mipc) and Wahguyhe Formation (Miw) onto the upper Variegated member of the Titus Canyon Formation (OGEOtv) in the upper west fork of Titus Canyon (Fig. 2.2). (E) Moderate offset steeply dipping normal fault in the upper west fork of Titus Canyon with an opposite dip direction (~NE) to the majority of faults (~SW) in the study area.

The depositional base of the Titus Canyon Formation is best exposed in the West Fork of Titus Canyon (in the vicinity of 36.8551°N, 117.0852°W), where the formation is deposited on the Cambrian Bonanza King Formation. Toward the southeast end of the mapping area near Indian Butte (Fig. 2.3, ~36.7015°N, 116.8117°W), the nature of the base of the Titus Canyon Formation becomes obscured by poor exposure and pervasive faulting but appears to lie primarily on the Cambrian Zabriskie Quartzite or Neoproterozoic to Cambrian Wood Canyon Formation (Fig. A.2). In many locations, especially near the southeastern extent of the map, extensive post-depositional normal faulting (Fig. 2.6) has put the Titus Canyon Formation in fault contact with underlying Paleozoic bedrock, making it difficult to determine the nature of the depositional base of

the formation. Preserved exposures of the Titus Canyon Formation all lie in the hanging wall of the late Miocene Boundary Canyon detachment fault (Fig. A.2; Wright and Troxel, 1993).

Revised Lithostratigraphy of the Titus Canyon Formation

Here, we redefine the internal stratigraphy of the Titus Canyon Formation from the previous descriptions provided by Reynolds (1969) and Snow and Lux (1999). Reynolds uses the term "facies" in the names of all his mapped sub-formation units (e.g., brown conglomerate facies). Our mapping indicates that the divisions between our proposed map units are laterally extensive and well defined; so we divide the stratigraphy of the Titus Canyon Formation into members, listed here from oldest to youngest: (1) the Basal breccia member (largely unmodified from Reynolds' sedimentary breccia facies); (2) the Redbed member (rocks that were originally included in the lower part of the variegated facies of Reynolds); and (3) the Variegated member (the remainder of the variegated facies of Reynolds after removing the Redbed member). We include the brown conglomerate facies of Reynolds in the Variegated member.

Basal breccia member. The lowest unit of the Titus Canyon Formation, the Basal breccia member, includes rocks previously called the sedimentary breccia facies by Reynolds (1969). The member is relatively thin (~0–30 m) and discontinuous, even where it is best exposed in the west fork of Titus Canyon and along the Titus Canyon Road southeast of Red Pass (Fig. 2.3). The base of the member is marked by the first occurrence of angular fragments of Bonanza King Formation (Fig. 2.6B), which are typically deposited onto intact Bonanza King Formation. The member consists of massive or weakly stratified matrix-supported breccia and conglomerate with pebble to boulder-sized (up to 2-m-diameter) clasts composed of primarily Paleozoic limestone, quartzite, and chert.

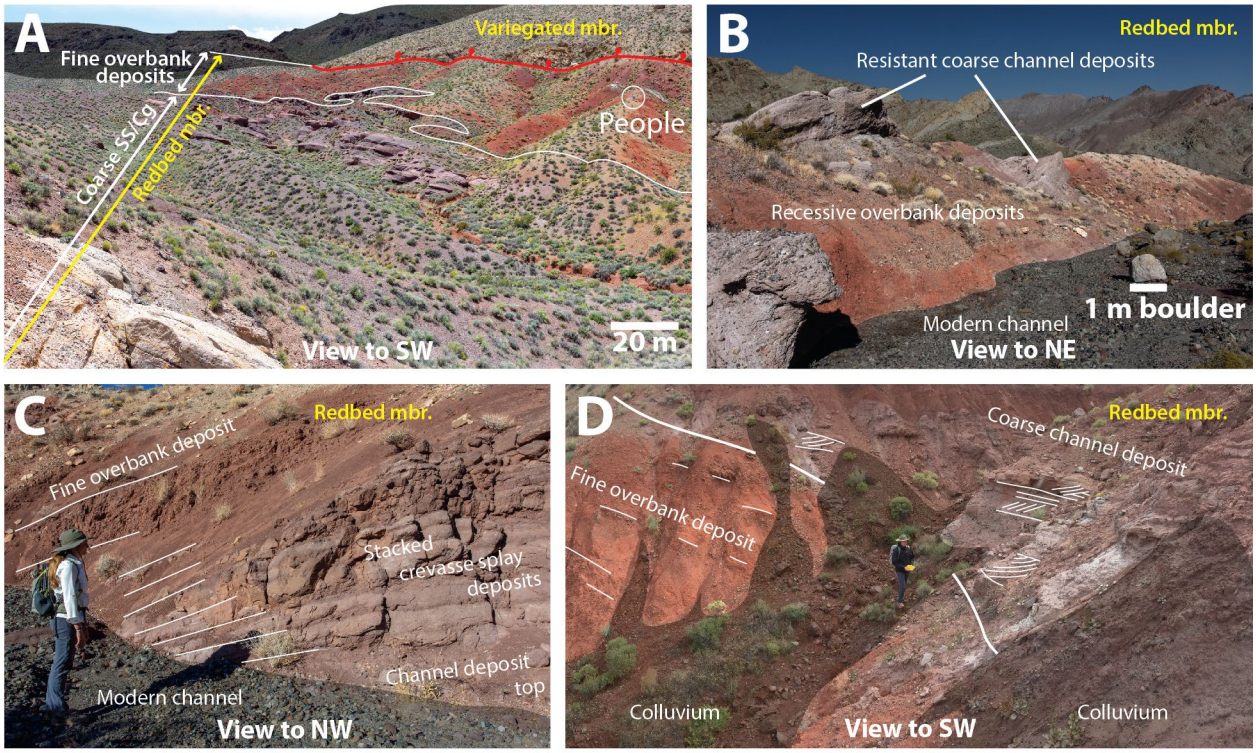


Figure 2.7: Images of the Redbed member of the Titus Canyon Formation. *Field photos of the Redbed member of the Titus Canyon Formation in the west fork of Titus Canyon (Fig. 2.2). (A) View of the transition between thick clast- supported quartzite conglomerates (bottom left) into overlying fine-grained brick-red siltstones (upper right). The Variegated member is visible at the top of the image across a fault. (B) Exposure of the fining-upward purplish-gray cross-bedded pebbly sandstone channel bodies cutting through brick-red overbank deposits that characterize the upper Redbed member. (C) Repeated ~20-cm-thick sandstone beds that thin and fine upwards into overlying red siltstone overbank deposits. These may represent episodic crevasse splay events from a nearby channel. (D) Typical exposure of resistant purple cross-bedded sandstone channel body above recessive brick-red siltstone overbank deposits. Visible on the left of the panel is a typical rhythmic sequence of slightly more resistant and calcareous beds within an overall recessive red siltstone. Abbreviations: SS—sandstone; Cg—conglomerate.*

Redbed member. We define the Redbed member of the Titus Canyon Formation as a succession of recessive brick-red calcareous siltstones to mudstones interfingered with resistant packages of grayish-purple sandstone and matrix-supported sandy conglomerate (Figs. 2.7B and 2.7D). This member approximately represents the lower third of the variegated facies defined by Reynolds (1969). The Redbed member comprises 250 m of strata at its thickest exposures, though many locations have as little as 50 m of section that may be truncated by faults (Fig. A.1). The Redbed member is present across the entire map area, identifiable by its distinct combination of purplish-gray conglomerate and sandstone with brick-red siltstone. The Redbed member fines upward

overall, with its base consisting of predominantly purplish-gray cross-bedded sandy conglomerate that transitions up-section to recessive brick-red siltstone, which quickly become the dominant lithology toward the top of the member (Fig. 2.7A). While the transition from dominantly purple-gray conglomerate to brick-red siltstone occurs at ~150 m above the base of the member in the west fork of Titus Canyon (Fig. 2.3), elsewhere the transition varies in stratigraphic position within the member, and we therefore did not interpret the transition as a mappable unit contact. The red recessive exposures of the member are characterized by massive or weakly stratified brick-red siltstone containing sparse secondary calcite veins, sparse light greenish-gray oxidation halos, and sparse knobby calcareous concretions. In some places, the recessive red siltstone is organized into 1–5-m-thick bedding packages that become slightly more resistant and calcareous up section before truncating at a planar surface and repeating (Fig. 2.7D). Intervals of resistant grayish-purple conglomerate contain well-rounded pebble- to cobble-sized clasts composed primarily of quartzite with some limestone and chert. Quartzite clasts are highly polished and have percussion marks. Conglomerate lenses generally fine upwards into grayish-purple sandstone consisting of fine to coarse sub-angular grains in planar beds or sets of 10–20-cm-tall cross-beds (Figs. 2.7C and 2.7D). The purple sandstone and conglomerate intervals weather into resistant, smooth, rounded outcrops, while the recessive brick-red siltstone forms steep slopes mantled with loose weathered material (Figs. 2.7A and 2.7B). All the Duchesnean fossil localities (Stock and Bode, 1935; Lander, 2019) that we were able to locate lie within the brick-red siltstone beds of the Redbed member (Fig. A.1).

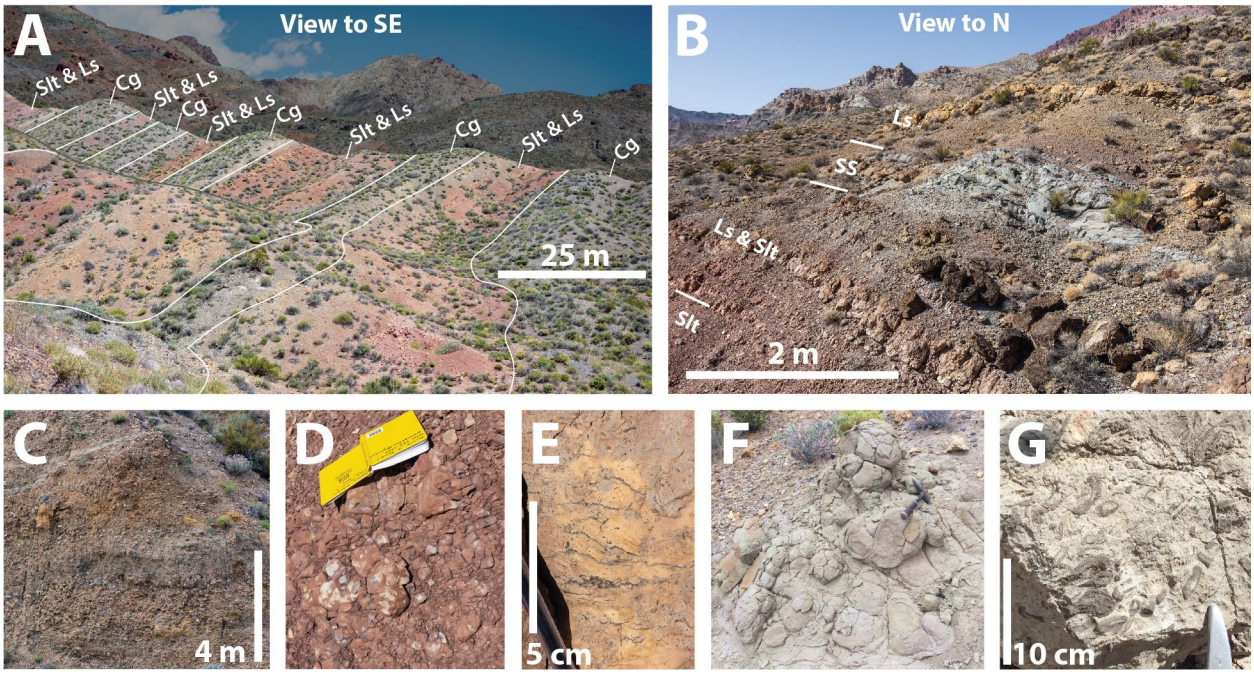


Figure 2.8: Images of the Variegated member of the Titus Canyon Formation. *Field photos of the Variegated member of the Titus Canyon Formation. (A) View to the southeast from east of Leadfield (Fig. 2.2) showing characteristic hills and saddles held up by alternating packages of resistant yellowish-greenish gray conglomerate (C) and recessive mottled reddish siltstone with yellow limestone interbeds (D and E). (B) The Variegated member becomes more limestone rich upsection, with thicker reddish-yellow recessive intervals between conglomerate channel bodies. A sequence of limestones and sandstones is shown in this image from below the middle green sandstone marker bed (not in view) near Leadfield (Fig. 2.2). (C) Thick exposure of weakly bedded to massive yellowish-gray conglomerate typical of the lower half of the Variegated member. Clasts range from granule up to 20 cm diameter. (D) Characteristic texture found within recessive red siltstones in the Variegated member, including reduction halos and mottled to massive bedding. (E) Limestone from a recessive interval of the Variegated member showing yellowish weathering color (fresh rock is gray) and distinctive fabric of bedding-parallel sparry laminae. (F) Distinctive spheroidal weathering texture of the middle green sandstone marker unit. (G) Example of oncoids found in 1–2-m-thick limestone beds of the Variegated member. Image taken near Indian Butte (Fig. 2.2). Abbreviations: Ls—limestone; Slt—siltstone; Cg—conglomerate.*

Variegated member. We redefine the Variegated member of the Titus Canyon Formation from the description of Reynolds (1969) as a sequence of colorful siltstones, sandstones, conglomerates, and limestones containing three marker units, including a distinctive green sandstone and conglomerate referred to as the middle green sandstone, and two tuffs (units 8 and 38 of Reynolds, 1969; Fig. A.1). The Variegated member is no more than 500 m thick and comprises repeating sequences (10–20 m thick) of moderately resistant pale greenish- or yellowish-gray sandy conglomerate separated by 5–10-m-thick recessive packages of interbedded red calcareous siltstone and yellow limestone (Fig.

2.8A and Fig. A.1). The member outcrops as rounded hills that reflect differences in the erodibility of the conglomerate and siltstone intervals (Fig. 2.8A). The sandy conglomerate intervals (Fig. 2.8C) are typically matrix-supported, massive to cross-bedded, and contain 0.5–30-cm-diameter clasts of limestone, quartzite, and distinctive small black chert pebbles 0.5–3 cm in diameter. Conglomerates are separated by red calcareous siltstone intervals that contain common reduction halos (Fig. 2.8D) and 0.5–1.5-m-thick gray or red micritic limestones that in some places show thin bedding-parallel sparry laminae (Fig. 2.8E) and commonly weather to a distinctive pale yellow (Fig. 2.8E). The micritic limestone beds are mostly devoid of allochems with the exception of a few oncolite beds in Titanothere Canyon and near Indian Butte (Fig. 2.3); these beds contain abundant oncoids (Fig. 2.8G; Titanothere Canyon outcrop, 36.8298°N, 117.0128°W; Indian Butte outcrop, 36.7025°N, 116.8088°W). Limestone-rich intervals have been previously used as marker intervals in the Titus Canyon Formation, though their lateral continuity is not clear between different sections. The tracing of a single limestone bed over significant distances is made difficult by their relatively thin lenticular nature and the pervasive faulting in the area. As such, we cannot demonstrate the continuity of an "algal limestone" marker bed (Stock and Bode, 1935; Reynolds, 1969; Saylor, 1991) as a distinctive, traceable unit throughout the Titus Canyon Formation. Overall, the Variegated member does not display upsection changes in grain size and has a relatively consistent grain-size distribution. While the member is lithologically uniform through its entire thickness, with the exception of the Middle green sandstone marker unit, discussed below, sandy conglomerate intervals within the Variegated member do take on a redder oxide-stained appearance upsection (Fig. A.1).

Middle green sandstone. The rhythmic bedding of the Variegated member is interrupted near its middle, where a distinctive sequence of greenish sandstones and conglomerates form a 50–60-m-thick marker unit originally identified by Stock and Bode (1935) as the "middle sandstone and conglomerate." We dub this interval the middle green sandstone, a marker unit that can be found at most localities throughout the map area, and which exhibits somewhat variable lithology but always includes a massive, recessive bluish gray-green, well-sorted medium sandstone near its base; the sandstone weathers into distinctive spheroidal outcrops (Fig. 2.8F). Many exposures of this marker unit also include resistant greenish-gray, matrix-supported sandy conglomerate, and

rarely recessive bluish green-gray mudstone and thin brown limestones. The conglomerates that accompany the middle green sandstone interval contain a similar clast composition to those in the rest of the Variegated member, but with a greener sandy matrix. The red siltstone intervals immediately above and below the middle green sandstone contain some of the most well-developed micrite limestone beds in the entire formation (Fig. 2.8B and Fig. A.1).

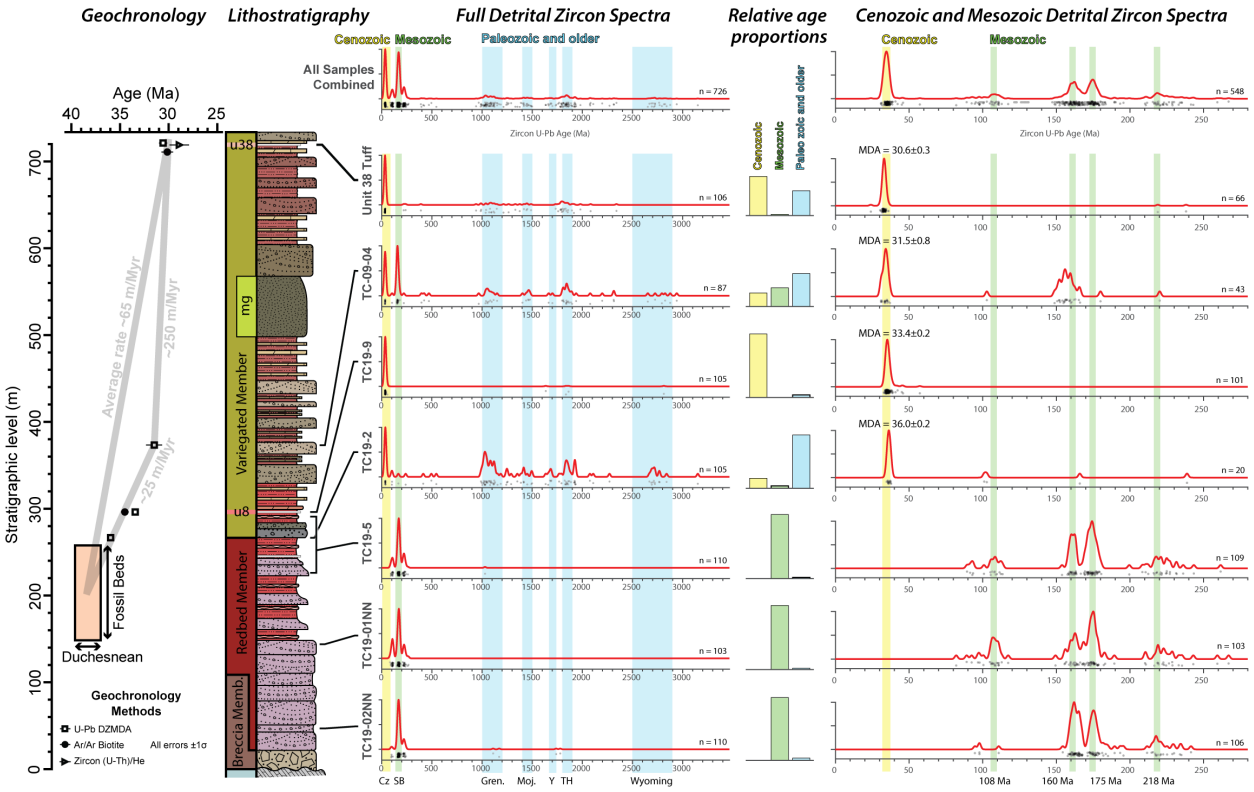


Figure 2.9: Detrital zircon spectra for the Titus Canyon Formation.
A plot of depositional age constraints versus stratigraphic level, a simplified lithostratigraphic column, and detrital zircon spectra for seven samples in the Titus Canyon Formation. Geochronology: Plot showing potential variation in deposition rates through time based on geochronology within the Titus Canyon Formation. Lithostratigraphy: Generalized stratigraphic column of the Titus Canyon Formation compiled from the measured sections shown in Fig. A.1. Leader lines indicate the approximate positions within the stratigraphy where samples were collected. Full Detrital Zircon Spectra: Each transparent dot represents a single zircon U-Pb age, and the red curves above the dots are kernel density estimates (made in MATLAB, bandwidth of 10 m.y.) for the distribution of zircon ages. Vertical bars indicate characteristic source peaks in the spectra. Relative age proportions: A bar graph showing the proportion of grains in a sample that are Cenozoic, Mesozoic, and Paleozoic and older. Each graph is normalized to the number of grains in the sample. Cenozoic and Mesozoic Detrital Zircon Spectra: Zoomed in spectra to highlight details in the distribution of 280 Ma and younger zircons (bandwidth of 1 m.y.). Maximum depositional age determinations are annotated onto the youngest Cenozoic grain cluster when present. Abbreviations: CZ—Cenozoic; SB—Sierra Nevada Batholith; Gren.—Grenville orogen; Moj.—Mojave basement; Y—Yavapai basement; TH—Trans Hudsonian orogen; Wyoming—Wyoming craton.

Marker tuffs. Within the Variegated member, we have mapped two additional marker beds previously identified by Reynolds (1969): the unit 8 tuff near the bottom of the member and the unit 38 tuff, which is near the top of the member. The unit 8 and unit 38 tuffs are tuffaceous sandstones with a slightly off-white color and fine powdery appearance. They appear rich in ash but in some places exhibit cross-bedding and a sandy composition that suggest they might be reworked, a possibility supported by the significant width of the Cenozoic age peaks in their detrital zircon spectra (Fig. 2.9).

Age Constraints from the Titus Canyon Formation

We report new geochronologic age information for the Titus Canyon Formation and develop an age model for the formation, based on a variety of geochronologic approaches, and we discuss this age model with respect to recognized paleontologic age constraints.

Maximum depositional age analysis from U-Pb detrital zircon geochronology. Of four Titus Canyon Formation samples from the vicinity of Titus and Titanothere canyons in the southern Grapevine Mountains (Fig. 2.3) that contained Cenozoic zircons, three came from the Variegated member, and a fourth came from the top of the Redbed member (Fig. 2.9 and Table 2.1). Samples from stratigraphically lower in the Redbed member contained primarily Mesozoic zircons (Fig. 2.9). Maximum depositional ages, based on MLA analysis (Fig. 2.5), and reported in stratigraphic order, are 36.0 ± 0.2 Ma from near the top of the Redbed member, and 33.4 ± 0.2 Ma, 31.5 ± 0.8 Ma, and 30.6 ± 0.3 Ma from the Variegated member (Figs. 2.2 and 2.9; Table 2.1). The MDA determinations are consistent with stratigraphic order.

$^{40}Ar/^{39}Ar$ geochronology. Of the six published and unpublished $^{40}Ar/^{39}Ar$ ages previously determined on tuffs in the southern Grapevine and northern Funeral Mountains (Saylor and Hodges, 1994; Snow and Lux, 1999; Murray, 2002; and Gutenkunst, 2006), two ages are from strata that we have mapped as the Variegated member of the Titus Canyon Formation (Table 2.1). One is a sample most likely collected from the unit 38 tuff which yielded a sanidine $^{40}Ar/^{39}Ar$ age of 30.4 ± 0.6 Ma (Saylor and Hodges, 1994), consistent with the zircon MDA that we determined for the same unit (30.6 ± 0.3 Ma). The second is a sample from near the base of the Variegated member which yielded

a biotite $^{40}Ar/^{39}Ar$ age of 34.5 ± 0.4 Ma (Saylor and Hodges, 1994). This age is similar to the 33.4 ± 0.2 Ma MDA from the base of the Variegated member near Leadfield (Fig. 2.3).

Zircon (U-Th)/He geochronology. The zircon (U-Th)/He method can be used to determine eruptive ages of tuffs and other volcanic rocks (e.g., Niemi, 2012); however, due to the relatively low closure temperature of helium in zircon (~180 °C), this method is susceptible to resetting in cases where samples have been modestly buried or reheated. We measured four zircon (U-Th)/He ages on samples from the southern Grapevine Mountains (Fig. 2.4 and Table 2.1), three of which were collected from the Titus Canyon Formation in Titus Canyon (Fig. 2.3). Of these three samples, one from the unit 38 tuff near the top of the Variegated member yielded an age (28.9 ± 1.0 Ma) that overlapped within error with other radiometric age determinations for the unit 38 tuff. Two ages determined on the unit 8 tuff, near the base of the Variegated member, yielded ages younger than the stratigraphically higher unit 38 tuff, in one case by 15 m.y. We hypothesize that middle Miocene emplacement of at least six major ignimbrite sheets across the region (Fig. A.2; Niemi, 2012) may have variably reset underlying zircon (U-Th)/He ages in the Titus Canyon area by inducing hydrothermal circulation (e.g., Abbey et al., 2018). We therefore note when zircon (U-Th)/He ages agree with other geo- and thermochronometers, but we do not find that this method produces consistently reliable eruption ages in the Titus Canyon region.

Paleontologic constraints on the age of the Titus Canyon Formation. Paleontologic evidence has been used to assign ages ranging from Eocene to Oligocene to the Titus Canyon Formation (Stock and Bode, 1935; Stock, 1936; Lander, 2019), with more recent studies coalescing around agreement on a Duchesnean North American Land Mammal age (middle to late Eocene, 37–40 Ma; e.g., Mason, 1988). A recent reassessment of fossils from the Titus Canyon Formation resulted in the identification of nine new local faunas, eight of which are found in the southern Grapevine Mountains in Titus and Titanothere canyons, all of which are inferred to be late Duchesnean in age (Lander, 2019).

Depositional age of the Titus Canyon Formation. The age of the base of the Titus Canyon Formation remains unresolved, as does the age of the Basal breccia member. The age of the Redbed member is partially constrained by both paleontologic and geochronologic data. Geochronologically, the 36.0 ± 0.2 Ma MDA from a sandstone

near the top of the Redbed member, and the 34.5 ± 0.4 Ma $^{40}Ar/^{39}Ar$ from the base of the Variegated member tightly bracket the age of the top of the Redbed member at ca. 35 Ma. This age places the ca. 34 Ma Eocene– Oligocene boundary and climate transition (e.g., Liu et al., 2009; Fan et al., 2018) at or just above the Redbed– Variegated member contact. A Duchesnean age for fossils in the Titus Canyon Formation is consistent with the geochronologic constraints, as all the fossil localities are found within the Redbed member below the stratigraphic level of the 36.0 ± 0.2 Ma MDA constraint. We find the correlation between the Titus Canyon local fauna and the Upper Porvenir local fauna that yields an age of ca. 37–38 Ma at the stratigraphic position of the fossil localities within the Titus Canyon Formation to be reasonable, given other existing age constraints. In the western West Fork and Upper East Fork sections (Fig. 2.3 and Fig. A.1), 100–200 m of strata of the Redbed member underlie the stratigraphic position of the fossil localities. No Cenozoic zircons were recovered from samples collected from these strata. Given the ages of the fossils in the Titus Canyon Formation, and an estimated rate of deposition for the Redbed member (Fig. 2.9), it would be surprising if the base of the Redbed member were older than middle Eocene. However, determining the age of the lower portions of the Redbed member may require approaches with limited reliance on absolute age dating, such as magnetostratigraphy, and the coarse conglomeratic nature of these deposits may prove challenging in that regard.

The age of the Variegated member is well constrained by our data and spans from ca. 35 Ma at the base of the member, as described above, to ca. 30 Ma at the top, as recorded by multiple age measurements on the unit 38 tuff near the top of this member (Fig. A.1). No more than a few meters of Variegated member strata overlie the unit 38 tuff at any measured section, suggesting that this age is representative of the preserved top of the Titus Canyon Formation.

In summary, the Titus Canyon Formation is middle Eocene to early Oligocene in age, contains a fossil record of Duchesnean land mammals, and encompasses the Eocene–Oligocene boundary.

Provenance of the Titus Canyon Formation

In addition to their use in determining maximum depositional ages, detrital zircon U-Pb ages also provide information about provenance (e.g., Thomas, 2011). In samples

from the Titus Canyon Formation, three distinct populations of zircon U-Pb ages are identifiable (Fig. 2.9). The oldest population of grains range from 3.1 Ga to 400 Ma, forming significant peaks at ca. 2.7 Ga, 1.9–1.8 Ga, 1.5–1.4 Ga, and 1.1–1.0 Ga (blue shaded peaks on Fig. 2.9). An intermediate age population forms a distinctive triple peak distribution of 105 Ma, 170 Ma, and 220 Ma (the prominent 170 Ma peak is shaded green on Fig. 2.9). The youngest zircon age population is Cenozoic and forms a cluster ranging from 40 Ma to 30 Ma (yellow shaded peak on Fig. 2.9). Broadly speaking, these three populations represent derivation from the Neoproterozoic and Paleozoic miogeocline (e.g., Gehrels et al., 1995), the Sierran arc (e.g., Lechler and Niemi, 2011), and Cenozoic volcanic centers of the Basin and Range (e.g., McQuarrie and Oskin, 2010).

The relative proportion of each of these three populations changes as a function of stratigraphic position in the Titus Canyon Formation (Fig. 2.9). The lowest three samples, all collected from the Redbed member, include almost entirely Mesozoic zircons, with no Cenozoic zircons and very few Paleozoic and Precambrian zircons. Samples from the Variegated member have a more variable detrital zircon age population distribution. Sierran zircons are the subordinate population in all samples from the Variegated member, while the major populations are characterized by either a Paleozoic and older miogeoclinal source or a Cenozoic volcanic source, presumably depending on whether the sample was dominated by fluvial erosion and transport or volcanic airfall deposition.

2.5.2 Rocks of Porter Mine

In the vicinity of the type section of the Titus Canyon Formation, near Leadfield (Fig. 2.3), the Variegated member of the Titus Canyon Formation is overlain in angular unconformity by distinctive green conglomerates of the middle Miocene Panuga Formation (Reynolds, 1969; Snow and Lux, 1999; Niemi, 2012). Both of these units can be traced southward along the eastern side of the Grapevine Mountains, where they remain juxtaposed across an unconformity. However, south of Daylight Pass (Fig. 2.3), which approximately separates the Grapevine Mountains from the Funeral Mountains, the two units continue to be distinguishable but are separated by an intervening package of strata that is not readily ascribed to either of these two units (Fig. A.2). Where exposures of this intervening sequence of strata have been previously mapped, they have been variably assigned to the Panuga Formation (or Green conglomerate facies) (Murray,

2002; Gutenkunst, 2006), the Titus Canyon Formation (Saylor, 1991; Gutenkunst, 2006) or referred to as Miocene Tuffaceous Sandstone and Volcanic Breccia (Wright and Troxel, 1993). We describe the lithostratigraphy and geochronologic age control on these strata below and demonstrate that these strata are lithologically and temporally distinct from the Titus Canyon Formation. We informally name these strata the Rocks of Porter Mine, for exposures south of Daylight Pass near Porter Mine (Fig. 2.3; 36.7741°N, 116.9129°W), and we discuss correlation of these strata with a succession of late Oligocene to early Miocene rocks that are regionally widespread in the Death Valley region and collectively termed the Ubehebe Formation (Snow and Lux, 1999; Fridrich and Thompson, 2011).

Lithostratigraphy

An intact section of the Rocks of Porter Mine previously mapped as Titus Canyon Formation (Saylor, 1991) is found in the Funeral Mountains, ~2 km southeast of Daylight Pass, ~1 km west of the abandoned Porter Mine (Fig. 2.3; Fig. A.2; 36.7741°N, 116.9129°W). These exposures can be traced southeastward to exposures near Indian Butte (Figs. 2.3 and A.2; 36.6941°N, 116.8011°W) that were previously mapped as either Titus Canyon Formation or Panuga Formation (Saylor, 1991; Gutenkunst, 2006). The Rocks of Porter Mine consist of bluish-green and gray conglomerates with pebble- to cobble-sized clasts, coarse sandstones, and tuffaceous sandstones that fine upwards into yellowish-beige to white sandstones, brown resistant limestones, recessive pale mudstone, and thick airfall tuffs (Fig. 2.10). At the southeastern extent of the mapping area (Fig. A.2), the lowest part of the Rocks of Porter Mine consists of 1–4-m-thick greenish-gray sandy conglomerates interbedded with 1–4-m-thick beds of mudstone and coarse sandstones (Figs. 2.10D and 2.6G) that in some places take on a striking dark-green coloration. The unit fines upwards into less colorful beige, brown, and pale-yellow fissile shales, and 10-cm- to 1-m-thick fossiliferous limestones, some of which contain small gastropods (Figs. 2.10E and 2.10F). Fossil fish have also been reported from strata equivalent to those that we describe here (Nyborg et al., 2017).

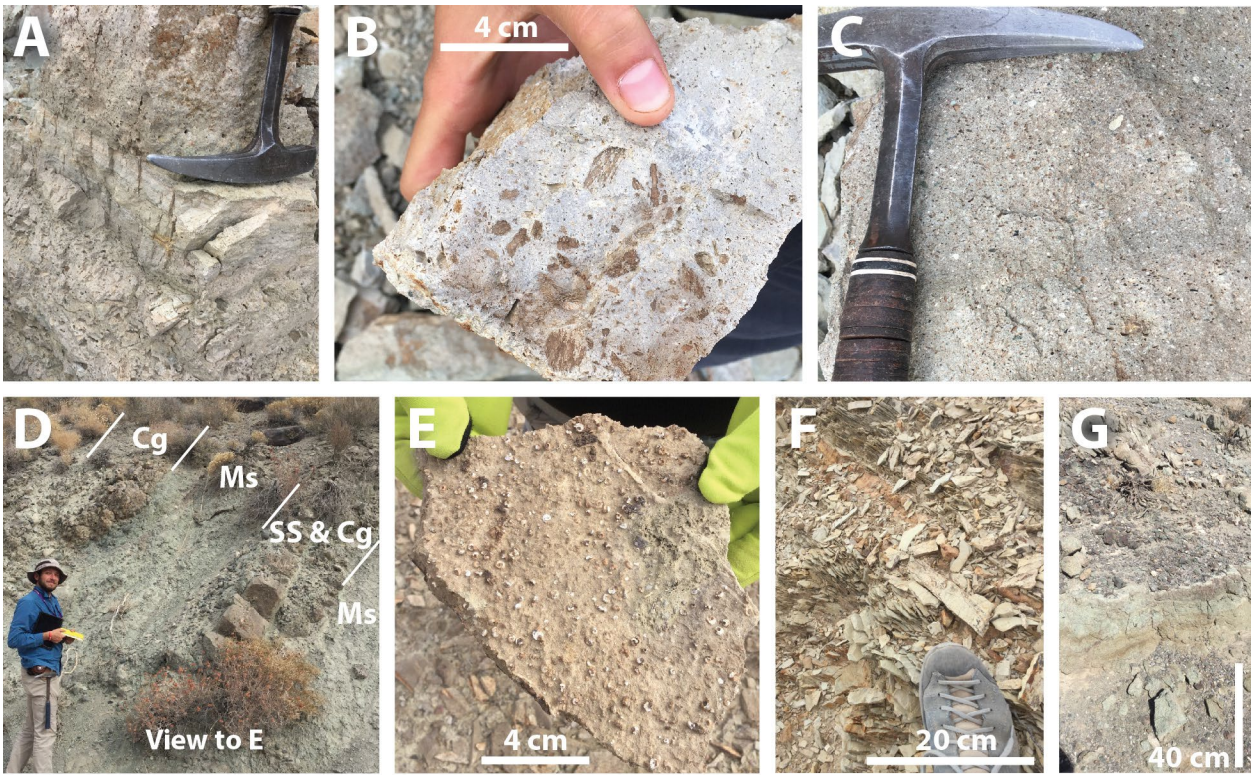


Figure 2.10: Images of the Rocks of Porter Mine.
Field photos of the Rocks of Porter Mine. (A) Welded tuff exposed just east of Red Pass (Fig. 2.2) exhibiting flow banding. Photo taken at 36.8298°N, 117.0259°W. (B) Examples of brown pumice clasts from the tuff shown in A. (C) Close-up photo of greenish-gray lapilli and weak horizontal fabric in the tuff shown in A. D, E, F, and G: Various examples of the sedimentary structures and rock types associated with the Ubehebe Formation, including: (D) Resistant greenish to bluish-gray sandstones (SS) and pebbly conglomerates (Cg) interbedded with recessive pale-green mudstone (Ms). (E) 1–3-cm-thick tan-brown limestone bed showing small 3–5-mm-diameter gastropod fossils. (F) Fissile ~0.5-cm-thick laminae of tan to pale orange shale. (G) Thickly bedded massive turquoise, green, pale brown, and gray coarse sandstone and pebble conglomerate typical of Rocks of Porter Mine exposures in the study area.

Northwest of Daylight Pass in the Grapevine Mountains, exposures of the Rocks of Porter Mine are incomplete, with the best exposure being a fault-bounded wedge in upper Titanothere Canyon directly below Red Pass (Fig. 2.3; 36.8302°N, 117.0251°W). Here, sandstone, conglomerate, and mudstone beds (Fig. 2.10D) take on a light blue-green color, similar to the lowest part of the Indian Butte stratigraphy. Below Red Pass, the Rocks of Porter Mine also contain an undated, highly resistant welded tuff with pumice fragments (Figs. 2.10A, 2.10B, and 2.10C; 36.8299°N, 117.0259°W). Overall, the Rocks of Porter Mine thicken to the southeast, a trend opposite that of the underlying Titus Canyon Formation. The Rocks of Porter Mine also display a greater degree of lateral variability in

thickness than the Titus Canyon Formation, possibly indicating deposition in small wedge-shaped basins bounded by syn-depositional normal faults (e.g., Fridrich and Thompson, 2011).

Depositional Age of the Rocks of Porter Mine from $^{40}Ar/^{39}Ar$ Analyses

Based on our field observations and mapping, the Rocks of Porter Mine include several $^{40}Ar/^{39}Ar$ age analyses that were previously reported as age constraints for the Titus Canyon or Panuga Formations but which instead represent the depositional age of the Rocks of Porter Mine (Table 2.1). Gutenkunst (2006) analyzed three $^{40}Ar/^{39}Ar$ ages from a measured section through the Rocks of Porter Mine near Indian Butte (Fig. 2.3 and Fig. A.2); we recalculated these ages to be 28.2 ± 0.2 Ma, 23.6 ± 0.1 Ma, and 19.3 ± 0.5 Ma (Fig. 2.4 and Table 2.1). A single sample from an exposure of the Rocks of Porter Mine near Chloride Cliff road (Fig. 2.3) produced a zircon (U-Th)/He age of 24.4 ± 2.1 Ma, which is consistent with ages from Gutenkunst (2006), but is subject to the caveats regarding potential resetting of zircon (U-Th)/He ages described in the Methods section (Table 2.1). In summary, recalculated $^{40}Ar/^{39}Ar$ ages from tuffs that we map as within the Rocks of Porter Mine span the interval 28.2 ± 0.2 Ma to 19.3 ± 0.5 Ma, indicating that these strata are approximately late Oligocene to early middle Miocene in age.

Regional Correlation of the Rocks of Porter Mine

The late Oligocene to early middle Miocene depositional age range for the Rocks of Porter Mine is consistent with the depositional age range of other packages of strata previously correlated with the regionally widespread Ubehebe Formation. These include strata at Bat Mountain, at the southernmost end of the Funeral Mountains (25–20 Ma; Fridrich and Thompson, 2011; Fridrich et al., 2012) and in the Cottonwood Mountains (24–19 Ma; Snow and Lux, 1999). In addition to a similar age of deposition, the Rocks of Porter Mine share the fining-upward stratigraphy and volcanic-rich nature of other known exposures of the Ubehebe Formation, traits that differentiate this formation from the Titus Canyon Formation. Based on the depositional age determinations for the Rocks of Porter Mine, their distinct lithology, and similarities to other strata ascribed to the Ubehebe Formation, we tentatively correlate the Rocks of Porter Mine with the Ubehebe Formation of Snow and Lux (1999), pending identification and description of a type-

section for this unit and targeted sampling for more comprehensive geochronologic constraints on the depositional age range of this unit.

2.6 Tectono-Stratigraphy and Formation of the Titus Canyon Basin

The Titus Canyon Formation records deposition from the Duchesnean (37–40 Ma) to the early Oligocene (30 Ma) (Figs. 2.9 and 2.11). Our differentiation of the Titus Canyon Formation from the Rocks of Porter Mine affords us an opportunity to revisit the evolution of the Titus Canyon basin and argue that its extent is limited to exposures in the northern Funeral and southern Grapevine Mountains. Depositional patterns in continental extensional basins are primarily controlled by the structural production of accommodation space and the climatically modulated supply of sediment (Carroll and Bohacs, 1999; Gawthorpe and Leeder, 2000), with a balance between basins that overfilled with sediment and host throughgoing drainages (i.e., exorheic), or underfilled and hydrologically closed (i.e., endorheic). The relative proportion of fluvial to lacustrine strata in a basin can serve as a proxy for overfilled and underfilled conditions, respectively (e.g., Geurts et al., 2020), and provides a useful framework for dividing the depositional history of the Titus Canyon basin into two phases. The following interpretations build on extensive previous sedimentologic and stratigraphic work in this region (Stock and Bode, 1935; Reynolds, 1969; Saylor, 1991; Murray, 2002; Gutenkunst, 2006; Ridgway et al., 2011; Niemi, 2012). Our goal is to summarize and correlate these works and place their observations within a common tectono-stratigraphic and geochronologic framework, as many of the previous studies were conducted in small, disconnected study areas without robust geochronology.

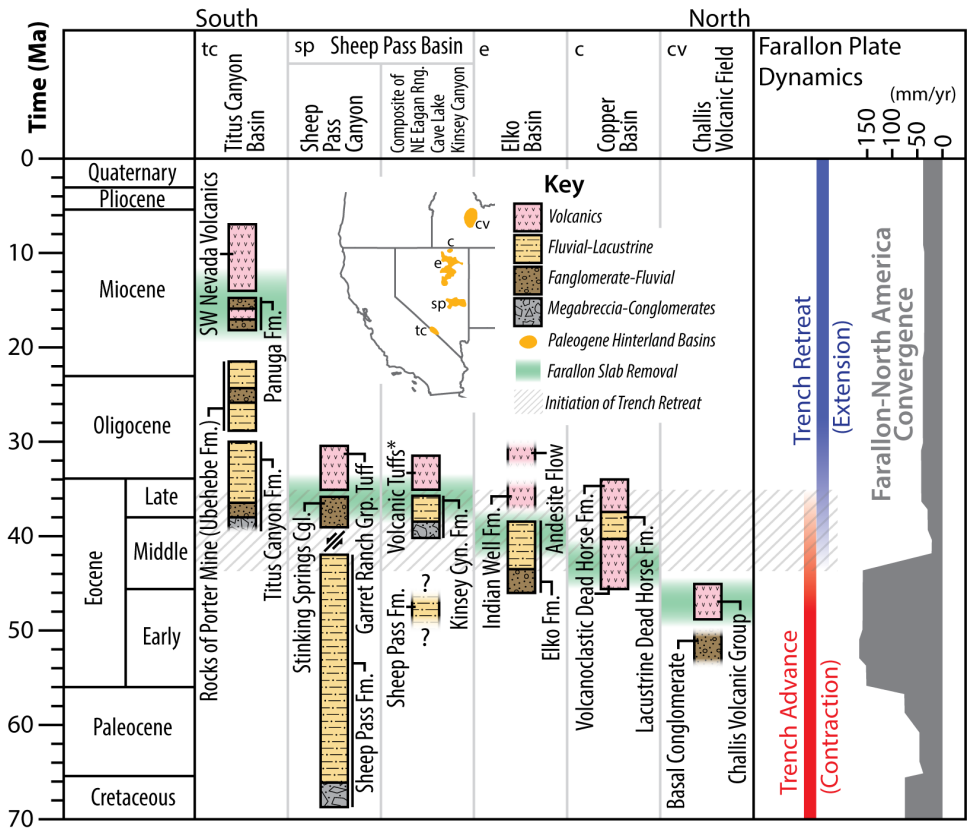


Figure 2.11:Simplified Cenozoic chronostratigraphy of the Nevadaplano. *Comparison of the timing of deposition in major hinterland basins of the Sevier orogenic belt. Hinterland basins are arranged approximately from south to north (left to right). Figure is adapted from Figure 10 in Druschke et al. (2009), with additional data for the Challis volcanic field from Sanford (2005) and Moye et al. (1988); Elko Basin from Haynes (2003), Lund Snee et al. (2016), and Smith et al. (2017); Copper Basin from McGrew et al. (2007) and Rahl et al. (2002); and Miocene rocks of the Titus Canyon Basin from Niemi (2012). Farallon plate dynamics are from Jurdy (1984) and Schellart et al. (2010). Timing of Farallon slab removal from Dickinson (2009), Konstantinou et al. (2012), and Smith et al. (2017). Note that some basins contain Miocene and younger deposits not shown here for visual simplicity, and the Elko Basin may contain some older deposits not shown here because their exact ages are unknown (e.g., Lund Snee et al., 2016). *Late Eocene sedimentary sections in the Sheep Pass basin are overlain by tuffs of latest Eocene to earliest Oligocene age, including the Charcoal Ovens tuff and Kalamazoo tuff.*

2.6.1 Extensional Basin Initiation and Fluvial Phase

The Titus Canyon basin initiated as an incipient extensional basin no later than 37 Ma, and early deposition of the Basal breccia and Redbed members continued until ca. 35 Ma. The overall fining-upwards stratigraphy of the Basal breccia and Redbed members of the Titus Canyon Formation records a progression from proximal rock avalanche breccias and coarse fanglomerate deposits to distal overbank deposits and conglomeratic channel

bodies (Reynolds, 1969; Murray, 2002; Gutenkunst, 2006; Ridgway et al., 2011). This progression is recognized in other early extensional basin sequences and arises from coarse scarp-derived deposits eventually yielding to a basin-floor fluvial system as the basin area expands (Gawthorpe and Leeder, 2000). The dominance of fluvial over lacustrine deposition during this early phase of basin formation implies an overfilled basin condition, and thus an exorheic hydrology with throughgoing drainages. Estimates of depositional rates of ~25 m/m.y., as derived from the geochronology and biostratigraphy of the Redbed member (Fig. 2.9) indicate a slower depositional rate than in the upper Titus Canyon Formation and a slower rate than observed in typical extensional basins (50–200 m/m.y.; Allen and Allen, 2013). Combined with the overfilled state of the basin, this implies a relatively slow tectonic subsidence rate during this period.

Provenance information from the Redbed member of the Titus Canyon Formation also sheds light on regional drainage geometries and extent at the time of Titus Canyon basin formation. Detrital zircon U-Pb provenance analysis of the Redbed member reveals consistent detrital zircon spectra throughout the unit, dominated by Mesozoic ages, with significant age peaks in the middle Jurassic (ca. 165 and 175 Ma), a broad peak of late Triassic ages, and subordinate Late Cretaceous ages (Fig. 2.9). These three age peaks are consistent with recognized pulses of Sierran arc magmatism (e.g., Ducea, 2001; Coleman et al., 2003; Cecil et al., 2019); however, a specific source for the observed age spectra in the Redbed member is challenging to pinpoint. The subordinate nature of the Late Cretaceous ages argues against derivation from the present-day eastern Sierra Nevada, where exposures of Late Cretaceous plutons are extensive (Chen and Moore, 1982; Coleman and Glazner, 1998).

The Titus Canyon basin was located just east of the boundary between primarily Mesozoic arc-related rocks of the Sierra Nevada to the west and Neoproterozoic through Paleozoic sedimentary strata of the Cordilleran miogeocline to the east (e.g., Jennings et al., 1977). Several ranges in the westernmost Basin and Range, including the White, Inyo, and Cottonwood mountains, expose minor Late Cretaceous and Triassic intrusive bodies and host large Jurassic batholiths, with ages that overlap the detrital zircon ages observed in the Redbed member (Chen and Moore, 1982; Snow et al., 1991; Niemi et al., 2001; Coleman et al., 2003), making them a viable source terrane for the early Titus Canyon Formation.

Conglomerate clast compositions in the Titus Canyon Formation further support derivation from a westerly source (Reynolds, 1969). Although lower Paleozoic carbonate and siliciclastic strata are exposed in most of the ranges that surround Death Valley, the identification of case-hardened carbonate clasts as being derived from Pennsylvanian-aged limestone, and the identification of Permian fusulinid-bearing limestones (Reynolds, 1969), limit the source for the Redbed member conglomerate clasts to sources on the western side of modern-day Death Valley (McAllister, 1952; Niemi et al., 2001). Clasts of quartz monzonite of inferred Jurassic age, and porphyritic granite clasts, are also observed within the Redbed member. The Cottonwood Mountains, on the northwestern side of Death Valley, are a compelling source terrane for

the combination of Paleozoic miogeoclinal clasts, Jurassic-aged monzonite clasts, and upper Paleozoic fusulinid-bearing limestones (Snow and Lux, 1999; Niemi et al., 2001), as well as the Jurassic and Triassic detrital zircon spectra. Further geochronologic analysis of individual clasts is needed to link specific clasts to unique source terranes. However, despite uncertainty in the exact provenance of the Redbed member of the Titus Canyon Formation, the basin was receiving sediment from a catchment that encompassed rocks not exposed in the local bedrock of the Grapevine and Funeral mountains, and which was almost certainly derived from the west, an inference also supported by paleocurrent and sedimentary structure observations (Stock and Bode, 1935; Reynolds, 1969; Gutenkunst, 2006).

2.6.2 Acceleration of Extension and Fluvial-Lacustrine Phase

The Variegated member records a shift in lithologic character, provenance, and fossil content of the Titus Canyon basin. Within the Variegated, conglomeratic channel bodies and silty overbank deposits rhythmically alternate with 0.5–1.5-m-thick lacustrine micrite beds, contrasting with the coarse, proximal deposition recorded by the Redbed member (Reynolds, 1969; Murray, 2002; Gutenkunst, 2006; Ridgway et al., 2011). The appearance of lacustrine conditions above the Redbed–Variegated member contact implies a transition from entirely exorheic (fluvial) to sometimes under-filled lacustrine conditions that could have been tectonically or climactically modulated. However, the similar timing of the Redbed to Variegated member transition (approx. 36–34 Ma) to the Eocene–Oligocene climate transition (ca. 34 Ma), during which northern latitudes cooled

~5–7 °C, may support a strong climatic influence during this time (Liu et al., 2009; Fan et al., 2018). Potential climatic influence on the Titus Canyon basin is not addressed in this manuscript, but it remains an important area for future investigation.

Sediment accumulation rates and provenance data from the Variegated member, however, potentially suggest a shift in the intensity of tectonic activity within the Titus Canyon basin. Deposition rates for the Variegated member are as high as ~250 m/m.y., distinctly faster than the ~25 m/m.y. sediment accumulation rate within the Redbed member, and fast compared to compiled extensional basin rates of 50–200 m/m.y. (Allen and Allen, 2013). Geologic evidence for increased rates of local tectonism as a cause for increased sediment accumulation rates are preserved within the Variegated member, which both coarsens and thickens into the Fall Canyon fault in the upper West Fork of Titus Canyon (Fig. A.2).

The increase in sediment accumulation rate in the Variegated member is accompanied by a shift in basin provenance signature. Detrital zircon spectra from the Variegated member record Cenozoic zircon grains, suggesting an increase in volcanic input to the basin, likely from the onset of Oligocene ignimbrite eruptions in northern and central Nevada (Coney, 1978; Best et al., 2013), although such a signature is not diagnostic of fluvial basin geometry or extent. More pronounced is the shift in provenance from a dominantly Mesozoic Sierran arc signature to a broad age spectrum, similar to the detrital zircon spectra of Paleozoic and Neoproterozoic miogeoclinal rocks. Three of the four detrital samples from the Variegated member yield no evidence of derivation from a Mesozoic arc source (Fig. 2.9), and in the one Variegated sample where Mesozoic ages are present, they are Late Jurassic to Early Cretaceous, markedly different from the mid-Jurassic and Triassic ages found in the Redbed member (Fig. 2.9). The greater variability in detrital zircon spectra observed within the Variegated member also reflects a departure from the Redbed member, which exhibits consistent detrital zircon signatures.

The provenance changes we observe in the detrital zircon age spectra between the Redbed and Variegated members match previous observations of changes in clast composition in the Titus Canyon Formation (Reynolds, 1969; Murray, 2002). The Variegated member does not contain clasts of upper Paleozoic (Permian and Pennsylvanian) carbonates, and granitoid clasts are less commonly observed than in the Redbed member (Reynolds, 1969). Together, these changes suggest a shift away from a

westerly source of sediment. The ubiquity of Neoproterozoic and Paleozoic miogeoclinal rocks in and around the Titus Canyon basin provides no compelling discrimination of the source area for the Variegated member. The Late Jurassic to Early Cretaceous age of detrital zircons in the Variegated member, however, requires derivation from plutons that are not well represented in the Sierran arc, while the lack of Late Triassic, Middle Jurassic, and Late Cretaceous zircon ages suggests that the source area cannot contain significant exposure of the most common plutonic ages (e.g., Ducea, 2001; Cecil et al., 2019). The Sylvania and Palmetto mountains, which lie ~50 km north of present-day exposures of the Titus Canyon basin, are underlain by Late Jurassic plutons that are intruded by small plutonic bodies of Late Cretaceous age. These plutonic ages are consistent with the detrital zircon spectra in the Variegated member, although geochronologic age constraints on the crystallization ages of these plutons (as opposed to cooling ages) are sparse (e.g., Maldonado et al., 1988), and the identification of this region as a source area for the Variegated member should be considered preliminary.

In summary, the Titus Canyon basin initiated as an extensional basin in the late Eocene on the easterly-facing slope of the paleo–Sierra Nevada arc. Early extensional rates are presumed to be low, due to the relatively low sediment accumulation rates and the persistent fluvial, and thus likely sediment overfilled, environment within the basin. The consistency of the detrital zircon spectra and clast composition throughout the Redbed member potentially suggests minimal drainage reorganization or evolution. The Variegated member of the Titus Canyon basin records major changes in the Titus Canyon basin, including significantly increased sediment accumulation rates and a transition to a fluvial-lacustrine sedimentary environment.

2.6.3 Extent of the Titus Canyon Basin and Regional Correlations of the Titus Canyon Formation

As one of the earliest recognized pre–Basin and Range extensional units in the Death Valley region (e.g., Stock and Bode, 1935; Reynolds, 1969), the Titus Canyon Formation has been tenuously correlated with multiple poorly dated units in the central Basin and Range. A number of presumed Paleogene rock exposures in and around the Death Valley region, including the Horse Spring Formation, the unnamed conglomerate of the Fallout and Jumbled Hills, the Rocks of Winapi Wash, and the unnamed

conglomerate of Gravel Canyon, among others, have been correlated with the Titus Canyon Formation on the basis of broad lithologic similarity and similar stratigraphic position above the sub-Tertiary unconformity (Niemi, 2002, and references therein). However, these deposits have neither biostratigraphic nor absolute age control that substantiates a temporal correlation with the Titus Canyon Formation. Moreover, such lithostratigraphy-based correlations were largely proposed prior to the recognition of the complex early Cenozoic depositional history of the Death Valley region that has been delineated in the past decades (e.g., Çemen et al., 1999; Snow and Lux, 1999; Fridrich and Thompson, 2011), and that we further refine here. Descriptions of these units, gleaned primarily from stratigraphic descriptions on published geologic maps, generally bear greater similarity to the Rocks of Porter Mine (Ubehebe Formation) as defined and described here than to the Titus Canyon Formation. Frequent descriptions of fossiliferous limestones and well-developed tuff beds are particularly more diagnostic of Ubehebe-equivalent strata than of Titus Canyon. Thus, our inference is that the Titus Canyon basin was of limited spatial extent and is preserved almost exclusively within the southern Grapevine and northern Funeral Mountains, while the Ubehebe Formation may have a much broader spatial distribution across the central Basin and Range.

2.7 Structure of the Titus Canyon Basin

For a long time, the Titus Canyon basin has been described as having an extensional or transtensional origin based on observations of basin-scale sedimentological architecture and facies analysis (e.g., Saylor, 1991; Gutenkunst, 2006; Fridrich and Thompson, 2011). However, a coherent structural framework for the Titus Canyon basin has not previously been defined, in part due to myriad geologic maps that partially encompass the extent of the Titus Canyon Formation (e.g., Cornwall and Kleinhampl, 1964; Reynolds, 1969; Saylor, 1991; Wright and Troxel, 1993; Niemi, 2012). In mapping the extent of the Titus Canyon Formation and synthesizing the structures that bound the formation, we find that the Titus Canyon Formation in the Grapevine Mountains is everywhere confined to the hanging wall of a complex fault system, the Fall Canyon– Titus Canyon fault system (Fig. A.2).

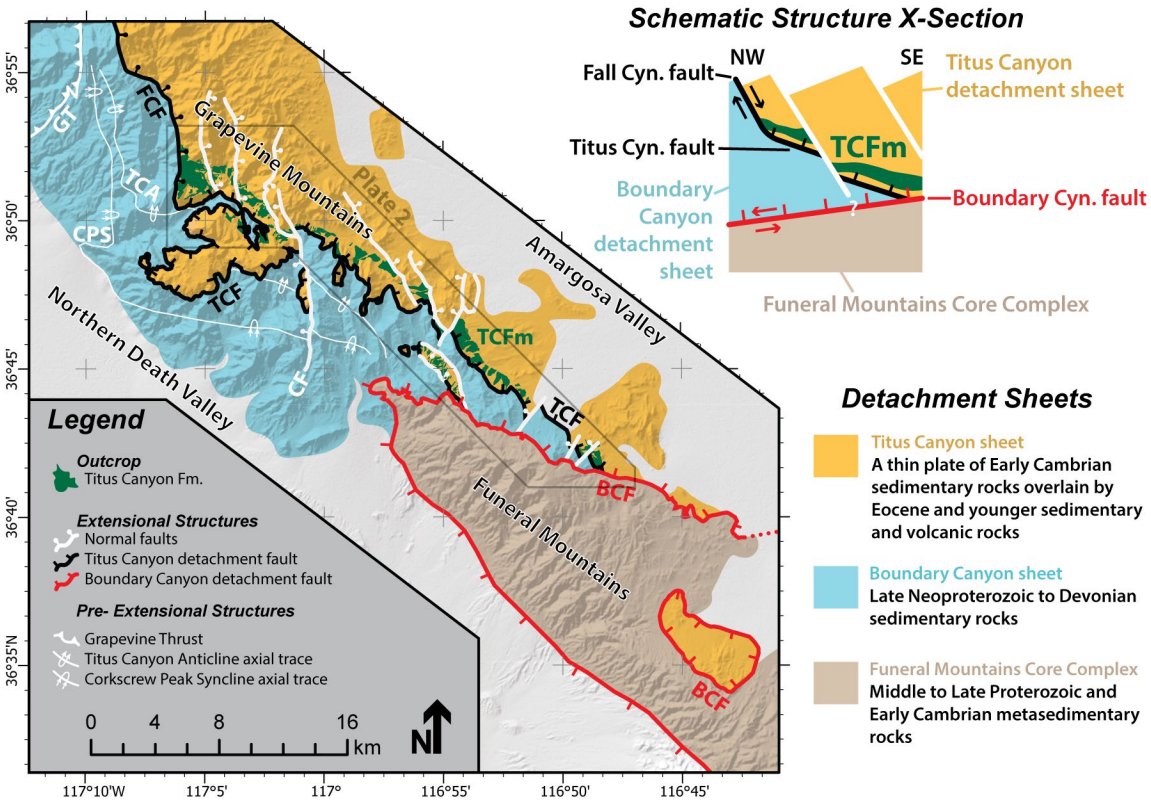


Figure 2.12: Simplified structural map of the Grapevine and Funeral Mountains. *Simplified tectonic map of the major contractile structures, detachment faults, and detachment sheets in the southern Grapevine and northern Funeral Mountains. Features compiled from this study (Fig. A.2, map extent shown on figure), Reynolds (1969), Niemi (2012), Wright and Troxel (1993), and Cornwall and Kleinhampl (1964). Note that teeth are drawn on the hanging walls of all faults, and the relative dips of the structures shown in the schematic structure cross section differ from their true orientations. Abbreviations: BCF—Boundary Canyon fault; CF—Corkscrew fault; CPS—Corkscrew Peak syncline; FCF—Fall Canyon fault; GT—Grapevine thrust; TCA—Titus Canyon anticline; TCF—Titus Canyon fault; TCFm—Titus Canyon Formation.*

2.7.1 Fall Canyon Fault

The Fall Canyon fault is a steeply east-dipping normal fault that extends northward from Titus Canyon, parallel to the range crest of the Grapevine Mountains (Fig. A.2). The Fall Canyon fault juxtaposes upright Paleozoic strata in the upper limb of a large west-vergent fold in its footwall (the Titus Canyon anticline–Corkscrew Peak syncline, or TCA-CPS) against Cenozoic strata, including the Titus Canyon Formation and younger strata, in its hanging wall (Figs. 2.12 and 2.13). Although the lower members of the Titus Canyon Formation are not exposed along the Fall Canyon fault, in the west fork of Titus Canyon (Fig. 2.3), conglomeratic intervals within the Variegated member both thicken and

coarsen westward toward the Fall Canyon fault. No single conglomerate is thicker than ~40 m in our measured sections, but these conglomerates merge into a single, >100-m-thick package toward the Fall Canyon fault. The thickening and coarsening of the conglomerates may represent sedimentological variability within the basin (e.g., of alluvial fans), but we prefer to interpret them as growth strata associated with the Fall Canyon fault, which would suggest that the Fall Canyon fault may have been an Eocene–Oligocene basin bounding fault to the Titus Canyon basin. This view agrees with previous interpretations of the Titus Canyon basin as asymmetric and west-deepening (Saylor, 1991; Niemi, 2002; Gutenkunst, 2006; Fridrich and Thompson, 2011).

2.7.2 Titus Canyon Fault

Where the trace of the Fall Canyon fault is exposed in Titus Canyon east of Leadfield (Fig. 2.3), it merges with the Titus Canyon fault, an enigmatic, nearly horizontal fault. The excellent exposure in Titus Canyon shows the Fall Canyon fault and Titus Canyon fault merging rather than crosscutting (Fridrich and Thompson, 2011). Additionally, the significant offset associated with the Fall Canyon fault does not continue into the footwall rocks of the Titus Canyon fault. The flat attitude of the Titus Canyon fault, and its exposure across the top of the southern Grapevine Mountains, originally led to the interpretation of this structure as a Mesozoic thrust fault (Reynolds, 1969). The recognition that this fault everywhere carries the depositional base of the Titus Canyon Formation, and that this fault is contiguous with the Fall Canyon fault, underscores the nature of this structure as a low-angle Eocene detachment fault. The Titus Canyon fault places upright lower Paleozoic strata and overlying Titus Canyon Formation in its hanging wall on upper Neoproterozoic and lower Paleozoic strata of the overturned limb of the TCA-CPS (Fig. 2.13; Reynolds, 1969; Fall Canyon fault zone of Lutz et al., 2021). The Titus Canyon fault has multiple structural levels that appear to localize along relatively weak shale intervals within the Cambrian Carrara Formation and Neoproterozoic Wood Canyon Formation (Fig. A.2). The lower Paleozoic and upper Neoproterozoic strata are significantly structurally thinned (< 1 km thick) and form the floor of the Titus Canyon basin, on which the Basal breccia member of the Titus Canyon Formation was deposited. A top-to-the-southeast sense of displacement on the Titus Canyon fault is inferred from both its continuity with the east-dipping Fall Canyon fault and a likely northwesterly

source for the upright Paleozoic strata carried in the Titus Canyon fault hanging wall (Niemi, 2012).

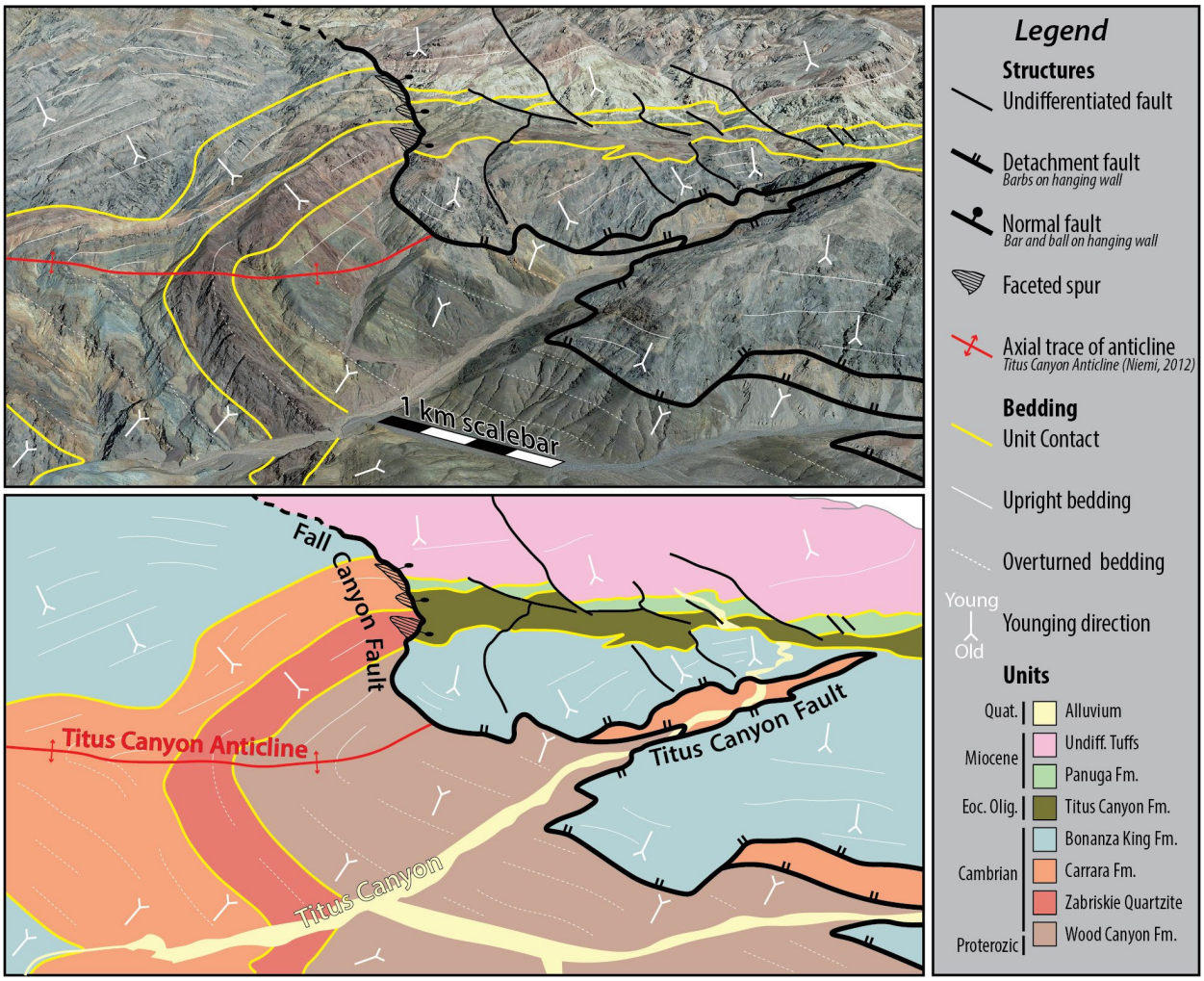


Figure 2.13: Oblique view of the Titus Canyon Anticline and Titus Canyon Fault. *Annotated oblique view of the upper reaches of Titus Canyon (Fig. 2.2) showing key structural relationships between the Titus Canyon anticline, Titus Canyon fault, Fall Canyon fault, and variably upright and overturned strata. View is toward the north and centered on 36.8404°N, 117.1006°W (Fig. 2.3). Several key relationships are visible: (1) The Titus Canyon fault smoothly steepens and links into the Fall Canyon fault. (2) The Titus Canyon fault emplaces upright strata of the Bonanza King Formation onto overturned strata in the limb of the Titus Canyon anticline. (3) The Titus Canyon fault cuts across the axial trace of the Titus Canyon anticline, and neither the strata in the hanging wall of the Titus Canyon fault, nor the fault itself, participate in the folding of the Titus Canyon anticline. Note that the axial plane of the west-vergent Titus Canyon anticline is subhorizontal, and thus the axial trace of the fold can appear to trend east-west where it intersects with the steep topography of Titus Canyon. Imagery is © 2021 Google Earth and Maxar Technologies.*

2.7.3 Boundary Canyon Detachment

To the south, in the vicinity of Daylight Pass, all structures in the Grapevine Mountains (including the Titus Canyon fault and Titus Canyon anticline– Corkscrew Peak syncline) are truncated at the Boundary Canyon detachment (Fig. 2.12 and Fig. A.2), a top-to-the-northwest low-angle detachment fault that bounds the Funeral Mountains metamorphic core complex (Holm and Dokka, 1991; Hoisch and Simpson, 1993; Beyene, 2011; Fridrich and Thompson, 2011; Lutz et al., 2021). The Boundary Canyon detachment separates amphibolite-grade Neoproterozoic sedimentary rocks in its footwall from zeolite-grade strata in its hanging wall (Hoisch and Simpson, 1993; Wright and Troxel, 1993; Mattinson et al., 2007; Verdel et al., 2011; Hoisch et al., 2014; Affinati et al., 2020). The metamorphic history of the footwall rocks exhumed by the Boundary Canyon detachment is complex (Hoisch and Simpson, 1993; Applegate and Hodges, 1995; Mattinson et al., 2007; Wells and Hoisch, 2008; Affinati et al., 2020), but the timing of metamorphic core complex development is well constrained to the middle to late Miocene by a variety of low-temperature thermochronometric studies (e.g., Holm and Dokka, 1991; Lutz et al., 2021).

Where the Boundary Canyon detachment truncates the Titus Canyon fault along the eastern margin of the northern Funeral Mountains (near Indian Butte, Fig. 2.3), exposures of the Titus Canyon Formation are incomplete and primarily consist of the Variegated member of the Titus Canyon Formation (Fig. A.2). Near the Boundary Canyon detachment, the base of the Titus Canyon Formation is commonly faulted and juxtaposed against upper Neoproterozoic siliciclastic strata in the footwall of the detachment, recording disarticulation of the Titus Canyon Formation and associated Eocene structures during Miocene displacement on the Boundary Canyon detachment (Fig. A.2; Wright and Troxel, 1993; Gutenkunst, 2006).

Evidence for Miocene reactivation of the Eocene– Oligocene structures that bound the Titus Canyon basin is equivocal. Thick sequences of middle Miocene strata and ignimbrites from the Southwest Nevada volcanic field are exposed to the east of the

Fall Canyon fault but are conspicuously absent to the west of this structure, throughout the western central Basin and Range (Niemi, 2012). Despite the thickness of these Miocene volcanic and sedimentary units, there is no clear evidence of thickening or

growth fault relationships between them and the Fall Canyon fault. Moreover, we observed no unambiguous exposures that would clarify the nature of the contact between the Miocene units and the Fall Canyon fault as being structural rather than, for example, a depositional contact along a buttress unconformity. Given a lack of conclusive evidence for post-Oligocene activity on the Fall Canyon and Titus Canyon fault, we infer that the relationship observed between the Miocene ignimbrites and the Fall Canyon fault represents a buttress unconformity, but we acknowledge the challenge of preserving Oligocene structural relief into the middle Miocene.

2.7.4 Implications of Titus Canyon Basin Structures for Regional Palinspastic Reconstructions of Basin and Range Extension

Palinspastic restorations are key to understanding the magnitude and mechanisms of large-scale intracontinental extension (e.g., Wernicke et al., 1988; Snow and Wernicke, 2000; McQuarrie and Wernicke, 2005), and they form the basis for geodynamic models constructed to understand the internal and external forces that drive lithospheric deformation (e.g., Bahadori and Holt, 2019). In the central Basin and Range, geologic markers that constrain such reconstructions fall into two broad categories: (1) late Paleozoic to Mesozoic contractional structures formed during convergence on the North American plate boundary (e.g., Burchfiel and Davis, 1975; Giallorenzo et al., 2018), and proximal sedimentary deposits of late Cenozoic age that have been tectonically dismembered by extension (e.g., Salyards and Shoemaker, 1987; Topping, 1993; Niemi et al., 2001). The structural markers are commonly used to define the magnitude of Basin and Range extension but have limited utility for understanding timing or rates of extension, while syn-extensional sedimentary deposits can provide compelling information on the timing of deformation but generally less precise constraints on extensional magnitudes.

The Titus Canyon Formation and bounding structures are thus of significant interest for refining palinspastic reconstructions because both closely pre-date the onset of large-magnitude extension in the Basin and Range. In this context, the structural relationship between the Fall Canyon–Titus Canyon fault system and the Titus Canyon anticline–Corkscrew Peak syncline is of particular significance. The TCA-CPS is a west-vergent fold pair, a rare type of contractional structure in the Death Valley region, which

is dominated by east-directed thrust faults (e.g., Snow and Wernicke, 1989). As such, the TCA-CPS has been correlated with west-vergent folds in other mountain ranges surrounding Death Valley as a diagnostic structural marker (e. g. Wernicke et al., 1988; Snow and Wernicke, 1989), a correlation predicated on the assumption that the TCA-CPS, as well as the other west-vergent folds, are extensionally disrupted fragments of a single, originally contiguous, geologic structure.

The age of west-vergent folding in the Death Valley region is constrained only in the Cottonwood Mountains, where crosscutting dikes and growth strata bracket the timing of folding to Late Permian to early Triassic age (Snow et al., 1991; Stevens and Stone, 2005). Consequently, the question of whether all west-vergent folds throughout the Death Valley region are of this age, and thus correlative, is debated (e.g., Serpa and Pavlis, 1996; Renik and Christie-Blick, 2013; Lutz et al., 2021). In particular, the TCA-CPS has been the subject of debate with respect to the timing of its formation, with similarities to structures in the Cottonwood Mountains supporting a Permo-Triassic age (Snow and Wernicke, 2000; Niemi, 2012). Alternatively, the close association of the TCA-CPS to the late Miocene Boundary Canyon detachment has been used to argue for a model of syn-extensional folding synchronous with unroofing of the Funeral Mountains metamorphic core complex (Reynolds, 1974; Lutz et al., 2021).

Age constraints on the Fall Canyon fault–Titus Canyon fault, and crosscutting relationships between that structure and the TCA-CPS, do not provide absolute age constraints on the timing of TCA-CPS folding, but do provide relative timing on the development of these structures. The normal fault emplacement of upright Paleozoic strata and Titus Canyon Formation onto overturned Neoproterozoic strata of the Corkscrew Peak syncline (Fig. 2.12) requires that the TCA-CPS was developed prior to displacement on the Fall Canyon–Titus Canyon fault. The coarsening and thickening of the Titus Canyon Formation into the Fall Canyon fault in western Titus Canyon therefore imply that the TCA-CPS formed prior to the Eocene. This age constraint for folding of the TCA-CPS does not resolve all outstanding questions of structural correlations between west-vergent folds in the Death Valley region but does support the inference that the TCA-CPS is a pre-Cenozoic contractional structure associated with late Paleozoic or Mesozoic shortening of the Cordilleran margin.

2.8 Tectonic and Topographic Implications for the Evolution and Collapse of the Sevier Orogenic Belt

A variety of geodynamic mechanisms have been invoked as proximate causes for the onset of Eocene Basin and Range extension, including flexural and isostatic dynamics ahead of the delaminating Farallon slab (e.g., Smith et al., 2017; Cassel et al., 2018), changing plate boundary stresses (e.g., Atwater, 1970; Schellart et al., 2010), and gravitational collapse (Humphreys, 1995; Sonder and Jones, 1999). In northern Nevada, the close temporal association between Farallon slab removal and the onset of extension has been presumed to reflect a causal relationship between the two (e.g., Cassel et al., 2018). However, farther to the north, the earlier removal of the Farallon slab has been linked to an early Eocene phase of volcanism and extensional deformation that preceded a late Eocene phase of deformation, potentially related to a change in plate boundary stresses (e.g., Janecke, 1992). The southerly location of the Titus Canyon Basin may potentially record the opposite scenario, in which a late Eocene change in plate boundary stresses preceded the removal of the Farallon slab by 15 Ma, providing a unique and important constraint on the evolution of internal and external forces driving Basin and Range extension.

2.8.1 Stratigraphic Record of Crustal Extension along the Axis of the Sevier Orogenic Belt

In the central and northern Basin and Range, Late Cretaceous to Paleocene syn-convergent extension (e.g., Hodges and Walker, 1992; Wells et al., 2008; Druschke et al., 2009; Long et al., 2015) left a relatively sparse stratigraphic record in the hinterland of the Sevier orogen, primarily consisting of the Sheep Pass Formation (ca. 70–43 Ma) in central Nevada (Fig. 2.11, Druschke et al., 2009, 2011). Despite a sparse surficial record of syn-convergent extension, thermochronometric and isotopic data sets from several metamorphic core complexes record cooling during the late Cretaceous to early Cenozoic that may be attributable to early extensional exhumation, including in the Raft River–Albion metamorphic core complex (Wells et al., 2012), the Funeral Mountain metamorphic core complex (Applegate et al., 1992; Hoisch and Simpson, 1993; Applegate and Hodges, 1995), the Eureka Culmination (Long et al., 2015), and the Pequop

Mountains (Camilleri, 1996). Syn-convergent extension has been attributed to collapse driven by gravitational potential energy gradients produced by a lithosphere over-thickened by Sevier deformation (e.g., Vandervoort and Schmitt, 1990; Hodges and Walker, 1992; DeCelles, 2004; Platt, 2007; Druschke et al., 2009).

Compared to earlier deposition, the Eocene stratigraphic record of extensional tectonism is more widespread and better constrained temporally (Fig. 2.11). This stratigraphic record preserves a north-to-south sweep in the onset of Eocene basin deposition, with the earliest deposits preserved in the Challis volcanic field of southern Idaho, where a basal conglomerate records deposition prior to the eruption of overlying volcanic units that have been dated with $^{40}Ar/^{39}Ar$ at ca. 49.5 Ma (Fig. 2.11; Moye et al., 1988; Sanford, 2005). In northernmost Nevada, the Elko Formation (Elko Basin) and the Dead Horse Formation (Copper Basin) contain a large number of tuffs that have enabled robust $^{40}Ar/^{39}Ar$ geochronology that indicates deposition spanned ca. 46–38 Ma, with the exception of one earlier local pulse of deposition in the vicinity of Coal Mine Canyon at ca. 49 Ma (Rahl et al., 2002; Haynes, 2003; McGrew et al., 2007; Henry, 2008; Henry et al., 2015; Mulch et al., 2015; Lund Snee et al., 2016; Smith et al., 2017). The syn-convergent Sheep Pass Formation in central Nevada is overlain by Eocene strata, including the Stinking Springs Conglomerate and Kinsey Canyon Formation with depositional ages that range from ca. 37–35 Ma (Fig. 2.11; Druschke et al., 2009). Eocene deposition in the Sheep Pass Basin, in particular, overlaps with Redbed member deposition in the Titus Canyon basin.

Each basin displays a broadly similar depositional pattern, with early deposition dominated by coarse basal deposits and fluvial strata that transition upsection into lacustrine strata capped by volcanic or volcanic-rich units (Fig. 2.11). In the northern Basin and Range, the close temporal connection between clastic basin deposition and overlying volcanic deposition, combined with the southward sweep of basin initiation, has been taken to reflect subsidence and volcanism arising from the southward-propagating removal of the Farallon slab (e.g., Humphreys, 1995). In such a model, north to south delamination of the Farallon flat slab produced a south-directed, time-transgressive sweep of volcanism (Fig. 2.14; Humphreys, 1995; McQuarrie and Oskin, 2010), core complex exhumation (Fig. 2.14; e.g., MacCready and Snoke, 1997; Methner et al., 2015;

Lee et al., 2017), and hinterland basin deposition (Fig. 2.14; Smith et al., 2017; Cassel et al., 2018; Lund Snee, 2020).

The southerly location of the Titus Canyon basin with respect to the time-transgressive removal of the Farallon slab, however, yields a markedly different pattern (Fig. 2.11). Eocene basin initiation and clastic deposition occurred in the Titus Canyon basin coeval with Eocene basin formation in northern Nevada, but the detaching Farallon slab, and associated volcanism, did not reach the central Basin and Range until the middle Miocene, coincident with widespread ignimbrite production in the Southwest Nevada volcanic field (Sawyer et al., 1994) and the exhumation of the Funeral Mountains metamorphic core complex (Holm and Dokka, 1991; Hoisch and Simpson, 1993; Lutz et al., 2021).

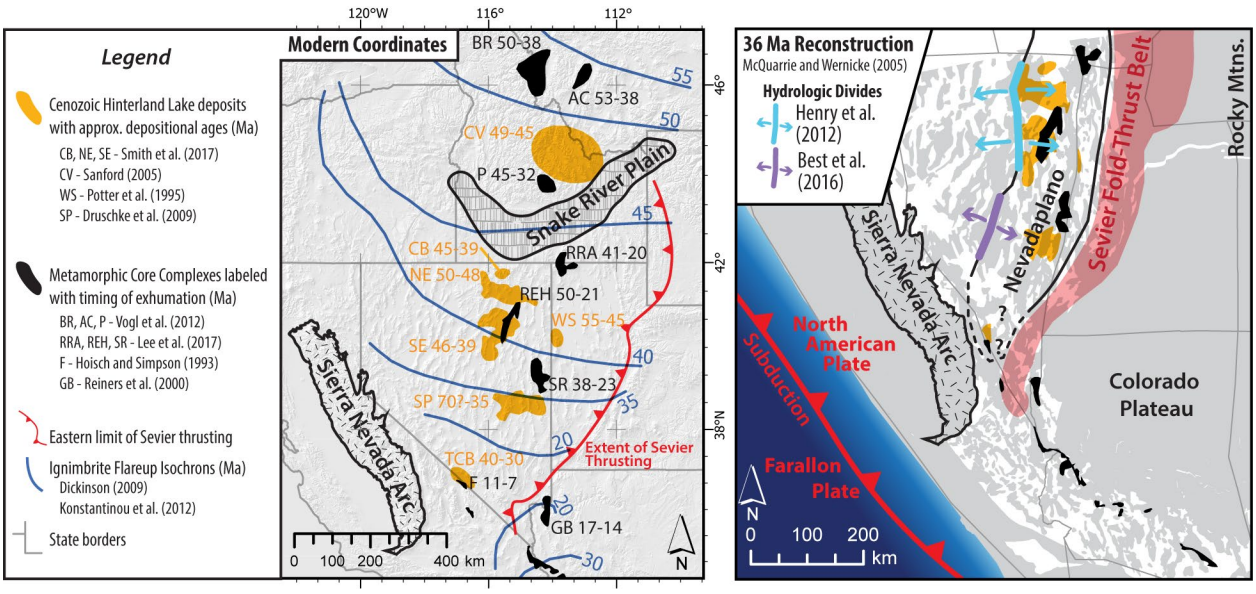


Figure 2.14: Geography of the Nevadaplano and Sevier hinterland basins. *Geologic data in modern coordinates (left) and retrodeformed (right) to their approximate 36 Ma positions and sizes according to the tectonic reconstruction of McQuarrie and Wernicke (2005). Left: Hillshade base map with overlaid metamorphic core complexes, hinterland basins, and isochron contours of the north to south sweep of ignimbrite volcanism associated with delamination of the Farallon slab. Right: 36 Ma reconstruction of range positions from McQuarrie and Wernicke (2005) overlain with the estimated position of the Paleogene hydrologic divide, and the possible extent of the Nevadaplano assuming it contains the major hinterland basins, lies east of the hypothesized Cordilleran hydrologic divide (Henry et al., 2012; Best et al., 2016), and west of the Sevier fold-thrust belt (Yonkee and Weil, 2015). Abbreviations: BR—Bitterroot Core Complex; AC—Anaconda Core Complex; P—Pioneer Core Complex; RRA—Raft River–Albion Core Complex; REH—Ruby–East Humboldt Core Complex; SR—Snake Range Core Complex; F—Funeral Mountains Core Complex; GB—Gold Butte Core Complex; CV—Challis volcanic field; CB—Copper Basin; NE—Northern Elko Basin; SE—Southern Elko Basin; WS—White Sage Basin; SP—Sheep Pass Basin; TCB—Titus Canyon Basin.*

In the northern Basin and Range, Eocene hinterland basin development could reasonably represent a dynamic response to the southward removal of the Farallon slab (Smith et al., 2017; Cassel et al., 2018; Lund Snee, 2020), but the 15 m.y. gap between Eocene basin formation and volcanism and metamorphic core complex formation in the central Basin and Range would appear to be inconsistent with a singular driving force at the latitude of Titus Canyon. Throughout the Paleogene, ongoing subduction resulted in the fragmentation of the Farallon slab (e.g., Schellart et al., 2010). Between ca. 48 and 30 Ma, the trench-parallel length of the Farallon slab decreased by 75%, at the same time that the Farallon–North America convergence rate rapidly slowed (Fig. 2.11; Jurdy, 1984; Gordon and Jurdy, 1986; Schellart et al., 2010). From the Eocene to Miocene, the Farallon slab steepened or foundered, from north to south across the northern Basin and Range (Fig. 2.11; Humphreys, 1995; McQuarrie and Oskin, 2010). The slowdown in Farallon–North America plate convergence rate was less time transgressive than Farallon detachment, consisting of a rapid transition from trench advance to trench retreat along the full length of the Farallon plate boundary at ca. 40 Ma (Fig. 2.11; Schellart et al., 2010).

In the northern Basin and Range, the transition from trench advance to trench retreat along the Farallon–North America plate boundary is temporally indistinguishable from the passage of the detaching Farallon slab (Fig. 2.11). However, these two events are separated by ~25 m.y. at the latitude of the Titus Canyon basin. Extensional basin formation and deposition of the Titus Canyon Formation is approximately coeval with the transition from trench advance to trench retreat along the plate margin, while the subsequent onset of local volcanism and metamorphic core complex formation is contemporaneous with the removal of the Farallon slab at that latitude (Fig. 2.11). We infer that the complex history of extensional tectonism, deposition, and basin formation in the central Basin and Range results from multiple discrete episodes of deformation. In the Eocene, extensional basin formation was driven by stress changes along the plate boundary, coupled with localized gravitational collapse of possibly over-thickened lithosphere (e.g., Vandervoort and Schmitt, 1990; Hodges and Walker, 1992; Platt, 2007; Druschke et al., 2009; Wells et al., 2012; Bahadori et al., 2018). These early extensional basins were overprinted by middle Miocene volcanism and core complex formation that accompanied extension driven by lithospheric weakening and heating during removal of

the Farallon slab (e.g., Armstrong and Ward, 1991; Axen et al., 1993; Humphreys et al., 2003). Such a model is compatible with early clastic basin formation and subsequent volcanism and core complex formation in the northern Basin and Range, but the temporal overlap between these two geodynamic processes precludes their effects from being assessed separately in that region.

2.8.2 Spatial Extent of an Early Eocene Nevadaplano

Thickened crust within the Sevier orogenic belt is hypothesized to have supported a high-elevation, low-relief orogenic plateau called the Nevadaplano (Ernst, 2009). The spatial extent and elevation of this plateau are the subjects of considerable debate (e.g., Chamberlain et al., 2012; Long, 2012; Lechler et al., 2013; Snell et al., 2014) and are of particular interest in relating the distribution and magnitude of Basin and Range extension to the pre-extensional distribution of topography and crustal thickness (e.g., Bahadori et al., 2018). Approaches that directly constrain pre-extensional topography of the Nevadaplano are limited by the small number of deposits of appropriate age and composition for paleoelevation analysis, the thermal resetting of paleoaltimetric proxies such as carbonate clumped isotopes (Lechler et al., 2013), and the relatively large elevation uncertainties associated with paleofloral data and stable isotopic proxies (e.g., Chamberlain et al., 2012; Snell et al., 2014). The low spatial and temporal density of paleoelevation, paleotopographic, and paleocrustal thickness estimates has resulted in a number of competing models for the topographic profile of the Sevier orogenic belt (Cecil et al., 2010; Cassel et al., 2014; Bahadori and Holt, 2019). Among the most pronounced discrepancies in these models is the recognition of a paleotopographic divide, based on ignimbrite sheet distributions (Henry et al., 2012; Best et al., 2016), that lies ~150 km west (in pre-extensional coordinates) of the belt of core complexes and presumed greatest pre-extensional crustal thickness (Fig. 2.14; Bahadori and Holt, 2019).

The distribution of Eocene hinterland extensional basin deposits, including the Titus Canyon Formation, sheds some light on the potential paleotopography in the hinterland of the Sevier orogenic belt. All Eocene basins lie east of the paleotopographic divide and west of the inferred axis of thick crust produced by Sevier shortening (Fig. 2.14). In particular, the large areal extents of the lacustrine-dominated Elko Formation and the Sheep Pass Formation imply basin development across a region of relatively low-

relief topography. An interpretation of low-relief paleotopography in this region is supported by the general lack of structural relief across the inferred Nevadaplano (Gans and Miller, 1983; Miller and Gans, 1989; DeCelles and Coogan, 2006; Van Buer et al., 2009; Konstantinou et al., 2012; Long, 2012, 2018), and the local relief on the base of ignimbrite sheets, as well as their long outflow distances and broad aprons (Henry et al., 2012). Together, these observations suggest the existence of a low-relief, and perhaps internally drained, portion of the Nevadaplano that can be extended along the belt of Eocene basins, from the Copper Basin in northern Nevada to the Titus Canyon basin in eastern California (Fig. 2.14). The extent of large paleo-lakes and lacustrine basins has been invoked as a proxy for low-relief topography on elevated plateau surfaces (Zhenhan et al., 2008), and the presence of such basins along the axis of the Sevier orogenic belt in Eocene time should be considered in paleotopographic reconstructions of western U.S. topography at that time (e.g., Bahadori and Holt, 2019).

2.9 Conclusions

In this study, we redefine the internal stratigraphy of the Eocene–Oligocene Titus Canyon Formation and clarify its correlation to regionally similar units through a combination of detailed stratigraphic descriptions and geochronology. A combination of mammalian biostratigraphy, new detrital zircon U-Pb maximum depositional age constraints and relocated $^{40}Ar/^{39}Ar$ ages indicate that the Titus Canyon basin spans ca. 40–30 Ma and may record the earliest hinterland sedimentation in the central Basin and Range following the Mesozoic Sevier orogeny. The stratigraphy and structural position of the Titus Canyon Formation in the hanging wall of the linked Fall Canyon and Titus Canyon faults support previous interpretations of the formation as an extensional basin deposit. A change in detrital zircon provenance from an entirely Mesozoic Sierran arc source to a dominantly Paleozoic and Neoproterozoic miogeoclinal source may record progressive extensional unroofing of deeper miogeoclinal formations that contain greater concentrations of zircons, which along with the basin subsidence itself, supports continued extensional tectonism throughout the deposition of the formation. The phase of low-magnitude extension recorded by the Titus Canyon Formation predates large-magnitude exhumation of the nearby Funeral Mountains metamorphic core complex and suggests that extensional deformation in the central Basin and Range may have initiated

because of changes in plate boundary forces and was later over-printed by deformation associated with removal of the Farallon slab.

2.10 Acknowledgments

This work was supported by the U. S. Geological Survey National Cooperative Geologic Mapping Program under USGS award number G19AC00138, with matching support from the University of Michigan. The views and conclusions contained in this document are those of the authors and should not be interpreted as necessarily representing the official policies, either expressed or implied, of the U.S. Government. Additional support came from National Science Foundation grant EAR-1151247 to NAN, a Geological Society of America Graduate Student Research Grant to NM, and a University of Michigan Department of Earth and Environmental Sciences Turner Award to NM. Fieldwork in Death Valley National Park was conducted under permit DEVA-2017- SCI-0037, issued to Torrey Nyborg. John Stark (DVNP) provided access to National Park Service GIS data. We thank Bruce Lander for providing the impetus to revisit the Titus Canyon Formation, and for many stimulating conversations with both him and Torrey Nyborg in the field. Tom Kelly, Brandt Nyborg, and John Sifling are thanked for participating in field expeditions. Thank you to Ken Ridgway for granting permission to publish $^{40}Ar/^{39}Ar$ data produced under U.S. Nuclear Regulatory Commission Contract NRC-02-07-006. This manuscript was improved by constructive criticism from Marin Clark, Michael Wells, Jens-Erik Lund Snee, Ryan Leary, and Jeff Lee. We acknowledge the Indigenous peoples who are the original inhabitants of the lands this work examines—the Newe Segobia (Western Shoshone) and Nuwuvi (Southern Paiute) tribes. We thank Mel for breakfast.

2.11 References

Abbey, A.L., Niemi, N.A., Geissman, J.W., Winkelstern, I.Z., and Heizler, M., 2018, Early Cenozoic exhumation and paleotopography in the Arkansas River valley, southern Rocky Mountains, Colorado: Lithosphere, v. 10, p. 239–266, doi:10.1130/L673.1.

Affinati, S.C., Hoisch, T.D., Wells, M.L., and Vervoort, J.D., 2020, Pressure-temperature-time paths from the Funeral Mountains, California, reveal Jurassic retroarc underthrusting during early Sevier orogenesis: Geological Society of America Bulletin, v. 132, p. 1047–1065, doi:*10.1130/B35095.1*.

Allen, P.A., and Allen, J.R., 2013, Basin Analysis: Principles and Application to Petroleum Play Assessment: Wiley-Blackwell, 549 p.

Applegate, J.D.R., and Hodges, K.V., 1995, Mesozoic and Cenozoic extension recorded by metamorphic rocks in the Funeral Mountains, California: Geological Society of America Bulletin, v. 107, p. 1063–1076, doi:*10.1130/0016-7606(1995)107<1063:MACERB>2.3.CO;2*.

Applegate, J.D.R., Walker, J.D., and Hodges, K.V., 1992, Late Cretaceous extensional unroofing in the Funeral Mountains metamorphic core complex, California: Geology, v. 20, p. 519–522.

Armstrong, R.L., and Ward, P., 1991, Evolving geographic patterns of Cenozoic magmatism in the North American Cordillera: The temporal and spatial association of magmatism and metamorphic core complexes: Journal of Geophysical Research, v. 96, p. 13201–13201, doi:*10.1029/91JB00412*.

Atwater, T., 1970, Implications of plate tectonics for the Cenozoic tectonic evolution of western North America: Geological Society of America Bulletin, v. 81, p. 3513–3536.

Axen, G.J., Taylor, W.J., and Bartley, J.M., 1993, Space-time patterns and tectonic controls of Tertiary extension and magmatism in the Great Basin of the western United States: Geological Society of America Bulletin, v. 105, p. 56–76, doi:*10.1130/0016-7606(1993)105<0056:STPATC>2.3.CO;2*.

Bahadori, A., and Holt, W.E., 2019, Geodynamic evolution of southwestern North America since the Late Eocene: Nature Communications, v. 10, 5213, doi:*10.1038/s41467-019-12950-8*.

Bahadori, A., Holt, W.E., and Rasbury, E.T., 2018, Reconstruction modeling of crustal thickness and paleotopography of western North America since 36 Ma: Geosphere, v. 14, p. 1207–1231, doi:*10.1130/GES01604.1*.

Best, M.G., Barr, D.L., Christiansen, E.H., Gromme, S., Deino, A.L., and Tingey, D.G., 2009, The Great Basin Altiplano during the middle Cenozoic ignimbrite flareup: insights from volcanic rocks: International Geology Review, v. 51, p. 589–633.

Best, M.G., Christiansen, E.H., and Gromme, S., 2013, The 36–18 Ma southern Great Basin, USA, ignimbrite province and flareup: Swarms of subduction-related supervolcanoes: Geosphere, v. 9, p. 260–274.

Best, M.G., Christiansen, E.H., de Silva, S., and Lipman, P.W., 2016, Slab-rollback ignimbrite flareups in the southern Great Basin and other Cenozoic American arcs: A distinct style of arc volcanism: Geosphere, v. 12, p. 1097–1135, doi:*10.1130/GES01285.1*.

Beyene, M.A., 2011, Mesozoic burial, Mesozoic and Cenozoic exhumation of the Funeral Mountains core complex, Death Valley, southeastern California [Ph.D. thesis]: University of Nevada, 363 p.

Bindeman, I.N., Schmitt, A.K., and Valley, J.W., 2006, U–Pb zircon geochronology of silicic tuffs from the Timber Mountain/Oasis Valley caldera complex, Nevada: rapid generation of large volume magmas by shallow-level remelting: Contributions to Mineralogy and Petrology, v. 152, p. 649–665, doi:*10.1007/s00410-006-0124-1*.

Burchfiel, B.C., and Davis, G.A., 1975, Nature and controls of Cordilleran orogenesis, western United States: Extensions of an earlier synthesis: American Journal of Science, v. 275-A, p. 363–396.

Camilleri, P.A., 1996, Evidence for Late Cretaceous-Early Tertiary(?) extension in the Pequop Mountains, Nevada: Implications for the nature of the early Tertiary unconformity, in Taylor, W.J. and Langrock, H. eds., Cenozoic Structure and Stratigraphy of Central Nevada, Reno, Nevada Petroleum Society Inc., 1996 Field Conference Volume, p. 19–28.

Camilleri, P.A., and Chamberlain, K.R., 1997, Mesozoic tectonics and metamorphism in the Pequop Mountains and Wood Hills region, northeast Nevada: Implications for the architecture and evolution of the Sevier orogen: Geological Society of America Bulletin, v. 109, p. 74–94.

Canada, A.S., Cassel, E.J., McGrew, A.J., Smith, M.E., Stockli, D.F., Foland, K.A., Jicha, B.R., and Singer, B.S., 2019, Eocene exhumation and extensional basin formation in the Copper Mountains, Nevada, USA: Geosphere, v. 15, p. 1577–1597, doi:*10.1130/GES02101.1*.

Canada, A.S., Cassel, E.J., Stockli, D.F., Smith, M.E., Jicha, B.R., and Singer, B.S., 2020, Accelerating exhumation in the Eocene North American Cordilleran hinterland: Implications from detrital zircon (U-Th)/(He-Pb) double dating: Geological Society of America Bulletin, v. 132, p. 198–214, doi:*10.1130/B35160.1*.

Carr, M.D., Sawyer, D.A., Nimz, K., Maldonado, F., and Swadley, W.C., 1996, Digital bedrock geologic map database of the Beatty 30 x 60-minute quadrangle, Nevada and California: U.S. Geological Survey Open-File Report 96–291, doi:*10.3133/ofr96291*.

Carroll, A.R., and Bohacs, K.M., 1999, Stratigraphic classification of ancient lakes: Balancing tectonic and climatic controls: Geology, v. 27, p. 99–102, doi:*10.1130/0091-7613(1999)027<0099:SCOALB>2.3.CO;2*.

Cassel, E.J., Breecker, D.O., Henry, C.D., Larson, T.E., and Stockli, D.F., 2014, Profile of a paleo-orogen: High topography across the present-day Basin and Range from 40 to 23 Ma: Geology, v. 42, p. 1007–1010, doi:*10.1130/G35924.1*.

Cassel, E.J., Smith, M.E., and Jicha, B.R., 2018, The impact of slab rollback on earth's surface: Uplift and extension in the hinterland of the North American Cordillera: Geophysical Research Letters, v. 45, p. 10966–11004, doi:*10.1029/2018GL079887*.

Cecil, M.R., Ducea, M.N., Reiners, P., Gehrels, G., Mulch, A., Allen, C., and Campbell, I., 2010, Provenance of Eocene river sediments from the central northern Sierra Nevada and implications for paleotopography: Tectonics, v. 29, TC6010, p. 13, doi:*10.1029/2010TC002717*.

Cecil, M.R., Ferrer, M.A., Riggs, N.R., Marsaglia, K., Kylander-Clark, A., Ducea, M.N., and Stone, P., 2019, Early arc development recorded in Permian–Triassic plutons of the northern Mojave Desert region, California, USA: GSA Bulletin, v. 131, p. 749–765, doi:*10.1130/B31963.1*.

Çemen, I., Drake, R., and Wright, L.A., 1982, Stratigraphy and chronology of the Tertiary sedimentary and volcanic units at the southeastern end of the Funeral Mountains, Death Valley region, California, in Cooper, J.D., Troxel, B.W., and Wright, L.A. eds., Geology of Selected Areas in the San Bernardino Mountains, Western Mojave Desert, and Southern Great Basin, California, Shoshone, Calif., Death Valley Pub. Co., p. 77–87.

Çemen, I., and Wright, L.A., 1990, Effect of Cenozoic extension on Mesozoic thrust surfaces, in Wernicke, B.P. ed., Basin and Range Extensional Tectonics Near the Latitude of Las Vegas, Nevada, Boulder, Colorado, Geological Society of America Memoir 176, p. 305–316.

Çemen, I., Wright, L.A., Drake, R.E., and Johnson, F.C., 1985, Cenozoic sedimentation and sequence of deformational events at the southeastern end of the Furnace Creek strike slip fault zone, Death Valley region California, in Biddle, K.T. and Christie-Blick, N. eds., Strike-slip Deformation and Basin Formation, Society of Economic Paleontologists and Mineralogists, Special Publication 37, p. 127–141.

Çemen, I., Wright, L.A., and Prave, A.R., 1999, Stratigraphy and tectonic implications of the latest Oligocene and early Miocene sedimentary succession, southernmost Funeral Mountains, Death Valley region, California, in Wright, L.A. and Troxel, B.W. eds., Cenozoic Basins of the Death Valley Region, Boulder, Colorado, Geological Society of America Special Paper 333, p. 65–86, doi:*10.1130/0-8137-2333-7.65*.

Chamberlain, C.P., Mix, H.T., Mulch, A., Hren, M.T., Kent-Corson, M.L., Davis, S.J., Horton, T.W., and Graham, S.A., 2012, The Cenozoic climatic and topographic evolution of the western North American Cordillera: American Journal of Science, v. 312, p. 213–262, doi:*10.2475/02.2012.05*.

Chapman, J.B., Ducea, M.N., DeCelles, P.G., and Profeta, L., 2015, Tracking changes in crustal thickness during orogenic evolution with Sr/Y: An example from the North American Cordillera: Geology, v. 43, p. 919–922, doi:*10.1130/G36996.1*.

Chen, J.H., and Moore, J.G., 1982, Uranium-lead isotopic ages from the Sierra Nevada batholith, California: Journal of Geophysical Research: Solid Earth, v. 87, p. 4761–4784.

Coleman, D.S., Briggs, S., Glazner, A.F., and Northrup, C.J., 2003, Timing of plutonism and deformation in the White Mountains of eastern California: Geological Society of America Bulletin, v. 115, p. 48–57.

Coleman, D.S., and Glazner, A.F., 1998, The Sierra Crest magmatic event: Rapid formation of juvenile crust during the Late Cretaceous in California, in Ernst, W.G. ed., Integrated Earth and environmental evolution of the Southwestern United States, Columbia, Maryland, Bellwether Publishing, p. 253–272.

Coney, P.J., 1978, Mesozoic-Cenozoic Cordilleran plate tectonics, in Smith, R.B. and Eaton, G.P. eds., Cenozoic Tectonics and Regional Geophysics of the Western Cordillera, Boulder, Colorado, Geological Society of America Memoir 152, p. 33–50.

Coney, P.J., and Harms, T.A., 1984, Cordilleran metamorphic core complexes: Cenozoic extensional relics of Mesozoic compression.: Geology, v. 12, p. 550–554, doi:*10.1130/0091-7613(1984)12<550:CMCCCE>2.0.CO;2*.

Cornwall, H.R., and Kleinhampl, F.J., 1964, Geology of Bullfrog Quadrangle and ore deposits related to Bullfrog Hills Caldera, Nye County, Nevada and Inyo County, California: United States Geological Survey Professional Paper Professional Paper 454-J, 29 p.

Coutts, D.S., Matthews, W.A., and Hubbard, S.M., 2019, Assessment of widely used methods to derive depositional ages from detrital zircon populations: Geoscience Frontiers, v. 10, p. 1421–1435, doi:*10.1016/j.gsf.2018.11.002*.

DeCelles, P.G., 2004, Late Jurassic to Eocene evolution of the cordilleran thrust belt and foreland basin system, western U.S.A.: American Journal of Science, v. 304, p. 105–168, doi:*10.2475/ajs.304.2.105*.

DeCelles, P.G., and Coogan, J.C., 2006, Regional structure and kinematic history of the Sevier fold-and-thrust belt, central Utah: Geological Society of America Bulletin, v. 118, p. 841–864, doi:*10.1130/B25759.1*.

Dickinson, W.R., 2009, Anatomy and global context of the North American Cordillera, in Backbone of the Americas: Shallow Subduction, Plateau Uplift, and Ridge and Terrane Collision, Geological Society of America, doi:*10.1130/2009.1204(01)*.

Dickinson, W.R., 2002, The Basin and Range Province as a composite extensional domain: International Geology Review, v. 44, p. 1–38, doi:*10.2747/0020-6814.44.1.1*.

Dickinson, W.R., and Gehrels, G.E., 2009, Use of U–Pb ages of detrital zircons to infer maximum depositional ages of strata: A test against a Colorado Plateau Mesozoic database: Earth and Planetary Science Letters, v. 288, p. 115–125, doi:*10.1016/j.epsl.2009.09.013*.

Druschke, P., Hanson, A.D., and Wells, M.L., 2009, Structural, stratigraphic, and geochronologic evidence for extension predating Palaeogene volcanism in the Sevier hinterland, east-central Nevada: International Geology Review, v. 51, p. 743–775, doi:*10.1080/00206810902917941*.

Druschke, P., Hanson, A.D., Wells, M.L., Gehrels, G.E., and Stockli, D., 2011, Paleogeographic isolation of the Cretaceous to Eocene Sevier hinterland, east-central Nevada: Insights from U-Pb and (U-Th)/He detrital zircon ages of hinterland strata: Geological Society of America Bulletin, v. 123, p. 1141–1160, doi:*10.1130/B30029.1*.

Dubiel, R.F., Potter, C.J., Good, S.C., and Snee, L.W., 1996, Reconstructing an Eocene extensional basin: The White Sage Formation, eastern Great Basin, in Beratan, K.K. ed., Reconstructing the History of Basin and Range Extension Using Sedimentology and Stratigraphy, Boulder, Colorado, Geological Society of America Special Paper 303, p. 1–14.

Ducea, M.N., 2001, The California arc: Thick granitic batholiths, eclogitic residues, lithospheric-scale thrusting, and magmatic flare-ups: GSA today, v. 11 (11), p. 4–10, doi:*10.1130/1052-5173(2001)011<0004:TCATGB>2.0.CO;2*.

Ernst, W.G., 2009, Rise and fall of the Nevadaplano: International Geology Review, v. 51, p. 583–588, doi:*10.1080/00206810903063315*.

Evans, S.L., Styron, R.H., van Soest, M.C., Hodges, K.V., and Hanson, A.D., 2015, Zircon and apatite (U-Th)/He evidence for Paleogene and Neogene extension in the Southern Snake Range, Nevada, USA: Tectonics, v. 34, p. 2142–2164, doi:*10.1002/2015TC003913*.

Fan, M., Ayyash, S.A., Tripati, A., Passey, B.H., and Griffith, E.M., 2018, Terrestrial cooling and changes in hydroclimate in the continental interior of the United States across the Eocene-Oligocene boundary: Geological Society of America Bulletin, v. 130, p. 1073–1084, doi:*10.1130/B31732.1*.

Foster, D.A., and Raza, A., 2002, Low-temperature thermochronological record of exhumation of the Bitterroot metamorphic core complex, northern Cordilleran Orogen: Tectonophysics, v. 349, p. 23–36, doi:*10.1016/S0040-1951(02)00044-6*.

Fridrich, C.J., and Thompson, R.A., 2011, Cenozoic tectonic reorganizations of the Death Valley region, southeast California and southwest Nevada: U.S. Geological Survey Professional Paper Professional Paper 1783, 47 p.

Fridrich, C.J., Thompson, R.A., Slate, J.L., Berry, M.E., and Machette, M.N., 2012, Geologic map of the southern Funeral Mountains including nearby groundwater discharge sites in Death Valley National Park, California and Nevada: U.S. Geological Survey Scientific Investigations Map 3151, scale 1:50,000.

Galbraith, R.F., and Laslett, G.M., 1993, Statistical models for mixed fission track ages: Nuclear Tracks and Radiation Measurements, v. 21, p. 459–470, doi:*10.1016/1359-0189(93)90185-C*.

Gans, P.B., and Miller, E.L., 1983, Style of mid-Tertiary extension in east-central Nevada, in Gurgel, K.D. ed., Geologic Excursions in the Overthrust Belt and Metamorphic Core Complexes of the Intermountain Region, Salt Lake City, Utah, Utah Geological and Mineral Survey, Special Studies 59, p. 107–139.

Gawthorpe, R.L., and Leeder, M.R., 2000, Tectono-sedimentary evolution of active extensional basins: Basin Research, v. 12, p. 195–218, doi:*10.1111/j.1365-2117.2000.00121.x*.

Gehrels, G.E., Dickinson, W.R., Ross, G.M., Stewart, J.H., and Howell, D.G., 1995, Detrital zircon reference for Cambrian to Triassic miogeoclinal strata of western North America: Geology, v. 23, p. 831–834, doi:*10.1130/0091-7613(1995)023<0831:DZRFCT>2.3.CO;2*.

Gehrels, G.E., Valencia, V.A., and Ruiz, J., 2008, Enhanced precision, accuracy, efficiency, and spatial resolution of U-Pb ages by laser ablation-multicollector-inductively coupled plasma-mass spectrometry: Geochemistry, Geophysics, Geosystems, v. 9, Q03017, doi:*10.1029/2007GC001805*.

Geurts, A.H., Whittaker, A.C., Gawthorpe, R.L., and Cowie, P.A., 2020, Transient landscape and stratigraphic responses to drainage integration in the actively extending central Italian Apennines: Geomorphology, v. 353, 107013, doi:*10.1016/j.geomorph.2019.107013*.

Ghosh, A., Holt, W.E., and Bahadori, A., 2019, Role of large-scale tectonic forces in intraplate earthquakes of central and eastern North America: Geochemistry, Geophysics, Geosystems, v. 20, p. 2134–2156, doi:*10.1029/2018GC008060*.

Giallorenzo, M.A., Wells, M.L., Yonkee, W.A., Stockli, D.F., and Wernicke, B.P., 2018, Timing of exhumation, Wheeler Pass thrust sheet, southern Nevada and California: Late Jurassic to middle Cretaceous evolution of the southern Sevier fold-and-thrust belt: GSA Bulletin, v. 130, p. 558–579, doi:*10.1130/B31777.1*.

Gordon, R.G., and Jurdy, D.M., 1986, Cenozoic global plate motions: Journal of Geophysical Research: Solid Earth, v. 91, p. 12389–12406, doi:*10.1029/JB091iB12p12389*.

Gutenkunst, M., 2006, Stratigraphic and geochronologic analysis of Eocene-Miocene synextensional strata in the Grapevine and Funeral mountains of southwestern

Nevada and southeastern California: Implications for regional correlation of "pre-basin and range" stratigraphy [M.S. thesis]: Purdue University, 265 p.

Haynes, S.R., 2003, Development of the Eocene Elko Basin, Northeastern Nevada: Implications for Paleogeography and Regional Tectonism [M.S. thesis]: University of British Columbia, 159 p.

Henry, C.D., 2008, Ash-flow tuffs and paleovalleys in northeastern Nevada: Implications for Eocene paleogeography and extension in the Sevier hinterland, northern Great Basin: Geosphere, v. 4, p. 1, doi:*10.1130/GES00122.1*.

Henry, C.D., Hinz, N.H., Faulds, J.E., Colgan, J.P., John, D.A., Brooks, E.R., Cassel, E.J., Garside, L.J., Davis, D.A., and Castor, S.B., 2012, Eocene-Early Miocene paleotopography of the Sierra Nevada-Great Basin-Nevadaplano based on widespread ash-flow tuffs and paleovalleys: Geosphere, v. 8, p. 1–27, doi:*10.1130/GES00727.1*.

Henry, C.D., Jackson, M.R., Mathewson, D.C., Koehler, S.R., and Moore, S.C., 2015, Eocene igneous geology and relation to mineralization: Railroad District, southern Carlin Trend, Nevada, in Pennell, W.M. and Garside, L.J. eds., New Concepts and Discoveries, Geological Society of Nevada, p. 939–965.

Hodges, K.V., and Walker, J.D., 1992, Extension in the Cretaceous Sevier orogen, North American Cordillera: Geological Society of America Bulletin, v. 104, p. 560–569, doi:*10.1130/0016-7606(1992)104<0560:EITCSO>2.3.CO;2*.

Hoisch, T.D., and Simpson, C., 1993, Rise and tilt of metamorphic rocks in the lower plate of a detachment fault in the Funeral Mountains, Death Valley, California: Journal of Geophysical Research: Solid Earth, v. 98, p. 6805–6827, doi:*10.1029/92JB02411*.

Hoisch, T.D., Wells, M.L., Beyene, M.A., Styger, S., and Vervoort, J.D., 2014, Jurassic Barrovian metamorphism in a western U.S. Cordilleran metamorphic core complex, Funeral Mountains, California: Geology, v. 42, p. 399–402, doi:*10.1130/G35352.1*.

Holm, D.K., and Dokka, R.K., 1991, Major Late Miocene cooling of the middle crust associated with extensional orogenesis in the Funeral Mountains, California: Geophysical Research Letters, v. 18, p. 1775–1778, doi:*10.1029/91GL02079*.

Humphreys, E.D., 1995, Post-Laramide removal of the Farallon slab, western United States: Geology, v. 23, p. 987–990, doi:*10.1130/0091-7613(1995)023<0987:PLROTF>2.3.CO;2*.

Humphreys, E., Hessler, E., Dueker, K., Farmer, G.L., Erslev, E., and Atwater, T., 2003, How Laramide-age hydration of North American lithosphere by the Farallon slab controlled subsequent activity in the western United States: International Geology Review, v. 45, p. 575–595, doi:*10.2747/0020-6814.45.7.575*.

Janecke, S.U., 1992, Kinematics and timing of three superposed extensional systems, east central Idaho: Evidence for an Eocene tectonic transition: Tectonics, v. 11, p. 1121–1138, doi:*10.1029/92TC00334*.

Jennings, C.W., Strand, R.G., and Rogers, T.H., 1977, Geologic map of California: California Division of Mines and Geology , scale 1:750,000.

Jones, C.H., Sonder, L.J., and Unruh, J.R., 1998, Lithospheric gravitational potential energy and past orogenesis: implications for conditions of initial Basin and Range and Laramide deformation: Geology, v. 26, p. 639–642, doi:*10.1130/0091-7613(1998)026<0639:LGPEAP>2.3.CO*.

Jones, C.H., Unruh, J.R., and Sonder, L.J., 1996, The role of gravitational potential energy in active deformation in the southwestern United States: Nature, v. 381, p. 37–41, doi:*10.1038/381037a0*.

Jurdy, D.M., 1984, The subduction of the Farallon Plate beneath North America as derived from relative plate motions: Tectonics, v. 3, p. 107–113, doi:*10.1029/TC003i002p00107*.

Konstantinou, A., Strickland, A., Miller, E.L., and Wooden, J.P., 2012, Multistage Cenozoic extension of the Albion-Raft River-Grouse Creek metamorphic core complex: Geochronologic and stratigraphic constraints: Geosphere, v. 8, p. 1429–1466, doi:*10.1130/GES00778.1*.

Lander, E.B., 2019, Early Late Duchesnean (Late Middle Eocene) Titus Canyon Fauna, Titus Canyon Formation, Death Valley National Park, Inyo County, southeastern California, in Miller, D.M. ed., Exploring Ends of Eras in the Eastern Mojave Desert, 2019 Desert Symposium Field Guide and Proceedings, p. 141–152.

Lechler, A.R., and Niemi, N.A., 2011, Sedimentologic and isotopic constraints on the Paleogene paleogeography and paleotopography of the southern Sierra Nevada, California: Geology, v. 39, p. 379–382, doi:*10.1130/G31535.1*.

Lechler, A.R., Niemi, N.A., Hren, M.T., and Lohmann, K.C., 2013, Paleoelevation estimates for the northern and central proto-Basin and Range from carbonate clumped isotope thermometry: Tectonics, v. 32, p. 295–316, doi:*10.1002/tect.20016*.

Lee, J., 1995, Rapid uplift and rotation of mylonitic rocks from beneath a detachment fault: Insights from potassium feldspar $^{40}Ar/^{39}Ar$ thermochronology, northern Snake Range, Nevada: Tectonics, v. 14, p. 54–77, doi:*10.1029/94TC01508*.

Lee, J., Blackburn, T., and Johnston, S., 2017, Timing of mid-crustal ductile extension in the northern Snake Range metamorphic core complex, Nevada: Evidence from U/Pb zircon ages: Geosphere, v. 13, p. 439–459, doi:*10.1130/GES01429.1*.

Lee, J.K.W., Williams, I.S., and Ellis, D.J., 1997, Pb, U and Th diffusion in natural zircon: Nature, v. 390, p. 159–162, doi:*10.1038/36554*.

Levandowski, W., Zellman, M., and Briggs, R., 2017, Gravitational body forces focus North American intraplate earthquakes: Nature Communications, v. 8, p. 14314, doi:*10.1038/ncomms14314*.

Liu, Z., Pagani, M., Zinniker, D., DeConto, R., Huber, M., Brinkhuis, H., Shah, S.R., Leckie, R.M., and Pearson, A., 2009, Global cooling during the Eocene-Oligocene climate transition: Science, v. 323, p. 1187–1190, doi:*10.1126/science.1166368*.

Long, S.P., 2018, Geometry and magnitude of extension in the Basin and Range Province (39°N), Utah, Nevada, and California, USA: Constraints from a province-scale cross section: GSA Bulletin, v. 131, p. 99–119, doi:*10.1130/B31974.1*.

Long, S.P., 2012, Magnitudes and spatial patterns of erosional exhumation in the Sevier hinterland, eastern Nevada and western Utah, USA: Insights from a Paleogene paleogeologic map: Geosphere, v. 8, p. 881–901, doi:*10.1130/GES00783.1*.

Long, S.P., Thomson, S.N., Reiners, P.W., and Di Fiori, R.V., 2015, Synorogenic extension localized by upper-crustal thickening: An example from the Late Cretaceous Nevadaplano: Geology, v. 43, p. 351–354, doi:*10.1130/G36431.1*.

Lund Snee, J.E., 2020, State of stress in North America: Seismicity, tectonics, and unconventional energy development [Ph.D. thesis]: Stanford University, 273 p.

Lund Snee, J.E., Miller, E.L., Grove, M., Hourigan, J.K., and Konstantinou, A., 2016, Cenozoic paleogeographic evolution of the Elko Basin and surrounding region, northeast Nevada: Geosphere, v. 12, p. 464–500, doi:*10.1130/GES01198.1*.

Lund Snee, J.E., and Zoback, M.D., 2020, Multiscale variations of the crustal stress field throughout North America: Nature Communications, v. 11, p. 1951, doi:*10.1038/s41467-020-15841-5*.

Lutz, B.M., Ketcham, R.A., Axen, G.J., Beyene, M.A., Wells, M.L., van Wijk, J.W., Stockli, D.F., and Ross, J.I., 2021, Thermo-kinematic modeling of detachment-dominated extension, northeastern Death Valley area, USA: Implications for mid-crustal thermal-rheological evolution: Tectonophysics, p. 228755, doi:*10.1016/j.tecto.2021.228755*.

MacCready, T., and Snoke, A.W., 1997, Mid-crustal flow during Tertiary extension in the Ruby Mountains core complex, Nevada: Geological Society of America Bulletin, v. 109, p. 1576–1594, doi:*10.1130/0016-7606(1997)109<1576:MCFDTE>2.3.CO;2*.

Maldonado, F., Spengler, R.W., Hanna, W.F., and Dixon, G.L., 1988, Index of granitic rock masses in the State of Nevada: U.S. Geological Survey Bulletin 1831, 86 p.

Mason, M.A., 1988, Mammalian Paleontology and stratigraphy of the Early to Middle Tertiary Sespe and Titus Canyon Formations, Southern California [Ph.D. thesis]: University of California, Berkeley, 257 p.

Mattinson, C.G., Colgan, J.P., Metcalf, J.R., Miller, E.L., and Wooden, J.L., 2007, Late Cretaceous to Paleocene metamorphism and magmatism in the Funeral Mountains metamorphic core complex, Death Valley, California, in Cloos, M., Carlson, W.D., Gilbert, M.C., Liou, J.G., and Sorenson, S.S. eds., Convergent Margin Terranes and Associated Regions: A Volume in Honor of W.G. Ernst, Boulder, Colorado, Boulder, Colo.; Geological Society of America; 1999, Geological Society of America Special Paper 419, p. 205–223.

McAllister, J.F., 1971, Preliminary geologic map of the Funeral Mountains in the Ryan quadrangle, Death Valley region, Inyo County, California: United States Geological Survey Open-File Report 71–187.

McAllister, J.F., 1952, Rocks and structure of the Quartz Spring area, northern Panamint Range, California: United States Geological Survey Open-File Report 51–73, 143 p.

McGrew, A.J., Foland, K.A., and Stockli, D., 2007, Evolution of Cenozoic volcanism and extension in the copper mountains, northeastern nevada: Geological Society of America Abstracts with Programs,.

McQuarrie, N., and Oskin, M., 2010, Palinspastic restoration of NAVDat and implications for the origin of magmatism in southwestern North America: Journal of Geophysical Research, v. 115, B10401, doi:*10.1029/2009JB006435*.

McQuarrie, N., and Wernicke, B.P., 2005, An animated tectonic reconstruction of southwestern North America since 36 Ma: Geosphere, v. 1, p. 147–172, doi:*10.1130/GES00016.1*.

Mercer, C.M., and Hodges, K.V., 2016, ArAR — A software tool to promote the robust comparison of K–Ar and $^{40}Ar/^{39}Ar$ dates published using different decay, isotopic, and monitor-age parameters: Chemical Geology, v. 440, p. 148–163, doi:*10.1016/j.chemgeo.2016.06.020*.

Methner, K., Mulch, A., Teyssier, C., Wells, M.L., Cosca, M.A., Gottardi, R., Gébelin, A., and Chamberlain, C.P., 2015, Eocene and Miocene extension, meteoric fluid infiltration, and core complex formation in the Great Basin (Raft River Mountains, Utah): Tectonics, v. 34, p. 680–693, doi:*10.1002/2014TC003766*.

Miller, E.L., and Gans, P.B., 1989, Cretaceous crustal structure and metamorphism in the hinterland of the Sevier thrust belt, western U.S. Cordillera: Geology, v. 17, p. 59–62, doi:*10.1130/0091-7613(1989)017<0059:CCSAMI>2.3.CO;2*.

Molnar, P., 1983, Average regional strain due to slip on numerous faults of different orientations: Journal of Geophysical Research, v. 88, p. 6430–6432, doi:*10.1029/JB088iB08p06430*.

Molnar, P., England, P.C., and Jones, C.H., 2015, Mantle dynamics, isostasy, and the support of high terrain: Journal of Geophysical Research: Solid Earth, v. 120, p. 1932–1957, doi:*10.1002/2014JB011724*.

Moye, F.J., Hackett, W.R., Blakley, J.D., and Snider, L.G., 1988, Regional geologic setting and volcanic stratigraphy of the Challis Volcanic Field, central Idaho, in Link, P.K. and Hackett, W.R. eds., Guidebook to the Geology of Central and Southern Idaho, Idaho Geological Survey Bulletin 27, p. 87–97.

Mulch, A., Chamberlain, C.P., Cosca, M.A., Teyssier, C., Methner, K., Hren, M.T., and Graham, S.A., 2015, Rapid change in high-elevation precipitation patterns of western North America during the Middle Eocene Climatic Optimum (MECO): American Journal of Science, v. 315, p. 317–336, doi:*10.2475/04.2015.02*.

Murray, D.A., 2002, Oligocene to Lower Miocene Stratigraphy and extensional basin development, southwestern Nevada and southeastern California [M.S. thesis]: Purdue University, 179 p.

Niemi, N.A., 2002, Extensional tectonics in the Basin and Range province and the geology of the Grapevine Mountains, Death Valley region, California and Nevada [Ph.D. thesis]: California Institute of Technology, 344 p.

Niemi, N.A., 2012, Geologic map of the central Grapevine Mountains, Inyo County, California, and Esmeralda and Nye Counties, Nevada: Geological Society of America Digital Map and Chart Series 12, doi:*10.1130/2012.DMCH012*.

Niemi, N.A., and Clark, M.K., 2018, Long-term exhumation rates exceed paleoseismic slip rates in the central Santa Monica Mountains, Los Angeles County, California: Geology, v. 46, p. 63–66, doi:*10.1130/G39388.1*.

Niemi, N.A., Wernicke, B.P., Brady, R.J., Saleeby, J.B., and Dunne, G.C., 2001, Distribution and provenance of the middle Miocene Eagle Mountain Formation, and implications for regional kinematic analysis of the Basin and Range province: Geological Society of America Bulletin, v. 113, p. 419–442, doi:*10.1130/0016-7606(2001)113<0419:DAPOTM>2.0.CO;2*.

Nyborg, T., Nyborg, B., Fairfield, H., and Jansen, B., 2017, Fossil fishes of Death Valley National Park, California: Reconstructing the origins and geographical distribution of the indigenous ichthyofauna of southeastern California: Geological Society of America Abstracts with Programs, v. 49, doi:*10.1130/abs/2017AM-302235*.

Platt, J.P., 2007, From orogenic hinterlands to Mediterranean-style back-arc basins: A comparative analysis: Journal of the Geological Society, v. 164, p. 297–311, doi:*10.1144/0016-76492006-093*.

Potter, C.J., Dubiel, R.F., Snee, L.W., and Good, S.C., 1995, Eocene extension of early Eocene lacustrine strata in a complexly deformed Sevier-Laramide hinterland, northwest Utah and northeast Nevada: Geology, v. 23, p. 181–184, doi:*10.1130/0091-7613(1995)023<0181:EEOEEL>2.3.CO;2*.

Rahl, J.M., McGrew, A.J., and Foland, K.A., 2002, Transition from Contraction to Extension in the Northeastern Basin and Range: New Evidence from the Copper Mountains, Nevada: The Journal of Geology, v. 110, p. 179–194, doi:*10.1086/338413*.

Reiners, P.W., Brady, R., Farley, K.A., Fryxell, J.E., Wernicke, B., and Lux, D., 2000, Helium and argon thermochronometry of the Gold Butte block, south Virgin Mountains, Nevada: Earth and Planetary Science Letters, v. 178, p. 315–326, doi:*10.1016/S0012-821X(00)00080-7*.

Renik, B., and Christie-Blick, N., 2013, A new hypothesis for the amount and distribution of dextral displacement along the Fish Lake Valley-northern Death Valley-Furnace Creek fault zone, California-Nevada: Tectonics, v. 32, p. 123–145, doi:*10.1029/2012TC003170*.

Renne, P.R., Balco, G., Ludwig, K.R., Mundil, R., and Min, K., 2011, Response to the comment by W.H. Schwarz et al. on "Joint determination of 40K decay constants and 40Ar*/40K for the Fish Canyon sanidine standard, and improved accuracy for $^{40}Ar/^{39}Ar$ geochronology" by P.R. Renne et al. (2010): Geochimica et Cosmochimica Acta, v. 75, p. 5097–5100, doi:*10.1016/j.gca.2011.06.021*.

Renne, P.R., Mundil, R., Balco, G., Min, K., and Ludwig, K.R., 2010, Joint determination of 40K decay constants and $^{40}Ar*/^{40}K$ for the Fish Canyon sanidine standard, and improved accuracy for $^{40}Ar/^{39}Ar$ geochronology: Geochimica et Cosmochimica Acta, v. 75, p. 5349–5367.

Reynolds, M.W., 1974, Geology of the Grapevine Mountains, Death Valley, California: A summary, in Guidebook, Death Valley Region, California and Nevada, Geological Society of America Cordilleran Section Fieldtrip 1, Shoshone, California, Death Valley Publishing Company, p. 92–99.

Reynolds, M. W., 1969, Stratigraphy and structural geology of the Titus and Titanothere Canyons area, Death Valley, California [Ph.D. thesis]: University of California, Berkeley, 310 p.

Ridgway, K., Stamatakos, J., Gutenkunst, M., and Dubreuilh, P., 2011, Stratigraphic analysis and regional correlation of Oligocene and Early Miocene strata in the Yucca Mountain area: U.S. Nuclear Regulatory Commission Contract NRC-02-07-006, 60 p.

Salyards, S.L., and Shoemaker, E.M., 1987, Landslide and debris flow deposits in the Thumb Member of the Miocene Horse Spring Formation on the east side of Frenchman Mountain, Nevada: A measure of basin-range extension, in Hill, M. ed., Centennial Field Guide (Cordilleran Section), p. 49–51.

Sanford, R.F., 2005, Geology and stratigraphy of the Challis Volcanic Group and related rocks, Little Wood River area, south-central Idaho, with a section on Geochronology by Lawrence W. Snee: United States Geological Survey Bulletin 2064–II, 22 p., doi:*10.3133/b2064II*.

Satarugsa, P., and Johnson, R.A., 2000, Cenozoic tectonic evolution of the Ruby Mountains metamorphic core complex and adjacent valleys, northeastern Nevada: Rocky Mountain Geology, v. 35, p. 205–230, doi:*10.2113/35.2.205*.

Sawyer, D.A., Fleck, R.J., Lanphere, M.A., Warren, R.G., Broxton, D.E., and Hudson, M.R., 1994, Episodic caldera volcanism in the Miocene southwestern Nevada volcanic field: Revised stratigraphic framework, $^{40}Ar/^{39}Ar$ geochronology, and implications for magmatism and extension: Geological Society of America Bulletin, v. 106, p. 1304–1318, doi:*10.1130/0016-7606(1994)106<1304:ECVITM>2.3.CO;2*.

Saylor, B.Z., 1991, The Titus Canyon Formation: Evidence for early Oligocene extension in the Death Valley area, CA [M.S. thesis]: Massachusetts Institute of Technology, 65 p.

Saylor, B.Z., and Hodges, K.V., 1994, $^{40}Ar/^{39}Ar$ age constraints on the depositional history of the Oligocene Titus Canyon Formation, Death Valley, CA: Geological Society of America Abstracts with Programs,.

Schellart, W.P., Stegman, D.R., Farrington, R.J., Freeman, J., and Moresi, L., 2010, Cenozoic tectonics of western North America controlled by evolving width of Farallon slab: Science, v. 329, p. 316–319.

Serpa, L., and Pavlis, T.L., 1996, Three-dimensional model of the late Cenozoic history of the Death Valley region, southeastern California: Tectonics, v. 15, p. 1113–1128, doi:*10.1029/96TC01633*.

Smith, M.E., Cassel, E.J., Jicha, B.R., Singer, B.S., and Canada, A.S., 2017, Hinterland drainage closure and lake formation in response to middle Eocene Farallon slab removal, Nevada, U.S.A.: Earth and Planetary Science Letters, v. 479, p. 156–169, doi:*10.1016/j.epsl.2017.09.023*.

Snell, K.E., Koch, P.L., Druschke, P., Foreman, B.Z., and Eiler, J.M., 2014, High elevation of the “Nevadaplano” during the Late Cretaceous: Earth and Planetary Science Letters, v. 386, p. 52–63, doi:*10.1016/j.epsl.2013.10.046*.

Snow, J.K., 1990, Cordilleran orogenesis, extensional tectonics, and geology of the Cottonwood Mountains area, Death Valley region, California and Nevada [Ph.D. thesis]: Harvard University, 533 p.

Snow, J.K., 1993, Tertiary strata of the Ubehebe basin and northern Cottonwood Mountains, Death Valley region, California, in Tertiary Stratigraphy of Highly Extended Terranes, California, Arizona, and Nevada, U.S. Geological Survey Bulletin 2053, p. 7–11, doi:*10.3133/b2053*.

Snow, J.K., Asmerom, Y., and Lux, D.R., 1991, Permian-Triassic plutonism and tectonics, Death Valley region, California and Nevada: Geology, v. 19, p. 629–632, doi:*10.1130/0091-7613(1991)019<0629:PTPATD>2.3.CO;2*.

Snow, J.K., and Lux, D.R., 1999, Tectono-sequence stratigraphy of Tertiary rocks in the Cottonwood Mountains and northern Death Valley area, California and Nevada, in Wright, L.A. and Troxel, B.W. eds., Cenozoic Basins of the Death Valley Region, Boulder, Colorado, Geological Society of America Special Paper 333, p. 17–64, doi:*10.1130/0-8137-2333-7.17*.

Snow, J.K., and Wernicke, B.P., 2000, Cenozoic tectonism in the central basin and range: Magnitude, rate, and distribution of upper crustal strain: American Journal of Science, v. 300, p. 659–719, doi:*10.2475/ajs.300.9.659*.

Snow, J.K., and Wernicke, B., 1989, Uniqueness of geological correlations: An example from the Death Valley extended terrain: Geological Society of America Bulletin, v. 101, p. 1351–1362, doi:*10.1130/0016-7606(1989)101<1351:UOGCAE>2.3.CO;2*.

Snow, J.K., and White, C., 1990, Listric normal faulting and synorogenic sedimentation, northern Cottonwood Mountains, Death Valley region, California: Basin and Range extensional tectonics near the latitude of Las Vegas, Nevada: Geological Society of America Memoir, v. 176, p. 413–445, doi:*10.1130/MEM176-p413*.

Snyder, N.P., and Hodges, K.V., 2000, Depositional and tectonic evolution of a supradetachment basin: $^{40}Ar/^{39}Ar$ geochronology of the Nova Formation, Panamint Range, California: Basin Research, v. 12, p. 19–30, doi:*10.1046/j.1365-2117.2000.00108.x*.

Sonder, L.J., England, P.C., Wernicke, B.P., and Christiansen, R.L., 1987, A physical model for Cenozoic extension of western North America: Geological Society, London, Special Publications, v. 28, p. 187–201, doi:*10.1144/GSL.SP.1987.028.01.14*.

Sonder, L.J., and Jones, C.H., 1999, Western United States extension: How the west was widened: Annual Review of Earth and Planetary Sciences, v. 27, p. 417–462, doi:*10.1146/annurev.earth.27.1.417*.

Spell, T.L., and McDougall, I., 2003, Characterization and calibration of $^{40}Ar/^{39}Ar$ dating standards: Chemical Geology, v. 198, p. 189–211, doi:*10.1016/S0009-2541(03)00005-6*.

Stevens, C., and Stone, P., 2005, Interpretation of the Last Chance thrust, Death Valley region, California, as an Early Permian décollement in a previously undeformed shale basin: Earth-Science Reviews, v. 73, p. 79–101, doi:*10.1016/j.earscirev.2005.04.005*.

Stock, C., 1936, Titanotheres from the Titus Canyon Formation, California: Proceedings of the National Academy of Science, v. 22, p. 656–661, doi:*10.1073/pnas.22.11.656*.

Stock, C., and Bode, F.D., 1935, Occurrence of Lower Oligocene mammal-bearing beds near Death Valley, California: Proceedings of the National Academy of Sciences, v. 21, p. 571–579, doi:*10.1073/pnas.21.10.571*.

Sullivan, W.A., and Snoke, A.W., 2007, Comparative anatomy of core-complex development in the northeastern Great Basin, U.S.A.: Rocky Mountain Geology, v. 42, p. 1–29, doi:*10.2113/gsrocky.42.1.1*.

Thomas, W.A., 2011, Detrital-zircon geochronology and sedimentary provenance: Lithosphere, v. 3, p. 304–308, doi:*10.1130/RF.L001.1*.

Topping, D.J., 1993, Paleogeographic reconstruction of the Death Valley extended region: Evidence from Miocene large rock-avalanche deposits in the Amargosa Chaos Basin, California: Geological Society of America Bulletin, v. 105, p. 1190–1213.

Van Buer, N.J., Miller, E.L., and Dumitru, T.A., 2009, Early Tertiary paleogeologic map of the northern Sierra Nevada batholith and the northwestern Basin and Range: Geology, v. 37, p. 371–374, doi:*10.1130/G25448A.1*.

Vandervoort, D.S., and Schmitt, J.G., 1990, Cretaceous to early Tertiary paleogeography in the hinterland of the Sevier thrust belt, east-central Nevada: Geology, v. 18, p. 567–570, doi:*10.1130/0091-7613(1990)018<0567:CTETPI>2.3.CO;2*.

Verdel, C., Niemi, N., and van der Pluijm, B.A., 2011, Variations in the illite to muscovite transition related to metamorphic conditions and detrital muscovite content: insight from the Paleozoic passive margin of the southwestern United States: The Journal of Geology, v. 119, p. 419–437, doi:*10.1086/660086*.

Vermeesch, P., 2018, IsoplotR: A free and open toolbox for geochronology: Geoscience Frontiers, v. 9, p. 1479–1493, doi:*10.1016/j.gsf.2018.04.001*.

Vermeesch, P., 2021, Maximum depositional age estimation revisited: Geoscience Frontiers, v. 12, p. 843–850, doi:*10.1016/j.gsf.2020.08.008*.

Vogl, J.J., Foster, D.A., Fanning, C.M., Kent, K.A., Rodgers, D.W., and Diedesch, T., 2012, Timing of extension in the Pioneer metamorphic core complex with implications for the spatial-temporal pattern of Cenozoic extension and exhumation in the northern U.S. Cordillera: Tectonics, v. 31, TC1008, doi:*10.1029/2011TC002981*.

Wagner, F.H., and Johnson, R.A., 2006, Coupled basin evolution and late-stage metamorphic core complex exhumation in the southern Basin and Range Province, southeastern Arizona: Tectonophysics, v. 420, p. 141–160, doi:*10.1016/j.tecto.2006.01.012*.

Wells, M.L., Dallmeyer, R.D., and Allmendinger, R.W., 1990, Late Cretaceous extension in the hinterland of the Sevier thrust belt, northwestern Utah and southern Idaho: Geology, v. 18, p. 929–933, doi:*10.1130/0091-7613(1990)018<0929:LCEITH>2.3.CO;2*.

Wells, M.L., and Hoisch, T.D., 2008, The role of mantle delamination in widespread Late Cretaceous extension and magmatism in the Cordilleran orogen, western United States: Geological Society of America Bulletin, v. 120, p. 515–530, doi:*10.1130/B26006.1*.

Wells, M.L., Hoisch, T.D., Cruz-Uribe, A.M., and Vervoort, J.D., 2012, Geodynamics of synconvergent extension and tectonic mode switching: Constraints from the Sevier-Laramide orogen: Tectonics, v. 31, TC1002, doi:*10.1029/2011TC002913*.

Wells, M.L., Spell, T.L., Hoisch, T.D., Arriola, T., and Zanetti, K.A., 2008, Laser-probe 40Ar/ 39Ar dating of strain fringes: Mid-Cretaceous synconvergent orogen-parallel extension in the interior of the Sevier orogen: Tectonics, v. 27, TC3012, doi:*10.1029/2007TC002153*.

Wernicke, B., Axen, G.J., and Snow, J.K., 1988, Basin and Range extensional tectonics at the latitude of Las Vegas, Nevada: Geological Society of America Bulletin, v. 100, p. 1738–1757, doi:*10.1130/0016-7606(1988)100<1738:BARETA>2.3.CO;2*.

Wright, L.A., and Troxel, B.W., 1993, Geologic map of the central and northern Funeral Mountains and adjacent areas, Death Valley region, southern California: United States Geological Survey Miscellaneous Investigations Series Map I-2305, scale 1:48,000.

Yonkee, W.A., and Weil, A.B., 2015, Tectonic evolution of the Sevier and Laramide belts within the North American Cordillera orogenic system: Earth-Science Reviews, v. 150, p. 531–593, doi:*10.1016/j.earscirev.2015.08.001*.

Zhenhan, W., Barosh, P.J., Zhonghai, W., Daogong, H., Xun, Z., and Peisheng, Y., 2008, Vast early Miocene lakes of the central Tibetan Plateau: Geological Society of America Bulletin, v. 120, p. 1326–1337, doi:*10.1130/B26043.1*.

Zhou, Q., and Liu, L., 2019, Topographic evolution of the western United States since the early Miocene: Earth and Planetary Science Letters, v. 514, p. 1–12, doi:*10.1016/j.epsl.2019.02.029*.

Chapter 3
Multi-thermochronometer Analysis Reveals Strain Heterogeneity in the Northern Basin and Range Extensional Province, Utah and Nevada[1]

3.1 Abstract

Low-temperature thermochronology is a powerful tool for testing competing hypotheses for which geodynamic mechanisms and rheological factors exert the greatest control over the distribution, rates, and style of continental extension in the Basin and Range province. However, the bedrock of the northern Basin and Range is primarily limestone and shale which lack the apatite and zircon minerals needed for thermochronologic analysis. To overcome this limitation, we targeted small plutonic bodies that contain the necessary minerals but are too small for standard multi-sample transect thermochronology techniques, instead analyzing individual samples with multiple thermochronometers that span a range of closure temperatures. We present new apatite and zircon (U-Th)/He and apatite fission-track analyses from twelve localities across the northern Basin and Range. We interpret the cooling ages through inverse thermal modeling. Modeled time-temperature histories are highly variable, with the most rapid phase of extension occurring in the Miocene. Modeled thermal histories indicate minimal cooling during the Eocene-Oligocene, a time hypothesized to have been a major extensional phase in much of the northern Basin and Range. In locations that did not experience significant extensional exhumation, our time-temperature histories instead record changes in rock exhumation during the Cretaceous-Paleogene construction of the Sevier orogenic belt and the topographic isolation of the Nevadaplano.

[1] *Midttun, N., and Niemi, N.A., in prep. for submission to Tectonics*

3.2 Introduction

Continental deformation constitutes a key control on global topography, climate, biodiversity, and lithospheric structure. In many geologic settings, there remains little consensus around which geodynamic mechanisms and rheological factors exert the greatest control over continental deformation on orogenic timescales. Deforming continents exhibit complex patterns of past deformation, which geologists are only able to observe through the imperfect lens of sparse data with incomplete spatial and temporal coverage. These challenges leave even the most comprehensive integrative models of continental deformation at times contradictory, under-constrained by geologic data, and highly uncertain (e.g., Snow and Wernicke, 2000; McQuarrie and Wernicke, 2005; Bennett et al., 2016; Gion et al., 2017; Bahadori et al., 2018). These numerous challenges are exemplified in the Basin and Range extensional province of western North America, one of the most intensely studied regions of continental deformation in the world, and a place where fundamental questions around the distribution, magnitudes, and styles of extensional deformation remain debated.

The process of continental extension is a primary step in the Wilson cycle that displays a high degree of variability in style, rate, and spatial geometry across the globe (Benes and Davy, 1996). Many mechanisms have been proposed to control strain localization in continental extensional settings. For example, deformation may concentrate onto weak pre-existing discontinuities such as fault zones (e.g., Holdsworth et al., 2001), tectonic sutures (e.g., Holdsworth et al., 2001; van Wijk, 2005; Glorie et al., 2012; Cavazza et al., 2015), stratigraphic intervals of weak rock (e.g., Singleton et al., 2018), or volcanic features like sills and dikes (e.g., Parsons and Thompson, 1993). Spatially variable crustal thickness modifies existing stress fields by imposing gravitationally potential energy (GPE) stress gradients, potentially driving extension in areas with steep topographic gradients (Coney and Harms, 1984; Jones et al., 1996; Bahadori and Holt, 2019). Periodic instability above a hot, fluid-like lower crust or asthenosphere may lead to the development of lithosphere-scale Rayleigh-Taylor instabilities, resulting in alternating regions of enhanced and diminished strain during extension (e.g., Ricard and Froidevaux, 1986; Zuber et al., 1986; Corti, 2005). Magmatism can heat and weaken the crust, enhancing deformation (e.g., Gans et al., 1989; Axen et al.,

1993; Liu, 2001). Many of these proposed mechanisms for localizing strain also interact with other mechanisms, or with deformation itself, further complicating the task of linking observed patterns of strain to specific governing mechanisms and reconstructing deformation in the geologic past. Testing these hypothesized controls on continental deformation requires large datasets that can constrain deformation across both space and time. As the type-locality for prolonged continental rifting, and the subject of an extraordinary amount of geological research, the Basin and Range extensional province is an ideal natural laboratory within which to compare these geodynamic mechanisms.

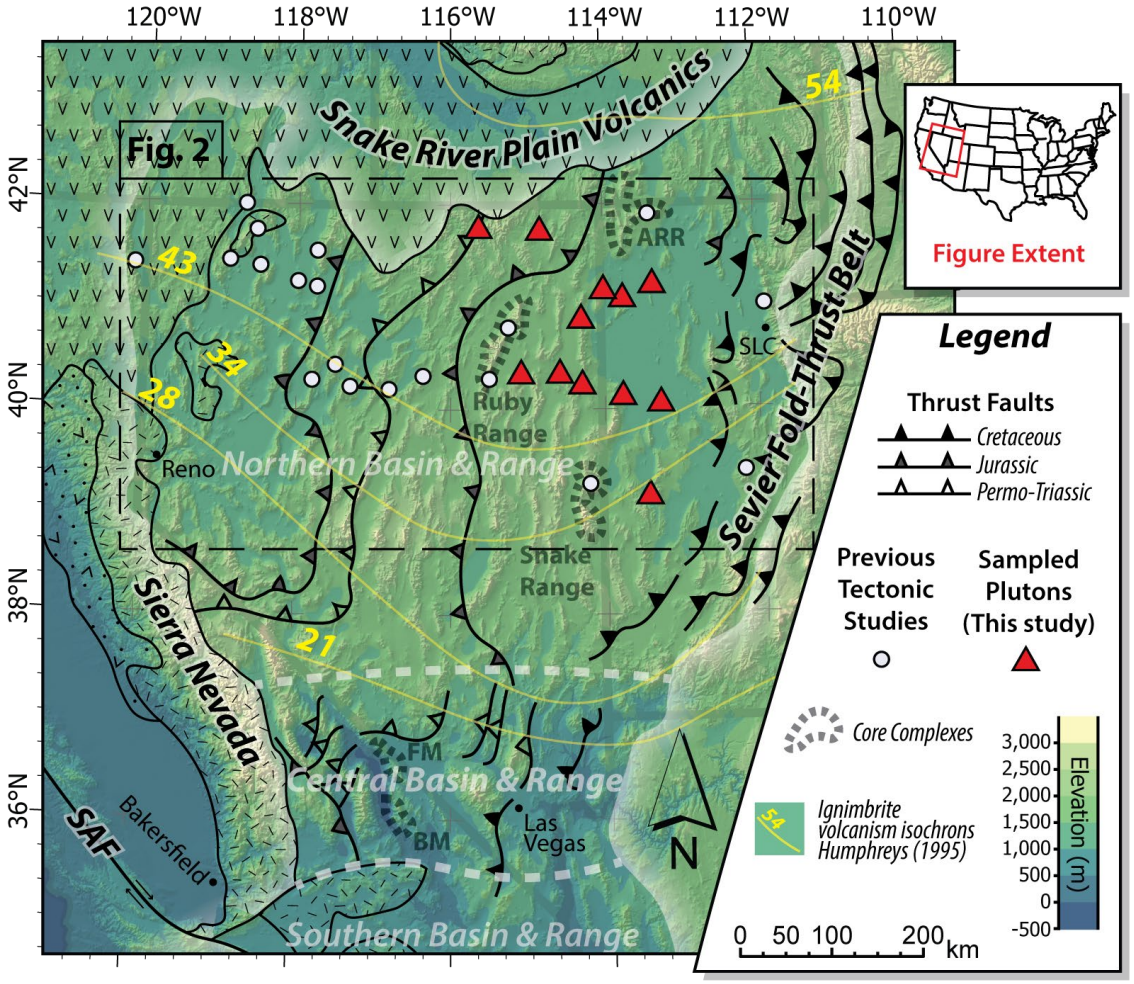


Figure 3.1: Overview map of the northern Basin and Range.
Shaded elevation map of the Basin and Range extensional province showing thermochronology studies (Fig. 3.2), major thrust belts, the locations of metamorphic core complexes, contours of the north-south sweep of ignimbrite volcanism that tracks the delamination of the Farallon slab (Humphreys, 1995), and the locations and names of geologic sub-provinces. ARR = Albion-Raft River, FM = Funeral Mountains, BM = Black Mountains. SLC = Salt Lake City, SAF = San Andreas Fault.

The geologic history of the Basin and Range region (Fig. 3.1) can be broadly described as a complex transition from Mesozoic contraction to Cenozoic orogenic collapse followed by protracted extension and right-lateral shear (Dickinson, 2002; 2006). Following Neoproterozoic and early Paleozoic accumulation of thick marine strata on a passive margin, subduction initiated along the western margin of North America in the late Paleozoic (Dickinson, 2004). Subduction of the Farallon plate beneath North America drove episodic mountain building, initially through accretion of island arcs, and later through the development of a continuous subduction zone during the Mesozoic (Dickinson, 2009; Yonkee and Weil, 2015). By the Late Cretaceous, a significant mountain range had been constructed along the North American Cordillera, and the future site of the Basin and Range province was occupied by a high-elevation (~2+ km elevation), low-relief orogenic plateau called the Nevadaplano (DeCelles, 2004; Ernst, 2009).

The end of major contraction and transition to a primarily extensional tectonic regime was marked by a series of tectonic events starting in the Eocene, when at ~40 Ma the approach of the Pacific-Farallon spreading ridge (i.e. the East Pacific Rise) to the subduction zone caused a sharp slowdown in the rate of subduction (Schellart et al., 2010), along with a corresponding reduction in the dip of the down going Farallon plate that eventually led to the slab flattening against, cooling, and hydrating the base of the North American lithosphere (Yonkee and Weil, 2015; DeCelles, 2004). Later removal of the Farallon flat slab from beneath the North American lithosphere proceeded diachronously north to south from Paleocene to Miocene time, as evidenced by a sweep of ignimbrite volcanism triggered by asthenospheric upwelling against the hydrated North American lithosphere (Fig. 3.1; Humphreys, 1995; McQuarrie and Oskin, 2010). This sweep of volcanism, known as the ignimbrite flareup, started in the Paleocene in southern British Columbia and ended in the Miocene at the latitude of Death Valley, and is hypothesized to have triggered deeply rooted rapid extensional exhumation of metamorphic core complexes along the Cordillera through thermal weakening of potentially unstable overthickened crust (Fig. 3.1; Coney and Harms, 1984; Armstrong and Ward, 1991; Axen et al., 1993; Liu and Shen, 1998; Rahl et al., 2002; Canada et al., 2020). In the latest Oligocene to early Miocene (starting ca. 25-23 Ma), the East Pacific

Rise spreading ridge began subducting beneath North America, initiating a transform plate boundary along western North America that eventually became the San Andreas transform fault (Fig. 3.1; Atwater, 1970; Dickinson, 2002).

The sharp reduction of convergence at the plate boundary in the Eocene (~40 Ma; Schellart et al., 2010), the diachronous Paleocene-Miocene removal of the Farallon flat slab (~55-10 Ma; Dickinson and Snyder, 1978; Humphreys, 1995), and the Neogene transition from a subduction to a transform plate boundary (~23 Ma to present; Atwater, 1970) each potentially triggered changes in the style and rates of extensional tectonism in the Basin and Range. We can temporally and spatially differentiate these three trigger mechanisms using the fact that the slowdown in Eocene convergence was synchronous along the plate boundary, Farallon removal was strongly time transgressive from north to south, and Miocene initiation of the transform boundary was time transgressive from south to north. However, differentiating these three processes requires precise data constraining the strain histories across the northern Basin and Range; data that is currently lacking outside of the well-studied metamorphic core complexes (Fig. 3.1).

The extensional history of the Basin and Range is heterogeneous in space and time (Dickinson, 2002; Snow and Wernicke, 2000; McQuarrie and Wernicke, 2005). The modern spatial uniformity of topography and crustal thickness across the Basin and Range could be simplistically interpreted as suggesting a degree of spatial uniformity in the distribution of extensional strain. However, thermochronological data and cross section and map view restorations identify significant spatial variability in the magnitude of extension in the region. In the central Basin and Range, the Spring Mountains and Sheep Mountains form a 30-40 km wide undeformed belt separating the highly extended Death Valley and Lake Meade domains (Wernicke et al., 1982; Snow and Wernicke, 2000). In the northeastern Basin and Range, Gans (1987) described highly extended crustal domains separated by intact crustal blocks, a similar pattern to spatial variability in Miocene extensional magnitudes identified by Colgan and Henry (2009) in a 200 km transect from the Stillwater Range to the Medicine Range in the central northern Basin and Range. Long (2018) observed east-west variability in the magnitude of extension based on a province wide cross section. Such geologic variations in strain are also consistent with present-day geodetic studies, which identify regions of low strain rate in

the center of the Basin and Range, and higher strain rates along the eastern and western margins, matching patterns of historic seismicity (e.g., Bennett et al., 2003).

The origin of small-scale (50-200 km wavelength) variability in Miocene extensional strain, along with the distribution of Miocene extension within the broader Basin and Range, remains unclear. If gravitational potential energy was a dominant driver of Miocene extension, then variability in the spatial distribution of extension may be the result of variations in pre-extensional crustal thickness inherited from the Sevier orogeny (e.g., Coney and Harms, 1984; Bahadori et al., 2018; Long, 2018). If the locations and dip-directions of major detachment faults controlled the distribution of later upper crustal extension, then highly extended and rigid domains may correlate with their position relative to deeply rooted detachment faults or inherited structures from the Sevier orogeny (e.g., Wernicke, 1985).

Here we explore the distribution and potential controls on small-scale variability of extensional strain within the northern Basin and Range province using low-temperature thermochronology. Previous studies of extensional strain have focused on metamorphic core complexes, where deep exhumation and abundant igneous and metamorphic rocks generate suitable targets for detailed thermochronologic analysis. Outside of the belt of metamorphic core complexes, the bedrock of the eastern Basin and Range is dominated by carbonate sedimentary rocks of the Paleozoic passive margin which lack sufficient high-quality apatite and zircon grains for low-temperature thermochronological analysis. To overcome the shortage of amenable geologic materials for thermochronology, we sampled a series of small plutons and stocks (Fig. 3.1) that were emplaced during contractional orogenesis in the Jurassic, well before extension initiated across the Basin and Range. These small plutons are generally too small for standard elevation or stratigraphic thermochronology transects, so we instead applied three different low-temperature thermochronometers to individual samples from each pluton, thus enabling inverse modeling of full thermal histories without sampling across a range of paleodepths. These thermal histories describe the tectonic evolution of a broad swath of the northern Basin and Range, revealing the character of Cenozoic extensional deformation, and allowing us to connect observed patterns of deformation back to likely geodynamic and rheological controls.

Table 3.1: Sample locations and pluton names.

Sample	Latitude (Nº)	Longitude (Wº)	Elevation (m)	Range/Locality Name	Intrusion Name
GP102605-3	40.08783	113.27942	1450	Granite Peak	Granite Peak pluton
NBR18-C1	41.77735	114.83203	2186	Salmon River Range	Contact pluton
NBR18-CP1	41.79685	115.63399	2336	Copper Mountains	Coffepot (Bruneau River) stock
NBR18-DB1	40.37836	115.08669	1902	Delcer Buttes	Delcer Buttes pluton
NBR18-DV1	40.38055	114.58346	1945	Dolly Varden Mts.	Melrose stock
NBR18-GH1	40.16065	113.76767	1596	N. Deep Creek Range	Gold Hill pluton
NBR18-PR1	41.19702	114.00376	1943	Pilot Range	McGinty/Patterson Pass pluton
NBR18-SI1	41.11493	113.75377	1431	Silver Island Mountains	Crater Island pluton
NBR18-T1	40.91377	114.29954	1795	Toano Range	Silver Zone Pass pluton
NBR18-WH1	40.27242	114.29366	1888	White Horse Mt.	White Horse intrusion
NBR19-NM1	41.24514	113.36159	1391	Newfoundland Mts.	Newfoundland stock
NPQM1612	39.1872	113.4482	1612	House Range	Notch Peak pluton
NPQM1800	39.18275	113.4355	1827	House Range	Notch Peak pluton
NPQM2000	39.18304	113.4252	2018	House Range	Notch Peak pluton
NPQM2200	39.18059	113.4233	2201	House Range	Notch Peak pluton
NPQM2600	39.16813	113.4077	2652	House Range	Notch Peak pluton
NPQM2800	39.17683	113.4156	2789	House Range	Notch Peak pluton
95BR009	39.17778	113.41306	2688	House Range	Notch Peak pluton
95BR011	39.17833	113.42667	2275	House Range	Notch Peak pluton
95BR014	39.18389	113.44056	1850	House Range	Notch Peak pluton

Table 3.2: Compiled estimates of pluton emplacement-depths.

		Emplacement Depths		
Sample	Pluton	Depth (km)	Method	Source Study
GP102605-3	Granite Peak pluton	-	-	-
NBR18-C1	Contact pluton	9.3±3.5	Al-in-hornblende geobarometry & overburden estimates	Miller & Hoisch (1995)
NBR18-CP1	Coffeepot (Bruneau River) stock	11±3	Metamorphic mineralogy of contact aureole	Rahl et al. (2002)
NBR18-DB1	Delcer Buttes pluton	Hypabyssal	Estimated stratigraphic overburden	Colgan & Henry (2009)
NBR18-DV1	Melrose stock	7.7±1	Mineralogy	El-Shazly et al. (2011)
NBR18-GH1	Gold Hill pluton	-	-	-
NBR18-PR1	McGinty/Patterson Pass pluton	12.2±1	Al-in-hornblende geobarometry & overburden estimates	Miller & Hoisch (1995)
NBR18-SI1	Crater Island pluton	6.9±2.6	Al-in-hornblende geobarometry & overburden estimates	Miller & Hoisch (1995)
NBR18-T1	Silver Zone Pass pluton	14.9±3.2	Al-in-hornblende geobarometry & overburden estimates	Miller & Hoisch (1995)
NBR18-WH1	White Horse pluton	8.3±1.2	Al-in-hornblende geobarometry & overburden estimates	Miller & Hoisch (1995)
NBR19-NM1	Newfoundland stock	9.8±2.5	Al-in-hornblende geobarometry & overburden estimates	Miller & Hoisch (1995)
NPQM…	Notch Peak pluton	5.6±1.9	Estimated stratigraphic overburden	Granath et al. (1983)

Table 3.3: Compiled Ar geochronology.

		Argon Cooling Ages		
Sample	Pluton	Age (Ma)	Method	Source Study
GP102605-3	Granite Peak pluton	16.0±0.04	Plateau Ar/Ar Biotite	UGS OFR-542
NBR18-C1	Contact pluton	152	K/Ar Biotite	Coats et al. (1965)
NBR18-CP1	Coffeepot (Bruneau River) stock	103±0.4	Plateau Ar/Ar Biotite	Rahl et al. (2002)
NBR18-DB1	Delcer Buttes pluton	-	-	-
NBR18-DV1	Melrose stock	125+19-6	K/Ar Bio. - Hbl. Mix	Armstrong and Hansen (1966)
NBR18-GH1	Gold Hill pluton	152	K/Ar Biotite	Moore and McKee, 1983
NBR18-PR1	McGinty/Patterson Pass pluton	37	K/Ar Biotite	Miller et al. (1987)
NBR18-SI1	Crater Island pluton	-	-	-
NBR18-T1	Silver Zone Pass pluton	148	K/Ar Biotite	Coats et al. (1965)
NBR18-WH1	White Horse pluton	-	-	-
NBR19-NM1	Newfoundland stock	-	-	-
NPQM…	Notch Peak pluton	165±1.9	Ar/Ar Biotite	Nabelek et al. (1986)

Table 3.4: Compiled pluton emplacement ages.

		Emplacement Age		
Sample	Pluton	Age (Ma)	Method	Source Study
GP102605-3	Granite Peak pluton	150	U-Pb Zircon	Christiansen and Vervoort (2009)
NBR18-C1	Contact pluton	160	U-Pb Zircon	Zens (2019)
NBR18-CP1	Coffeepot (Bruneau River) stock	108-111	U-Pb Zircon	Canada et al. (2019)
NBR18-DB1	Delcer Buttes pluton	150-161	U-Pb Zircon	King (2020)
NBR18-DV1	Melrose stock	165	U-Pb Zircon	Zamudio (1992)
NBR18-GH1	Gold Hill pluton	152	K-Ar Biotite	Moore and McKee (1983)
NBR18-PR1	McGinty/Patterson Pass pluton	37	K-Ar Biotite	Miller et al. (1987)
NBR18-SI1	Crater Island pluton	159	K-Ar Biotite	Moore and McKee (1983)
NBR18-T1	Silver Zone Pass pluton	162	U-Pb Zircon	Miller et al. (1990)
NBR18-WH1	White Horse pluton	160	K-Ar Bio. Hbl. Mix	Miller and Hoisch (1995)
NBR19-NM1	Newfoundland stock	153	K-Ar Biotite	Miller et al. (1990)
NPQM…	Notch Peak pluton	169	U-Pb Zircon	Lee et al. (1984)

Table 3.5: Apatite and zircon (U-Th)/He ages, apatite fission-track ages, and apatite fission-track track length distributions.

Sample	Intrusion Name	(U-Th)/He Apatite Mean±SE (Ma)	Fission-Track Apatite Mean±1σ (Ma)	(U-Th)/He Zircon Mean±SE (Ma)	AFT Track Length Distributions Mean±SE (μm)	SD (μm)	Number (n)	Data source
GP102605-3	Granite Peak pluton	7.97±0.12	9.76±0.77	9.27±0.21	13.77±0.16	1.11	50	This study
NBR18-C1	Contact pluton	70.47±0.95	95.7±4.2	123.41±6.85	13.55±0.11	1.12	100	This study
NBR18-CP1	Coffepot (Bruneau River) stock	38.42±0.76	64.16±3.37	80.11±3.47	13.4±0.22	1.33	39	This study
NBR18-DB1	Delcer Buttes pluton	41.29±0.78	127.95±7.02	158.79±3.01	13.09±0.12	1.21	100	This study
NBR18-DV1	Melrose stock	6.38±0.62	-	22.09±1.83	-	-	-	This study
NBR18-GH1	Gold Hill pluton	14.11±1.9	14.88±1.05	19.21±1.9	13.78±0.20	1.16	34	This study
NBR18-PR1	McGinty/Patterson Pass pluton	11.96±0.36	17.73±3.26	11.92±0.85	14.77±0.87	1.23	3	This study
NBR18-SI1	Crater Island pluton	22.07±0.95	66.93±4.03	119.0±3.12	12.07±0.22	1.97	84	This study
NBR18-T1	Silver Zone Pass pluton	14.64±1.08	22.38±2.04	17.9±1.23	13.94±0.35	1.36	16	This study
NBR18-WH1	White Horse intrusion	26.07±0.82	35.61±2.63	106.17±3.41	12.70±0.31	1.5	24	This study
NBR19-NM1	Newfoundland stock	59.15±2.48	82.99±4.76	139.02±5.88	13.25±0.14	1.24	84	This study
NPQM1612	Notch Peak pluton	16.3±1.4	-	-	-	-	-	This study
NPQM1800	Notch Peak pluton	35.1±3.1	-	90.5±2.9	-	-	-	This study
NPQM2000	Notch Peak pluton	39.5±2.8	-	-	-	-	-	This study
NPQM2200	Notch Peak pluton	64.9±9.4	-	-	-	-	-	This study
NPQM2600	Notch Peak pluton	92.0±2.7	-	-	-	-	-	This study
NPQM2800	Notch Peak pluton	85.3±3.0	-	120.0±5.0	-	-	-	This study
95BR009	Notch Peak pluton	-	112.8±10.5	-	13.13±0.12	1.3	100	Stockli (1999)
95BR011	Notch Peak pluton	-	46.4±4.1	-	12.89±0.18	1.2	100	Stockli (1999)
95BR014	Notch Peak pluton	-	32.4±2.9	-	12.31±0.18	1.8	150	Stockli (1999)

3.3 Methods

Thermochronologic analysis applied across a landscape can inform both spatial and temporal patterns of strain, thus providing a powerful investigative approach to explore the complex behavior of strain within deforming continents, and potentially provide a rich view of the character of deformation in time and space. Thermochronology requires rocks containing sufficient target accessory minerals for low-temperature techniques (i.e. apatites and zircons). Traditionally, these rocks are sampled across a range of paleodepths, thus allowing for a long cooling history to be elucidated using a single thermochronometric system applied to multiple samples with a known spatial (paleodepth) relationship.

The abundance of felsic intrusive rocks increases westward across the northern Basin and Range towards the Sierra Nevada arc, resulting in widespread exposure of apatite- and zircon-bearing rocks in the western Basin and Range. However, ranges in the central and eastern parts of the northern Basin and Range are dominated by shales and limestones of the Paleozoic Miogeocline, which contain too few apatite and zircon crystals of appropriate size to enable low-temperature thermochronologic analysis. To resolve the lack of large plutonic bodies to sample standard paleodepth profiles across, we applied an approach using multiple thermochronometers to individual samples from small plutons within the central and eastern Basin and Range.

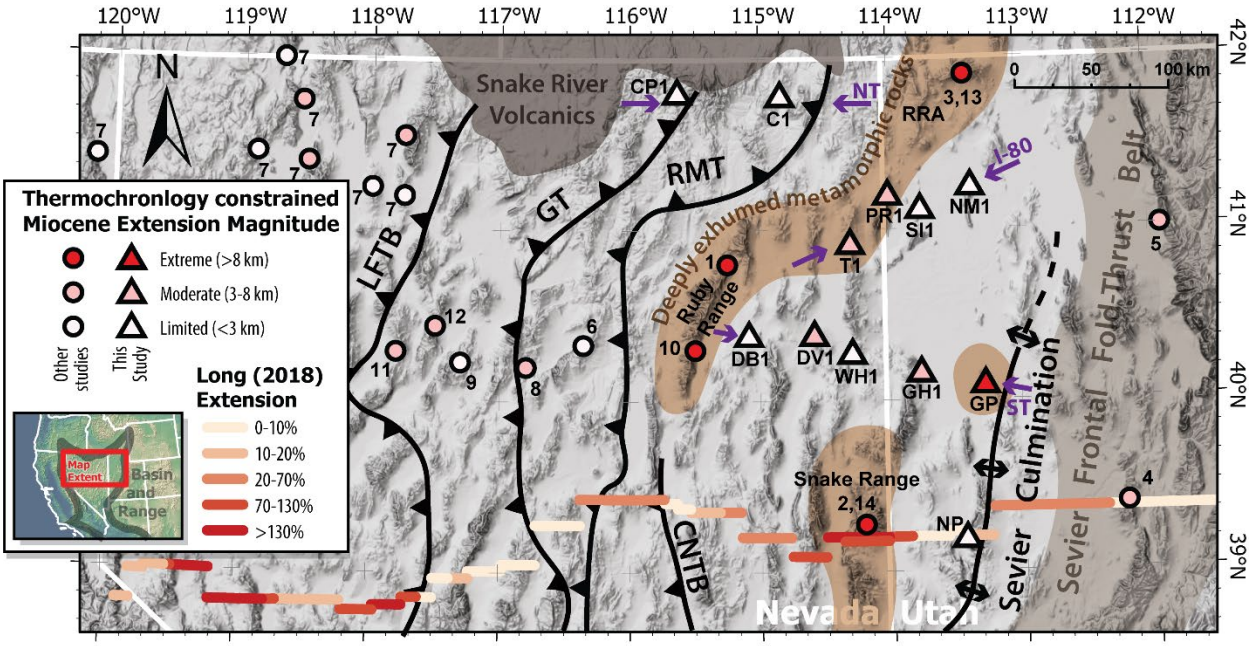


Figure 3.2: Detailed map of thermochronology in the northern Basin and Range. *Map of sample locations and compiled studies of extension in the Basin and Range. Transects described in the results section are indicated in purple, with NT=Northern Transect, I-80=Interstate-80 Corridor, and ST=Southern Transect. Sources for other studies: 1-Dokka et al. (1986), 2-Miller et al. (1999), 3-Wells et al. (2000), 4-Stockli et al. (2001), 5-Armstrong et al. (2004), 6-Colgan and Metcalf (2006), 7-Colgan et al. (2006), 8-Colgan et al. (2008), 9-Colgan and Henry (2009), 10-Colgan et al. (2010), 11-Fosdick and Colgan (2008), 12-Gonsior and Dilles (2008), 13-Konstantinou et al. (2012), 14-Lee et al. (2017). Abbreviations: LFTB=Luning-Fencemaker Thrust Belt, GT=Goconda Thrust, RMT=Roberts Mountain Thrust, CNTB=Central Nevada Thrust Belt, RRA=Raft River-Albion Mountains.*

3.3.1 Sampling approach

Across the northern Basin and Range, there exist a number of small Jurassic stocks, plugs, and plutons known as the Nevada Jurassic Magmatic Province (Elison et al., 1995), whose linear east-west trend may represent magmatism above a tear in the Farallon slab, or back-arc extensional plutonism driven by asthenospheric flow (Miller and Allmendinger, 1991; Elison et al., 1995). These stocks are generally too small for effective spacing of thermochronology samples into elevation, stratigraphic, or paleo-depth transects that would allow the extraction of a full cooling history using a single thermochronometer. To overcome the small size of the exposed granitoids, we apply apatite and zircon (U-Th)/He and apatite fission-track thermochronology to individual samples from 11 intrusions across the northeastern Basin and Range (Fig. 3.2; Tables 3.1 and 3.5). We inverse model robust thermal histories from a single sample at each site by

integrating these cooling ages with additional constraints, including conservative estimates of emplacement-depth (Table 3.2), emplacement timing (Table 3.4), published Ar thermochronology (Table 3.3), estimates of the timing of exhumation to the surface based on deposition of unconformably overlying strata, and apatite fission-track length distributions (Fig. 3.3; Table 3.5).

Whole-rock samples were collected from surface outcrops of plutons selected from 1:250,000 and 1:500,000 scale geologic maps (Hintze, 1980; Coats, 1987; Crafford, 2010). Most plutons in the region are either Mesozoic or Eocene (Moore and McKee, 1983). We prioritized the sampling and analysis of Mesozoic plutons since they have the greatest potential to record thermal histories spanning the entire extensional history of the region.

In addition to individual samples from small plutons, a six-sample vertical transect spanning 1.2 km of elevation was collected from the Jurassic Notch Peak pluton in the House Range (NP on Fig. 3.2; Table 3.1). The high relief and large size of the Notch Peak pluton enabled this more standard sampling approach, although we still incorporated multiple thermochronometers into our analysis. All six of the Notch Peak samples were analyzed for their apatite (U-Th)/He age, and two of these samples were also analyzed for their zircon (U-Th)/He age. Three previously analyzed apatite fission-track ages from the Notch Peak pluton were also incorporated into the inverse thermal modeling (Table 3.5; Stockli, 1999).

3.3.2 Thermochronologic analyses

We applied three thermochronometers to our samples to capture a range of closure temperatures. The apatite (U-Th)/He thermochronometer records the time since a sample cooled below 40-70 °C, temperatures found at 1-3 km depths, assuming typical continental geothermal gradients (Farley, 2002). The higher temperature zircon (U-Th)/He thermochronometer tracks the time since a sample cooled below 180-200 °C, temperatures which translate to 5-8 km depths, assuming typical continental geothermal gradients (Reiners et al., 2002). Apatite fission-track analysis records the time since samples cooled through 90-120 °C, slotting in between apatite and zircon (U-Th)/He closure temperatures (Gallagher et al., 1998; Donelick et al., 2005). Additionally, fission-track analysis provides track-length distributions which reflect the residence time of a

sample within the partial annealing zone (90-120 °C; Gallagher et al., 1998; Donelick et al., 2005).

Samples were crushed, pulverized, and sieved before undergoing standard magnetic and heavy liquid mineral separation procedures. Individual apatite and zircon grains were hand-picked and checked for inclusions before undergoing (U-Th)/He analysis at the University of Michigan following the analytical methods of Niemi and Clark (2018). Measurements of U, Sm, and Th concentrations were performed at the University of Arizona following the methods of Reiners and Nicolescu (2006). Reported (U-Th)/He ages are averages of 2-6 individual grains from each sample after screening for outliers using the Dean and Dixon Q-test for a single outlier and the Grubbs test for two outliers (Tables 3.5 and B.1; Dean and Dixon, 1951; Grubbs, 1969; Boddy and Smith, 2010).

A portion of concentrated mineral separate from all samples, except for those collected from the Notch Peak pluton, were sent to the University of Arizona Fission-track Laboratory for apatite fission-track analysis following the methods of Thomson (2002). Grains were etched with 5 M etchant, with the IRMM 540R dosimeter glass used to monitor neutron fluence during irradiation at the Oregon State TRIGA Reactor. Counting was performed by Nikolas Midttun (Zeta=258.1±10) and Stuart Thomson (Zeta=351.9±3.8) (Table B.1). Confined-track lengths and the compositional parameter *dpar* (Donelick et al., 2005) were collected for all samples, except for sample NBR18-DV1, which contained insufficient apatite for fission-track analysis (Table B.2, Fig. 3.3).

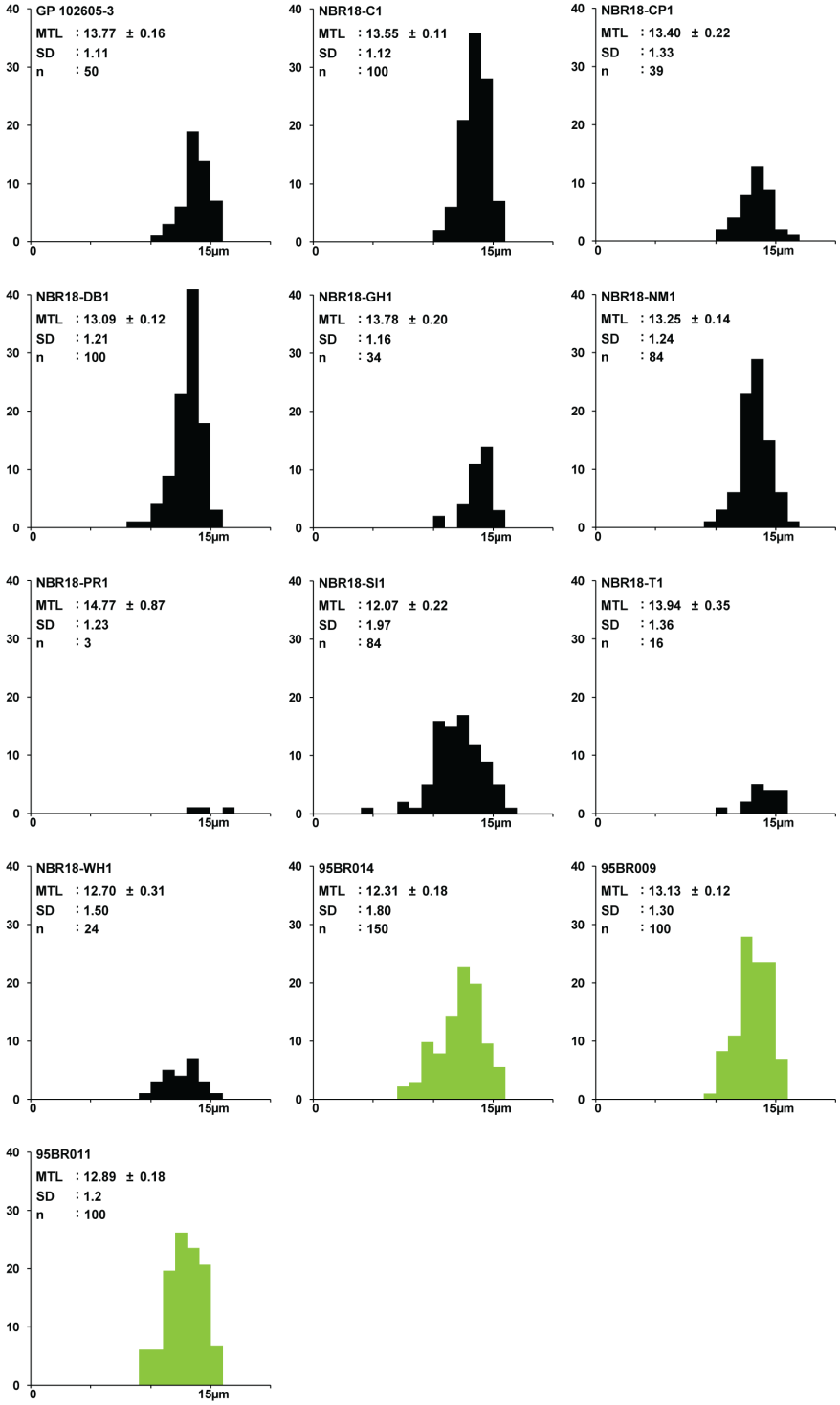


Figure 3.3: Histograms of apatite fission-track length distributions.
Histograms showing the distribution of confined track lengths in apatites. Only confined spontaneous fission-tracks subparallel to the polished surface of the grain were measured. Black histograms are samples analyzed in this study, while green histograms are distributions for three samples from Stockli (1999) (Table 3.5).

3.3.3 QTQt Thermal modeling: Criteria for selecting modeling inputs and additional constraints on allowable time-temperature paths

Because thermochronology cooling ages alone do not define unique time-temperature histories, we employed the Bayesian inverse modelling program QTQt to identify the range of time-temperature paths that could produce the cooling ages we observed in our samples (Gallagher, 2012). QTQt is a flexible program that accepts multiple types of model constraints. For each sample, we included as many of the following constraints as available: (1) timing of pluton emplacement (T=600-700°C) constrained by the oldest published zircon U-Pb, biotite K-Ar, or biotite $^{40}Ar/^{39}Ar$ age; (2) argon thermochronology in the form of biotite K-Ar or biotite $^{40}Ar/^{39}Ar$ ages; (3) published emplacement-depth estimates from barometry and structural observations; (4) low-temperature thermochronology cooling ages (i.e. apatite and zircon (U-Th)/He, and apatite fission-track ages); (5) apatite fission-track length distributions; and (6) minimum age of pluton surface exposure inferred from the age of sedimentary or volcanic rocks deposited unconformably above the pluton. We describe each of these constraint types below, and summarize constraint information for each sample in the results section and Tables 1-5.

1. **Pluton emplacement.** The timing of pluton emplacement was determined from the oldest published U-Pb zircon age for the pluton, or if none were available, the oldest argon age. Within the model, the emplacement constraint box spans 600 to 700 °C and a conservative 10 Myr window around the geochronologic emplacement age (a significantly longer window than the analytical uncertainty on the emplacement geochronology). The emplacement timing constraint was included as a hard constraint in the data file for each sample (i.e. a time-temperature path *must* pass through the constraint box).
2. **Argon thermochronology.** We included previously published biotite-argon ages (either K-Ar or $^{40}Ar/^{39}Ar$) as high-temperature cooling constraints (Table 3.3). Previously published biotite-argon ages effectively constrained the range of acceptable time-temperature paths at temperatures above ~300 °C (the closure temperature of argon in biotite; Harrison et al., 1985). For example, the relatively old ~148 Ma argon age for the Silver Zone Pass pluton limits its time-temperature

paths to below the biotite-argon closure temperature (~300 ºC) from ~148 Ma to the present, limiting the maximum amount of cooling possible during that time to less than 300 ºC. For modeling, argon thermochronologic ages were converted into a K/Ar parent-to-daughter ratio using the decay constant of Renne et al., (2010, 2011), and entered as a K-Ar/Ar-type age in the QTQt data file.

3. **Emplacement depth.** Some models include a constraint representing the estimated emplacement-depth based on published paleo-barometric or structural observations of the pluton. Published emplacement-depth estimates are typically given as range of pressures or depths, depending on the source data (Table 3.2). Sources include Miller and Hoisch (1995), who compiled estimates of emplacement-depths for the Contact pluton, McGinty pluton, Crater Island pluton, Silver Zone Pass pluton, White Horse pluton, and Newfoundland stock based on aluminum-in-hornblende geobarometry and estimated stratigraphic and structural overburden. Additionally, Granath et al. (1983) and Colgan and Henry (2009) estimated emplacement-depths from stratigraphic overburdens for the Notch Peak pluton and Delcer Buttes, respectively. Rahl et al. (2002) used metamorphic barometry of the contact aureole to estimate the emplacement-depth of the Coffeepot pluton, and El-Shazly et al. (2011) used the mineralogy of the Melrose stock to estimate its emplacement-depth. We converted the emplacement-depth estimates to a range of temperatures assuming a 3.74 km/kbar lithostatic pressure (Miller and Hoisch, 1995) and 30 ºC/km geothermal gradient (Colgan et al., 2010). A time-temperature constraint box starting at the beginning of the emplacement age constraint window, and continuing for 30 Myr, with the estimated depths converted to a temperature range, was included in the thermal history file as a soft constraint (i.e. a time-temperature path *is preferred* if it passes through the constraint box). This constraint reflects the general observation that the plutons were emplaced at ambient crustal temperatures well below the closure temperatures of the geochronometers that record pluton emplacement.
4. **Low-temperature thermochronology.** All low-temperature thermochronometers analyzed in each sample (i.e. zircon (U-Th)/He, apatite (U-Th)/He, and apatite fission-track) were included in each QTQt data input file. Sample NBR18-DV1 lacked

sufficient apatite for fission-track analysis, and therefore only included apatite and zircon (U-Th)/He cooling ages.

5. **Fission-track length distributions.** Samples that underwent apatite fission-track analysis had the lengths of any confined spontaneous fission-tracks measured in order to populate fission-track length distributions for each sample (Tables 3.5 and B.1; Fig 3.3). Track length distributions were included in the QTQt data input files when available (Table 3.5). For three samples from the House Range, binned fission-track distributions were extracted from histograms (Stockli, 1999) and included in the QTQt data files.
6. **Subcrop surface constraints.** The age of sedimentary or volcanic rocks deposited immediately above an unconformity gives a minimum age for erosional exposure of that unconformity surface and therefore provides a minimum age for when that unconformity was exposed. For the plutons that we sampled, we included these subcrop constraints to determine when the pluton must have already been exhumed to the surface. Based on published geologic maps, we determined if the plutons we sampled were bounded by nonconformities overlain by Cenozoic sedimentary or volcanic strata, and if so, the age of the overlying unit. The surface constraint is implemented in the model as a time-temperature constraint with a temperature range of 0-40 ºC, and the same time length as the Epoch during which the overlying strata were deposited. Only five samples had a useful surface constraint (each is noted in the results section below). The subcrop constraint was included in the thermal history file as a soft constraint (i.e. a time-temperature path *is preferred* if it passes through the constraint box).

3.4 Results

Cooling ages from our samples ranged from middle Miocene to Cretaceous. Except for NBR18-PR1 and NBR18-T1, all samples produced cooling ages in expected order based on the closure temperatures of each thermochronometer, and elevation-order in the case of the vertical transect from Notch Peak (Table 3.5). In the case of NBR18-PR1 and NBR18-T1, the apatite fission-track ages were slightly older than their corresponding zircon (U-Th)/He ages (Table 3.5). In both cases, the ages overlap within 2σ, and no ages were eliminated from thermal modeling. The results are described in three groups

according to their location within three east-west trending transects (Fig. 3.2): northern Nevada, the I-80 corridor, and a southern transect (including the House Range). For range names and locations, refer to Fig. 3.4 and Table 3.1.

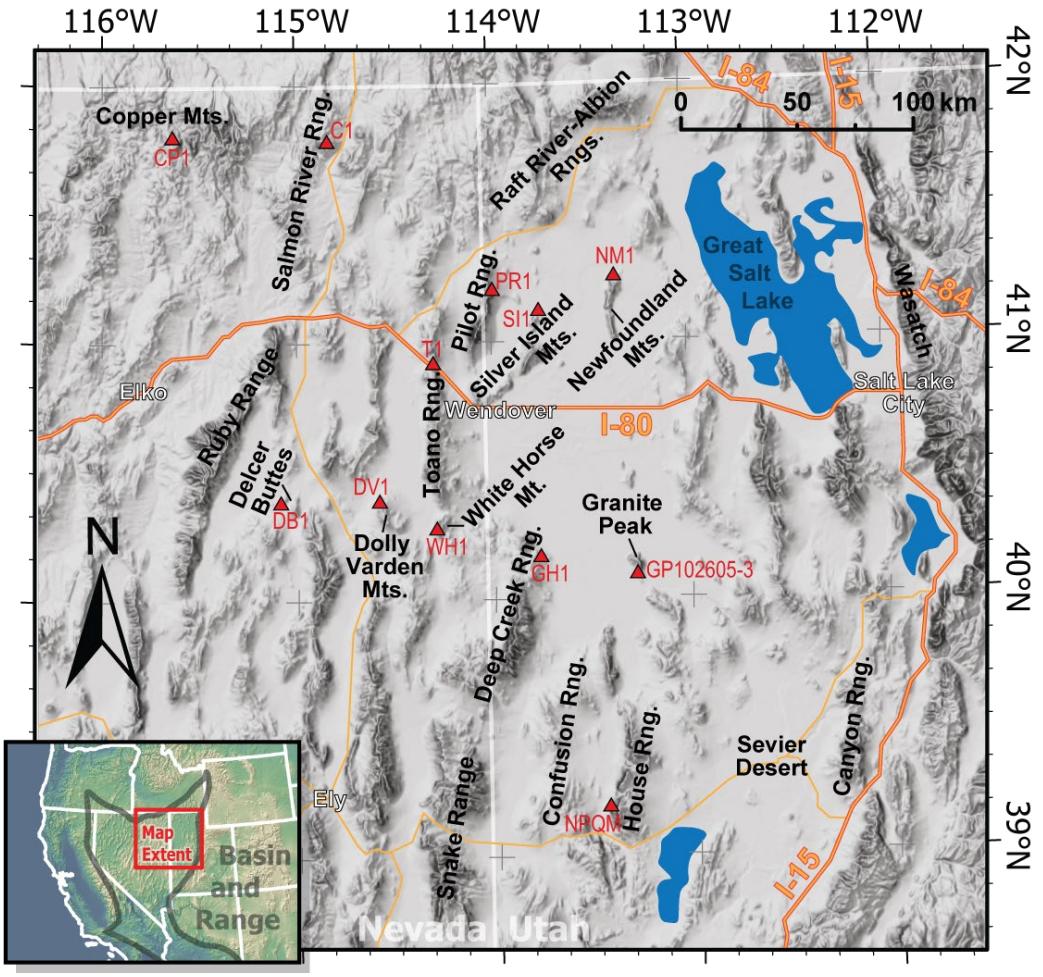


Figure 3.4: Selected geographic names in the northern Basin and Range.
The names of selected ranges mentioned in the text, along with major interstates and highways. Red triangles show the locations of samples collected in this study, with abbreviated sample IDs in red (see Table 3.1).

3.4.1 Northern Nevada

Copper Mountains (Coffeepot/Bruneau River stock, sample CP1)

We sampled NBR18-CP1, a medium-grained granodiorite, from the late Cretaceous (108-111 Ma) Coffeepot stock (Table 3.4; McGrew et al., 2000; Rahl et al., 2002; Canada et al., 2019). The sample was collected near Tennessee Mountain, close to

the margin of the pluton, and west of the approximately north-south striking Bruneau Valley Fault which divides the main body of the Coffeepot stock in two. The sample is located close to sample 980730-7 of Rahl et al. (2002) and Canada et al. (2019). Sample NBR18-CP1 produced well-behaved cooling ages, with an apatite (U-Th)/He age of 38.42±0.76 Ma, an apatite fission-track age of 64.16±3.37 Ma, and a zircon (U-Th)/He age of 80.11±3.47 Ma. These ages are in good agreement with the (U-Th)/He analyses of sample 980730-7 from Canada et al. (2019), which were 32.6±2.0 Ma on apatite and 81.3±3.8 Ma on zircon.

In addition to the three cooling ages described above, the thermal model for NBR18-CP1 included a middle Miocene surface constraint (9-19 Ma; Coats, 1964; 1987), 8-14 km emplacement-depth constraint (Rahl et al., 2002), and a previously published ~103 Ma $^{40}Ar/^{39}Ar$ cooling age for the nearby sample 980730-7 of Rahl et al. (2002). The resulting acceptable time-temperature paths show well-constrained gradual cooling from 85-60 Ma, with the sample remaining below 75°C since 50 Ma, limiting the amount of possible Cenozoic cooling. All four observed cooling ages are well predicted by the expected time-temperature path (Fig. 3.5).

Salmon River Range (Contact pluton, sample C1)

We sampled NBR18-C1, a medium-grained granodiorite, from the late Jurassic (~160 Ma) Contact pluton (Table 3.4; Coats et al., 1965; Zens, 2019). The sample was collected near the western margin of the pluton below Ellen D Mountain. Sample NBR18-C1 produced well behaved cooling ages, with an apatite (U-Th)/He age of 70.47±0.95 Ma, an apatite fission-track age of 95.7±4.2 Ma, and a zircon (U-Th)/He age of 123.41±6.85 Ma.

In addition to the three cooling ages described above, the thermal model for NBR18-C1 included a middle Miocene surface constraint (9-19 Ma, Armstrong et al., 1975; Coats, 1987), 6-13 km emplacement-depth constraint (Miller and Hoisch, 1995), and a previously published ~152 Ma biotite K/Ar cooling age (Coats et al., 1965). The resulting acceptable time-temperature paths show well constrained gradual cooling from 130-80 Ma, and the sample remaining below 50°C since 80 Ma. All four observed cooling ages are well predicted by the expected time-temperature path (Fig. 3.5).

3.4.2 I-80 Corridor

Toano Range (Silver Zone Pass pluton, sample T1)

We sampled NBR18-T1, a coarse-grained granodiorite, from the late Jurassic (~162 Ma) Silver Zone Pass pluton (Table 3.4; Miller et al., 1990). The sample was collected near the center of the pluton north of Interstate-80. Sample NBR18-T1 produced tightly clustered low-temperature cooling ages, with an apatite (U-Th)/He age of 14.64±1.08 Ma, an apatite fission-track age of 22.38±2.04 Ma, and a zircon (U-Th)/He age of 17.9±1.23 Ma. Note that the apatite fission-track and zircon (U-Th)/He ages are inverted from their expected order based on their closure temperatures. The fission-track age is approximately 2σ older than the zircon age, potentially a result of low U concentration (<20 ppm, Table B.2) and a young fission-track age resulting in a low spontaneous track density, and therefore greater uncertainty on the fission-track age.

In addition to the three cooling ages described above, the thermal model for NBR18-T1 included a Miocene surface constraint (4-24 Ma; Coats, 1987), 12-18 km emplacement-depth constraint (Miller and Hoisch, 1995), and a previously published ~148 Ma biotite K/Ar cooling age (Coats et al., 1965). The resulting acceptable time-temperature paths indicate the sample remained below 250 °C from 140 to 30 Ma, then rapidly cooled from at least 200 °C to near-surface temperatures between 30 and 15 Ma. All four observed cooling ages are reasonably well predicted by the expected time-temperature path, despite the slight inversion between the apatite fission-track and zircon (U-Th)/He cooling ages (Fig. 3.5).

Pilot Range (Patterson Pass/McGinty pluton, sample PR1)

We sampled NBR18-PR1, a medium-grained granodiorite, from the Eocene (>37 Ma) Patterson Pass/McGinty pluton (Table 3.4; Miller et al., 1987). The sample was collected near the southern end of the pluton along Patterson Pass Road. Sample NBR18-PR1 produced Miocene low-temperature cooling ages, with an apatite (U-Th)/He age of 11.96±0.36 Ma, an apatite fission-track age of 17.73±3.26 Ma, and a zircon (U-Th)/He age of 11.92±0.85 Ma. While these cooling ages are not in expected order, they still collectively describe a rapid middle Miocene cooling event. Similar to the Toano Range sample, the fission-track age is approximately 2σ older than the zircon age, again a possible result of

low U concentration (<20 ppm, Table B.2) and a young fission-track age, resulting in a low spontaneous track density, and therefore greater uncertainty on the fission-track age.

In addition to the three cooling ages described above, the thermal model for NBR18-PR1 included a previously published ~37 Ma biotite K/Ar cooling age (Miller et al., 1987). The resulting acceptable time-temperature paths show rapid cooling from at least 200 °C to near-surface temperatures at ~15 Ma. The apatite fission-track age is consistently underestimated, as the model appears to prefer fitting the younger and lower-uncertainty (U-Th)/He ages (Fig. 3.5).

Silver Island Mountains (Crater Island pluton, sample SI1)

We sampled NBR18-SI1, a coarse-grained granodiorite, from the late Jurassic (~159 Ma) Crater Island pluton (Table 3.4; Moore and McKee, 1983). The sample was collected from the northern end of Crater Island, the northernmost part of the Silver Island Mountains. Sample NBR18-SI1 produced well behaved low-temperature cooling ages, with an apatite (U-Th)/He age of 22.07±0.95 Ma, an apatite fission-track age of 66.93±4.03 Ma, and a zircon (U-Th)/He age of 119.0±3.12 Ma.

In addition to the three cooling ages described above, the thermal model for NBR18-SI1 included a 4-9 km emplacement-depth constraint (Miller and Hoisch, 1995). The resulting acceptable time-temperature paths show well-constrained slow monotonic cooling from 110 to 25 Ma down to 75 °C, then a slight acceleration of cooling rate from 25 Ma to the present. All three observed cooling ages are well predicted by the expected time-temperature path (Fig. 3.5).

Newfoundland Mountains (Newfoundland stock, sample NM1)

We sampled NBR19-NM1, a coarse-grained granite, from the late Jurassic (~153 Ma) Newfoundland stock (Table 3.4; Miller et al., 1990). The sample was collected from the western end of the stock, which lies in the northernmost part of the Newfoundland Mountains. Sample NBR19-NM1 produced well behaved low-temperature cooling ages, with an apatite (U-Th)/He age of 59.15±2.48 Ma, an apatite fission-track age of 82.99±4.76 Ma, and a zircon (U-Th)/He age of 139.02±5.88 Ma.

In addition to the three cooling ages described above, the thermal model for NBR19-NM1 included a 7-12 km emplacement-depth constraint (Miller and Hoisch, 1995). The resulting acceptable time-temperature paths show cooling from 130 Ma to 70

Ma to below 50 °C, where the sample remains to the present. The three observed cooling ages are reasonably well predicted by the expected time-temperature path, although both the apatite fission-track and apatite (U-Th)/He ages are slightly overpredicted (Fig. 3.5).

3.4.3 Southern Transect and House Range

Northern Deep Creek Range (Gold Hill pluton, sample abbreviation GH1)

We sampled NBR18-GH1, a medium-grained granodiorite, from the late Jurassic (~152 Ma) Gold Hill pluton (Table 3.4; Moore and McKee, 1983). The sample was collected near the center of the pluton north of Interstate-80. Sample NBR18-T1 produced tightly clustered low-temperature cooling ages, with an apatite (U-Th)/He age of 14.11±1.9 Ma, an apatite fission-track age of 14.88±1.05 Ma, and a zircon (U-Th)/He age of 19.21±1.9 Ma.

In addition to the three cooling ages described above, the thermal model for NBR18-GH1 included a previously published ~152 Ma K/Ar biotite cooling age (Moore and McKee, 1983). The resulting acceptable time-temperature paths indicate that the sample remained below 250 °C from 140 to 25 Ma, then rapidly cooled from at least 200 °C to near-surface temperatures between 25 and 10 Ma. All four observed cooling ages are well predicted by the expected time-temperature path (Fig. 3.5).

Granite Peak (Granite Peak pluton, sample abbreviation GP)

Access to Granite Peak (Fig. 3.4) is limited due to its location within the U.S. Army Dugway Proving Ground. Eric Christiansen provided us apatite and zircon mineral separates from sample GP102605-3, a granodiorite previously collected within the proving ground from the late Jurassic (149.8±1.3 Ma) Granite Peak pluton (Table 3.4; Christiansen and Vervoort, 2009). Sample GP102605-3 produced tightly clustered Miocene low-temperature cooling ages, with an apatite (U-Th)/He age of 7.97±0.12 Ma, an apatite fission-track age of 9.76±0.77 Ma, and a zircon (U-Th)/He age of 9.27±0.21 Ma.

In addition to the three cooling ages described above, the thermal model for GP102605-3 included a previously published 16±0.036 Ma $^{40}Ar/^{39}Ar$ biotite cooling age (Utah Geological Survey and New Mexico Geochronology Research Laboratory, 2009).

The resulting acceptable time-temperature paths are unconstrained prior to 16 Ma, but exhibit well constrained rapid cooling from at least 250 ºC to near-surface temperatures between 16 and 7 Ma. All four observed cooling ages are well predicted by the expected time-temperature path (Fig. 3.5).

Delcer Buttes (sample abbreviation DB1)

We sampled NBR18-DB1, a fine-grained porphyritic granitoid, from the late Jurassic (~159 Ma) pluton located in Delcer Buttes, Nevada (Table 3.4; Miller et al., 1990). Sample NBR18-DB1 produced poor-quality low-temperature cooling ages, with an apatite (U-Th)/He age of 41.29±0.78 Ma, an apatite fission-track age of 127.95±7.02 Ma, and a zircon (U-Th)/He age of 158.79±3.01 Ma.

Resulting acceptable time-temperature paths for Delcer Buttes support previous interpretations of the pluton as being hypabyssal, showing rapid cooling to less than 100 ºC at ~150 Ma, shortly after emplacement, and no indication of later reheating. The apatite fission-track and zircon (U-Th)/He cooling ages are reasonably well predicted by the expected time-temperature path, but the model does significantly overpredict the apatite (U-Th)/He age (Fig. 3.5).

Dolly Varden Mountains (Melrose stock, sample abbreviation DV1)

Sample NBR18-DV1 is an Eocene (39-43 Ma; Brooks et al., 1995) andesitic porphyritic ignimbrite collected just above its contact with the Jurassic Melrose stock (Table 3.4). The sample was collected on the northwest end of the Dolly Varden mountains in Nevada. Sample NBR18-DV1 produced well behaved low-temperature cooling ages, with an apatite (U-Th)/He age of 6.38±0.62 Ma and a zircon (U-Th)/He age of 22.09±1.83 Ma.

The proximity of sample NBR18-DV1 to the Jurassic Melrose stock allows us to model the thermal history of the combined granite-ignimbrite rock package, and therefore include thermal history constraints from the Melrose stock in the thermal model. In addition to the two cooling ages described above, the thermal model for NBR18-DV1 included an Eocene surface constraint (35-55 Ma, Brooks et al., 1995), emplacement of the Melrose stock at 165 Ma (Zamudio, 1992), and a previously published ~125 Ma K/Ar cooling age for the Melrose stock (Armstrong and Hansen, 1966). The resulting acceptable time-temperature paths are relatively unconstrained prior to the Eocene

emplacement of the ignimbrite, after which the model indicates rapid reheating of the sample to at least 175 ºC between 40 and 25 Ma, then cooling back to surface temperatures from ~25 Ma to the present. All three observed cooling ages are well predicted by the expected time-temperature path (Fig. 3.5).

House Range (Notch Peak pluton, sample abbreviation NPQM)

We collected six samples arranged in a 1.2 km elevation-transect from the middle Jurassic (~169 Ma) Notch Peak pluton (Table 3.4; Lee et al., 1984). The samples were collected along the steep western flank of the House Range, Utah. The transect produced well behaved low-temperature cooling ages, with six apatite (U-Th)/He ages ranging from 16.3±1.4 Ma at the base, to 85.3±3.0 Ma at the highest sample; and two zircon (U-Th)/He ages of 90.5±2.9 Ma near the base, and 120.0±5.0 Ma at the highest sample (Table 3.5).

In addition to the eight cooling ages described above, the thermal model for NBR18-GH1 included three previously published apatite fission-track ages of 32.4±2.9 Ma, 46.4±4.1 Ma, and 112.8±10.5 Ma (Stockli, 1999), previously published 165±1.9 Ma $^{40}Ar/^{39}Ar$ biotite cooling age (Nabelek et al., 1986), an Eocene surface constraint (33-43 Ma; Gregory-Wodzicki, 1997), and a 4-8 km emplacement-depth constraint (Nabalek et al., 1986). The resulting acceptable time-temperature paths show an overall trend of gradual cooling from 130-40 Ma, and the sample remaining below 50ºC since 40 Ma. The plot of observed versus predicted cooling reveals a systematic pattern of underpredicting low elevation samples and overpredicting high-elevation samples within any single thermochronometer (Fig. 3.5). This may suggest that some degree of fault-block rotation occurred during exhumation, violating our assumption of one-dimensional simple exhumation.

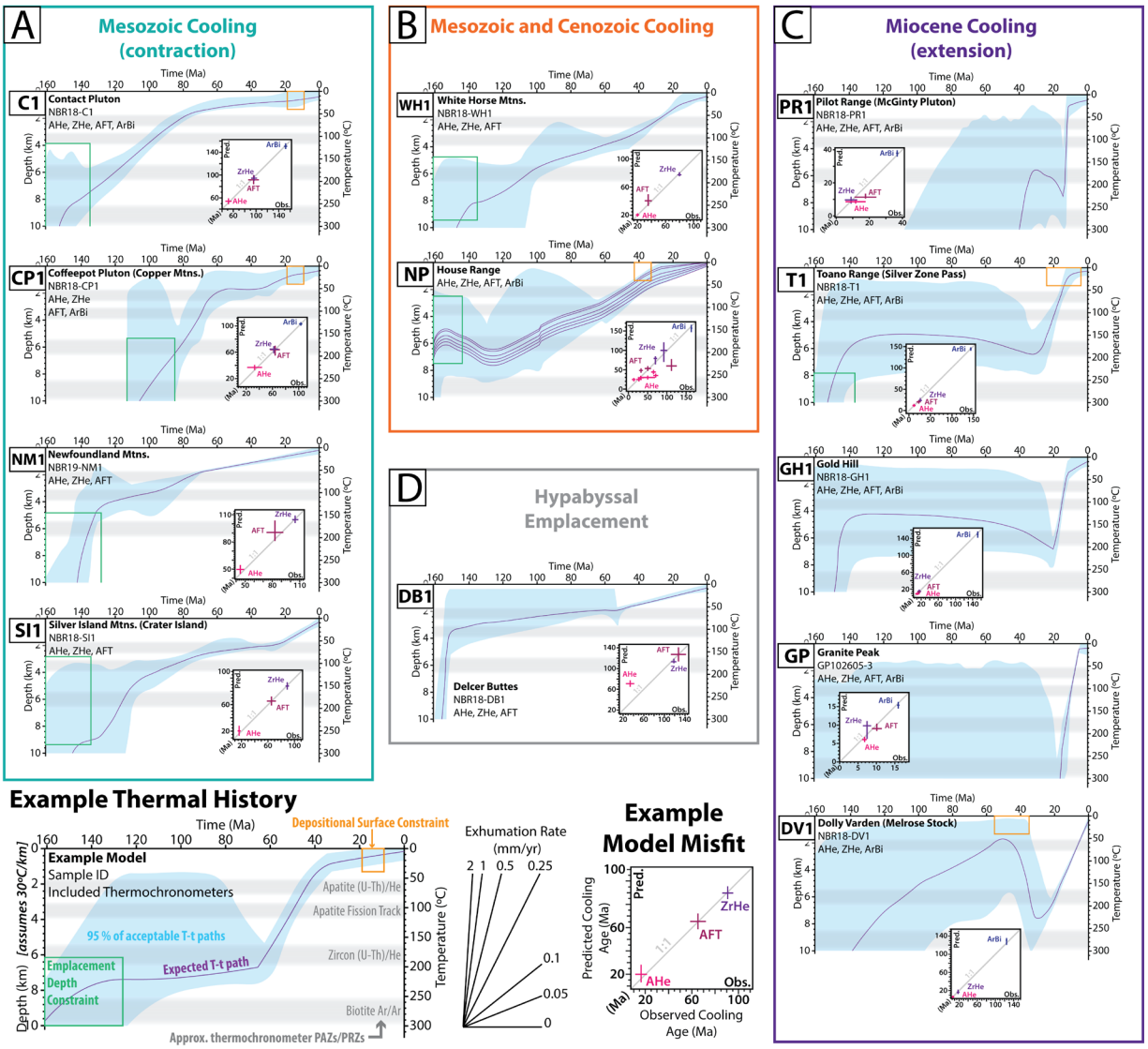


Figure 3.5: Modeled time-temperature histories for the northern Basin and Range. *Modeled time-temperature histories for plutons in the northern Basin and Range (Fig. 3.2). Models are binned into broad descriptive categories based on the timing of their cooling (i.e. Mesozoic cooling, Mesozoic-Cenozoic cooling, Miocene cooling, along with a single hypabyssally emplaced sample; see text for discussion). The depth scale and exhumation rate diagram assume a 30 °C/km geothermal gradient. Square inset plots on each time-temperature diagram show the predicted versus observed cooling ages for each thermal model, with a gray 1:1 line for evaluating the model misfit. The horizontal gray bars show the temperature ranges over which the indicated thermochronometers transition from open to closed, commonly referred to as partial annealing zones (PAZ) and partial retention zones (PRZ)(e.g., Wolf et al., 1998).*

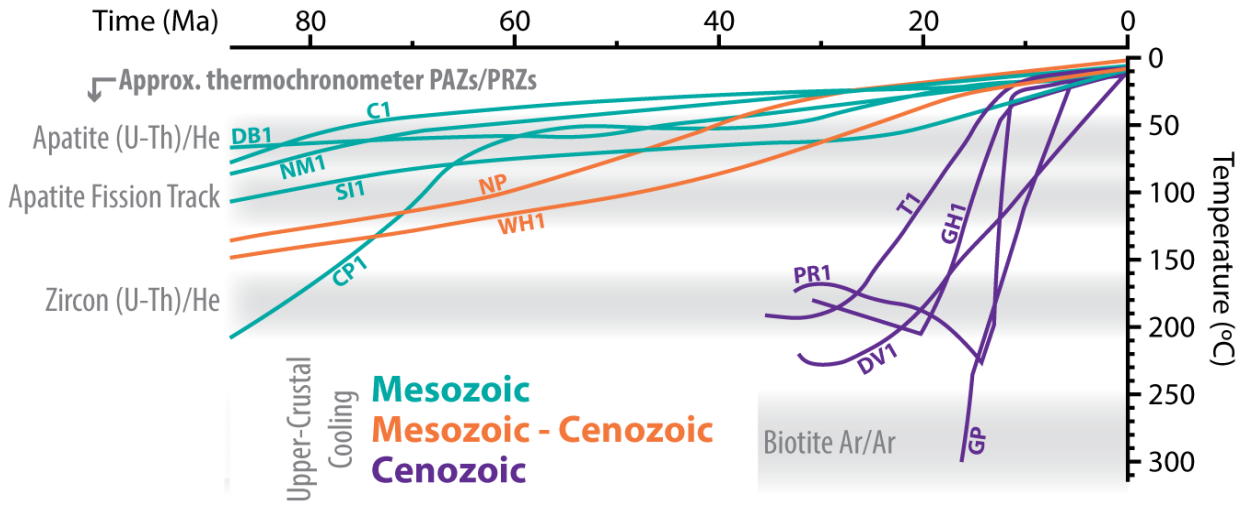


Figure 3.6: Categorized cooling histories in the northern Basin and Range. *Expected cooling paths from Fig. 3.4 overlain onto shared axes and colorized according to the three cooling history categories described in the text. Labels correspond to the sample IDs in Tables 3.1-3.5. The horizontal gray bars show the temperature ranges over which the indicated thermochronometers transition from open to closed, commonly referred to as partial annealing zones (PAZ) and partial retention zones (PRZ)(e.g., Wolf et al., 1998).*

3.4.4 Patterns of thermochronologically constrained cooling histories

The modeled cooling histories of ranges in the northern Basin and Range fall into three categories that differ in both the timing and maximum rate of exhumation (Figs. 3.5 and 3.6). The first group comprises samples from the Contact pluton, Delcer Buttes pluton, Coffeepot stock, Crater Island pluton, and Newfoundland stock (Fig. 3.5). These thermal histories all preserve Paleogene to Mesozoic apatite (U-Th)/He ages, and exclusively Mesozoic apatite fission-track and zircon (U-Th)/He ages (Table 3.5), thus limiting the amount of Cenozoic exhumation to less than ~2-3 km (green paths in Fig. 3.6).

The second group consists of the White Horse intrusion and Notch Peak pluton (Fig. 3.5), both of which show protracted slow cooling histories that start in the Mesozoic, but unlike the first group, continue well into the Cenozoic (orange paths in Fig. 3.6). These samples produce a broad range of cooling ages, including Mesozoic zircon (U-Th)/He ages, Paleogene apatite fission-track ages, and Eocene or Oligocene apatite (U-Th)/He ages (Table 3.5).

The final group contains the remaining samples, including the McGinty pluton, Silver Zone Pass pluton, Gold Hill pluton, Granite Peak pluton, and Melrose pluton (Fig. 3.5), which collectively show a pattern of rapid early- to mid-Miocene exhumation (purple paths in Fig. 3.6). All samples in this group produced Miocene cooling ages for all three thermochronometers (zircon and apatite (U-Th)/He, and apatite fission-track). The depth of Miocene exhumation is relatively consistent within this third group of samples, with most cooling from above zircon (U-Th)/He closure (>6 km of exhumation assuming a 30 °C/km geothermal gradient), and one sample, the Granite Peak pluton, cooling from at least biotite $^{40}Ar/^{39}Ar$ closure temperature (>10 km of exhumation assuming a 30 °C/km geothermal gradient). A more detailed description of the rates and magnitudes of cooling for each of these categories follows. All reported exhumation rates assume a 30 °C/km geothermal gradient.

3.4.5 Mesozoic contractional exhumation

The low-temperature cooling ages from the Contact pluton, Delcer Buttes pluton, Coffeepot stock, Crater Island pluton, and Newfoundland stock pre-date Neogene extension, and therefore potentially reveal a record of Mesozoic contractional exhumation. The clearest examples of Mesozoic cooling are in the Coffeepot stock and Contact plutons (Figs. 3.2 and 3.6), both of which are located in northern Nevada near the southern margin of the Snake River plain (Fig. 3.1). The Contact and Coffeepot plutons have emplacement-depth estimates of at least 6 km and 8 km, respectively (Miller and Hoisch, 1995; Rahl et al., 2002), independently confirming that we can interpret their cooling histories as reflecting tectonic exhumation, as opposed to isobaric cooling after shallow emplacement. The well-constrained cooling paths of both models during the Mesozoic suggest long-term averaged exhumation rates of approximately 0.1-0.2 mm/yr, similar to background erosion rates in orogenic belts (e.g., Rohrmann et al., 2012; Wang et al., 2012).

Other samples from this group also reveal a history of Mesozoic cooling, but at even slower rates than the Coffeepot stock or Contact pluton. The thermal model for the Newfoundland stock (NM1 on Figs. 3.6 and 3.7) implies relatively shallow emplacement at less than 6 km depth, followed by slow exhumation to the surface at less than 0.1 mm/yr. The thermal model for the Crater Island pluton is overall less well constrained in

the Mesozoic, but appears to prefer deeper emplacement, below 8 km, and slow exhumation to the surface in the Mesozoic at a rate of 0.05-0.1 mm/yr. The Delcer Buttes are perhaps the most anomalous of this group, with cooling ages indicating hypabyssal emplacement in the Jurassic, below apatite fission-track closure temperatures, and extremely slow subsequent exhumation.

The samples that retain a Mesozoic cooling history each contain a distinctive inflection point between ~60-80 Ma separating slow (~0.1 mm/yr) exhumation in the Cretaceous from even slower average exhumation rates (~0.03 mm/yr) during the Cenozoic (Fig. 3.7). Thermal histories showing primarily Mesozoic cooling are concentrated in the north of the study area, just south of the Snake River Plain (i.e. the Coffeepot, Contact, Crater Island, and Newfoundland plutons; Fig. 3.2).

3.4.6 Protracted Mesozoic and Cenozoic cooling

The Notch Peak and White Horse plutons experienced extended cooling paths that span the Mesozoic and Cenozoic at slow average exhumation rates of approximately 0.05 mm/yr. Neither the Notch Peak nor White Horse plutons exhibit the distinctive inflection point observed in the other samples that cooled primarily in the Mesozoic. The Notch Peak pluton is a particularly well constrained example of this phenomenon, as it contains a full 1.2 km elevation transect of (U-Th)/He samples ranging in age from 92 to 16 Ma. The inverse thermal model for the Notch Peak pluton supports slow and steady cooling starting in the Mesozoic and continuing well into the Cenozoic (Fig. 3.5). The White Horse pluton has a similar thermal history of protracted cooling from the Cretaceous to the Miocene (Fig. 3.5).

3.4.7 Miocene exhumation

The best constrained, largest magnitude, and most consistently observed exhumation interval amongst our samples occurred in the Miocene from approximately 24 to 10 Ma. Five samples experienced rapid Miocene exhumation, all cooling from at least zircon (U-Th)/He closure temperatures (180-200 °C) to below apatite (U-Th)/He closure (40-70 °C) in less than 10 Myr, implying exhumation rates of between 0.2 and 0.6 mm/yr (Figs. 3.5, 3.6, and 3.7). The Granite Peak pluton cooled from above biotite $^{40}Ar/^{39}Ar$ closure temperatures (Utah Geological Survey and New Mexico Geochronology

Research Laboratory, 2009) to the surface in less than 10 Myr, implying a relatively rapid exhumation rate of ~1 mm/yr. Ranges which show rapid Miocene cooling do not conform to any obvious geographic patterns in relation to Mesozoic contractional structures or the belt of metamorphic core complexes.

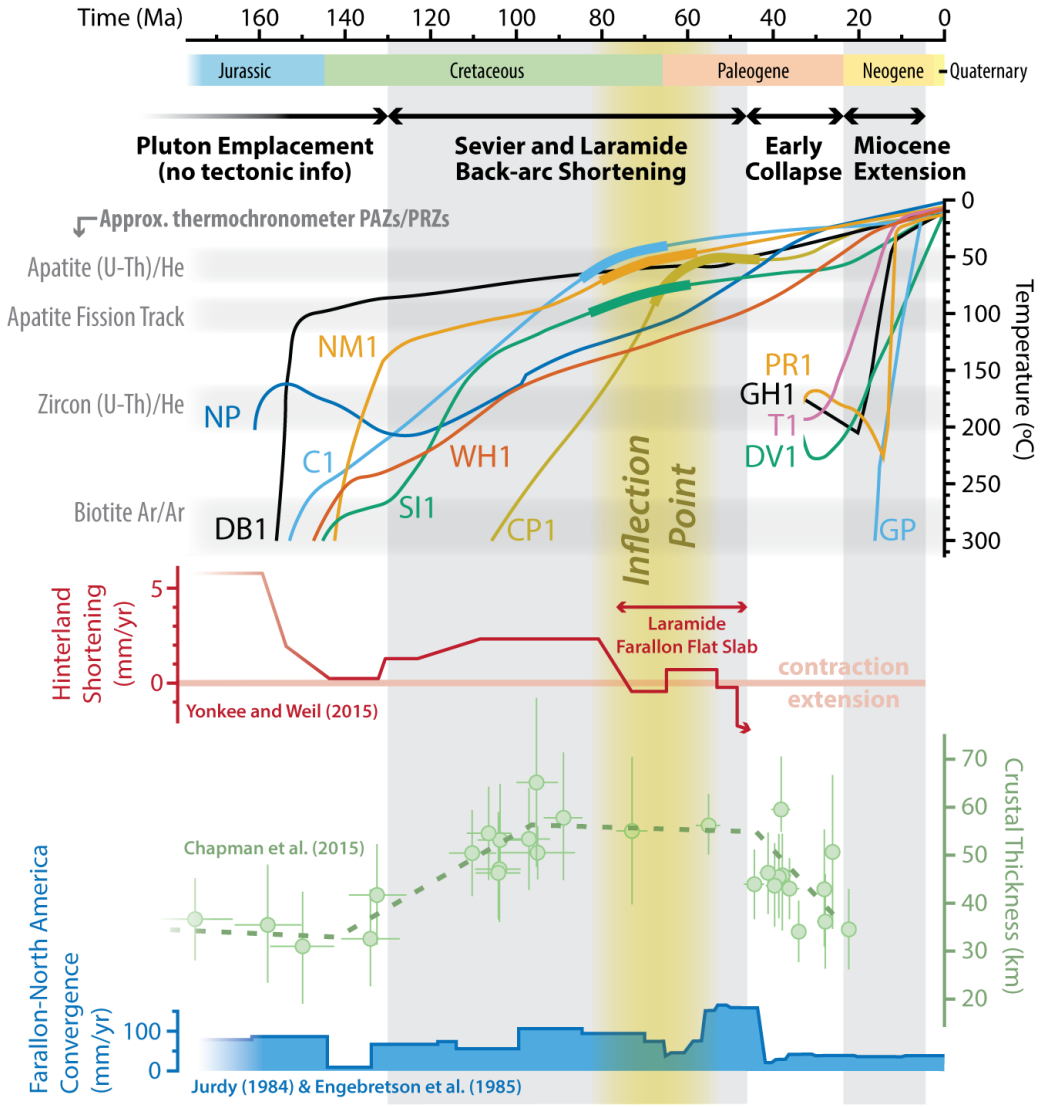


Figure 3.7: Comparison of cooling histories to geologic context data.
Stacked thermal histories from Fig. 3.5 with compiled geologic and tectonic data from the Basin and Range (Jurdy, 1984; Engebretson et al., 1985Yonkee and Weil, 2015; Chapman et al., 2015). Parts of some cooling paths are thickened to accentuate an inflection point at approximately 75-60 Ma.

3.5 Discussion

The thermochronologically constrained thermal histories presented above provide a view into the timing and character of exhumation during the evolution of the Sevier orogen into the Basin and Range province. We sorted our results into three characteristic cooling histories which speak to different stages of this tectonic evolution. Our record of Mesozoic cooling illuminates the nature of rock exhumation within the Cordillera during construction of the Nevadaplano. The distribution and magnitude of Miocene cooling, and lack of evidence for Eocene or Oligocene cooling, constrain the geodynamic evolution of the northern Basin and Range during post-orogenic collapse and rapid Miocene extension.

3.5.1 Pre-extensional and early-extensional tectonic history

Changes in rock exhumation during Sevier orogenesis

Samples that retain a Mesozoic cooling history (Contact pluton, Coffeepot stock, Crater Island pluton, and Newfoundland stock) show an inflection point in their cooling histories at approximately 75-60 Ma (Fig. 3.7), a time of tectonic transition within the hinterland of the Sevier orogen. The inflection comes shortly after the Cordillera attained its maximum crustal thickness, as recorded by Sr/Y in igneous rocks (Fig. 3.7; Chapman et al., 2015). Additionally, the inflection occurs at the same time as the hinterland of the orogen is transitioning from contractional deformation to extensional deformation. The change from hinterland contraction to extension is recorded by the end of sedimentation in the Newark Canyon Formation at ~99 Ma, which was a flexural foreland basin to a contractional hinterland fold-thrust belt (Di Fiori et al., 2020), and the initiation of deposition in the Sheep Pass Formation in the latest Cretaceous, which is an early hinterland extensional basin (Druschke et al., 2009; 2011). Additionally, this time period saw the Farallon Slab flattening against the North American lithosphere, shutting off the Sierran arc and initiating the transition from thin-skinned hinterland deformation of the Sevier orogeny to Laramide style foreland uplifts (Fig. 3.7; Yonkee and Weil, 2015). The observed inflection in exhumation rate at 70-60 Ma may therefore represent the transition from slow exhumation during construction of a thickened back-arc to slower exhumation after hinterland crustal thickness stabilized (Chapman et al., 2015; Fig. 3.7).

In addition to recording a change in tectonics within the back-arc orogenic wedge, the inflection point may also represent a transition from slow background orogenic erosion to effectively no erosion following hydrologic closure of the Nevadaplano (Druschke et al., 2011). Multiple lines of evidence indicate that the Nevadaplano was a low relief and potentially hydrologically closed topographic feature, including analysis of extensive ignimbrite volcanics that blanketed the plateau (Best et al. 2016, Henry et al., 2016), the existence of extensive hinterland lacustrine deposits (Lund Snee et al., 2016; Smith et al., 2017; Chapter 2), and reconstructions of paleo-structural relief (Long, 2012; 2018). Retention of sediments within the hinterland after hydrologic closure of the Nevadaplano around 75-60 Ma could explain the lack of rock exhumation following the inflection point.

Absence of evidence for Eocene-Oligocene extensional cooling

It has been hypothesized that the earliest major phase of extension in the northern Basin and Range occurred in the Eocene and Oligocene, when significant crustal thinning and upper crustal extension occurred along the belt of Cordilleran metamorphic core complexes (Fig. 3.1). Indirect evidence for Eocene-Oligocene extension comes from local studies of syn-extensional basins such as the Challis Volcanic field of east-central Idaho (Janecke, 1992), the Muddy Creek Basin in southwest Montana (Janecke et al., 1999), and the Elko and White Sage formations in northeastern Nevada (Potter et al., 1995; Dubiel et al., 1996; Haynes, 2003). More direct evidence for Eocene and Oligocene extensional exhumation comes almost exclusively from metamorphic core complexes in the form of both thermochronologic data (Holm and Dokka, 1991; Lee, 1995; Foster and Raza, 2002; Vogl et al., 2012; Evans et al., 2015; Lee et al., 2017), and dated stratigraphic sequences deposited in hanging wall sedimentary basins (Satarugsa and Johnson, 2000; Wagner and Johnson, 2006; Smith et al., 2017; Canada et al., 2020). Much of the thermochronologic evidence for pre-Miocene exhumation within core complexes comes from higher temperature thermochronometers, especially $^{40}Ar/^{39}Ar$ analysis of K-feldspar and biotite (e.g., Applegate and Hodges, 1992). Studies that apply low-temperature thermochronometers such as apatite (U-Th)/He and apatite fission-track analyses find rapid pulses of cooling in the middle Miocene (e.g., Wells et al., 2000;

Gonzalez, 2019; Mueller, 2019), similar to the pronounced pulse of Miocene cooling shown by our data outside of the core complexes.

Our data lack any indication of significant extensional cooling during the Eocene or Oligocene, supporting the view that Eocene-Oligocene upper-crustal extension was likely confined to the belt of metamorphic core complexes. Within our data, samples that show significant Miocene cooling are most likely not obscuring a previous phase of Eocene-Oligocene rapid cooling, since compiled emplacement-depth estimates for the plutons average 9±2.8 km (Table 3.2), which is almost entirely accounted for by our estimates of 5-8 km of middle Miocene exhumation.

Our data therefore support an emerging view that diminishes the importance of Eocene-Oligocene extension, describing it as a potentially broadly distributed but relatively small magnitude extensional phase in response to ~40 Ma plate boundary reorganization (Chapter 2), or possibly a minor topographic response to flexural subsidence related to the foundering of the Farallon slab (Lund Snee et al., 2016; Smith et al., 2017). Regardless of the specific driving mechanisms, Eocene-Oligocene extension was likely not a major phase of extension that reset low-temperature thermochronometers across a broad region.

Accommodation of crustal thinning in the Eocene-Oligocene

The timing and mechanism for thinning the 50-60 km thick crust of the Cretaceous-Paleogene Cordillera down to its modern 30-35 km thickness remain uncertain. Multiple lines of evidence support the presence of overthickened crust along the Cordillera during the early Cenozoic following protracted shortening during the Sevier orogeny, including palinspastic reconstructions (Coney and Harms, 1984; Bahadori et al., 2018), estimates of paleotopography (Chamberlain et al., 2012; Lechler et al., 2013; Snell et al., 2014; Cassel et al., 2014), and isotopic estimates of crustal thickness (Best et al., 2009; Chapman et al., 2015). Some workers describe Cordilleran orogenic collapse as a pulsed event beginning at ~40 Ma and lasting 10-15 Myr (Liu and Shen, 1992; Constenius, 1996; Chapman et al., 2015), while others ascribe major upper crustal extension observed in the Miocene as accommodating orogenic collapse (Colgan and Henry, 2009; Colgan et al., 2008; Henry et al., 2011). If, as our data indicate, significant upper crustal extension did not occur until the Miocene (~25-20 Ma) for much of the northern Basin and Range,

then some other mechanism must be invoked to explain any thinning of overthickened crust during the Eocene or Oligocene.

The lack of evidence for a regional upper crustal cooling event in the Eocene or Oligocene, when extensional collapse is thought to have been most rapid (Chapman et al., 2015), points towards geodynamic mechanisms that can thin the crust without leaving an upper crustal strain signature. Hypothesized mechanisms for significant exhumation and extension in deeper levels of the crust without minimal upper crustal deformation include the removal of material through intracrustal flow to adjacent areas of thinner crust (Block and Royden, 1990; McQuarrie and Chase, 2000), expulsion of a midcrustal allochthon (Hodges and Walker, 1992; Applegate and Hodges, 1995), midcrustal gravity currents following burial of upper crust (Wernicke and Getty, 1997), or movements of diapiric gneiss domes (Whitney et al., 2004; Konstantinou et al., 2012). Any of these mechanisms would allow compensation of the gravitational field without leaving easily interpretable upper crustal strain signatures.

3.5.2 Miocene to present extensional tectonism

Variability in the distribution and magnitude of extension

In map view, our data show zones of enhanced Miocene exhumation distributed among zones that experienced minimal Miocene exhumation (Fig. 3.2). These zones alternate with a period longer than a single horst and graben couplet (i.e. the pattern has a greater complexity than alternating hanging wall-footwall pairs). The spatially variable cooling behavior exhibited by our samples matches prior descriptions of spatial strain variability in the Basin and Range (e.g., Dickinson, 2002; Colgan et al., 2008; Fosdick and Colgan, 2008; Henry et al., 2011; Long, 2018). Colgan and Henry (2009) previously identified the apparent mismatch between Miocene extensional strain heterogeneity and modern horst-and-graben spacing and inferred that the modern Basin and Range topography must be a result of a post-Miocene tectonic phase with a more evenly distributed and lower magnitude character than the preceding Miocene phase of extension. A complete lack of post-Miocene cooling ages within our data support this interpretation, limiting spatially extensive post-Miocene extension to less than ~2 km of exhumation. Given the steep (i.e. ~50°-60°, e.g., Colgan et al., 2008) dips of range-bounding normal faults that characterize Pliocene to present extension in the Basin and

Range, a 2 km limit on exhumation significantly limits the amount of horizontal extension that could have been accommodated during this time period (e.g., Colgan et al., 2008; Colgan and Henry, 2009). A reduction in widely distributed extension across the Basin and Range province after the Miocene may reflect the migration aand consolidation of deformation to the margins of the province. Geodetic observations of active extension in the Basin and Range place the majority of strain along the far eastern and western boundaries of the region, with the center of the province behaving as a rigid block (Bennett et al., 2003; Kreemer et al., 2014).

Within our data, the magnitude of middle Miocene extension appears to be spatially heterogeneous, a type of variability that has been observed in other studies of extensional strain in the northern Basin and Range. Colgan and Henry (2009) observed that middle Miocene strain was partitioned into approximately 30-60 km wide high-strain domains separated by rigid crustal blocks of similar width. Long (2018) palinspastically restored extension in a province wide cross-section and found total extensional strain varied on a similar scale, oscillating between areas of 100-150% extension and internally rigid blocks. In both studies, variability of Miocene strain appears to have a wavelength of approximately 60-120 km, with little correlation to pre-existing Mesozoic contractional structures that could have localized strain. Such periodic variability in extensional strain was speculated to originate from periodic necking instabilities (Fletcher and Hallet, 1983; Zuber et al., 1986).

Periodic instability during rapid Miocene extension

The distinct spatial variability that characterizes middle Miocene extension may be an expression of periodic fluid instability in a low-viscosity lower crust during extension (e.g., Fletcher and Hallet, 1983; Ricard and Froideveaux, 1986; Zuber et al., 1986). Analog models of extension demonstrate that layered mediums composed of competent (i.e. high viscosity) and weak (i.e. low viscosity) materials produce periodic instabilities (boudinage) resulting in periodic variability in extensional strain at the surface of the material similar to what our data show for Miocene extension in the northern Basin and Range. Simplistically, the thickness of the competent layer controls the resulting wavelength of periodic instability, and the viscosity contrast between the strong and weak layers regulates the amplitude and timescale of deformation (Ricard and Froidevaux,

1986; Bassi and Bonnin, 1988). If periodic necking instability was a major control on the distribution of Miocene extension, it may be possible to use a model of periodic necking instability to invert observed wavelengths, timescales, and magnitudes of Miocene extension for constraints on the Miocene lithospheric strength profile. Such a calculation is beyond the scope of this manuscript but may be a useful approach to estimate past lithospheric structure.

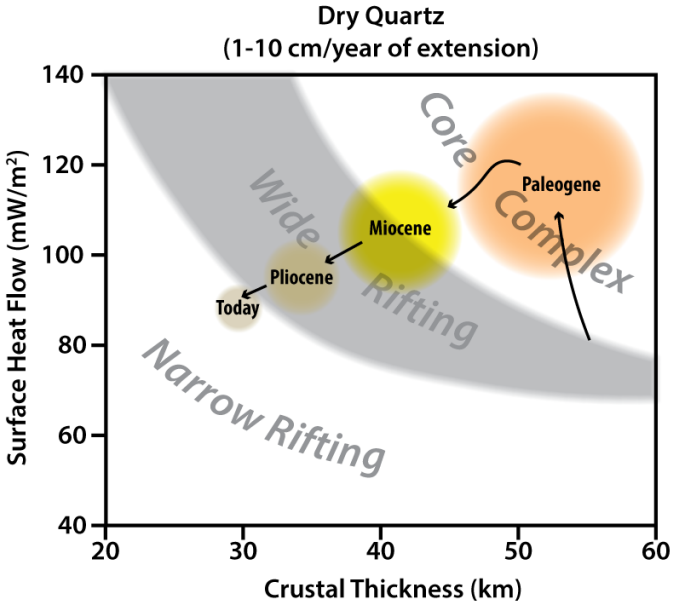


Figure 3.8: Phase diagram of extensional styles.
Model for the evolution of Basin and Range extensional style in response to changes in crustal heat and thickness, modified from Buck (1991). The style of extensional tectonism depends on the crustal thickness, thermal structure of the lithosphere (here represented by surface heat flow), and extension rate. This diagram assumes a 1-10 cm/yr rate of extension, comparable to the long-term average extension rate of the Basin and Range of 1-2 cm/yr (McQuarrie and Wernicke, 2005). The evolution of the extensional styles in the northern Basin and Range can be visualized as a progression through this diagram, starting with heating of the lithosphere during Farallon slab removal in the Paleogene, followed by gradual thermal equilibration and crustal thinning.

Evolution of Basin and Range Extension

The progression of Basin and Range extensional style from core complex development in the Paleogene, through wide-rifting in the Miocene, and eventually to narrow rifting today, can be considered in terms of the coevolution of thickness and thermal structure of the lithosphere (Fig. 3.8; Buck, 1991). Fig. 3.9 shows an interpretation of how evolving lithospheric structure and the distribution of heat within the lithosphere could lead to the observed patterns of extensional deformation in the

northern Basin and Range. The key initial conditions prior to extension, in the Paleogene, include a thickened (45-55 km) crust and a cold geothermal gradient due to the presence of the Farallon flat slab chilling the base of the North American lithosphere. Eocene-Oligocene removal of the Farallon slab brought hot asthenosphere into contact with the base of the North American lithosphere, inducing partial melting and heating of the lithosphere through magmatism. This thermal heating weakened the lithosphere, allowing gravitational stresses along the belt of overthickened crust of the Sevier orogen (variations in crustal thickness are not shown in Fig. 3.9) to drive intense local extension producing a narrow belt of metamorphic core complexes (Fig. 3.9).

Following Farallon delamination, modeling suggests that it may take as long as 10-20 Myr for the full thickness of the lithosphere to warm and thermally equilibrate (Liu et al., 2021). The significant delay for heat to diffuse into the lithosphere, especially all the way into the upper crust, may explain the significant delay between Eocene-Oligocene Farallon slab removal and major extension in the Miocene (). Miocene extension affected a broad region (e.g., McQuarrie and Wernicke, 2005; Colgan and Henry, 2009), potentially reflecting the widespread nature of broad thermal weakening after Farallon removal (Fig. 3.9; e.g., Liu and Shen, 1998).

Continued thermal equilibration and crustal thinning may have transitioned the Basin and Range away from broadly distributed extension in favor of narrow rifting (Fig. 3.8). In the modern, geodetic data indicate that most of the extension across the Basin and Range is accommodated along its eastern and western margins, conforming to models of narrow rifting (Fig. 3.8; Buck, 1991; Bennett et al., 2003; Kreemer et al., 2014).

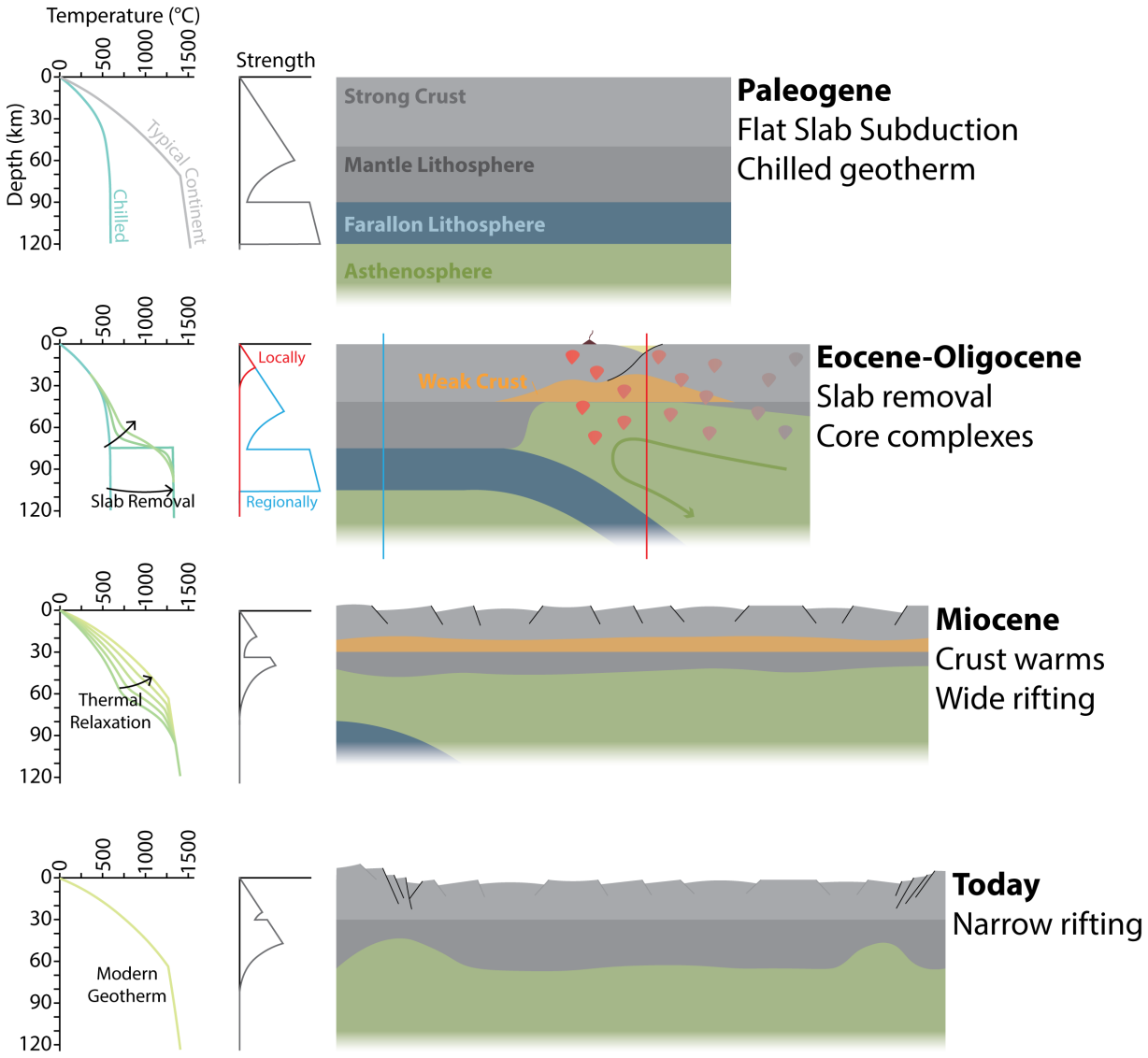


Figure 3.9: Simplified model for the evolution of Basin and Range extension. *Time-series of simplified cross sections showing the thermal and rheological evolution of the North American lithosphere during extension. On the left are geothermal gradients and schematic strength profiles of the lithosphere. The evolution of Basin and Range extensional style shown here corresponds to the progression depicted in Fig. 3.8 (Buck, 1991).*

3.6 Conclusions

Our new low-temperature thermochronology from across the northern Basin and Range reveals a heterogeneous distribution of Miocene extensional deformation, and potentially provides a record of exhumation during Cretaceous-Paleogene Sevier orogenesis. Modeled time-temperature histories are highly variable, with the most rapid

phase of extension occurring in the Miocene. A lack of cooling in the Eocene-Oligocene challenges models that interpret a major upper-crustal extensional phase at that time. Without upper-crustal extension, Eocene-Oligocene crustal thinning may have been accommodated by more cryptic deformation mechanisms such as lower crustal flow. Some samples were not reset during Miocene extension and retain a protracted history of Cretaceous-Paleogene cooling that might reflect changes in rock exhumation during the Sevier orogeny. In these longer cooling histories, slow Cretaceous exhumation changes to almost no exhumation at ~75-60 Ma, potentially recording the tectonic transition of the hinterland of the Sevier orogen from contraction to extension and associated topographic isolation and hydrologic closure of a low-relief Nevadaplano.

3.7 Acknowledgments

This material is based upon work supported by the National Science Foundation under Grant Nos. EAR-1759200 and EAR-1759353. Any opinions, findings, and conclusions or recommendations expressed in this material are those of the authors and do not necessarily reflect the views of the National Science Foundation. Thanks to the AGeS program for its support. Thanks to Eric Christiansen for providing mineral separates of the Granite Peak pluton.

3.8 References

Allmendinger, R.W., and Jordan, T.E., 1984, Mesozoic structure of the Newfoundland Mountains, Utah: Horizontal shortening and subsequent extension in the hinterland of the Sevier belt: Geological Society of America Bulletin, v. 95, p. 1280–1292.

Applegate, J.D.R., Walker, J.D., and Hodges, K.V., 1992, Late Cretaceous extensional unroofing in the Funeral Mountains metamorphic core complex, California: Geology, v. 20, p. 519–522.

Armstrong, R.L., and Hansen, E., 1966, Cordilleran infrastructure in the eastern Great Basin: American Journal of Science, v. 264, p. 112–127.

Armstrong, R.L., Leeman, W.P., and Malde, H.E., 1975, K-Ar dating, Quaternary and Neogene volcanic rocks of the snake river plain, Idaho: American Journal of Science, v. 275, p. 225–251, doi:10.2475/ajs.275.3.225.

Armstrong, P.A., Taylor, A.R., and Ehlers, T.A., 2004, Is the Wasatch fault footwall (Utah, United States) segmented over million-year time scales? Geology, v. 32, p. 385, doi:10.1130/G20421.1.

Axen, G.J., Taylor, W.J., and Bartley, J.M., 1993, Space-time patterns and tectonic controls of Tertiary extension and magmatism in the Great Basin of the western United States: Geological Society of America Bulletin, v. 105, p. 56–76, doi:10.1130/0016-7606(1993)105<0056:STPATC>2.3.CO;2.

Bahadori, A., Holt, W.E., and Rasbury, E.T., 2018, Reconstruction modeling of crustal thickness and paleotopography of western North America since 36 Ma: Geosphere, v. 14, p. 1207–1231, doi:10.1130/GES01604.1.

Bennett, S.E.K., Darin, M.H., Dorsey, R.J., Skinner, L.A., Umhoefer, P.J., and Reynolds, R E, 2016, Animated tectonic reconstruction of the Lower Colorado River region: implications for Late Miocene to Present deformation, *in* Going LOCO: Investigations along the Lower Colorado River, California State University Desert Studies Center Desert Symposium Field Guide and Proceedings, p. 73–86.

Bennett, R.A., Wernicke, B.P., Niemi, N.A., Friedrich, A.M., and Davis, J.L., 2003, Contemporary strain rates in the northern Basin and Range province from GPS data: Tectonics, v. 22, 1008, doi:10.1029/2001TC001355.

Best, M.G., Barr, D.L., Christiansen, E.H., Gromme, S., Deino, A.L., and Tingey, D.G., 2009, The Great Basin Altiplano during the middle Cenozoic ignimbrite flareup: insights from volcanic rocks: International Geology Review, v. 51, p. 589–633.

Block, L., and Royden, L.H., 1990, Core complex geometries and regional scale flow in the lower crust: Tectonics, v. 9, p. 557–567, doi:10.1029/TC009i004p00557.

Boddy, R., and Smith, G., 2010, Effective Experimentation: For Scientists and Technologists: Chichester, UK, John Wiley & Sons, Ltd, doi:10.1002/9780470666654.

du Bray, E.A., 2007, Time, space, and composition relations among northern Nevada intrusive rocks and their metallogenic implications: Geosphere, v. 3, p. 381, doi:10.1130/GES00109.1.

Brooks, W.E., Thorman, C.H., and Snee, L.W., 1995, The $^{40}Ar/^{39}Ar$ ages and tectonic setting of the middle Eocene northeast Nevada volcanic field: Journal of Geophysical Research: Solid Earth, v. 100, p. 10403–10416, doi:10.1029/94JB03389.

Buck, W.R., 1991, Modes of Continental Lithospheric Extension: Journal of Geophysical Research, v. 96, p. 20161–20178, doi:10.1029/91JB01485.

Camilleri, P., Deibert, J., and Perkins, M., 2017, Middle Miocene to Holocene tectonics, basin evolution, and paleogeography along the southern margin of the Snake

River Plain in the Knoll Mountain–Ruby–East Humboldt Range region, northeastern Nevada and south-central Idaho: Geosphere, v. 13, p. 1901–1948, doi:10.1130/GES01318.1.

Canada, A.S., Cassel, E.J., McGrew, A.J., Smith, M.E., Stockli, D.F., Foland, K.A., Jicha, B.R., and Singer, B.S., 2019, Eocene exhumation and extensional basin formation in the Copper Mountains, Nevada, USA: Geosphere, v. 15, p. 1577–1597, doi:10.1130/GES02101.1.

Canada, A.S., Cassel, E.J., Stockli, D.F., Smith, M.E., Jicha, B.R., and Singer, B.S., 2020, Accelerating exhumation in the Eocene North American Cordilleran hinterland: Implications from detrital zircon (U-Th)/(He-Pb) double dating: Geological Society of America Bulletin, v. 132, p. 198–214, doi:10.1130/B35160.1.

Cassel, E.J., Breecker, D.O., Henry, C.D., Larson, T.E., and Stockli, D.F., 2014, Profile of a paleo-orogen: High topography across the present-day Basin and Range from 40 to 23 Ma: Geology, v. 42, p. 1007–1010, doi:10.1130/G35924.1.

Cavazza, W., Albino, I., Zattin, M., and Galoyan, G., 2015, Thermochronometric evidence for Miocene tectonic reactivation of the Sevan–Akera suture zone (Lesser Caucasus): a far-field tectonic effect of the Arabia – Eurasia collision? The Geological Society of London Special Publications, v. 428, doi:10.1144/SP428.4.

Chamberlain, C.P., Mix, H.T., Mulch, A., Hren, M.T., Kent-Corson, M.L., Davis, S.J., Horton, T.W., and Graham, S.A., 2012, The Cenozoic climatic and topographic evolution of the western North American Cordillera: American Journal of Science, v. 312, p. 213–262, doi:10.2475/02.2012.05.

Chapman, J.B., Ducea, M.N., DeCelles, P.G., and Profeta, L., 2015, Tracking changes in crustal thickness during orogenic evolution with Sr/Y: An example from the North American Cordillera: Geology, v. 43, p. 919–922, doi:10.1130/G36996.1.

Christiansen, E.H., and Vervoort, J.D., 2009, U-Pb zircon geochronology results for the Granite Peak and Granite Peak SE quadrangles, Utah: Utah Geological Survey Open-File Report 546, doi:10.34191/OFR-546.

Coats, R.R., 1987, Geology of Elko County, Nevada: Nevada Bureau of Mines and Geology Bulletin 101.

Coats, R.R., 1964, Geology of the Jarbidge quadrangle, Nevada-Idaho: U.S. Geological Survey U.S. Geological Survey Bulletin 1141-M.

Coats, R.R., Marvin, R.F., and Stern, T.W., 1965, Reconnaissance of mineral ages of plutons in Elko county, Nevada, and vicinity: U.S. Geological Survey Professional Paper 525-D, D11–D15 p.

Colgan, J.P., Dumitru, T.A., Reiners, P.W., Wooden, J.L., and Miller, E.L., 2006, Cenozoic tectonic evolution of the basin and range province in northwestern Nevada: American Journal of Science, v. 306, p. 616–654, doi:10.2475/08.2006.02.

Colgan, J.P., and Henry, C.D., 2009, Rapid middle Miocene collapse of the Mesozoic orogenic plateau in north-central Nevada: International Geology Review, v. 51, p. 920–961, doi:10.1080/00206810903056731.

Colgan, J.P., Howard, K.A., Fleck, R.J., and Wooden, J.L., 2010, Rapid middle Miocene extension and unroofing of the southern Ruby Mountains, Nevada: Tectonics, v. 29, p. n/a-n/a, doi:10.1029/2009TC002655.

Colgan, J.P., John, D.A., Henry, C.D., and Fleck, R.J., 2008a, Large-magnitude Miocene extension of the Eocene Caetano caldera, Shoshone and Toiyabe Ranges, Nevada: Geosphere, v. 4, p. 107–130, doi:10.1130/GES00115.1.

Colgan, J.P., and Metcalf, J.R., 2006, Apatite fission-track and (U-Th)/He dating of slip on the Crescent Fault, Nevada, *in* American Geophysical Union.

Colgan, J.P., Shuster, D.L., and Reiners, P.W., 2008b, Two-phase Neogene extension in the northwestern basin and range recorded in a single thermochronology sample: Geology, v. 36, p. 631–634, doi:10.1130/G24897A.1.

Coney, P.J., and Harms, T.A., 1984, Cordilleran metamorphic core complexes: Cenozoic extensional relics of Mesozoic compression.: Geology, v. 12, p. 550–554, doi:10.1130/0091-7613(1984)12<550:CMCCCE>2.0.CO;2.

Constenius, K.N., 1996, Late Paleogene extensional collapse of the Cordilleran foreland fold and thrust belt: Geological Society of America Bulletin, v. 108, p. 20–39, doi:10.1130/0016-7606(1996)108<0020:LPECOT>2.3.CO;2.

Crafford, A.E.J., 2010, Geologic terrane map of Nevada: Nevada Bureau of Mines and Geology Open File Report 10-04.

Dean, R.B., and Dixon, W.J., 1951, Simplified statistics for small numbers of observations: Analytical Chemistry, v. 23, p. 636–638, doi:10.1021/ac60052a025.

DeCelles, P.G., 2004, Late Jurassic to Eocene evolution of the cordilleran thrust belt and foreland basin system, western U.S.A.: American Journal of Science, v. 304, p. 105–168, doi:10.2475/ajs.304.2.105.

DePaolo, D.J., and Daley, E.E., 2000, Neodymium isotopes in basalts of the southwest basin and range and lithospheric thinning during continental extension: Chemical Geology, v. 169, p. 157–185, doi:10.1016/S0009-2541(00)00261-8.

Di Fiori, R.V., Long, S.P., Fetrow, A.C., Snell, K.E., Bonde, J.W., and Vervoort, J., 2020, Syncontractional deposition of the Cretaceous Newark Canyon Formation, Diamond Mountains, Nevada: Implications for strain partitioning within the U.S. Cordillera: Geosphere, v. 16, p. 546–566, doi:10.1130/GES02168.1.

Dickinson, W.R., 2009, Anatomy and global context of the North American Cordillera, *in* Backbone of the Americas: Shallow Subduction, Plateau Uplift, and Ridge and Terrane Collision, Geological Society of America, doi:10.1130/2009.1204(01).

Dickinson, W.R., 2004, Evolution of the North American Cordillera: Annual Review of Earth and Planetary Sciences, v. 32, p. 13–45, doi:10.1146/annurev.earth.32.101802.120257.

Dickinson, W.R., 2006, Geotectonic evolution of the Great Basin: Geosphere, v. 2, p. 353–368, doi:10.1130/GES00054.1.

Dickinson, W.R., 2002, The Basin and Range Province as a composite extensional domain: International Geology Review, v. 44, p. 1–38, doi:10.2747/0020-6814.44.1.1.

Dickinson, W.R., and Snyder, W.S., 1978, Plate tectonics of the Laramide orogeny, *in* Matthews, V. ed., Laramide Folding Associated with Basement Block Faulting in the Western United States, Boulder, Colorado, Geological Society of America Memoir 151, p. 355–366.

Dokka, R.K., Mahaffie, M.J., and Snoke, A.W., 1986, Thermochronologic evidence of major tectonic denudation associated with detachment faulting, Northern Ruby Mountains - East Humboldt Range, Nevada: Tectonics, v. 5, p. 995–1006, doi:10.1029/TC005i007p00995.

Donelick, R.A., O'Sullivan, P.B., and Ketcham, R.A., 2005, Apatite fission-track analysis: Reviews in Mineralogy and Geochemistry, v. 58, p. 49–94, doi:10.2138/rmg.2005.58.3.

Druschke, P., Hanson, A.D., Wells, M.L., Gehrels, G.E., and Stockli, D., 2011, Paleogeographic isolation of the Cretaceous to Eocene Sevier hinterland, east-central Nevada: Insights from U-Pb and (U-Th)/He detrital zircon ages of hinterland strata: Geological Society of America Bulletin, v. 123, p. 1141–1160, doi:10.1130/B30029.1.

Druschke, P., Hanson, A.D., Wells, M.L., Rasbury, T., Stockli, D.F., and Gehrels, G., 2009, Synconvergent surface-breaking normal faults of Late Cretaceous age within the Sevier hinterland, east-central Nevada: Geology, v. 37, p. 447–450, doi:10.1130/G25546A.1.

Dubiel, R.F., Potter, C.J., Good, S.C., and Snee, L.W., 1996, Reconstructing an Eocene extensional basin: The White Sage Formation, eastern Great Basin, *in* Beratan, K.K. ed., Reconstructing the History of Basin and Range Extension Using

Sedimentology and Stratigraphy, Boulder, Colorado, Geological Society of America Special Paper 303, p. 1–14.

Elison, M.W., 1995, Causes and consequences of Jurassic magmatism in the northern Great Basin: Implications for tectonic development, *in* Miller, D.M. and Busby, C. eds., Jurassic Magmatism and Tectonics of the North American Cordillera, Boulder, Colorado, Geological Society of America, Geological Society of America Special Papers 299, p. 249–265, doi:10.1130/SPE299-p249.

El-Shazly, A.K., Sanderson, D.D., and Napier, J., 2011, Petrogenesis of I-type granitoids from the Melrose Stock, east-central Nevada: International Geology Review, v. 53, p. 1522–1558, doi:10.1080/00206811003755396.

Engebretson, D.C., Cox, A., and Gordon, R.G., 1985, Relative Motions Between Oceanic and Continental Plates in the Pacific Basin: Geological Society of America, Geological Society of America Special Papers, v. 206, doi:10.1130/SPE206.

Ernst, W.G., 2009, Rise and fall of the Nevadaplano: International Geology Review, v. 51, p. 583–588, doi:10.1080/00206810903063315.

Evans, S.L., Styron, R.H., van Soest, M.C., Hodges, K.V., and Hanson, A.D., 2015, Zircon and apatite (U-Th)/He evidence for Paleogene and Neogene extension in the Southern Snake Range, Nevada, USA: Tectonics, v. 34, p. 2142–2164, doi:10.1002/2015TC003913.

Fosdick, J.C., and Colgan, J.P., 2008, Miocene extension in the East Range, Nevada: A two-stage history of normal faulting in the northern basin and range: Bulletin of the Geological Society of America, v. 120, p. 1198–1213, doi:10.1130/B26201.1.

Foster, D.A., and Raza, A., 2002, Low-temperature thermochronological record of exhumation of the Bitterroot metamorphic core complex, northern Cordilleran Orogen: Tectonophysics, v. 349, p. 23–36, doi:10.1016/S0040-1951(02)00044-6.

Gallagher, K., 2012, Transdimensional inverse thermal history modeling for quantitative thermochronology: Journal of Geophysical Research: Solid Earth, v. 117, p. 1–16, doi:10.1029/2011JB008825.

Gallagher, K., Brown, R., and Johnson, C., 1998, Fission track analysis and its applications to geological problems: Annual Review of Earth and Planetary Sciences, v. 26, p. 519–572, doi:10.1146/annurev.earth.26.1.519.

Gans, P.B., 1987, An open-system, two-layer crustal stretching model for the Eastern Great Basin: Tectonics, v. 6, p. 1–12, doi:10.1029/TC006i001p00001.

Gans, P.B., Mahood, G.A., and Schermer, E., 1989, Synextensional magmatism in the Basin and Range Province; A case study from the eastern Great Basin: Boulder, Colorado, Geological Society of America, doi:10.1130/SPE233.

Gion, A.M., Williams, S.E., and Müller, R.D., 2017, A reconstruction of the Eurekan Orogeny incorporating deformation constraints: A Reconstruction of the Eurekan Orogeny Incorporating Deformation Constraints: Tectonics, v. 36, p. 304–320, doi:10.1002/2015TC004094.

Glorie, S., De Grave, J., Buslov, M.M., Zhimulev, F.I., Elburg, M.A., and Van den haute, P., 2012, Structural control on Meso-Cenozoic tectonic reactivation and denudation in the Siberian Altai: Insights from multi-method thermochronometry: Tectonophysics, v. 544–545, p. 75–92, doi:10.1016/j.tecto.2012.03.035.

Gonsior, Z.J., and Dilles, J.H., 2008, Timing and evolution of Cenozoic extensional normal faulting and magmatism in the southern Tobin Range, Nevada: Geosphere, v. 4, p. 687, doi:10.1130/GES00137.1.

Gonzalez, N., 2019, Thermochronology of upper crustal rocks in the Wood Hills, Nevada: Documenting exhumation in the U.S. Cordillera [B.S. thesis]: University of Colorado, 27 p.

Granath, V.C.H., Papike, J.J., and Labotka, T.C., 1983, The Notch Peak Contact Metamorphic Aureole, Utah: Petrology of the Big Horse Limestone Member of the Orr Formation: Geological Society of America Bulletin, v. 94, p. 889–906.

Gregory-Wodzicki, K.M., 1997, The Late Eocene House Range Flora , Sevier Desert , Utah : Paleoclimate and Paleoelevation: Palaios, v. 12, p. 552–567, doi:10.2307/3515411.

Grubbs, F.E., 1969, Procedures for detecting outlying observations in samples: Technometrics, v. 11, p. 1–21, doi:10.1080/00401706.1969.10490657.

Harrison, T.M., Duncan, I., and McDougall, I., 1985, Diffusion of ^{40}Ar in biotite: Temperature, pressure and compositional effects: Geochimica et Cosmochimica Acta, v. 49, p. 2461–2468, doi:10.1016/0016-7037(85)90246-7.

Haynes, S.R., 2003, Development of the Eocene Elko Basin, Northeastern Nevada: Implications for Paleogeography and Regional Tectonism [M.S. thesis]: University of British Columbia, 159 p.

Henry, C.D., Mcgrew, A.J., Colgan, J.P., Snoke, A.W., and Brueseke, M.E., 2011, Timing, distribution, amount, and style of Cenozoic extension in the northern Great Basin: GSA Field Guide, v. 21, p. 1–40, doi:10.1130/2011.0021(02).

Hintze, L.F., 1980, Geologic map of Utah: Utah Geological and Mineral Survey Map A-1.

Holdsworth, R.E., Stewart, M., Imber, J., and Strachan, R.A., 2001, The structure and rheological evolution of reactivated continental fault zones: a review and case study: Geological Society, London, Special Publications, v. 184, p. 115–137, doi:10.1144/GSL.SP.2001.184.01.07.

Holm, D.K., and Dokka, R.K., 1991, Major Late Miocene cooling of the middle crust associated with extensional orogenesis in the Funeral Mountains, California: Geophysical Research Letters, v. 18, p. 1775–1778, doi:10.1029/91GL02079.

Humphreys, E.D., 1995, Post-Laramide removal of the Farallon slab, western United States: Geology, v. 23, p. 987–990, doi:10.1130/0091-7613(1995)023<0987:PLROTF>2.3.CO;2.

Jurdy, D.M., 1984, The subduction of the Farallon Plate beneath North America as derived from relative plate motions: Tectonics, v. 3, p. 107–113, doi:10.1029/TC003i002p00107.

Ketner, K.B. et al., 1998, An outline of tectonic, igneous, and metamorphic events in the Goshute-Toano range between Silver Zone Pass and White Horse Pass, Elko county, Nevada: A history of superposed contractional and extensional deformation: U.S. Geological Survey Professional Paper Professional Paper 1593.

King, C.A., 2020, Geology and Alteration at Delcer Buttes, Nevada, *in* Vision for Discovery, Geology and Ore Deposits of the Basin and Range, Reno, Nevada, p. 1273–1297.

Konstantinou, A., Strickland, A., Miller, E.L., and Wooden, J.P., 2012, Multistage Cenozoic extension of the Albion-Raft River-Grouse Creek metamorphic core complex: Geochronologic and stratigraphic constraints: Geosphere, v. 8, p. 1429–1466, doi:10.1130/GES00778.1.

Kreemer, C., Blewitt, G., and Klein, E.C., 2014, A geodetic platemotion and Global Strain Rate Model: Geochemistry, Geophysics, Geosystems, v. 15, p. 3849–3889, doi:10.1002/2014GC005407.Received.

Lechler, A.R., Niemi, N.A., Hren, M.T., and Lohmann, K.C., 2013, Paleoelevation estimates for the northern and central proto-Basin and Range from carbonate clumped isotope thermometry: Tectonics, v. 32, p. 295–316, doi:10.1002/tect.20016.

Lee, J., 1995, Rapid uplift and rotation of mylonitic rocks from beneath a detachment fault: Insights from potassium feldspar $^{40}Ar/^{39}Ar$ thermochronology, northern Snake Range, Nevada: Tectonics, v. 14, p. 54–77, doi:10.1029/94TC01508.

Lee, J., Blackburn, T., and Johnston, S., 2017, Timing of mid-crustal ductile extension in the northern Snake Range metamorphic core complex, Nevada: Evidence from U/Pb zircon ages: Geosphere, v. 13, p. 439–459, doi:10.1130/GES01429.1.

Liu, M., 2001, Cenozoic extension and magmatism in the North American Cordillera: the role of gravitational collapse: Tectonophysics, v. 342, p. 407–433, doi:10.1016/S0040-1951(01)00173-1.

Liu, M., and Shen, Y., 1998, Crustal collapse, mantle upwelling, and Cenozoic extension in the North American Cordillera: Tectonics, v. 17, p. 311–311, doi:10.1029/98TC00313.

Liu, X., Currie, C.A., and Wagner, L.S., 2021, Cooling of the continental plate during flat-slab subduction: Geosphere, doi:10.1130/GES02402.1.

Long, S.P., 2018, Geometry and magnitude of extension in the Basin and Range Province (39°N), Utah, Nevada, and California, USA: Constraints from a province-scale cross section: GSA Bulletin, v. 131, p. 99–119, doi:10.1130/B31974.1.

McGrew, A.J., Vanderbeek, G.A., and Ali, O.E., 2000, New insights into the deformational history of the Sevier hinterland from the Copper Mountains, northeastern Nevada: Geological Society of America Abstracts with Programs, v. 32.

McQuarrie, N., and Oskin, M., 2010, Palinspastic restoration of NAVDat and implications for the origin of magmatism in southwestern North America: Journal of Geophysical Research, v. 115, B10401, doi:10.1029/2009JB006435.

McQuarrie, N., and Wernicke, B.P., 2005, An animated tectonic reconstruction of southwestern North America since 36 Ma: Geosphere, v. 1, p. 147–172, doi:10.1130/GES00016.1.

Miller, E.L., Dumitru, T.A., Brown, R.W., and Gans, P.B., 1999, Rapid miocene slip on the Snake Range-Deep Creek Range fault system, east-central Nevada: Bulletin of the Geological Society of America, v. 111, p. 886–905, doi:10.1130/0016-7606(1999)111<0886:RMSOTS>2.3.CO;2.

Miller, D.M., Hillhouse, W.C., Zartman, R.E., and Lanphere, M.A., 1987, Geochronology of intrusive and metamorphic rocks in the Pilot Range, Utah and Nevada, and comparison with regional patterns: Geological Society of America Bulletin, v. 99, p. 866–879, doi:10.1130/0016-7606(1987)99<866:GOIAMR>2.0.CO;2.

Miller, D.M., and Hoisch, T.D., 1995, Jurassic tectonics of northeastern Nevada and northwestern Utah from the perspective of barometric studies, *in* Geological Society of America Special Papers, Geological Society of America, v. 299, p. 267–294, doi:10.1130/SPE299-p267.

Miller, D.M., Nakata, J.K., and Glick, L.L., 1990, K-Ar Ages of Jurassic to Tertiary plutonic and metamorphic rocks, northwestern Utah and northeastern Nevada: U.S. Geological Survey Bulletin 1906, doi:10.3133/b1906.

Moore, W.J., and McKee, E.H., 1983, Phanerozoic magmatism and mineralization in the Tooele 1°x2° quadrangle, Utah, *in* Miller, D.M., Todd, V.R., and Howard, K.A. eds., Tectonic and Stratigraphic Studies in the Eastern Great Basin, Geological Society of America Memoir 157, p. 183–190.

Mueller, C., 2019, Thermochronology of the deep crust in the northern Ruby Mountains, NV [B.S. thesis]: University of Colorado, 30 p.

Nabelek, P.I., Papike, J.J., and Laul, J.C., 1986, The Notch Peak granitic stock, Utah: Origin of reverse zoning and petrogenesis: Journal of Petrology, v. 27, p. 1035–1069, doi:10.1093/petrology/27.5.1035.

Niemi, N.A., Wernicke, B.P., Friedrich, A.M., Simons, M., Bennett, R.A., and Davis, J.L., 2004, BARGEN continuous GPS data across the eastern Basin and Range province, and implications for fault system dynamics: Geophysical Journal International, v. 159, p. 842–862, doi:10.1111/j.1365-246X.2004.02454.x.

Peace, A.L., 2021, Beyond 'crumple zones': recent advances, applications and future directions in deformable plate tectonic modelling: Geological Magazine, v. 158, p. 1704–1710, doi:10.1017/S0016756821000534.

Potter, C.J., Dubiel, R.F., Snee, L.W., and Good, S.C., 1995, Eocene extension of early Eocene lacustrine strata in a complexly deformed Sevier-Laramide hinterland, northwest Utah and northeast Nevada: Geology, v. 23, p. 181–184, doi:10.1130/0091-7613(1995)023<0181:EEOEEL>2.3.CO;2.

Rahl, J.M., McGrew, A.J., and Foland, K.A., 2002, Transition from Contraction to Extension in the Northeastern Basin and Range: New Evidence from the Copper Mountains, Nevada: The Journal of Geology, v. 110, p. 179–194, doi:10.1086/338413.

Renne, P.R., Balco, G., Ludwig, K.R., Mundil, R., and Min, K., 2011, Response to the comment by W.H. Schwarz et al. on "Joint determination of ^{40}K decay constants and $^{40}Ar^*/^{40}K$ for the Fish Canyon sanidine standard, and improved accuracy for $^{40}Ar/^{39}Ar$ geochronology" by P.R. Renne et al. (2010): Geochimica et Cosmochimica Acta, v. 75, p. 5097–5100, doi:10.1016/j.gca.2011.06.021.

Renne, P.R., Mundil, R., Balco, G., Min, K., and Ludwig, K.R., 2010, Joint determination of ^{40}K decay constants and $^{40}Ar^*/^{40}K$ for the Fish Canyon sanidine standard, and improved accuracy for $^{40}Ar/^{39}Ar$ geochronology: Geochimica et Cosmochimica Acta, v. 75, p. 5349–5367.

Rohrmann, A., Kapp, P., Carrapa, B., Reiners, P.W., Guynn, J., Ding, L., and Heizler, M., 2012, Thermochronologic evidence for plateau formation in central Tibet by 45 Ma: Geology, v. 40, p. 187–190.

Satarugsa, P., and Johnson, R.A., 2000, Cenozoic tectonic evolution of the Ruby Mountains metamorphic core complex and adjacent valleys, northeastern Nevada: Rocky Mountain Geology, v. 35, p. 205–230, doi:10.2113/35.2.205.

Schellart, W.P., Stegman, D.R., Farrington, R.J., Freeman, J., and Moresi, L., 2010, Cenozoic tectonics of western North America controlled by evolving width of Farallon slab: Science, v. 329, p. 316–319.

Singleton, J.S., Wong, M.S., and Johnston, S.M., 2018, The role of calcite-rich metasedimentary mylonites in localizing detachment fault strain and influencing the structural evolution of the Buckskin-Rawhide metamorphic core complex, west-central Arizona: Lithosphere, v. 10, p. 172–193, doi:10.1130/L699.1.

Smith, M.E., Cassel, E.J., Jicha, B.R., Singer, B.S., and Canada, A.S., 2017, Hinterland drainage closure and lake formation in response to middle Eocene Farallon slab removal, Nevada, U.S.A.: Earth and Planetary Science Letters, v. 479, p. 156–169, doi:10.1016/j.epsl.2017.09.023.

Snell, K.E., Koch, P.L., Druschke, P., Foreman, B.Z., and Eiler, J.M., 2014, High elevation of the "Nevadaplano" during the Late Cretaceous: Earth and Planetary Science Letters, v. 386, p. 52–63, doi:10.1016/j.epsl.2013.10.046.

Snow, J.K., and Wernicke, B.P., 2000, Cenozoic tectonism in the central basin and range: Magnitude, rate, and distribution of upper crustal strain: American Journal of Science, v. 300, p. 659–719, doi:10.2475/ajs.300.9.659.

Stockli, D.F., 1999, Regional timing and spatial distribution of Miocene extension in the northern Basin and Range Province [Ph.D. thesis].

Stockli, D.F., Linn, J.K., Douglas Walker, J., and Dumitru, T.A., 2001, Miocene unroofing of the Canyon Range during extension along the Sevier Desert Detachment, west central Utah: Tectonics, v. 20, p. 289–307, doi:10.1029/2000TC001237.

Thatcher, W., 2009, How the Continents Deform: The Evidence From Tectonic Geodesy: Annual Review of Earth and Planetary Sciences, v. 37, p. 237–262, doi:10.1146/annurev.earth.031208.100035.

Thomson, S.N., 2002, Late Cenozoic geomorphic and tectonic evolution of the Patagonian Andes between latitudes 42°S and 46°S: An appraisal based on fission-track results from the transpressional intra-arc Liquiñe-Ofqui fault zone: Geological Society of America Bulletin, v. 114, p. 1159–1173.

Tummers, B., 2006, DataThief III:, https://datathief.org/.

Vogl, J.J., Foster, D.A., Fanning, C.M., Kent, K.A., Rodgers, D.W., and Diedesch, T., 2012, Timing of extension in the Pioneer metamorphic core complex with implications for the spatial-temporal pattern of Cenozoic extension and exhumation in the northern U.S. Cordillera: Tectonics, v. 31, TC1008, doi:10.1029/2011TC002981.

Wagner, F.H., and Johnson, R.A., 2006, Coupled basin evolution and late-stage metamorphic core complex exhumation in the southern Basin and Range Province, southeastern Arizona: Tectonophysics, v. 420, p. 141–160, doi:10.1016/j.tecto.2006.01.012.

Wang, E., Kirby, E., Furlong, K.P., van Soest, M., Xu, G., Shi, X., Kamp, P.J.J., and Hodges, K.V., 2012, Two-phase growth of high topography in eastern Tibet during the Cenozoic: Nature Geoscience, v. 5, p. 640–645, doi:10.1038/ngeo1538.

Wells, M.L., Snee, L.W., and Blythe, A.E., 2000, Dating of major normal fault systems using thermochronology: An example from the Raft River detachment, Basin and Range, western United States: Journal of Geophysical Research, v. 105, B7, p. 16303–16327, doi:10.1029/2000JB900094.

Wernicke, B., 1985, Uniform-sense normal simple shear of the continental lithosphere: Canadian Journal of Earth Sciences, v. 22, p. 108–125, doi:10.1139/e85-009.

Wernicke, B., and Burchfiel, B.C., 1982, Modes of extensional tectonics: Journal of Structural Geology, v. 4, p. 105–115, doi:10.1016/0191-8141(82)90021-9.

Wolf, R.A., Farley, K.A., and Kass, D.M., 1998, Modeling of the temperature sensitivity of the apatite (U-Th)/He thermochronometer: Chemical Geology, v. 148, p. 105–114, doi:10.1016/S0009-2541(98)00024-2.

van Wijk, J.W., 2005, Role of weak zone orientation in continental lithosphere extension: Geophysical Research Letters, v. 32, p. L02303, doi:10.1029/2004GL022192.

Yonkee, W.A., and Weil, A.B., 2015, Tectonic evolution of the Sevier and Laramide belts within the North American Cordillera orogenic system: Earth-Science Reviews, v. 150, p. 531–593, doi:10.1016/j.earscirev.2015.08.001.

Zamudio, J.A., 1992, A synthesis of geologic mapping and remote sensing data analysis for the Dolly Varden Mountains and Currie Hills, Elko County, Vevada [Ph.D. thesis]: University of Colorado, 152 p.

Zens, Z.A., 2019, Geology and geochronology of the contact copper porphyry [Ph.D. thesis]: New Mexico Institute of Mining and Technology, 150 p.

Zuber, M.T., Parmentier, E.M., and Fletcher, R.C., 1986, Extension of continental lithosphere: A model for two scales of basin and range deformation: Journal of Geophysical Research, v. 91, p. 4826, doi:10.1029/JB091iB05p04826.

Chapter 4
Low-temperature Thermochronology Limits Recent Uplift in the Lesser Caucasus and Eastern Pontides During the Initiation of Continent-continent Collision [2]

4.1 Abstract

The over-riding and down-going plates of a continent-continent collision experience different amounts of shortening and deformation, an asymmetry that can result in asymmetric topography and structure within the resulting collisional orogen. Asymmetric accommodation of deformation across continental collisions may originate from asymmetries during the very initial stages of the transition from subduction to continent-continent collision. However, there are few modern examples of young collisional orogens in which the complex and rapid evolution of continental deformation following the initiation of collision can be examined. Located at the far northern margin of the Arabia-Eurasia collision zone, the Caucasus orogen is undergoing a transition from subduction to continental collision that initiated at 5 Ma and continues through today. Thermochronologic and structural data in the overriding plate (the Greater Caucasus mountain belt) document major deformation in response to the initiation of collision at 5 Ma. However, comparable data from the down-going plate in the collision (the Lesser Caucasus and Eastern Pontides mountain belts) remain sparse, leaving the structure and recent tectonic history of the down-going plate uncertain, and precluding evaluations of asymmetry within the broader collision. We present new apatite (U-Th)/He analyses and geomorphic observations in the Lesser Caucasus and Eastern Pontides mountains that limit the magnitude of rock to less than 1-2 km since 10 Ma. Such limited rock exhumation suggests that any shortening across the ranges during this period was most likely

[2] *Midttun, N., Niemi, N.A., and Orhan, K, in prep. for submission to Geological Magazine*

accommodated on continental-scale strike-slip faults (i.e. the Pembak-Sevan, Northern Anatolian, and Northeastern Anatolian faults). These faults are understood to reactivate major tectonic sutures of the Arabia-Eurasia collision zone, providing an example of preexisting discontinuities controlling the distribution of later continental deformation. Our results illuminate asymmetry in the style and magnitude of deformation between the overriding and down-going plates in the Caucasus continental collision, highlighting the importance of considering inherited lithospheric structures when interpreting asymmetric continental deformation in active and ancient collisional orogens.

4.2 Introduction

The relative partitioning of strain into the over-riding and down-going continental plates during and immediately following the initiation of continent-continent collision is a critical process that establishes the initial geometry for subsequent collisional orogenesis and may explain structural asymmetries and complex patterns of shortening across collision zones (Liao and Gerya, 2017; and references therein). The partitioning of strain between the over-riding and down-going plates may be influenced by several factors, including the geometry of the colliding plates and intervening basin (e.g., Schoettle-Greene and Pysklywec, 2014), the rheology of the colliding continents (e.g., Rosenberg and Kissling, 2013; Liao and Gerya, 2017), and preexisting structures that might act as weak zones onto which deformation can localize (e.g., Liao et al., 2018; Cavazza et al., 2018). The relative importance of each of these factors is difficult to establish using real-world examples because while subduction and continent-continent collision are each relatively long-lived phases of the Wilson cycle, the critical transition between them is a comparatively brief geologic event that produces a diachronous and complex geologic record which gets consumed and deformed by the ensuing collisional orogeny.

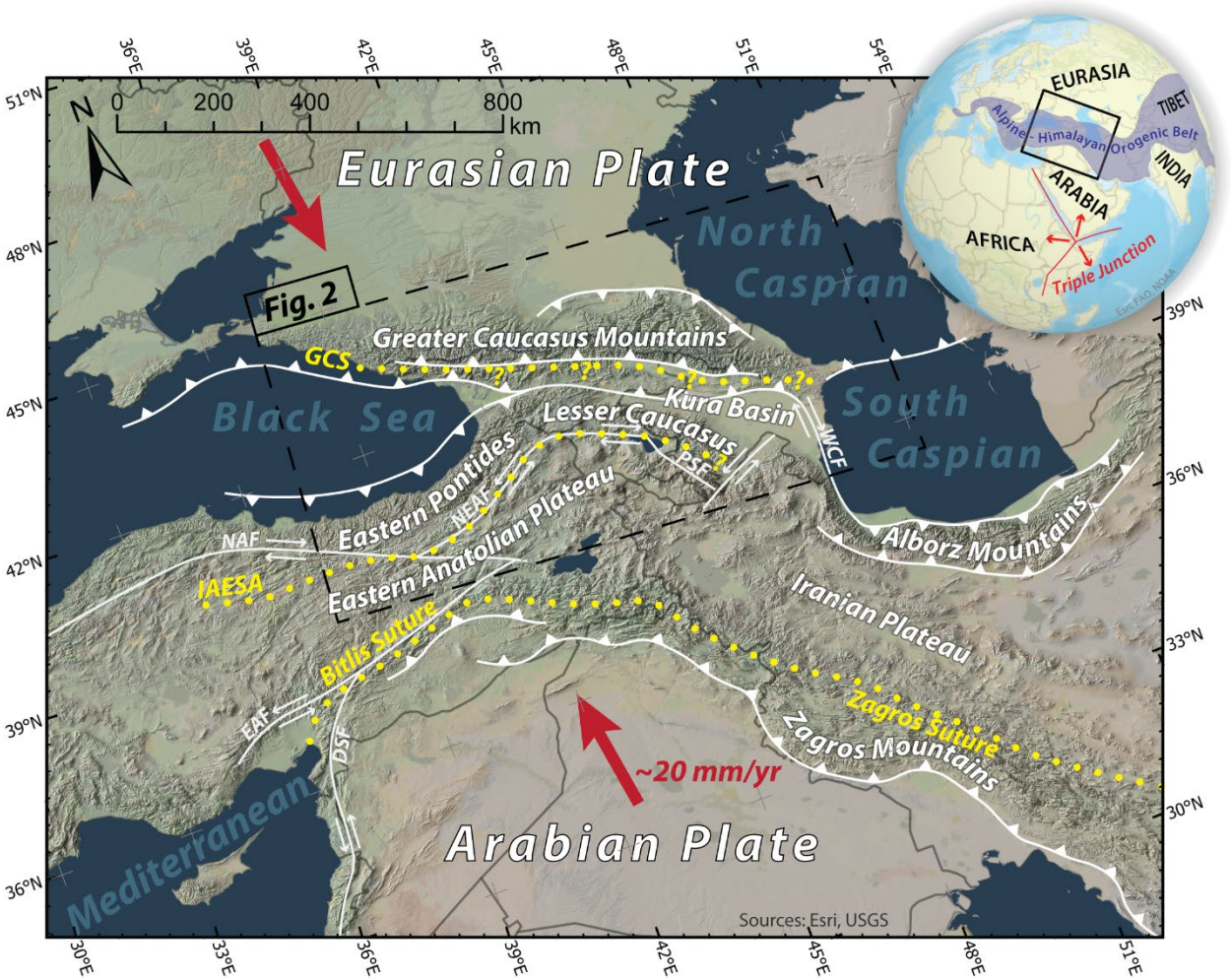


Figure 4.1: Overview of the Arabia-Eurasia collision zone.
Map showing major tectonic structures, place names, and the extent of Fig. 4.2 in the context of the Arabia-Eurasia collision zone. Red arrows show direction of Arabia-Eurasia convergence as determined by GPS geodesy (Reilinger et al., 2006). The precise location of the Greater Caucasus Suture is unknown (GCS; Cowgill et al., 2016). The Sanandaj-Sirjan and Eastern Pontides-Lesser Caucasus arcs are disconnected Jurassic arcs (Hassanzadeh and Wernicke, 2016). NAF=North Anatolian Fault, NEAF=Northeast Anatolian Fault, PSF=Pembak-Sevan Fault, WCF=West Caspian Fault, DSF=Dead Sea Fault, GCS=Greater Caucasus Suture, IAESA=İzmir-Ankara-Erzincan and Sevan-Akera Suture.

The transition from subduction to collision between the Lesser Caucasus and Greater Caucasus (Fig. 4.1) began at ~5 Ma and continues today, providing a rare opportunity to examine the geologic processes associated with the earliest stages of collision. In the Caucasus collision, we focus on two dynamics that remain poorly constrained: (1) the partitioning of collisional shortening between the over-riding and down-going plates, and (2) the importance of inherited lithospheric discontinuities in localizing deformation. Recent research has clarified our understanding of the over-riding

plate within this collision (i.e., the Greater Caucasus; Fig. 4.1) as an orogenic system consistent with models of climatically and tectonically modulated critical-taper orogenesis. In the Greater Caucasus, shortening is accommodated primarily by reverse faulting and folding, and topography is supported by a thickened crustal root (Forte et al., 2014; 2016; Mumladze et al., 2015; Cowgill et al., 2016; Vincent et al., 2016; 2020; Gunnels et al., 2021; Tye et al., 2021). In contrast, the down-going plate (i.e. the Lesser Caucasus-Eastern Pontides; LCEP; Fig. 4.1) is a more enigmatic orogen where fundamental questions regarding the structure, recent tectonic and topographic histories, and nature of support for high topography remain unanswered (Cavazza et al., 2015; Cowgill et al., 2016; Sokhadze et al., 2018; Gusmeo et al., 2021).

Previous attempts to answer these questions in the LCEP through integrative geologic, geophysical, and neotectonic studies are sparse, in part because political considerations limit access to much of the Lesser Caucasus, but also because, as we will show, low uranium concentrations in Eocene volcanic rocks from across the region provide poor material for standard low-temperature thermochronologic analysis. Furthermore, modern geodetic estimates of 1-2 mm/yr of shortening across the Lesser Caucasus are slow compared to the 5-10 mm/yr of shortening across the frontal faults of the Greater Caucasus to the north (Reilinger et al., 2006; Karakhanyan et al., 2013), suggesting that Lesser Caucasus uplift events may not be rapid nor large enough to easily distinguish from background erosion rates.

Despite the challenges of low uranium concentrations and potentially slow tectonic rates, we present new thermochronologic data that, in the context of geologic and geomorphic observations, clearly differentiate the tectonic response of the LCEP from that of the adjacent Greater Caucasus. These difference in how shortening was accommodated between the Greater and Lesser Caucasus provides meaningful insights into the partitioning of deformation between the lower and upper plates of an evolving collisional orogen. Furthermore, the timing of exhumation indicated by our thermochronology data potentially link the topographic history of the LCEP to that of the Eastern Anatolian Plateau (Fig. 4.1), where significant uplift occurred prior to Pliocene collision in the Caucasus.

4.2.1 Discontinuities in the Arabia-Eurasia Collision Zone

Beginning as early as the Eocene (e.g., Allen and Armstrong, 2008), the region between Arabia and Eurasia experienced a ~30 Myr phase of "soft" collision, in which Arabia-Eurasia convergence was largely absorbed by the subduction of small intervening ocean basins opened during back-arc rifting within the collision zone (Avdeev and Niemi, 2011; Cowgill et al., 2016). Prior to ~5 Ma, the Black Sea and South Caspian basins were connected by the Caucasus Basin, a back-arc basin which separated the Lesser and Greater Caucasus (Fig. 4.1; Cowgill et al., 2016). Over the past 30 Myr, the Caucasus Basin subducted to the north beneath the Greater Caucasus until ~ 5 Ma when "soft" collision transitioned into "hard" collision due to buoyant Lesser Caucasus lithosphere entering the subduction zone, mechanically connecting Arabia and Eurasia through a continuous band of continental lithosphere (Cowgill et al., 2016).

This hard collision initiated first in the western Greater Caucasus at ~5 Ma and is currently propagating east (Mumladze et al., 2015; Gunnels et al., 2021). The primary evidence for the initiation of collision in the western Greater Caucasus is low-temperature thermochronology which records rapid rock exhumation starting at ~5 Ma (Avdeev and Niemi, 2011; Vincent et al., 2020). The east-west diachronous nature of the transition from subduction to collision in the Caucasus is supported by seismic data, which show the lithosphere of the Caucasus Basin continuing to subduct beneath the eastern Greater Caucasus, while beneath the western Greater Caucasus the slab is missing, presumably having detached following the ~5 Ma initiation of collision (Mumladze et al., 2015; Gunnels et al., 2021).

Over the Cenozoic, the closure of multiple intervening ocean basins (similar to the Caucasus Basin) sutured together a series of microcontinents to form the core of the Arabia-Eurasia collision zone (the Anatolide-Tauride-Armenian block, Fig. 4.2; Cowgill et al., 2016). The sutures dividing the different accreted terranes within the collision zone may serve as weak lithosphere-scale discontinuities onto which deformation may localize (e.g., Avagyan et al., 2005; Cavazza et al., 2015; Gusmeo et al., 2021). One suture that has been interpreted as being tectonically reactivated in response to the initiation of hard continent-continent collision is the İzmir-Ankara-Erzincan-Sevan-Akera Suture (IAESA; Figs. 4.1 and 4.2; Cavazza et al., 2015; 2019). The IAESA is a well-mapped ophiolitic suture between the LCEP arc to the north and the Anatolide-Tauride-Armenian tectonic block to the south (Fig. 4.2). The IAESA suture closed in the Late Cretaceous or Paleogene,

and the two largest active faults in the region, the Pembak-Sevan Fault and Northeast Anatolian Fault, both follow the trace of the IAESA suture (Allen et al., 2004; Karakhanian et al., 2016). The existence of these active faults along the IAESA suture, along with sparse low-temperature thermochronology that potentially support a phase of Miocene exhumation near the faults (Cavazza et al., 2015; 2019), support the interpretation of the faults as examples of tectonic reactivation of a weak suture during the transition from subduction to collision (Allen et al., 2004; Cavazza et al., 2015; 2019). Similar weak sutures are not observed in the Greater Caucasus, presenting an opportunity to compare deformational responses in the upper and lower plates of a young collision zone that have contrasting inherited lithospheric structure.

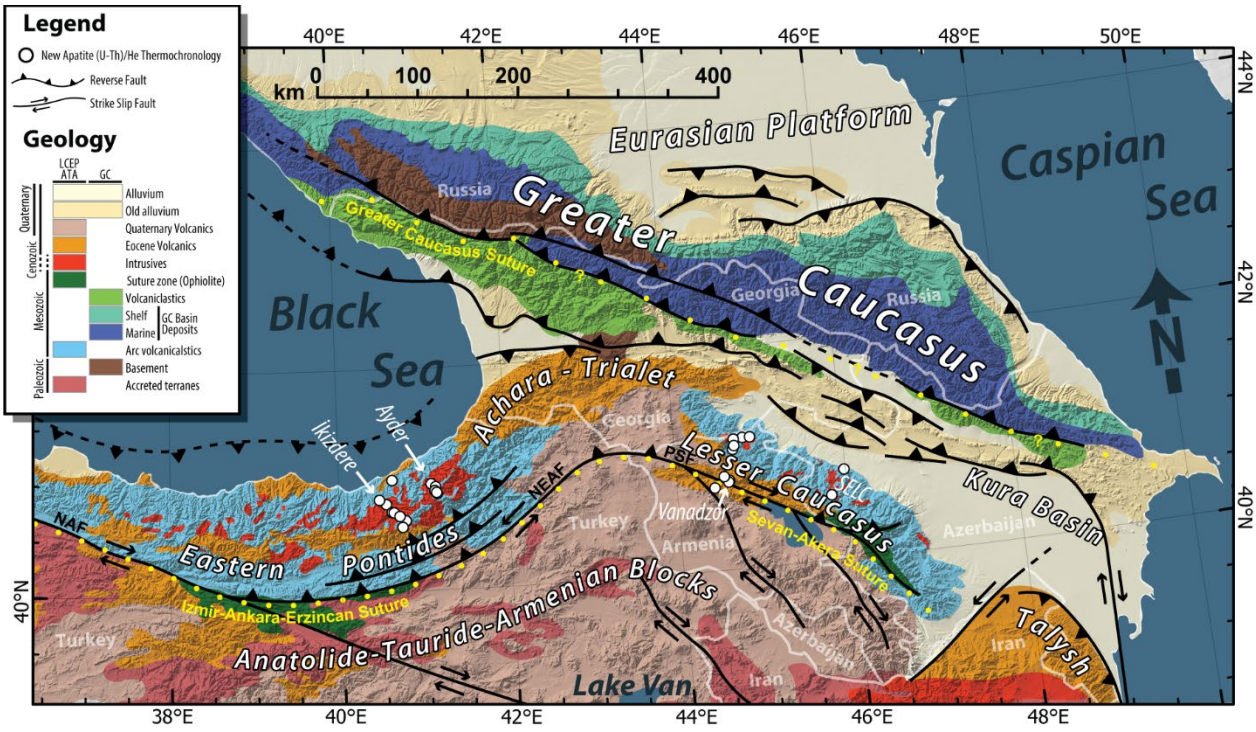


Figure 4.2: Regional geology of the Caucasus collision.
Simplified geologic map of the Caucasus region with major tectonic structures, geologic terrane names, and country borders. Note the continuity and similar geologic composition of the Eastern Pontides and Lesser Caucasus volcanic arcs, both a result of Jurassic to Cretaceous (?) north-directed subduction along the İzmir-Ankara-Erzincan and Sevan-Akera Sutures (i.e. the IAESA suture; Hässig et al., 2013). Geology compiled from Akdeniz and Güven (2002), Karakhanian et al. (2004), Cowgill et al. (2016), and Rolland et al. (2020). Some volcanic and intrusive rocks outside of the Lesser Caucasus and Eastern Pontides have been neglected for visual clarity. NAF=North Anatolian Fault, NEAF=Northeastern Anatolian Fault, PSF=Pembak-Sevan Fault, SELC=Southeastern Lesser Caucasus, LCEP/ATA=Lesser Caucasus-Eastern Pontides-Anatolide Tauride Armenian blocks, GC=Greater Caucasus.

4.2.2 Geology and Topography of the Lesser Caucasus and Eastern Pontides

The LCEP are a continuous mountain range that forms a topographic ramp between the high (1.5-2 km average elevation) Eastern Anatolian Plateau to the south and the low (approximately sea level) foreland of the Greater Caucasus orogen and Black Sea to the north (Fig. 4.1). Lithologically, the LCEP comprise the deformed remnants of an intra-oceanic volcanic arc formed during Jurassic to late Cretaceous north-directed subduction of Neo-Tethys (Yilmaz et al., 2000; Hässig et al., 2013; Meijers et al., 2015). This period of arc-volcanism is recorded in thick volcaniclastic marine sediments of Jurassic to Late Cretaceous age, punctuated by Jurassic and Cretaceous plutons (Fig. 4.2). Subduction beneath the LCEP ended in the Late Cretaceous, or possibly Paleogene, forming the ophiolitic İzmir-Ankara-Erzincan and Sevan-Akera sutures (IAESA, Figs. 4.1 and 4.2; Hässig et al., 2013).

All along the LCEP, Mesozoic arc-volcanic rocks are unconformably overlain by middle Eocene volcaniclastics and volcanics (Fig. 4.2) that may represent either arc or collision related volcanism in the Pontides (Arslan and Aliyazicioglu, 2001; Kandemir et al., 2019), back-arc extension in the Achara-Trialet (Adamia et al., 2010), and either arc, back-arc, or post-collisional volcanism in the Lesser Caucasus (Yilmaz et al., 2000; Sosson et al., 2010; Sahakyan et al., 2017; Sokół et al., 2018). In the Eastern Pontides, these middle Eocene volcanogenic rocks are locally overlain by upper Eocene to Miocene marine strata (Yilmaz et al., 2000), though the full extent of these marine deposits is not well established in Eastern Anatolia and the Lesser Caucasus. Potentially similar Miocene marine rocks deposited on the Eastern Anatolian Plateau near modern day Lake Van (Fig. 4.2) provide the most robust evidence that much of the uplift of Eastern Anatolia occurred after the middle Miocene (~11-12 Ma; Schildgen et al., 2014).

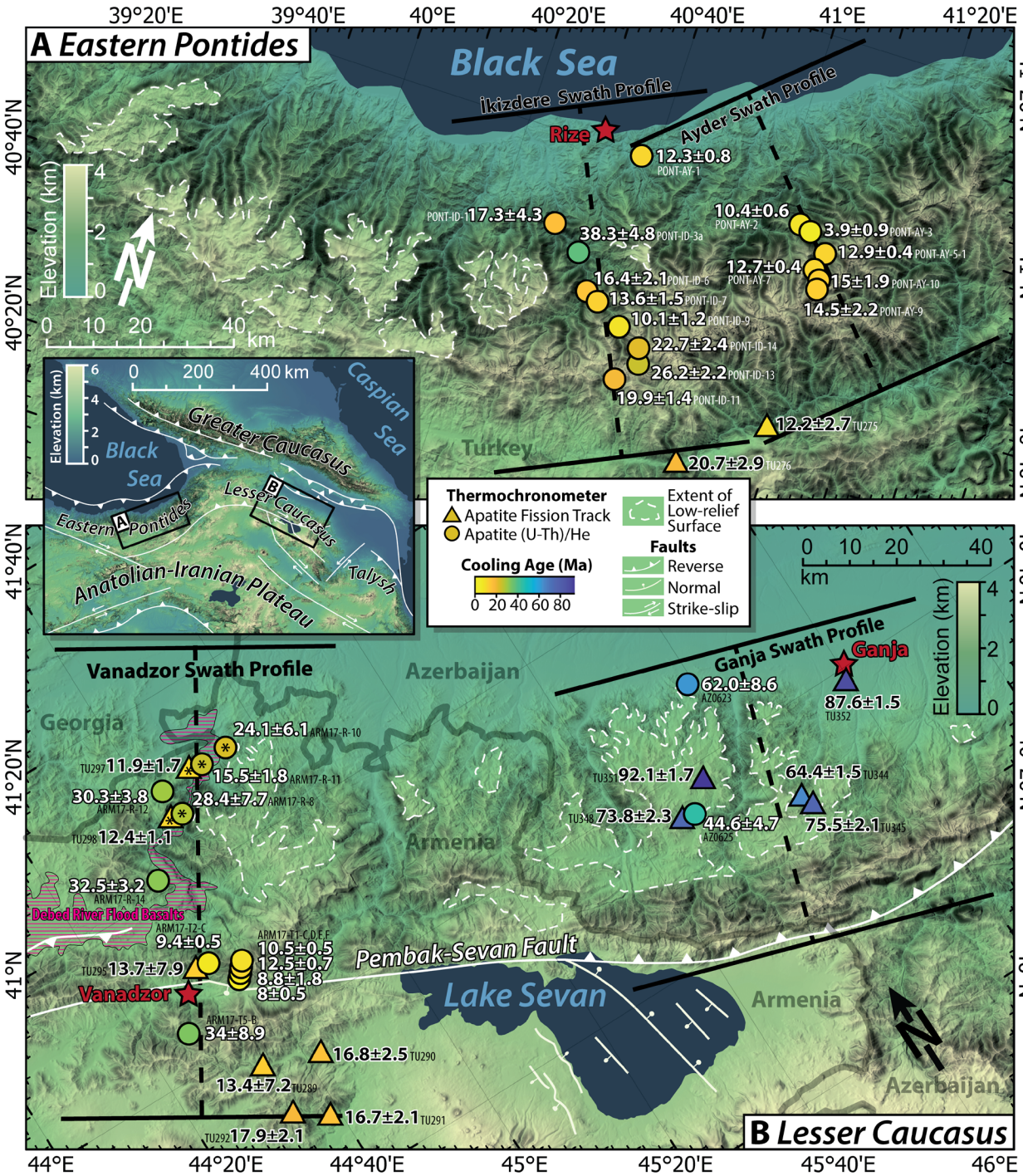


Figure 4.3: Lesser Caucasus and Pontides topography and thermochronology. *Enhanced shaded topographic maps of the Lesser Caucasus and Eastern Pontides showing major tectonic structures, the extent of elevated low relief surfaces, the locations of the topographic swath profiles shown in Figure 4.9, apatite (U-Th)/He cooling ages (Ma) from this study (Table 4.1), and compiled apatite fission-track analyses from Albino (2013), Albino et al. (2014), and Cavazza et al. (2015) (Table 4.2). The basemap is a combination of rasters derived from 30-meter resolution SRTM elevation data that are designed to visually enhance occurrences of the elevated low-relief surface. These rasters include an elevation raster, a hillshade raster, a slope raster that lightens shallow slopes, and a raster that brightens areas with low standard deviation of*

*elevation within a 1 km diameter moving circular window. Thermochronology marked with a * may be partially reset by Pliocene-Pleistocene flood basalts of the Debed River.*

The Eastern Anatolian Plateau and Lesser Caucasus experienced widespread, continuous, and increasingly alkaline volcanism from the Pliocene into the Quaternary, interpreted as a product of asthenospheric upwelling following collision related removal of mantle lithosphere (Dilek et al., 2010; Schleiffarth et al., 2018). In the Lesser Caucasus, Pliocene and Quaternary volcanism includes voluminous fissure eruptions of basalt that flowed out valleys in the Armenian and Georgian Lesser Caucasus, including 3.3-2 Ma valley-filling flood basalts of the Debed watershed in northwestern Armenia (left side of panel B in Fig. 4.3; Lebedev et al., 2007; Sheth et al., 2015; Trifonov et al., 2016).

The LCEP constitute the topographic margin of the Eastern Anatolian Plateau, with which it might share a similar history of uplift. However, the origin of post-middle Miocene uplift and nature of modern support of the 1.5-2 km average elevations of the Eastern Anatolian Plateau is not resolved. The uplift may have resulted from mantle lithosphere removal and corresponding asthenospheric inflow following the north to south foundering of the subducted northern Arabian plate from beneath the Anatolian lithosphere (Şengör et al., 2003; Göğüş and Pysklywec, 2008). Alternatively, a mantle plume source of uplift was proposed by Ershov and Nikishin (2004), described as an asthenospheric channel routing hot buoyant mantle from the African superplume into the Arabia-Eurasia collision zone. Whether one of these competing models for the origin of buoyancy in the Eastern Anatolian Plateau may also explain the elevation and tectonic history of the LCEP requires data constraining the structure and uplift history of the LCEP, data which are currently lacking.

Detailed study of the recent tectonic history and structure of the LCEP is hindered by relatively slow deformation rates (Reilinger et al., 2006; Karakhanyan et al., 2013), poor exposure beneath thick Neogene and Quaternary volcanic cover on the Eastern Anatolian Plateau, and inaccessibility of key field sites due to geopolitical conflict in the region, particularly along the disputed Armenian-Azerbaijani border (Fig. 4.2). The Eastern Pontides are generally understood to be situated above a north vergent thrust system, along with complex reverse faulting internal to the range (Fig. 4.2; Espurt et al., 2014; Softa et al., 2018). Both the Achara-Trialet and Talysh are mapped as containing

north vergent fold-thrust belts (Fig. 4.2; Vincent et al., 2005; Gusmeo et al., 2021). Between the Achara-Trialet and Talysh, the structure of the Lesser Caucasus is more uncertain, with the only confidently identified active structure being the oblique right-lateral and reverse Pembak-Sevan fault zone (Fig. 4.2; Philip et al., 2001; Karakhanian et al., 2004; Ritz et al., 2016). Other cryptic south vergent reverse faults are proposed to the north of the Pembak-Sevan fault, but evidence for these structures is mostly indirect, including sparse mapping and a cluster of young apatite fission-track cooling ages (Cavazza et al., 2015).

The geomorphic and thermochronologic analyses we present in this study clarify whether the LCEP deformed primarily through reverse or strike-slip faulting. If reverse faulting and folding were the primary modes of recent deformation within the LCEP, then the resulting crustal thickening could account for the high topography of the range. Alternatively, if strike-slip faulting accommodated most of the shortening across the range, then no crustal thickening would be implied, and other sources of support for the high topography of the LCEP would need to be considered.

In the remainder of the paper we will first present our geomorphic observations of an elevated low-relief surface, then describe our thermochronology results, and conclude by connecting both the geomorphology and thermochronology to constrain the recent tectonic history of the LCEP.

4.3 Geomorphic Observations of an Elevated Low-relief Surface

Initial examination of the LCEP in Google Earth revealed a series of elevated low-relief topographic surfaces throughout both mountain ranges (Fig. 4.4). The extent of these surfaces (Fig. 4.3) was mapped manually in ESRI ArcGIS Pro while referencing raster datasets including standard deviation of topography within a 1-km diameter circular moving window, hillshade, surface slope, and profile curvature, all derived from void-filled Shuttle-Radar-Topography-Mission (SRTM) elevation data with a 30 m resolution.

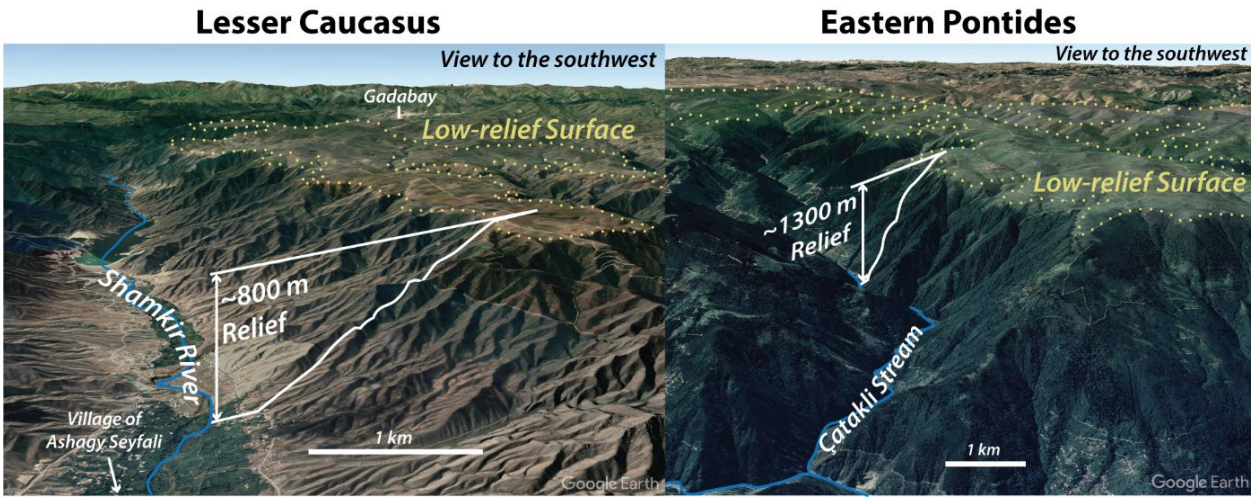


Figure 4.4: Low-relief surface in the Lesser Caucasus and Eastern Pontides. *Oblique Google Earth views of elevated low-relief surfaces in the Lesser Caucasus (left, approximately 40.7174°N, 46.0177°E) and the Eastern Pontides (right, approximately 40.6630°N, 40.1917°E). Both images have no elevation exaggeration. Imagery © 2021 Google Earth, CNES/Airbus, and Maxar Technologies.*

Swath profiles of topography (Fig. 4.5) were produced using MATLAB and TopoToolbox 2 (Schwanghart and Scherler, 2014). The locations of the swath profiles are shown in Fig. 4.3. The swath profiles show maximum, minimum, and mean elevations along the swath, in addition to a 2-D histogram that shows the distribution of elevations along the swath profile (Fig. 4.5). Some additional context was projected onto the swath profiles including modern and last glacial maximum equilibrium line altitudes (Sarıkaya et al., 2011; Forte et al., 2014; Reber et al., 2014), thermochronology samples (Table 4.1), the mapped extents of the elevated low-relief surface, and the tops of Pliocene-Pleistocene valley-filling flood basalts in the Debed watershed (Lebedev et al., 2007; Sheth et al., 2015; Trifonov et al., 2016).

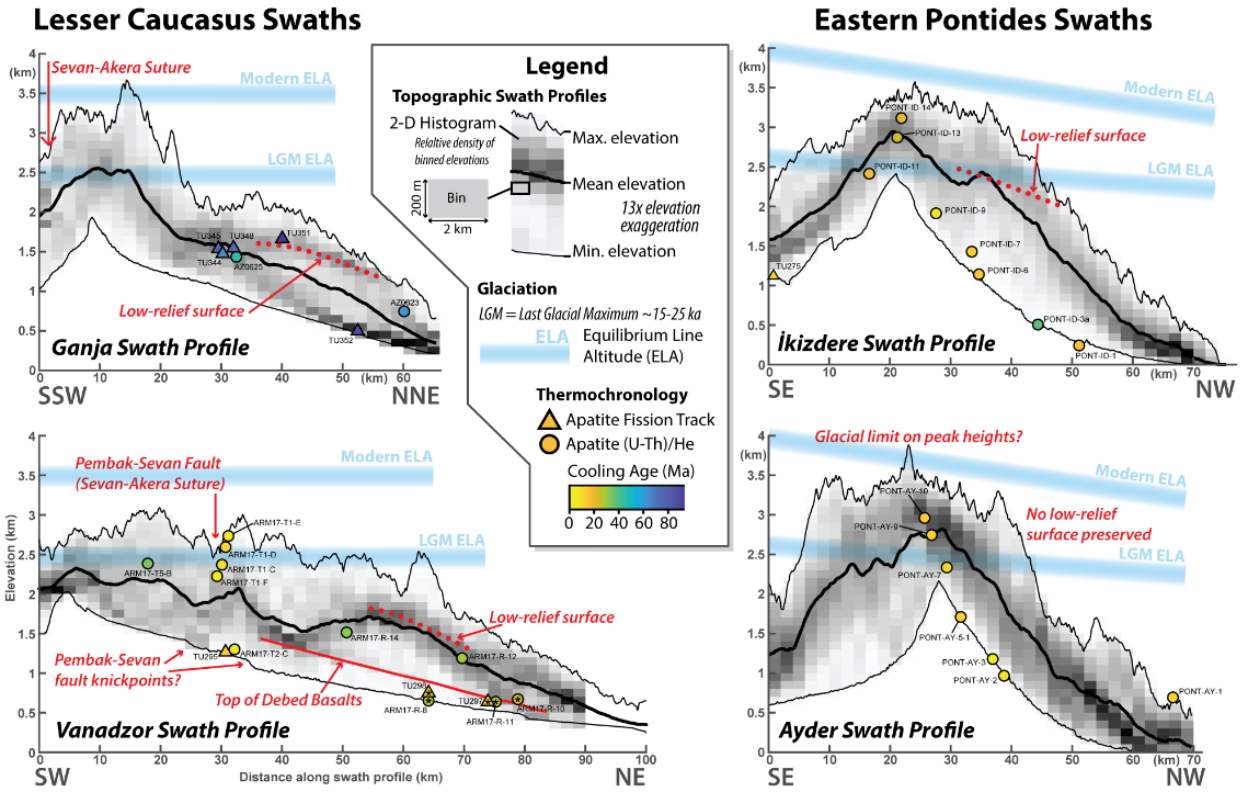


Figure 4.5: Elevation swath profiles in the Lesser Caucasus and Eastern Pontides. *Thermochronology samples, mapped low relief surfaces, and glacial equilibrium line altitudes (ELA) projected onto swath profiles of topography for two transects in the Lesser Caucasus and two transects in the Eastern Pontides. The geographic extent of each swath is shown in Fig. 4.3. All four plots share the same elevation to distance ratio of 13:1. Thermochronology samples marked with * are potentially reset by Pleistocene flood basalts of the Debed river (see text). Equilibrium line altitudes (ELA) approximated from Sarıkaya et al. (2011), Forte et al. (2014), and Reber et al. (2014). Note that the sloping ELAs in the Eastern Pontides are a result of steep range-perpendicular precipitation gradients that are not present in the Lesser Caucasus.*

4.3.1 Characteristics of the Elevated Low-Relief Surface

Mountainous topography can encode information about the local tectonic and climatic history (e.g., Wobus et al., 2006), especially when the topography preserves elevated relict landscapes (e.g., Clark et al., 2005; Calvet et al., 2015). We remotely mapped the extent of elevated low-relief surfaces throughout the LCEP (Fig. 4.3). In the Lesser Caucasus, incised remnants of the low-relief surface extend from almost the northern range front deep into the range, elevated between 600-1,000 m above the channels of the modern drainages (Figs. 4.3, 4.5, and 4.4). In the Eastern Pontides, remnants of the low-relief surface are smaller and higher than in the Lesser Caucasus,

elevated to more than a kilometer above the active channel. The low-relief surfaces in the Eastern Pontides are also less distinct in terms of topographic metrics like slope, standard deviation of elevation, and profile curvature (Fig. 4.3). Both surfaces gently tilt towards the range front (generally northward), away from the Eastern Anatolian Plateau (Fig. 4.5).

Additional differences between the mountainous topography of the Lesser Caucasus and Eastern Pontides are revealed when comparing the distributions of elevation (i.e. hypsometry) within each of the four swath profiles in Fig. 4.5. Each swath profile shows the distribution of elevations within rectangular swaths 60-80 km-wide running from the range front to at least the hydrologic divide of the range. The extent of each swath is shown on Fig. 4.3. Because the swaths capture whole watersheds, and the majority of streams in the LCEP run perpendicular to the trend of the ranges, the minimum elevation line on the profiles can be interpreted as an elevation profile of the largest channel within each swath.

The Ayder swath profile contains no preserved remnants of the low-relief surface that is exposed within the other swath profiles (Fig. 4.3). Therefore, the Ayder profile is relatively undisturbed, showing mean elevation monotonically increasing towards the range crest, a well-defined (unimodal) mean elevation, and constant ridge-channel relief along the northwest flank of the range (Fig. 4.5). In contrast, the Vanadzor, Ganja, and İkizdere swath profiles show deviations from the simple topography exhibited by the Ayder profile, reflecting the presence of the elevated low-relief surface (Fig. 4.5). The İkizdere swath profile is similar to the Ayder profile in overall shape, but shows changes in the distribution of elevations near the projected location of the low-relief surface (Fig. 4.5). The Vanadzor and Ganja swath profiles in the Lesser Caucasus show a bimodal distribution of elevations along their profiles (i.e. in their 2-D histograms of elevation), the upper peak representing the elevation of the low-relief surface, and the lower peak representing either the valley floors or the elevations of the tops of the flood basalts of the Debed watershed (Fig. 4.5). Both swath profiles from the Eastern Pontides are steeper compared to the profiles from the Lesser Caucasus (Fig. 4.5). This difference may result from differential tectonic uplift between the two ranges, but almost certainly also reflects climatic differences since the Eastern Pontides receive an order of magnitude more precipitation than the Lesser Caucasus, and therefore the Eastern Pontides presumably experience significantly faster erosion (Forte et al., 2014).

4.3.2 Age and Origin of Elevated Low-relief Topography in the Lesser Caucasus and Eastern Pontides

The existence of the observed elevated low-relief surface in both the Lesser Caucasus and Eastern Pontides suggests a disequilibrium landscape that has experienced limited rock uplift and erosion since the formation of the surface, though the age of the surface remains uncertain. Several possibilities for the origin of the surface can be considered. The low-relief surface may be erosional, beveled at regional base-level prior to being uplifted and incised.

The surface may reflect a strength difference in the sedimentary bedrock that compose the LCEP, wherein a weak unit is eroded from above a strong unit (e.g., Forte et al., 2016; Rosenkranz et al., 2017). This process could happen above base level, and therefore does not intrinsically imply any amount of surface uplift. Widely distributed Eocene volcaniclastics (Fig. 4.2) are a potential candidate for a weak overlying unit that may have been removed from above the stronger Mesozoic rocks that form the bedrock beneath much of the surface.

Alternatively, the surface may represent a continuation of the surface of the Eastern Anatolian Plateau, therefore sharing a similar uplift history and age with the plateau (Fig. 4.1). The small ranges and mountain peaks along the crest of the Pontides and Lesser Caucasus that divide the low-relief surface from the plateau may be products of strike-slip and reverse faulting along the Northeast Anatolian and Pembak-Sevan Faults (Figs. 4.2 and 4.3).

One constraint on the age of the low-relief surface in the Lesser Caucasus is the existence of the valley-filling flood basalts in the Debed watershed (pink shading on the left side of panel B in Fig. 4.3). The flood basalts were erupted from 3-2 Ma, based on K-Ar geochronology (Lebedev et al., 2007). The valley-filling nature of the basalt flows requires that the incised topography of the Lesser Caucasus existed prior to the eruption of the basalts, therefore implying that the elevated low-relief surface must have been uplifted prior to ~3 Ma. This age constraint, along with the fact that the surface is lower elevation than the last glacial maximum equilibrium line altitude in most places (Fig. 4.5), suggests that the low relief surface does not have a glacial origin.

The best maximum age constraint for the low-relief surface is the fact that it appears to cross-cut Eocene plutons in the Kaçkar batholith complex of the Eastern Pontides, and therefore post-dates the Eocene. In summary, the low-relief surface was eroded sometime after 40 Ma and uplifted prior to 3 Ma. More precise estimates for the age and origin of the elevated low-relief surface awaits additional field investigation of onlapping or cross-cutting relationships with units of known age.

4.4 (U-Th)/He Thermochronology Methods

To examine the relative role of strike-slip faulting and reverse faulting in the LCEP, we applied low-temperature thermochronology to infer the amount of exhumation at locations throughout the LCEP. Low-temperature thermochronology quantitatively tracks the cooling of rocks as they exhume through the upper 3-6 km of the crust, either through erosion of overlying rock or direct slip along faults. We applied (U-Th)/He thermochronology to bedrock samples collected from Eocene-Cretaceous igneous rocks and conducted modeling of the amount of rock exhumation allowed given the observed thermochronologic cooling ages. Because reverse faulting involves significantly more vertical uplift of rocks compared to strike-slip faulting, we would expect periods of significant reverse faulting to be accompanied by a clear cooling signal in the thermochronologic data, while strike-slip faulting would produce little to no erosional exhumation, and therefore no cooling signal in our thermochronologic data.

4.4.1 Sampling

We collected 28 bedrock samples from the LCEP arranged into three vertical transects and eight isolated spot samples (Fig. 4.3, Table 4.1). Two vertical transects were in the Eastern Pontides, the eight-sample İkizdere transect and the seven-sample Ayder transect (Fig. 4.3). One five-sample vertical transect was collected from the Armenian Lesser Caucasus near the town of Vanadzor (Fig. 4.3). All eight isolated spot samples were from the Armenian and Azerbaijani Lesser Caucasus (Fig. 4.3, Table 4.1).

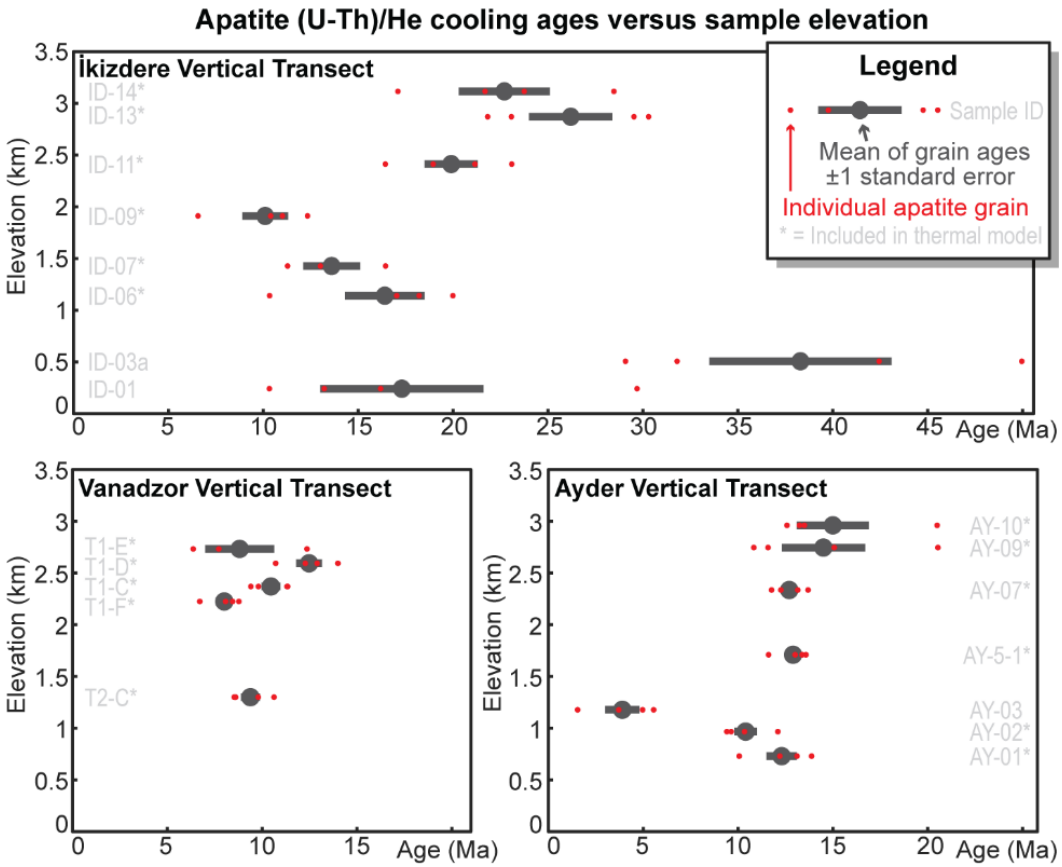


Figure 4.6: Thermochronologic cooling age versus elevation plots.
Plots of apatite (U-Th)/He cooling age versus sample elevation for the three elevation transects in this study (Table 4.1). Plots have identical horizontal scales to enable comparison of grain dispersion and age elevation relationships. Sample names in the İkizdere and Ayder vertical transects omit the "PONT-" prefix, and sample names in the Vanadzor transect omit the "ARM17-" prefix. The anomalously young cooling age of sample AY-03 may reflect resetting in a modern hydrothermal field (Temizel et al., 2020).

Table 4.1: Summary of (U-Th)/He samples and ages analyzed in this study.

Sample	Longitude (°)	Latitude (°)	Elevation (m)	(U-Th)/He Analysis				Notes	Thermal Model
				No. grains Apatite	Apatite Age (Ma, ± 1 S.E.)	No. grains Zircon	Zircon Age (Ma, ± 1 S.E.)		
AZ0623	45.984249	40.803329	746	5	62.0±8.6			Low eU*	Not modeled
AZ0625	45.810882	40.584	1460	5	44.6±4.7			Low eU*	SE L.C.[#]
ARM17-T5-B	44.445467	40.744938	2385	4	34±8.9			Low eU*	Not modeled
ARM17-R-8	44.711072	41.109865	660	2	28.4±7.7			Low eU*	Not modeled
ARM17-R-10	44.906847	41.175378	670	4	24.1±6.1			Low eU*	Not modeled
ARM17-R-11	44.818200	41.175927	645	3	15.5±1.8			Low eU*	Not modeled
ARM17-R-12	44.711710	41.167735	1189	4	30.3±3.8			Low eU*	Not modeled
ARM17-R-14	44.582913	41.026387	1515	4	32.5±3.2			Low eU*	Not modeled
ARM17-TI-C	44.618505	40.794313	2370	4	10.5±0.5				Vanadzor
ARM17-T1-D	44.624220	40.797917	2594	4	12.5±0.7				Vanadzor
ARM17-T1-E	44.625817	40.801991	2733	3	8.8±1.8				Vanadzor
ARM17-TI-F	44.613978	40.787981	2225	4	8±0.5				Vanadzor
ARM17-T2-C	44.566370	40.839930	1300	4	9.4±0.5				Vanadzor
PONT-ID-01	40.476187	40.827899	242	4	17.3±4.3			Low eU*	Not modeled
PONT-ID-03a	40.555193	40.788343	507	4	38.3±4.8			Low eU*	Not modeled
PONT-ID-06	40.620036	40.714737	1141	4	16.4±2.1				İkizdere
PONT-ID-07	40.643681	40.711493	1428	3	13.6±1.5				İkizdere
PONT-ID-09	40.710140	40.676306	1912	4	10.1±1.2				İkizdere
PONT-ID-11	40.739895	40.577834	2413	4	19.9±1.4				İkizdere
PONT-ID-13	40.780929	40.634446	2871	4	26.2±2.2				İkizdere
PONT-ID-14	40.776295	40.642967	3116	4	22.7±2.4				İkizdere
PONT-AY-01	40.632670	41.001750	730	4	12.3±0.8	3	36.7±0.4		Ayder
PONT-AY-02	41.079805	40.969434	967	4	10.4±0.6	3	59.7±15.6		Ayder
PONT-AY-03	41.094587	40.956989	1178	4	3.9±0.9				Not modeled
PONT-AY-5-1	41.147048	40.928911	1710	4	12.9±0.4				Ayder
PONT-AY-07	41.136885	40.894358	2336	4	12.7±0.4	3	35.6±1.7		Ayder
PONT-AY-09	41.156823	40.877791	2746	4	14.5±2.2	3	57.8±35.6		Ayder
PONT-AY-10	41.163161	40.867971	2961	4	15±1.9	3	38±0.2		Ayder

* Low eU means sample contains more than 1 grain with less than 10 eU

[#] Southeast Lesser Caucasus (Fig. 4.7)

Table 4.2: Summary of compiled apatite fission-track samples and ages.

				Fission Track					
Sample	Longitude	Latitude	Elevation	No. grains	Apatite Age	$P(\chi^2)$	Notes	Thermal Model	Data source
	(°)	(°)	(m)	Apatite	(Ma, ± 1σ)	(%)			
TU275	41.140619	40.582540	1055	20	12.2±2.7	80		Not modeled	Albino et al., 2014
TU276	40.949281	40.464175	1256	15	20.7±2.9	98		Not modeled	Albino et al., 2014
TU289	44.563942	40.620079	1889	6	13.4±7.2	34	Low P(χ2)	Not modeled	Albino, 2013
TU290	44.705622	40.583086	1846	17	16.8±2.5	99		Not modeled	Albino, 2013; Cavazza et al., 2015
TU291	44.643165	40.471127	1788	20	16.7±2.1	81		Not modeled	Albino, 2013; Cavazza et al., 2015
TU292	44.566126	40.512512	1923	20	17.9±2.1	96		Not modeled	Albino, 2013; Cavazza et al., 2015
TU295	44.564302	40.838900	1297	7	13.7±7.9	39	Low P(χ2)	Not modeled	Albino, 2013
TU297	44.818128	41.175748	665	21	11.9±1.7	99		Not modeled	Albino, 2013; Cavazza et al., 2015
TU298	44.709722	41.110479	665	20	12.4±1.1	100		Not modeled	Albino, 2013; Cavazza et al., 2015
TU344	46.078600	40.497662	1438	20	64.4±1.5	100		Not modeled	Cavazza et al., 2015
TU345	46.087378	40.489472	1545	20	75.5±2.1	98		Not modeled	Cavazza et al., 2015
TU348	45.801947	40.581632	1539	18	73.8±2.3	100		SE L.C.[#]	Cavazza et al., 2015
TU351	45.890056	40.636715	1677	21	92.1±1.7	90		Not modeled	Cavazza et al., 2015
TU352	46.327211	40.646652	507	20	87.6±1.5	88		Not modeled	Cavazza et al., 2015

[#] Southeast Lesser Caucasus (Fig. 4.7)

The Ayder and İkizdere vertical transects in the Eastern Pontides were both collected from medium- to coarse-grained plutonic rocks in the Kaçkar Mountains. These plutonic rocks are predominantly Late Mezosoic to early Cenozoic intrusions of the composite Kaçkar batholithic complex, which consists of at least ten distinct emplacement phases, the youngest of which is Eocene (Boztuğ et al., 2007).

The 7-sample Ayder transect consists of 6 samples collected from the northwest flank of the Eastern Pontides near the resort of Ayder, along the Kavran Creek in the Aden River watershed, and 1 sample near the town of Rize (Fig. 4.3). Regional geologic maps indicate that samples of the Ayder transect (PONT-AY prefix in Table 4.1) were collected from a silicic intrusion of Eocene age (~46 Ma, as based on a titanite fission-track age determination; Boztuğ et al., 2007).

The 8-sample İkizdere transect consists of 6 samples collected from the northwest flank of the Eastern Pontides along the İkizdere River, and 2 samples collected from the southeast flank of the range (Fig. 4.3). Samples of the İkizdere transect (PONT-ID prefix in Table 4.1) were collected from a Late Cretaceous granitoid, based on a 72 Ma zircon U-Pb age determination (Karslı et al., 2010) and a 71 Ma K-Ar isochron (Taner et al., 1979).

We collected 6 bedrock samples from the eastern footwall of the Vanadzor pull-apart basin, which is located along a major releasing bend of the Pembak-Sevan fault (Fig. 4.3; Karakhanian et al., 2004; Avagyan, 2007). All six samples came from Eocene volcanic and intrusive rocks in the vicinity of the ~41 Ma Tezhsar volcanic complex (Sokół et al., 2018). Only 4 of the 6 samples from the Vanadzor transect produced sufficient apatite for (U-Th)/He analysis, and the resulting samples only spanned approximately 500 m of elevation, less than the 1-2 km typically used in elevation transects. Combining these samples with a single successful apatite (U-Th)/He analysis from the nearby Pembak river valley (sample ARM17-T2-C), which was collected from the same footwall rocks of the Vanadzor pull-apart basin, created a five-sample vertical transect spanning a total of 1,433 m (Fig. 4.3).

4.4.2 Apatite and Zircon (U-Th)/He Analytical Procedure

All 28 bedrock samples in our study were analyzed using the apatite (U-Th)/He thermochronometer, which records the time since a sample cooled below 40-70 °C, temperatures found at 1-3 km depths assuming typical continental geothermal gradients

(Farley, 2002). A subset of five samples were also analyzed using the higher temperature zircon (U-Th)/He thermochronometer which tracks the time since a sample cooled below 180-200 °C, temperatures which translate to 5-8 km depths assuming typical continental geothermal gradients (Reiners et al., 2002).

To produce concentrated separates of apatite and zircon, whole rock samples were crushed, pulverized, and sieved before undergoing standard magnetic and heavy liquid mineral separation techniques. Individual grains were hand-picked from separates under a microscope, checked for inclusions, and analyzed for He concentration on an Alphachron instrument at the University of Michigan thermochronology lab following the procedures in Niemi and Clark (2018). After degassing, grains were analyzed for their U, Th, and Sm concentrations at the University of Arizona following the procedures in Reiners and Nicolescu (2006). Two grains selected as outliers by the Dean and Dixon Q-test (Dean and Dixon, 1951) were not included in the remaining analyses, and are noted in Table A.1.

4.4.3 Inverse Thermal Modeling in QTQt

We produced 4 inverse models of allowable time-temperature paths from our data, one for each of our three vertical transects (Ayder, İkizdere, and Vanadzor), and a single-sample model using both apatite (U-Th)/He and apatite fission-track ages from the southeastern Lesser Caucasus (samples AZ0625 and TU348, Fig. 4.7; Table 4.1). Inverse modeling was performed using the software QTQt (version R5.8.0 for Mac), which allows for simultaneous inversion of multiple samples and multiple thermochronometers for a suite of allowable time-temperature histories (Gallagher, 2012). For the purposes of thermal modeling, we assumed a geothermal gradient of 30±10 °C/km. Below we will discuss issues arising from the high sensitivity of our thermal models to the selected geothermal gradient. The only time-temperature constraint placed on models was to initiate cooling from 300-350 °C at the approximate emplacement age of the sampled pluton. Some samples were excluded from modeling due to potential resetting or low uranium concentrations, as described in the thermochronology results section below.

We assessed the impact of incorporating radiation damage models during our analysis (e.g., RDAAM, Flowers et al., 2009), but found that the inclusion of such models did not affect our thermal modeling results; therefore, the thermal modeling results we

present here do not apply a radiation damage model. We note this specifically here because of an age-eU (eU = [U] + 0.235*[Th]) relationship that can be observed in our data, and because such age-eU relationships are often interpreted and modeled as reflecting the effects of radiation damage on diffusion kinetics and thus sample age (e.g., Shuster et al., 2006; Willett et al., 2017). As discussed in greater detail below, we find that there are compelling reasons to interpret the age-eU relationship in our samples as resulting from helium implantation at low uranium concentrations (e.g., Spiegel et al., 2009), not as arising from modified diffusion kinetics due to radiation damage.

4.5 (U-Th)/He Thermochronology Results

Low-temperature thermochronologic cooling ages from the LCEP span the Mesozoic to the late Miocene (Table 4.1, Fig. 4.3). Samples from the northwestern Lesser Caucasus (Fig. 4.3) show a bimodal distribution of cooling ages, with one cluster around 9 Ma and another spanning approximately 25-35 Ma. Cooling ages from the southeastern Lesser Caucasus (Fig. 4.3) are distinctly older, with apatite (U-Th)/He and fission-track ages ranging from Eocene to Cretaceous. Samples from the Eastern Pontides (Fig. 4.3) show a largely unimodal distribution of cooling ages, centered around 13.5 Ma.

İkizdere and Ayder vertical transects.

Apatite (U-Th)/He cooling ages in the İkizdere elevation transect span from 10.1 Ma to 38.3 Ma and display a complex age-elevation relationship (Table 4.1; Fig. 4.6). Apatite (U-Th)/He cooling ages from the Ayder elevation transect range are tightly clustered between 10.3 Ma to 15.0 Ma, and display a typical age-elevation relationship, with the exception of the 3.9 Ma age of sample PONT-AY-03 (Table 4.1). This sample was collected near the Ayder geothermal field, which produces 55°C water from <200 m depths (Şimşek and Demir, 1991; Temizel et al., 2020); as such, we infer this age to have been reset by hydrothermal process (e.g., Berger et al., 2022). Both transects broadly have older cooling ages at higher elevations, as expected, but they also exhibit complex age-elevation relationships that may reflect sampling across unmapped faults, possible partial resetting due to volcanic or hydrothermal heating, and large grain-age dispersion. We will return to discuss how low uranium content may explain some of the grain-age variability observed, particularly in the İkizdere samples.

Five zircon (U-Th)/He analyses from the Ayder transect produced Eocene cooling ages indistinguishable from the emplacement age of the plutonic rocks from which they were sampled (Table 4.1), and therefore likely record rapid cooling to ambient temperatures immediately after emplacement, as opposed to post-emplacement tectonic exhumation through the zircon (U-Th)/He partial retention zone.

Vanadzor vertical transect and Armenian-Azerbaijani Lesser Caucasus.

Cooling ages in the Vanadzor elevation transect are generally invariant with elevation, ranging from 8.0±0.5 Ma to 12.5±0.7 Ma (Fig. 4.5). The Vanadzor transect was collected in Eocene volcanic and intrusive rocks exhumed in the footwall of a normal fault that bounds the Vanadzor depression, a pull-apart basin along the trace of the active Pembak-Sevan fault (Karakhanian et al., 2004). The active strands of the Pembak-Sevan fault are complex and anastamosing through the Vanadzor depression, but the exhumed pull-apart footwall is generally considered to be structurally intact (e.g., Avagyan, 2009). Provided that this is the case, the overall invariance of the Vanadzor cooling ages with elevation does suggest a phase of relatively rapid cooling at approximately 12-8 Ma, an inference that is supported by inverse thermal history modeling (Fig. 4.7).

Thermochronology in the Lesser Caucasus north of the Pembak-Sevan Fault.

In addition to the five analyses of the Vanadzor vertical transect, we analyzed seven apatite (U-Th)/He ages from the northern slope of the Lesser Caucasus range. The southeasternmost bedrock samples were AZ0623 and AZ0625 (Table 4.1, Fig. 4.3), collected in the vicinity of the villages of Shamkir and Gadabay in Azerbaijan. AZ0623 and AZ0625 produced ages of 62.0±8.6 Ma and 44.7±4.9 Ma respectively, in excellent agreement with five apatite fission-track samples from the same area, which range from 92-64 Ma (Cavazza et al., 2015; Table 4.1, Fig. 4.3).

We also analyzed five apatite (U-Th)/He samples collected from the Debed river watershed in Armenia (Fig. 4.3). The Debed river is the largest drainage in the Lesser Caucasus mountains, and the only Lesser Caucasus watershed that crosses the crest of the range to drain a significant portion of the high Armenian plateau south of the Pembak-Sevan fault (Fig. 4.3). Previous apatite fission-track studies of tectonic exhumation in the Lesser Caucasus targeted the rocks exposed along the Debed river, and several middle Miocene cooling ages were interpreted as evidence for Miocene tectonic reactivation of

the Pembak-Sevan suture zone (e.g., Albino, 2013; Cavazza et al., 2015; 2019). As noted above, the Debed River canyon is also known for exposures of intracanyon basalt flows that are sourced from a Pliocene-Pleistocene continental flood basalt province in Armenia (Fig. 4.3; Lebedev et al., 2007; Sheth et al., 2015; Trifonov et al., 2016).

We returned to the previously sampled locations for apatite fission-track ages (Albino, 2013; Cavazza et al., 2015; 2019) and found that samples TU297 and TU298, which yielded the youngest fission-track ages, were collected from silicic igneous bedrock exposures directly below the Plio-Pleistocene valley-filling flood basalts (Fig. 4.5; Lebedev et al., 2007; Sheth et al., 2015; Trifonov et al., 2016). Since the young ages from these samples feature prominently in interpretations of the Late Cenozoic tectonic activity of the northwestern Lesser Caucasus, we evaluated the possibility that the emplacement of the intracanyon basalt flows may have partially reset the fission-track ages in the rocks sampled by Albino (2013) and Cavazza et al. (2015, 2019) either through direct thermal conduction or by driving hydrothermal circulation in the rocks underlying the basalt flows (e.g., Abbey et al., 2018; Berger et al., 2022).

We resampled at the locations of samples TU297 and TU298 and obtained apatite (U-Th)/He ages on the new samples (ARM17-R-11 and ARM17-R-8 respectively, Table 4.1). Both samples produced older cooling ages (28.4±7.7 Ma and 15.5±1.8 Ma) than the corresponding apatite fission-track analyses (11.9±1.7 Ma and 12.4±1.1 Ma; Cavazza et al., 2015). This type of inversion between fission-track and helium thermochronology cooling ages has been shown to occur when a sample is subject to high temperature and short duration reheating, as might be expected from volcanic reheating (e.g., Reiners et al., 2007). Samples ARM17-R-11 and ARM17-R-8 both also have marked individual age grain dispersion, another potential indicator of partial resetting.

To further assess the potential role of volcanically-driven resetting of bedrock along the Debed River valley bottom, we collected samples ARM17-R-12 and ARM17-R-14 (Table 4.1) from higher in the Debed river valley, sufficiently above the elevation of the highest Pliocene-Pleistocene basalt flows that the samples were unlikely to have been thermally reset. Sample ARM17-R-12 was collected from an outcrop of what appeared to be Mesozoic marine sedimentary rock, but in an area mapped as having extensive Eocene age plutonism, and ARM17-R-14 was collected from Eocene volcanic rocks. These samples produced apatite (U-Th)/He ages of 30.3±3.8 Ma and 32.5±3.2 Ma (Table 4.1),

similar to the depositional age of ARM17-R-14, and similar to the timing of plutonism around sample ARM17-R-12.

That the two samples from above the Debed basalt flows yielded older, more reproducible, and overlapping cooling ages, as compared to samples from near the valley floor, supports our concern that volcanic reheating may have reset low-temperature thermochronometers along the Debed River canyon. The nature of the cooling ages from above the Debed basalts, from single samples to which only the apatite (U-Th)/He system was applied, and for which there are copious low-eU grains, limits our ability to draw detailed cooling information from these data. However, we do feel that we can now assert that there is no evidence for tectonically-driven Miocene or younger exhumation, and that cooling ages from the northern flank of the Lesser Caucasus are consistently older than ~30 Ma.

Spatial relationship between thermochronology and the low-relief surface

Many of the thermochronology samples collected within the LCEP, both from this study and previous studies (Albino, 2013; Cavazza et al., 2015; 2019), were collected in close proximity to the low-relief surfaces exposed in both the Lesser Caucasus and Eastern Pontides (Figs. 4.3 and 4.5). Therefore, any explanation for the origin and age of these low-relief surfaces must be compatible with the exhumation and erosion history implied by the thermochronology. In the Lesser Caucasus, ignoring samples likely reset by Pliocene-Pleistocene flood basalts of the Debed River (potentially affected samples are marked with an * in Figs. 4.3 and 4.5), the youngest cooling ages sampled directly below the low relief surface are Oligocene (ARM17-R-12, 30.3±3.8 Ma, and ARM17-R-14, 32.5±3.2 Ma; Figs. 4.3 and 4.5). Farther southeast along the Lesser Caucasus, the low-relief surface is in close association with even older cooling ages (~62-45 Ma apatite (U-Th)/He, and ~92-64 Ma apatite fission-track; Figs. 4.3 and 4.5).

4.5.2 Potential Helium Implantation and Quality of the Apatite (U-Th)/He Thermochronology

The concentration of radioactive parent nuclides in an apatite crystal, or eU (effective uranium concentration, which is calculated as eU = [U] + 0.235*[Th]), is a key parameter in the interpretation of (U-Th)/He cooling ages. High eU can cause radiation

damage to the crystal that modifies helium diffusivity, changing the effective closure temperature of the crystal (Willett et al., 2017). Conversely, very low eU can make a crystal vulnerable to helium implantation, a process by which an apatite accumulates helium produced by radioactive decay from neighboring minerals, skewing the cooling age of that apatite older than it would otherwise be (Spiegel et al., 2008).

Many of the apatite grains we sampled from across the LCEP exhibit low eU, with several samples containing apatite grains with no more than 10 ppm eU (Fig. 4.8, Table 4.1). To check for the effects of radiation damage and implantation in our apatite (U-Th)/He data, we plotted cooling ages against eU (Fig. 4.8). Individual grain ages increase significantly below ~15 ppm eU, and the spread in grain ages within a sample (i.e. the standard deviation of grain ages within a sample, Fig. 9A) increases below ~15 ppm eU. Both the increase in grain age and increase in intra-sample grain-age variance below ~15 ppm eU point towards helium implantation potentially skewing low eU grains older than they would otherwise be, reducing the reproducibility of our (U-Th)/he cooling ages (e.g., Spiegel et al., 2008).

Excluding grains with less than 15 ppm eU from further analysis would eliminate over 40% of our grains, severely impacting our ability to model thermal histories using our samples. Additionally, with the sparse geologic mapping in the LCEP, we are unable to eliminate the possibility that some of the relationship between age and eU is reflecting systematic differences in the cooling histories of rock units with different eU content. In light of these considerations, we only eliminated grains flagged as outliers by the Dean and Dixon Q-test (2 eliminated grains are listed in Table A.1; Dean and Dixon, 1951), and opted to leave all other grains in our thermal modeling. Our modeling approach does propagate larger uncertainties for samples with large grain dispersion (potentially caused by low eU) to the resulting thermal history models by using larger uncertainties on these cooling ages during the model inversion. Therefore excessive dispersion caused by low eU in may of our samples is potentially the primary source of uncertainty in our modeled thermal histories.

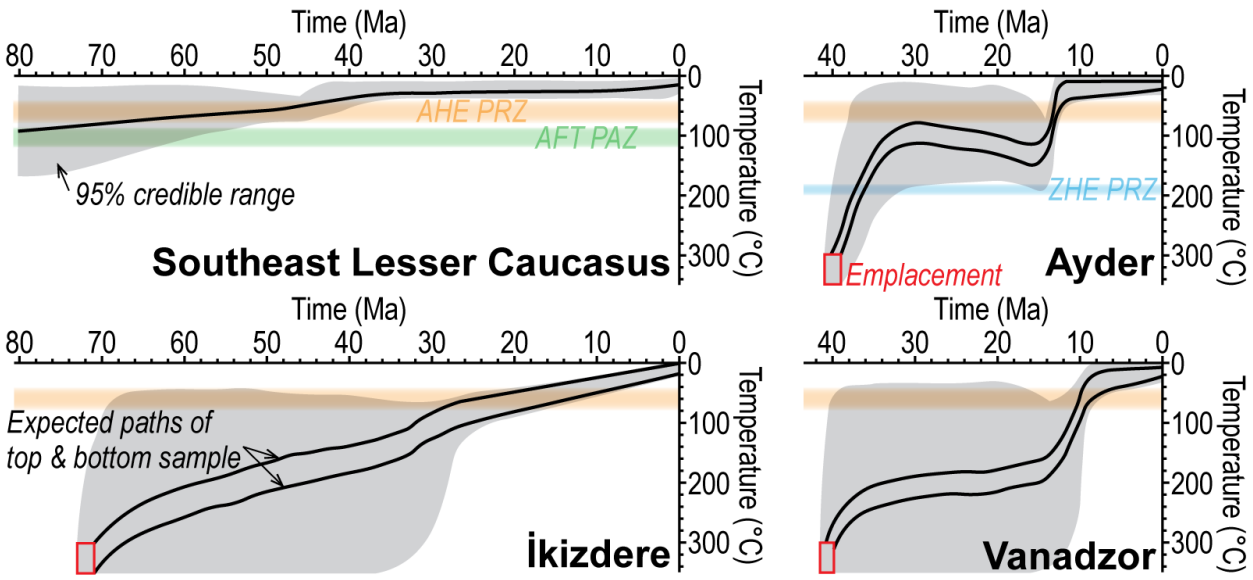


Figure 4.7: Modeled thermal histories in the Lesser Caucasus and Eastern Pontides. *Modeled time-temperature thermal histories for the Ayder, İkizdere, and Vanadzor elevation transects, as well as a time-temperature history for samples AZ0625 and TU348 (Southeast Lesser Caucasus; Fig. 4.3), which were collected within 800 meters of each other (Table 4.1). All four models assume a 30±10 °C/km geothermal gradient. Age-elevation plots for the three vertical transects are shown in Figure 4.5. The horizontal yellow, green, and blue bars show the temperature ranges over which the indicated thermochronometers (AHE=apatite-helium, ZHE=zircon-helium, and AFT=apatite fission-track) transition from open to closed, commonly referred to as partial annealing zones (PAZ) and partial retention zones (PRZ)(e.g., Wolf et al., 1998). Caution should be taken when interpreting these modeled histories, as many samples have low eU grains (Figs. 4.9 and 4.8, see text).*

4.5.3 Thermal Histories Produced by Inverse Modeling of Thermochronology

All four inverse thermal history models described below used the following parameters: a 30±10 °C/km geothermal gradient (i.e. paleo-thermal separation), a 10±5 °C/km atmospheric lapse rate (i.e. modern thermal separation), no radiation damage model (e.g., RDAAM; Flowers et al., 2009), and a model run of 10,000 burn-in iterations followed by 40,000 retained posterior samples. As is typical in thermal history modeling with QTQt, all models were allowed to resample the uncertainties on the cooling ages to allow for larger and more realistic grain-age uncertainty than those implied by the analytical error alone from the helium based thermochronology (e.g., McDowell et al., 2005; Niemi and Clark, 2017).

Ayder Elevation Transect

The inverse thermal history model for the Ayder transect was constrained to initiate at >300 ºC at 41-39 Ma (Fig. 4.7). The model incorporates six samples, all of which had apatite (U-Th)/He cooling ages, and five of which also had zircon (U-Th)/He ages (Table 4.1). The resulting model shows a single well-defined rapid cooling event in the middle Miocene (Fig. 4.7). Because the zircon (U-Th)/He ages are indistinguishable from the emplacement age of the pluton, the model requires cooling paths to stay below ~180 ºC after emplacement. The model indicates a pulse of cooling from 180 ºC to 30 ºC between ~15 and 12 Ma. The samples then remained below 40 ºC from ~12 Ma to the present.

İkizdere Elevation Transect

The inverse thermal history model for the İkizdere transect was constrained to initiate at >300 ºC at 72-70 Ma (Fig. 4.7). The model incorporates six samples with only apatite (U-Th)/He cooling ages (Table 4.1). The resulting model shows an overall poorly constrained thermal history characterized by slow continuous cooling (Fig. 4.7). From emplacement at ~71 Ma until ~30 Ma, the cooling paths are unconstrained. The model then shows a phase of slow cooling from ~100 ºC to 30 ºC from 30 Ma to present (Fig. 4.7). This slow cooling is necessitated by the large increase in cooling age from the bottom to the top of the İkizdere elevation transect (Fig. 4.6). Within its 95% credible interval, the İkizdere thermal model is unable to distinguish whether the samples cooled at a constant rate since emplacement or experienced a shorter pulsed phase of cooling in the Oligocene.

Vanadzor Elevation Transect

The inverse thermal history model for the Vanadzor transect was constrained to initiate at >300 ºC at 41-40 Ma (Fig. 4.7). The model incorporates five samples with only apatite (U-Th)/He cooling ages (Table 4.1). In testing, inclusion of nearby sample TU295 (13.7±7.9 Ma; Albino, 2013) did not affect the resulting modeled thermal history, likely due to the very low P(χ2) and correspondingly large age uncertainty for the sample (Table 4.2; Fig. 4.3). The resulting model for the Vanadzor transect shows a three-phase history (Fig. 4.7). From emplacement at ~40 Ma to ~14 Ma, the cooling history is unconstrained.

Then the model indicates a pulse of at least 30 °C of cooling from ~14-9 Ma. The samples then remain below 40 °C from ~9 Ma to the present.

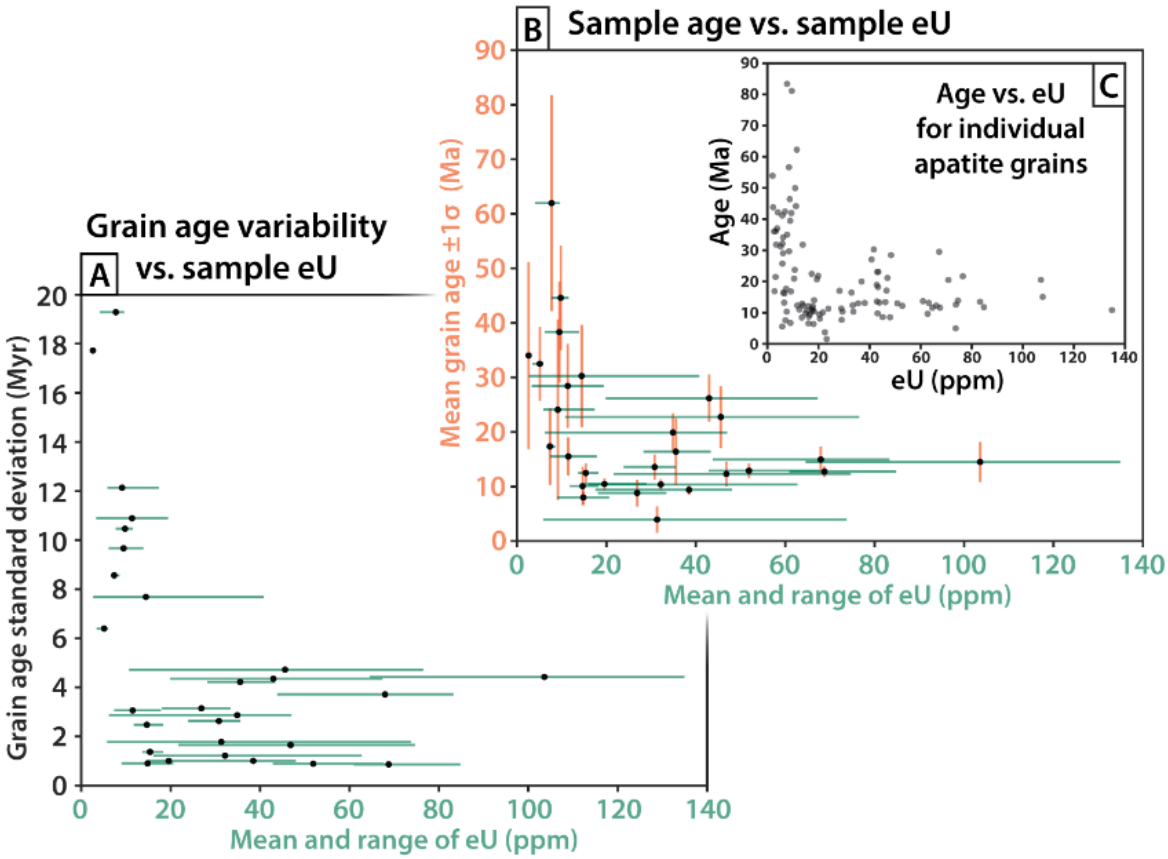


Figure 4.8: Age versus eU relationships in the apatite thermochronology.
Plots of apatite (U-Th)/He cooling age versus eU. Bottom left: Standard deviation of single-grain ages within a sample plotted against the mean and range of eU in each sample. Most samples contain 4 individual grains. Top right outer: Plot of mean grain age versus mean eU in each sample. Vertical error bars are the standard deviation of grain ages, and horizontal error bars are the range of observed eU in each sample. Top right inset: A plot of the single-grain data that underpins the other two plots; individual apatite (U-Th)/He analyses from this study plotted against their eU content (n=109). Two individual grains flagged as outliers by the Dean and Dixon Q test (P<0.05; Dean and Dixon, 1951) were excluded from the plots (57.6 Ma and 103.1 Ma; Table A.1).

Southeast Lesser Caucasus Samples

The inverse thermal history model for the southeast Lesser Caucasus had no emplacement constraint (Fig. 4.7). The model combines two samples that were collected within 0.5 km of one another: our apatite (U-Th)/He sample AZ0625 (44.7±4.9 Ma; Table 4.1) and apatite fission-track sample TU348 (73.8±2.3 Ma; Cavazza et al., 2015; Table

4.2). Modeling both ages as a single sample (i.e. without any thermal separation between the two ages), the resulting thermal history shows a simple history of limited exhumation since the Cretaceous, remaining below 100 °C since ~60 Ma, and below 40 °C since 38 Ma (Fig. 4.7).

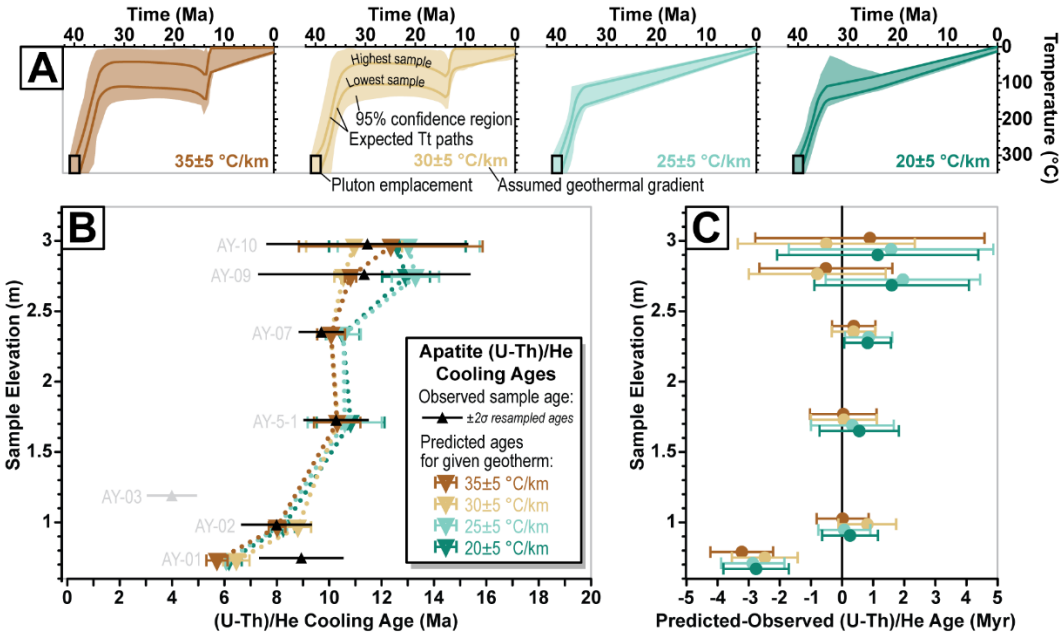


Figure 4.9: Tests of thermal model sensitivity to geothermal gradient.
Plots of time-temperature paths and model misfits for four thermal history models of six thermochronology samples in the Ayder elevation transect. Modeled time-temperature (Tt) paths exhibit a dependence on assumed geothermal gradient. Models were produced in the thermochronology inverse modeling program QTQt (Gallagher, 2012) and all horizontal error bars represent 95% credible ranges with the exception of observed ages in panel B. A: Time-temperature histories modeled using four different assumed geothermal gradients. Assuming a geotherm of 25±5 °C/km or less results in QTQt converging on a slower linear cooling history, while steeper geothermal gradients produce pulsed cooling histories. B: Plot of sample age versus sample elevation for the Ayder (PONT-AY) elevation transect, showing both observed ages and predicted ages for each of the models shown in panel A. Sample PONT-AY-03 was omitted from modeling due to possible later resetting in a hydrothermal field (Temizel et al., 2020). Sample names omit the "PONT-" prefix. C: Residual plot of the predicted cooling ages from panel B.

4.5.4 Sensitivity of Thermochronology Modeling to Geothermal Gradient

Low uranium content, slow overall tectonic rates, and uncertain geothermal gradients within the LCEP result in significant uncertainty around the precise interpretation of our helium thermochronology data. Our selection of a geothermal

gradient when inverse modeling time-temperature histories in QTQt has a significant effect on the resulting modeled thermal histories by controlling whether models favor pulsed or gradual cooling (Fig. 4.9). Little independent data is available to constrain the geothermal gradient in the LCEP region, with modern estimates ranging from 25-75 °C/km (Tezcan, 1995; Bektaş et al., 2007; Aydemir et al., 2020).

We performed sensitivity testing using the 6-sample Ayder elevation transect, which had the least grain-age dispersion, highest eU (and therefore least influence from helium implantation), and both zircon and apatite (U-Th)/He cooling ages (Table 4.1). As with previously described thermal modeling, sample PONT-AY-03 was excluded for potentially being thermally reset. Holding all parameters constant except for geothermal gradient, which varied between 20 °C/km and 35 °C/km, we observed that at geothermal gradients of 25±5 °C/km or less, QTQt preferred slower linear cooling histories. At geothermal gradients of 30±5 °C/km or more, QTQt preferred pulsed cooling histories (Fig. 4.9). The misfits between the predicted and observed cooling ages for all four models are almost identical (Fig. 4.9), with neither straight-line cooling nor pulsed cooling providing a better fit to the data.

Ideally, we would be able to clearly distinguish whether our samples experienced steady cooling, which might represent continuous background erosion, versus a pulsed cooling event, which is more likely to represent a phase of tectonically driven uplift. Because of the above described sensitivity to geothermal gradient, we urge caution when interpreting our modeled time-temperature histories, and emphasize the importance of corroborating our results with additional independent datasets from the region in the future. It may not be unrealistic to assume that typical geothermal gradients in the LCEP and Eastern Anatolian Plateau were at least 30 °C/km given the history of mantle lithosphere delamination and volcanism over the region since at least the Miocene (Dilek et al., 2010; Lebedev et al., 2007; Sheth et al., 2015; Trifonov et al., 2016; Schleiffarth et al., 2018).

4.5.5 Interpretations from Thermochronology Modeling

Evaluating our thermal modeling in terms of what time-temperature histories are prohibited by the data provides more robust interpretations than what we can infer about the rate of cooling through time. All four thermal models provide robust limits on the

magnitude of recent of cooling, unanimously excluding the possibility of more than 40 °C of cooling since ~10 Ma. This implies that since ~10 Ma, the samples remained in the shallow subsurface (<1.3 km deep assuming a 30 °C/km geothermal gradient), and therefore were not subject to significant rock exhumation.

Additionally, by assuming that geothermal gradients around the LCEP were 30 °C/km or higher during the Cenozoic, we can interpret a middle Miocene pulsed cooling event. Both the Ayder and Vanadzor vertical transects show a similarly timed pulse of cooling starting at ~15 Ma and ending by ~9 Ma (Fig. 4.7). Because the Ayder elevation transect includes both zircon and apatite (U-Th)/He analyses and is less affected by implantation due to low eU, its thermal model provides a more tightly constrained cooling history for this possible cooling event. The magnitude of modeled middle Miocene cooling for the Ayder transect (180-40 °C) translates to 6-1.3 km of rock exhumation assuming a 30 °C/km geothermal gradient.

For the Vanadzor transect, our sampling strategy of a collecting a vertical transect from the footwall of the Vanadzor pull-apart basin was intended to potentially capture exhumation related to slip on the Pembak Sevan fault. However, the 12-9 Ma cooling we record in the Vanazor transect likely pre-dates most of the slip on the Pembak Sevan, given its modest total displacement (10s of km) and moderate paleoseismically estimated slip rates (1-3 mm/yr; Philip et al., 2001; Karakhanyan et al., 2013). It therefore follows that our thermochronlogy may not be recording strike-slip motion of the Pembak-Sevan fault, but instead simply leveraging the relief exposed by the Vanadzor pull-apart basin to sample rocks which record a prior phase of uplift, which may have been accommodated on different structures than the Pembak-Sevan fault, or on a structural predecessor to the fault.

4.6 Discussion

The LCEP exhibits exclusively middle Miocene or older thermochronologic cooling ages and contains an elevated low-relief surface, observations that together limit the magnitude of rock exhumation in the range to less than 2-3 km since the middle Miocene. Therefore any north-south shortening across the LCEP since the middle Miocene must have been primarily accommodated by strike-slip motion along major faults like the Pembak-Sevan fault and the Northeastern Anatolian Fault, as opposed to reverse faulting,

which would have produced uplift and erosion that would have both destroyed the elevated low-relief surface and reset low-temperature thermochronology.

4.6.1 Strike-slip Faulting Accommodates Arabia-Eurasia Convergence in the LCEP

The lack of evidence for post-Miocene reverse faulting in the LCEP starkly contrasts with abundant evidence for Pliocene-Quaternary shortening and exhumation in the Greater Caucasus. Thermochronology from the Greater Caucasus supports rapid exhumation across the core of the range since ~5 Ma (Avdeev and Niemi, 2011; Vincent et al., 2020), and mapped deformation in the young sediments of the Greater Caucasus foreland shows that reverse faulting continues into the Quaternary along the front of the range (Forte et al. 2013; Tibaldi et al., 2017). Observations of accelerating deformation at 5 Ma in the Greater Caucasus are interpreted to represent the initiation of hard collision between Arabia and Eurasia in the western Greater Caucasus. A late Miocene to Pliocene acceleration of deformation is observed in multiple datasets from across the Arabia-Eurasia collision zone (Allen et al., 2003), including rapid uplift and erosion in the core of the Greater Caucasus at ~5 Ma (Avdeev and Niemi, 2011), increased subsidence recorded in the Selmo Formation in the foreland of the Bitlis-Zagros fold-thrust belt (Cavazza et al., 2018), increased exhumation starting at 7 Ma in the Alborz Mountains of Iran (Axen et al., 2002) and in the mid- to late Miocene along the Bitlis-Zagros fold thrust belt (Okay et al., 2010), and a ~5 Ma reorganization of faulting in Iran (Allen et al., 2011).

In the datasets recording tectonic reorganization around 5 Ma, it is apparent that different locations within the collision zone experienced either predominantly strike-slip faulting (e.g., the Anatolian and Iranian plateau interiors) or reverse faulting (e.g., Bitlis-Zagros and Greater Caucasus fold-thrust belts). In the LCEP, our thermochronologic analyses show that no more than 1-2 km of exhumation could have occurred since ~10 Ma (Fig. 4.7), in agreement with the presence of an elevated low-relief surface which limits the amount of rock exhumation and erosion that could have occurred since the surface formed (Figs. 4.3 and 4.4). These observations require that the LCEP experienced minimal rock uplift and erosion since 10 Ma, suggesting that over that time convergence between Arabia and Eurasia was accommodated by primarily strike slip faulting as opposed to reverse faulting. A dominance of strike-slip faulting over reverse faulting since

10 Ma agrees with GPS derived measurements of deformation in the Lesser Caucasus. Geodetic estimates of shortening rates across the Lesser Caucasus show that of the 20-30 mm/yr of total convergence between Arabia and Eurasia, only ~1-2 mm/yr are accommodated in the Lesser Caucasus, an amount of convergence that can be almost entirely explained by paleoseismic slip rates on the Pembak Sevan fault (Karakhanyan et al., 2013).

The distinct deformation responses exhibited by the Lesser and Greater Caucasus provides an ongoing example of deformation localizing primarily in the overriding plate in the early stages of continent-continent collision. In the case of the Caucasus collision, this contrast in deformation behavior appears to be controlled by the presence of weak suture zones south of the LCEP onto which deformation has localized.

4.6.2 Middle Miocene Erosional Event and the Support of Topography in the LCEP

Our thermal history modeling suggests that the LCEP may have experienced a pulse of uplift and erosion in the middle Miocene (ca. 15-10 Ma), significantly prior to the ~5 Ma closure of the Greater Caucasus Basin and associated hard collision between Arabia and Eurasia. A 15-10 Ma timing for the erosional event in the LCEP matches estimates for a reorganization within the Arabia-Eurasia collision in response to the ~20-15 Ma cessation of subduction along the Bitlis Suture. This transition is marked by increased volcanism in eastern Anatolia, broad uplift of the Eastern Anatolian Plateau, and the initiation of the conjugate North and East Anatolian Fault Zones (Şengör et al., 2005), initiating the westward extrusion of Anatolia out of the collision zone (Şengör et al., 2003; Hüsing et al., 2009; and references therein). This Miocene tectonic reorganization is hypothesized to have resulted in enhanced uplift and erosion from ~18 Ma to 10 Ma at the southern margin of the Arabia-Eurasia collision zone along the Bitlis suture zone, recorded in both thermochronologic data and foreland basin sedimentation rates (Okay et al., 2010; Cavazza et al., 2018). This increased tectonism along the Bitlis suture may be analogous to the 15-10 Ma erosional event in the LCEP, reflecting changes in the stress field within the collision following the transition of the Bitlis tectonic boundary from subduction to collision. Our thermochronology provides additional evidence for a middle Miocene phase of tectonic reorganization within the Arabia-Eurasia collision, potentially

triggered by a reorganization of stresses following soft collision between Arabia and the East Anatolian Accretionary Complex, as has been hypothesized along the Bitlis suture zone (Okay et al., 2010; Cavazza et al., 2018).

There is now a relatively robust temporal correlation of the tectonic events described above with the end of subduction south of the Eastern Anatolian Plateau, but the precise mechanism driving middle Miocene uplift around the Eastern Anatolian Plateau is debated, with most explanations involving some combination of crustal thickening, mantle lithosphere removal, and dynamic topography above hot flowing asthenosphere. The 15-10 Ma LCEP cooling event can potentially be explained as a marginal effect of middle Miocene mantle lithosphere removal, upper crustal shortening, and reorganization of faulting that resulted in widespread uplift of the Eastern Anatolian Plateau. Middle Miocene termination of subduction south of the Eastern Anatolian Plateau created the Bitlis suture and may have triggered the north to south removal of the mantle lithosphere from beneath the Anatolide-Tauride-Armenian block (Fig. 4.2), resulting in north to south uplift of the Eastern Anatolian Plateau (Fig. 4.1), and a north to south sweep of volcanism in response to asthenospheric heating of the base of the crust (Şengör et al., 2003; Bartol and Govers, 2013). Alternatively, uplift related to influx of hot, buoyant asthenosphere routed along a sublithospheric channel from the African superplume into the Arabia-Eurasia collision zone (Ershov and Nikishin, 2004) would create a protracted (~8-10 Myr) south to north sweep of uplift and magmatism across the Eastern Anatolian Plateau. The 15-10 Ma timing of cooling we observe in the LCEP is very similar in timing to the ~18-13 cooling event along the Bitlis suture, in disagreement with the strongly transgressive deformation expected from the migration of a sublithospheric channel of mantle material (Ershov and Nikishin, 2004). Our data therefore favor rapid mantle lithosphere removal as a mechanism driving uplift and volcanism across the Eastern Anatolian Plateau and LCEP.

4.7 Conclusions

Our results from the Lesser Caucasus and Eastern Pontides mountains illuminate the deformation response of the down-going plate in a young continental collision. New apatite (U-Th)/He analyses, inverse thermal history modeling, and geomorphic observations of an elevated low-relief surface limit the magnitude of rock exhumation

along much of the LCEP to less than 1-2 km since 10 Ma. Any shortening across the LCEP during this period was therefore most likely accommodated on continental-scale strike-slip faults that separate the LCEP from the Eastern Anatolian Plateau to the south, including the Pembak-Sevan, Northern Anatolian, and Northeastern Anatolian faults. These faults are understood to reactivate major tectonic sutures of the Arabia-Eurasia collision zone, presenting an example of preexisting discontinuities controlling the distribution of later continental deformation. Our results illuminate asymmetry in the deformation of the Greater Caucasus and Lesser Caucasus mountain belts (respectively the overriding and down-going plates in the Caucasus continental collision). The dominance of strike-slip faulting in the Lesser Caucasus contrasts with the contractional nature of deformation in the Greater Caucasus, and highlights the importance of considering inherited lithospheric structures when interpreting asymmetric continental deformation in active and ancient collisional orogens.

4.8 Acknowledgements

This work was funded by NSF grants EAR-0810067, EAR-1524304, and EAR-2050618 to NAN, a TÜBİTAK grant to OK, and a grant from the Scott Turner Fund from the University of Michigan Department of Earth and Environmental Sciences. Thanks to Arkady Karakhanian (deceased) who orchestrated our collaboration in Armenia. Samples from the Lesser Caucasus of Azerbaijan were collected by Boris Avdeev (deceased) on a field expedition in 2006 that was organized by Ibrahim Murtuzayev. Amanda Maslyn provided support for sample processing and mineral separations.

4.9 References

Abbey, A.L., Niemi, N.A., Geissman, J.W., Winkelstern, I.Z., and Heizler, M., 2018, Early Cenozoic exhumation and paleotopography in the Arkansas River valley, southern Rocky Mountains, Colorado: Lithosphere, v. 10, p. 239–266, doi:*10.1130/L673.1*.

Adamia, Sh., Alania, V., Chabukiani, A., Chichua, G., Enukidze, O., and Sadradze, N., 2010, Evolution of the Late Cenozoic basins of Georgia (SW Caucasus): a review: Geological Society, London, Special Publications, v. 340, p. 239–259, doi:*10.1144/SP340.11*.

Akdeniz, N., and Güven, İ.H., 2002, Geological Map of Turkey. Trabzon Sheet.: General Directorate of Mineral Research and Exploration Geological Maps of Turkey.

Albino, I., Cavazza, W., Zattin, M., Okay, A.I., Adamia, S., and Sadradze, N., 2014, Far-field tectonic effects of the Arabia–Eurasia collision and the inception of the North Anatolian Fault system: Geological Magazine, v. 151, p. 372–379, doi:*10.1017/S0016756813000952*.

Allen, M.B., and Armstrong, H.A., 2008, Arabia–Eurasia collision and the forcing of mid-Cenozoic global cooling: Palaeogeography, Palaeoclimatology, Palaeoecology, v. 265, p. 52–58, doi:*10.1016/j.palaeo.2008.04.021*.

Allen, M., Jackson, J., and Walker, R., 2004, Late Cenozoic reorganization of the Arabia-Eurasia collision and the comparison of short-term and long-term deformation rates: Tectonics, v. 23, p. 16, doi:*10.1029/2003TC001530*.

Allen, M.B., Kheirkhah, M., Emami, M.H., and Jones, S.J., 2011, Right-lateral shear across Iran and kinematic change in the Arabia-Eurasia collision zone: Geophysical Journal International, v. 184, p. 555–574, doi:*10.1111/j.1365-246X.2010.04874.x*.

Arslan, M., and Aliyazicioglu, I., 2001, Geochemical and Petrological Characteristics of the Kale (Gümüshane) Volcanic Rocks: Implications for the Eocene Evolution of Eastern Pontide Arc Volcanism, Northeast Turkey: International Geology Review, v. 43, p. 595–610, doi:*10.1080/00206810109465035*.

Avagyan, A.V., 2009, Active faulting and related seismic hazard in the Vanadzor depression area: Proceedings of the National Academy of Sciences of the Republic of Armenia, Earth Sciences, v. 62, p. 48–57.

Avdeev, B., and Niemi, N.A., 2011, Rapid Pliocene exhumation of the central Greater Caucasus constrained by low-temperature thermochronometry: Tectonics, v. 30, p. 1–16, doi:*10.1029/2010TC002808*.

Axen, G.J., Lam, P.S., Grove, M., Stockli, D.F., and Hassanzadeh, J., 2001, Exhumation of the west-central Alborz Mountains, Iran, Caspian subsidence, and collision-related tectonics: Geology, v. 29, p. 559–562, doi:*10.1130/0091-7613(2001)029<0559*.

Aydemir, A., Bilim, F., Avci, B., and Kosaroglu, S., 2020, Geophysical investigation of the geothermal potential under the largest volcanic cover in Anatolia: Kars Plateau, NE Turkey: Pure and Applied Geophysics, v. 177, p. 919–939, doi:*10.1007/s00024-019-02317-x*.

Bartol, J., and Govers, R., 2014, A single cause for uplift of the Central and Eastern Anatolian plateau? Tectonophysics, v. 637, p. 116–136, doi:*10.1016/j.tecto.2014.10.002*.

Bektaş, Ö., Ravat, D., Büyüksaraç, A., Bilim, F., and Ateş, A., 2007, Regional Geothermal Characterisation of East Anatolia from Aeromagnetic, Heat Flow and Gravity

Data: Pure and Applied Geophysics, v. 164, p. 975–998, doi:*10.1007/s00024-007-0196-5*.

Berger, A., Egli, D., Glotzbach, C., Valla, P.G., Pettke, T., and Herwegh, M., 2022, Apatite low-temperature chronometry and microstructures across a hydrothermally active fault zone: Chemical Geology, v. 588, p. 120633, doi:*10.1016/j.chemgeo.2021.120633*.

Boztuğ, D., Jonckheere, R., Wagner, G.A., Erçin, A.I., and Yeğingil, Z., 2007, Titanite and zircon fission-track dating resolves successive igneous episodes in the formation of the composite Kaçkar batholith in the Turkish eastern Pontides: International Journal of Earth Sciences, v. 96, p. 875–886, doi:*10.1007/s00531-006-0140-4*.

Calvet, M., Gunnell, Y., and Farines, B., 2015, Flat-topped mountain ranges: Their global distribution and value for understanding the evolution of mountain topography: Geomorphology, v. 241, p. 255–291, doi:*10.1016/j.geomorph.2015.04.015*.

Cavazza, W., Albino, I., Galoyan, G., Zattin, M., and Cattò, S., 2019, Continental accretion and incremental deformation in the thermochronologic evolution of the Lesser Caucasus: Geoscience Frontiers, v. 10, p. 2189–2202, doi:*10.1016/j.gsf.2019.02.007*.

Cavazza, W., Albino, I., Zattin, M., and Galoyan, G., 2015, Thermochronometric evidence for Miocene tectonic reactivation of the Sevan–Akera suture zone (Lesser Caucasus): a far-field tectonic effect of the Arabia – Eurasia collision? The Geological Society of London Special Publications, v. 428, doi:*10.1144/SP428.4*.

Cavazza, W., Cattò, S., Zattin, M., Okay, A.I., and Reiners, P., 2018, Thermochronology of the Miocene Arabia-Eurasia collision zone of southeastern Turkey: Geosphere, v. 14, p. 2277–2293, doi:*10.1130/GES01637.1*.

Clark, M.K., Maheo, G., Saleeby, J., and Farley, K.A., 2005, The non-equilibrium landscape of the southern Sierra Nevada, California: GSA Today, v. 15, p. 4–10, doi:*10:1130/1052-5173(2005)015<4:TNELOT>2.0.CO;2*.

Cowgill, E., Forte, A.M., Niemi, N., Avdeev, B., Tye, A., Trexler, C., Javakhishvili, Z., Elashvili, M., and Godoladze, T., 2016, Relict basin closure and crustal shortening budgets during continental collision: An example from Caucasus sediment provenance: Tectonics, v. 35, p. 2918–2947, doi:*10.1002/2016TC004295*.

Dean, R.B., and Dixon, W.J., 1951, Simplified statistics for small numbers of observations: Analytical Chemistry, v. 23, p. 636–638, doi:*10.1021/ac60052a025*.

Dewey, J.F., Hempton, M.R., Kidd, W.S.F., Saroglu, F., and Şengör, A.M.C., 1986, Shortening of continental lithosphere: the neotectonics of Eastern Anatolia - a young collision zone, *in* Coward, M.P. and Ries, A.C. eds., Collision Tectonics, Geological Society, London, Special Publications 19, p. 3–36, doi:*10.1144/GSL.SP.1986.019.01.01*.

Dilek, Y., 2006, Collision tectonics of the Mediterranean region: Causes and consequences, *in* Postcollisional Tectonics and Magmatism in the Mediterranean Region and Asia, Geological Society of America, Geological Society of America Special Paper 409, doi:*10.1130/2006.2409(01)*.

Dilek, Y., Imamverdiyev, N., and Altunkaynak, A., 2010, Geochemistry and tectonics of Cenozoic volcanism in the Lesser Caucasus (Azerbaijan) and the peri-Arabian region: collision-induced mantle dynamics and its magmatic fingerprint: International Geology Review, v. 52, p. 536–578, doi:*10.1080/00206810903360422*.

Ershov, A.V., and Nikishin, A.M., 2004, Recent geodynamics of the Caucasus-Arabia-East Africa region: Geotectonics, v. 38, p. 123–136.

Espurt, N., Hippolyte, J.-C., Kaymakci, N., and Sangu, E., 2014, Lithospheric structural control on inversion of the southern margin of the Black Sea Basin, Central Pontides, Turkey: Lithosphere, v. 6, p. 26–34, doi:*10.1130/L316.1*.

Farley, K.A., 2002, (U-Th)/He Dating: Techniques, Calibrations, and Applications: Reviews in Mineralogy and Geochemistry, v. 47, p. 819–844, doi:*10.2138/rmg.2002.47.18*.

Flowers, R.M., Ketcham, R.A., Shuster, D.L., and Farley, K.A., 2009, Apatite (U-Th)/He thermochronometry using a radiation damage accumulation and annealing model: Geochimica et Cosmochimica Acta, v. 73, p. 2347–2365, doi:*10.1016/j.gca.2009.01.015*.

Forte, A.M., Cowgill, E., Murtuzayev, I., Kangarli, T., and Stoica, M., 2013, Structural geometries and magnitude of shortening in the eastern Kura fold-thrust belt, Azerbaijan: Implications for the development of the Greater Caucasus Mountains: Tectonics, v. 32, p. 688–717, doi:*10.1002/tect.20032*.

Forte, A.M., Cowgill, E., and Whipple, K.X., 2014, Transition from a singly vergent to doubly vergent wedge in a young orogen: The Greater Caucasus: Tectonics, v. 33, p. 2077–2101, doi:*10.1002/2014TC003651*.

Forte, A.M., Whipple, K.X., Bookhagen, B., and Rossi, M.W., 2016a, Decoupling of modern shortening rates, climate, and topography in the Caucasus: Earth and Planetary Science Letters, v. 449, p. 282–294, doi:*10.1016/j.epsl.2016.06.013*.

Forte, A.M., Yanites, B.J., and Whipple, K.X., 2016b, Complexities of landscape evolution during incision through layered stratigraphy with contrasts in rock

strength: Earth Surface Processes and Landforms, v. 41, p. 1736–1757, doi:*10.1002/esp.3947*.

Gallagher, K., 2012, Transdimensional inverse thermal history modeling for quantitative thermochronology: Journal of Geophysical Research: Solid Earth, v. 117, p. 1–16, doi:*10.1029/2011JB008825*.

Göğüş, O.H., and Pysklywec, R.N., 2008, Mantle lithosphere delamination driving plateau uplift and synconvergent extension in eastern Anatolia: Geology, v. 36, p. 723, doi:*10.1130/G24982A.1*.

Gök, R. et al., 2011, Lithospheric velocity structure of the Anatolian plateau-Caucasus-Caspian region: Journal of Geophysical Research, v. 116, p. B05303, doi:*10.1029/2009JB000837*.

Gunnels, M., Yetrimishli, G., Kazimova, S., and Sandvol, E., 2021, Seismotectonic evidence for subduction beneath the Eastern Greater Caucasus: Geophysical Journal International, v. 224, p. 1825–1834, doi:*10.1093/gji/ggaa522*.

Gusmeo, T., Cavazza, W., Alania, V.M., Enukidze, O.V., Zattin, M., and Corrado, S., 2021, Structural inversion of back-arc basins–The Neogene Adjara-Trialeti fold-and-thrust belt (SW Georgia) as a far-field effect of the Arabia-Eurasia collision: Tectonophysics, v. 803, p. 228702, doi:*10.1016/j.tecto.2020.228702*.

Hassanzadeh, J., and Wernicke, B.P., 2016, The Neotethyan Sanandaj-Sirjan zone of Iran as an archetype for passive margin-arc transitions: Tectonics, v. 35, p. 586–621, doi:*10.1002/2015TC003926*.

Hässig, M., Rolland, Y., Sosson, M., Galoyan, G., Sahakyan, L., Topuz, G., Çelik, Ö.F., Avagyan, A., and Müller, C., 2013, Linking the NE Anatolian and Lesser Caucasus ophiolites: evidence for large-scale obduction of oceanic crust and implications for the formation of the Lesser Caucasus-Pontides Arc: Geodinamica Acta, v. 26, p. 311–330, doi:*10.1080/09853111.2013.877236*.

Haug, G.H., and Tiedemann, R., 1998, Effect of the formation of the Isthmus of Panama on Atlantic Ocean thermohaline circulation: Nature, v. 393, p. 673–676, doi:*10.1038/31447*.

Kaislaniemi, L., van Hunen, J., Allen, M.B., and Neill, I., 2014, Sublithospheric small-scale convection—A mechanism for collision zone magmatism: Geology, v. 42, p. 291–294, doi:*10.1130/G35193.1*.

Kandemir, Ö., Akbayram, K., Çobankaya, M., Kanar, F., Pehlivan, Ş., Tok, T., Hakyemez, A., Ekmekçi, E., Danacı, F., and Temiz, U., 2019, From arc evolution to arc-continent collision: Late Cretaceous–middle Eocene geology of the Eastern Pontides, northeastern Turkey: GSA Bulletin, v. 131, p. 1889–1906, doi:*10.1130/B31913.1*.

Karakhanian, A.S. et al., 2004, Active faulting and natural hazards in Armenia, eastern Turkey and northwestern Iran: Tectonophysics, v. 380, p. 189–219, doi:*10.1016/j.tecto.2003.09.020*.

Karakhanyan, A. et al., 2013, GPS constraints on continental deformation in the Armenian region and Lesser Caucasus: Tectonophysics, v. 592, p. 39–45, doi:*10.1016/j.tecto.2013.02.002*.

Karsli, O., Dokuz, A., Uysal, İ., Aydin, F., Chen, B., Kandemir, R., and Wijbrans, J., 2010, Relative contributions of crust and mantle to generation of Campanian high-K calc-alkaline I-type granitoids in a subduction setting, with special reference to the Harşit Pluton, Eastern Turkey: Contributions to Mineralogy and Petrology, v. 160, p. 467–487, doi:*10.1007/s00410-010-0489-z*.

Keskin, M., 2003, Magma generation by slab steepening and breakoff beneath a subduction-accretion complex: An alternative model for collision-related volcanism in Eastern Anatolia, Turkey: MODEL FOR COLLISION-RELATED VOLCANISM: Geophysical Research Letters, v. 30, doi:*10.1029/2003GL018019*.

Koçyiğit, A., Yilmaz, A., Adamia, S., and Kuloshvili, S., 2001, Neotectonic of East Anatolian Plateau (Turkey) and Lesser Caucasus: Implication for transition from thrusting to strike-slip faulting: Geodinamica Acta, v. 14, p. 177–195, doi:*10.1016/S0985-3111(00)01064-0*.

Lebedev, V.A., Bubnov, S.N., Chernyshev, I.V., Chugaev, A.V., Dudauri, O.Z., and Vashakidze, G.T., 2007, Geochronology and genesis of subalkaline basaltic lava rivers at the Dzhavakheti highland, lesser Caucasus: K-Ar and Sr-Nd isotopic data: Geochemistry International, v. 45, p. 211–225, doi:*10.1134/S0016702907030019*.

Liao, J., and Gerya, T., 2017, Partitioning of crustal shortening during continental collision: 2-D thermomechanical modeling: Journal of Geophysical Research: Solid Earth, v. 122, p. 592–606, doi:*10.1002/2016JB013398*.

Lindsay, J.F., Holliday, D.W., and Hulbert, A.G., 1991, Sequence stratigraphy and the evolution of the Ganges-Brahmaputra delta complex: The American Association of Petroleum Geologist Bulletin, v. 75, p. 1233–1254, doi:*10.1306/0C9B291B-1710-11D7-8645000102C1865D*.

Mahatsente, R., Önal, G., and Çemen, I., 2018, Lithospheric structure and the isostatic state of Eastern Anatolia: Insight from gravity data modelling: Lithosphere, v. 10, p. 279–290, doi:*10.1130/L685.1*.

McDowell, F.W., McIntosh, W.C., and Farley, K.A., 2005, A precise ^{40}Ar–^{39}Ar reference age for the Durango apatite (U–Th)/He and fission-track dating standard: Chemical Geology, v. 214, p. 249–263, doi:*10.1016/j.chemgeo.2004.10.002*.

Meijers, M.J.M. et al., 2015, Progressive orocline formation in the Eastern Pontides – Lesser Caucasus: Tectonic Evolution of the Eastern Black Sea and Caucasus., p. 428.8-428.8, doi:*10.1144/SP428.8*.

Moritz, R. et al., 2020, At the crossroads of the Lesser Caucasus and the Eastern Pontides: Late Cretaceous to early Eocene magmatic and geodynamic evolution of the Bolnisi district, Georgia: Lithos, v. 378–379, p. 105872, doi:*10.1016/j.lithos.2020.105872*.

Mumladze, T., Forte, A.M., Cowgill, E.S., Trexler, C.C., Niemi, N.A., Burak Yikilmaz, M., and Kellogg, L.H., 2015, Subducted, detached, and torn slabs beneath the Greater Caucasus: GeoResJ, v. 5, p. 36–46, doi:*10.1016/j.grj.2014.09.004*.

Neill, I., Meliksetian, K., Allen, M.B., Navasardyan, G., and Kuiper, K., 2015, Petrogenesis of mafic collision zone magmatism: The Armenian sector of the Turkish–Iranian Plateau: Chemical Geology, v. 403, p. 24–41, doi:*10.1016/j.chemgeo.2015.03.013*.

Niemi, N.A., and Clark, M.K., 2018, Long-term exhumation rates exceed paleoseismic slip rates in the central Santa Monica Mountains, Los Angeles County, California: Geology, v. 46, p. 63–66, doi:*10.1130/G39388.1*.

Okay, A.I., Zattin, M., and Cavazza, W., 2010, Apatite fission-track data for the Miocene Arabia-Eurasia collision: Geology, v. 38, p. 35–38, doi:*10.1130/G30234.1*.

Philip, H.H.H., Avagyan, A., Karakhanian, A., Ritz, J.F.F.F., and Rebai, S., 2001, Estimating slip rates and recurrence intervals for strong earthquakes along an intracontinental fault: Example of the Pambak-Sevan-Sunik fault (Armenia): Tectonophysics, v. 343, p. 205–232, doi:*10.1016/S0040-1951(01)00258-X*.

Philip, H., Cisternas, A., Gvishiani, A., and Gorshkov, A., 1989, The Caucasus: an actual example of the initial stages of continental collision: Tectonophysics, v. 161, p. 1–21, doi:*10.1016/0040-1951(89)90297-7*.

Rebaï, S., Philip, H., Dorbath, L., Borissoff, B., Haessler, H., and Cisternas, A., 1993, Active tectonics in the Lesser Caucasus: Coexistence of compressive and extensional structures: Tectonics, v. 12, p. 1089–1114, doi:*10.1029/93TC00514*.

Reber, R., Akçar, N., Yesilyurt, S., Yavuz, V., Tikhomirov, D., Kubik, P.W., and Schlüchter, C., 2014, Glacier advances in northeastern Turkey before and during the global Last Glacial Maximum: Quaternary Science Reviews, v. 101, p. 177–192, doi:*10.1016/j.quascirev.2014.07.014*.

Reilinger, R. et al., 2006, GPS constraints on continental deformation in the Africa-Arabia-Eurasia continental collision zone and implications for the dynamics of plate interactions: Journal of Geophysical Research: Solid Earth, v. 111, p. 1–26, doi:*10.1029/2005JB004051*.

Reiners, P.W., Farley, K.A., and Hickes, H.J., 2002, He diffusion and (U-Th)/He thermochronometry of zircon: Initial results from Fish Canyon Tuff and Gold Butte: Tectonophysics, v. 349, p. 297–308, doi:*10.1016/S0040-1951(02)00058-6*.

Reiners, P.W., and Nicolescu, S., 2006, Measurement of parent nuclides for (U-Th)/He chronometry by solution sector ICP-MS: ARHDL Report 1, 33 p., *http://www.geo.arizona.edu/~reiners/arhdl/arhdl.htm*.

Reiners, P.W., Thomson, S.N., McPhillips, D., Donelick, R.A., and Roering, J.J., 2007, Wildfire thermochronology and the fate and transport of apatite in hillslope and fluvial environments: Journal of Geophysical Research: Earth Surface, v. 112, doi:*10.1029/2007JF000759*.

Ritz, J.F. et al., 2016, Active tectonics within the NW and SE extensions of the Pambak-Sevan-Syunik fault: Implications for the present geodynamics of Armenia: Quaternary International, v. 395, p. 61–78, doi:*10.1016/j.quaint.2015.05.021*.

Rolland, Y., Hässig, M., Bosch, D., Bruguier, O., Melis, R., Galoyan, G., Topuz, G., Sahakyan, L., Avagyan, A., and Sosson, M., 2020, The East Anatolia–Lesser Caucasus ophiolite: An exceptional case of large-scale obduction, synthesis of data and numerical modelling: Geoscience Frontiers, v. 11, p. 83–108, doi:*10.1016/j.gsf.2018.12.009*.

Rosenkranz, R., Spiegel, C., Schildgen, T., and Wittmann, H., 2017, Coupling denudation rates and topographic development in the rainiest place on earth : Reconstructing the Shillong Plateau uplift history with cosmogenic 10Be: Earth and Planetary Science Letters, v. 19, p. 11215–11215, doi:*10.1016/j.epsl.2017.11.047*.

Sahakyan, L., Bosch, D., Sosson, M., Avagyan, A., Galoyan, Gh., Rolland, Y., Bruguier, O., Stepanyan, Zh., Galland, B., and Vardanyan, S., 2017, Geochemistry of the Eocene magmatic rocks from the Lesser Caucasus area (Armenia): evidence of a subduction geodynamic environment: Geological Society, London, Special Publications, v. 428, p. 73–98, doi:*10.1144/SP428.12*.

Sarıkaya, M.A., Çiner, A., and Zreda, M., 2011, Quaternary Glaciations of Turkey, *in* Developments in Quaternary Sciences, Elsevier, v. 15, p. 393–403, doi:*10.1016/B978-0-444-53447-7.00030-1*.

Schildgen, T.F., Yıldırım, C., Cosentino, D., and Strecker, M.R., 2014, Linking slab break-off, Hellenic trench retreat, and uplift of the Central and Eastern Anatolian plateaus: Earth-Science Reviews, v. 128, p. 147–168, doi:*10.1016/j.earscirev.2013.11.006*.

Schleiffarth, W.K., Darin, M.H., Reid, M.R., and Umhoefer, P.J., 2018, Dynamics of episodic Late Cretaceous–Cenozoic magmatism across Central to Eastern

Anatolia: New insights from an extensive geochronology compilation: Geosphere, v. 14, p. 1990–2008, doi:*10.1130/GES01647.1*.

Schoettle-Greene, P., and Pysklywec, R.N., 2014, Passive margin subduction and the dynamics of collisional orogenesis: Geophysical Research Letters, v. 41, p. 843–849, doi:*10.1002/2013GL058934*.

Şengör, A.M.C., Özeren, S., Genç, T., and Zor, E., 2003, East Anatolian high plateau as a mantle-supported, north-south shortened domal structure: Geophysical Research Letters, v. 30, p. 2–5, doi:*10.1029/2003GL017858*.

Şengör, A.M.C., Tüysüz, O., İmren, C., Sakınç, M., Eyidoğan, H., Görür, N., Le Pichon, X., and Rangin, C., 2005, The North Anatolian Fault: A new look: Annual Review of Earth and Planetary Sciences, v. 33, p. 37–112, doi:*10.1146/annurev.earth.32.101802.120415*.

Sheth, H., Meliksetian, K., Gevorgyan, H., Israyelyan, A., and Navasardyan, G., 2015, Intracanyon basalt lavas of the Debed River (northern Armenia), part of a Pliocene-Pleistocene continental flood basalt province in the South Caucasus: Journal of Volcanology and Geothermal Research, v. 295, p. 1–15, doi:*10.1016/j.jvolgeores.2015.02.010*.

Shuster, D.L., Flowers, R.M., and Farley, K.A., 2006, The influence of natural radiation damage on helium diffusion kinetics in apatite: Earth and Planetary Science Letters, v. 249, p. 148–161, doi:*10.1016/j.epsl.2006.07.028*.

Şimşek, Ş., and Demir, A., 1991, Reservoir and cap rock characteristics of some geothermal fields in Turkey and encountered problems based on lithology: Journal of the Geothermal Research Society of Japan, v. 13, p. 191–204, doi:*10.11367/grsj1979.13.191*.

Softa, M., Emre, T., Sözbilir, H., Spencer, J.Q.G., and Turan, M., 2018, Geomorphic evidence for active tectonic deformation in the coastal part of Eastern Black Sea, Eastern Pontides, Turkey: Geodinamica Acta, v. 30, p. 249–264, doi:*10.1080/09853111.2018.1494776*.

Sokhadze, G., Floyd, M., Godoladze, T., King, R., Cowgill, E.S., Javakhishvili, Z., Hahubia, G., and Reilinger, R., 2018, Active convergence between the Lesser and Greater Caucasus in Georgia: Constraints on the tectonic evolution of the Lesser–Greater Caucasus continental collision: Earth and Planetary Science Letters, v. 481, p. 154–161, doi:*10.1016/j.epsl.2017.10.007*.

Sokół, K., Halama, R., Meliksetian, K., Savov, I.P., Navasardyan, G., and Sudo, M., 2018, Alkaline magmas in zones of continental convergence: The Tezhsar volcano-intrusive ring complex, Armenia: Lithos, v. 320–321, p. 172–191, doi:*10.1016/j.lithos.2018.08.028*.

Spiegel, C., Kohn, B., Belton, D., Berner, Z., and Gleadow, A., 2009, Apatite (U–Th–Sm)/He thermochronology of rapidly cooled samples: The effect of He implantation: Earth and Planetary Science Letters, v. 285, p. 105–114, doi:*10.1016/j.epsl.2009.05.045*.

Taner, M.F., Delaloye, M., and Vuagnat, M., 1979, On the geochronology by K-Ar method of the Rize pluton in the region of Güneyce-Ikizdere, Eastern Pontids, Turkey: Schweizerische mineralogische und petrographische Mitteilungen, v. 59, p. 309–317, doi:*10.5169/SEALS-46068*.

Temizel, E.H., Gültekin, F., and Ersoy, A.F., 2020, Major, trace, and rare earth element geochemistry of the Ayder and İkizdere (Rize, NE Turkey) geothermal waters: Constraints for water–rock interactions: Geothermics, v. 86, p. 101810, doi:*10.1016/j.geothermics.2020.101810*.

Tezcan, A.K., 1995, Geothermal explorations and heat flow in Turkey, *in* Gupta, M.L. and Yamano, M. eds., Terrestrial Heat Flow and Geothermal Energy in Asia, New Delhi, India, Oxford and IBH Publishing Co. Pvt. Ltd., p. 23–42.

Tibaldi, A., Alania, V., Bonali, F.L., Enukidze, O., Tsereteli, N., Kvavadze, N., and Varazanashvili, O., 2017, Active inversion tectonics, simple shear folding and back-thrusting at Rioni Basin, Georgia: Journal of Structural Geology, v. 96, p. 35–53, doi:*10.1016/j.jsg.2017.01.005*.

Trifonov, V.G. et al., 2016, Stratigraphic and tectonic settings of Early Paleolithic of North-West Armenia: Quaternary International, v. 420, p. 178–198, doi:*10.1016/j.quaint.2015.08.019*.

Tye, A.R., Niemi, N.A., Safarov, R.T., Kadirov, F.A., and Babayev, G.R., 2021, Sedimentary response to a collision orogeny recorded in detrital zircon provenance of Greater Caucasus foreland basin sediments: Basin Research, v. 33, p. 933–967, doi:*10.1111/bre.12499*.

Vincent, S.J., Allen, M.B., Ismail-Zadeh, A.D., Flecker, R., Foland, K.A., and Simmons, M.D., 2005, Insights from the Talysh of Azerbaijan into the Paleogene evolution of the South Caspian region: Geological Society of America Bulletin, v. 117, p. 1513, doi:*10.1130/B25690.1*.

Vincent, S.J., Braham, W., Lavrishchev, V.A., Maynard, J.R., and Harland, M., 2016, The formation and inversion of the western Greater Caucasus Basin and the uplift of the western Greater Caucasus: Implications for the wider Black Sea region: Western Greater Caucasus Evolution: Tectonics, v. 35, p. 2948–2962, doi:*10.1002/2016TC004204*.

Vincent, S.J., Somin, M.L., Carter, A., Vezzoli, G., Fox, M., and Vautravers, B., 2020, Testing Models of Cenozoic Exhumation in the Western Greater Caucasus: Tectonics, v. 39, doi:*10.1029/2018TC005451*.

Willett, C.D., Fox, M., and Shuster, D.L., 2017, A helium-based model for the effects of radiation damage annealing on helium diffusion kinetics in apatite: Earth and Planetary Science Letters, v. 477, p. 195–204, doi:*10.1016/j.epsl.2017.07.047*.

Wobus, C., Whipple, K.X., Kirby, E., Snyder, N., Johnson, J., Spyropolou, K., Crosby, B., and Sheehan, D., 2006, Tectonics from topography: Procedures, promise, and pitfalls, *in* Tectonics, Climate, and Landscape Evolution, Geological Society of America, doi:*10.1130/2006.2398(04)*.

Yilmaz, A., Adamia, S., Chabukiani, A., Chkhotua, T., ErdoĞan, K., Tuzcu, S., and KarabiyikoĞlu, M., 2000, Structural Correlation of the Southern Transcaucasus (Georgia)-Eastern Pontides (Turkey): Geological Society, London, Special Publications, v. 173, p. 171–182, doi:*10.1144/GSL.SP.2000.173.01.08*.

Chapter 5
Conclusions

In the course of tectonics and structural geology research, there exists a tension between the elegant simplicity of broadly applicable geodynamic models and the more ad hoc explanations that field-based studies use to explain complex real-world datasets. There is a natural balance between these two approaches, and the tension between them guarantees that geodynamic models do not gloss over real-world complexity, and that field geologists do not describe the processes going on in their chosen study areas as wholly unique.

The findings of my three data chapters are firmly on the field geologist side of this dichotomy. The results reveal previously unrecognized details of the specific tectonic histories of the Basin and Range and Lesser Caucasus, embracing a great deal of complexity along the way. Chapter 2 examines the relative roles of plate boundary reorganization and Farallon slab removal in the extensional history of the Titus Canyon Formation in the central Basin and Range. Our basin analysis shows that extensional tectonism associated with subsidence of the Titus Canyon basin may have been triggered by a 40 Ma slowdown in convergence along the Farallon-North American plate boundary, suggesting that plate boundary dynamics, not just Farallon slab removal, should be considered when assessing Eocene low-magnitude extension in the Basin and Range.

The new thermochronologic data described in Chapter 3 reveal the timing of extensional deformation across a broad swath of the northern Basin and Range, indicating that the region experienced the highest rates of extension in the Miocene, 10-20 Myr after the removal of the Farallon slab at the time when the plate boundary was transitioning from subduction to transform motion. The 10-20 Myr delay between the removal of the Farallon flat slab in the Eocene-Oligocene and rapid Miocene extension may reflect the time it took for mantle heat to diffuse into the chilled North American crust following slab delamination. Additionally, our data reveal that Miocene extension

in the northern Basin and Range was spatially heterogeneous, which may reflect periodic instability of viscosity contrasts in the lithosphere during extension.

Our data from the Basin and Range (Chapters 2 and 3) follow a broad trend of recent datasets that deemphasize Eocene-Oligocene extension in favor of large-magnitude Miocene extension (e.g., Colgan and Henry, 2009; Lund Snee and Miller, 2022). Our success in applying multi-thermochronometer analysis to plutons and stocks in the northern Basin and Range (Chapter 3) shows the value in targeting smaller plutons for thermochronologic analysis. Low-temperature thermochronology remains powerful approach for determining the thermo-tectonic evolution of the Basin and Range.

Our thermochronology data in Chapter 3 also reveal places in the Basin and Range where low-temperature thermochronologic records of Mesozoic contractional tectonism have been preserved. These older cooling histories are preserved in places that behaved as rigid blocks during Cenozoic extension, such as the Spring Mountains of southern Nevada (Snow and Wernicke, 2000) or the Newfoundland Mountains in northwestern Utah (Chapter 3). These locations could be specifically targeted for thermochronologic analysis in the future to provide insight into pre-extensional tectonic phases in the Basin and Range.

Chapter 4 examines the Arabia-Eurasia collision zone, where new geomorphic observations and thermochronologic data in the Lesser Caucasus and Eastern Pontides mountains indicate that the most recent significant phase of uplift and erosion occurred in the middle Miocene. The limited rock uplift allowed by our data since the middle Miocene suggests that any shortening since 5 Ma, during the initiation of continent-continent collision, was most likely accommodated along strike-slip faults that reactivated weak suture zones. Additionally, we show that the middle Miocene phase of tectonism observed in the Lesser Caucasus and Eastern Pontides is well timed to correlate with regional delamination of mantle lithosphere from beneath the adjacent eastern Anatolian Plateau.

Our work in the Lesser Caucasus and Eastern Pontides shows that in addition to posing a significant seismic hazard, the major strike-slip faults in the region (including the Pembak-Sevan Fault and Northeastern Anatolian Fault) may represent key structures in accommodating shortening across the Arabia-Eurasia collision zone. Much is known about the geodetic and paleoseismic slip-rates on these structures (e.g. Karakhanian et

al., 2016), but relatively little is known about the long-term tectonic evolution of these faults, including their total displacement and age. Research into when these strike-slip faults activated, and their full slip histories, will be important for understanding how shortening is distributed across the Arabia-Eurasia collision.

The variety of the mechanisms invoked in these studies suggests that future integrative models of the tectonic and topographic evolution of continents must be able to incorporate a broad range of geodynamic processes to reproduce the complex patterns of deformation we observe in field-studies.

5.1 References

Colgan, J.P., and Henry, C.D., 2009, Rapid middle Miocene collapse of the Mesozoic orogenic plateau in north-central Nevada: International Geology Review, v. 51, p. 920–961, doi:10.1080/00206810903056731.

Karakhanian, A.S., Arakelyan, A., Avagyan, A., and Sadoyan, T., 2016, Aspects of the seismotectonics of Armenia : New data and reanalysis: Geological Society of America Special Paper 525, v. 2525, p. 1–32, doi:10.1130/2016.2525(14).

Lund Snee, J.-E., and Miller, E.L., 2022, Magmatism, migrating topography, and the transition from Sevier shortening to Basin and Range extension, western United States, in Craddock, J.P., Malone, D.H., Foreman, B.Z., and Konstantinou, A. eds., Tectonic Evolution of the Sevier-Laramide Hinterland, Thrust Belt, and Foreland, and Postorogenic Slab Rollback (180–20 Ma), Boulder, Colorado, Geological Society of America, Geological Society of America Special Paper 555, doi:10.1130/2021.2555(13).

McQuarrie, N., and Wernicke, B.P., 2005, An animated tectonic reconstruction of southwestern North America since 36 Ma: Geosphere, v. 1, p. 147–172, doi:10.1130/GES00016.1.

Snow, J.K., and Wernicke, B.P., 2000, Cenozoic tectonism in the central basin and range: Magnitude, rate, and distribution of upper crustal strain: American Journal of Science, v. 300, p. 659–719, doi:10.2475/ajs.300.9.659.

Appendix A
Supplementary Information for Chapter 2

A.1 Titus Canyon $^{40}Ar/^{39}Ar$ data recalculations

We recalculate and report $^{40}Ar/^{39}Ar$ ages from early Cenozoic strata of the eastern Death Valley region from two sources relevant to understanding the age of the Titus Canyon Formation and overlying strata.

The first data set are unpublished $^{40}Ar/^{39}Ar$ ages reported in a meeting abstract (Hodges and Saylor, 1994). These ages are from the Titus Canyon Formation in the southern Grapevine and northern Funeral mountains. Context for these samples is provided by Saylor (1991), although sample locations are not presented in that dissertation. Original analytical data files and tables for these samples are no longer available (K. Hodges, personal commun., 2020). Parameters necessary to calculate the $^{40}Ar/^{39}Ar$ ages presented on the inverse isochron diagrams were assumed to be the same as those used for published $^{40}Ar/^{39}Ar$ ages generated by the same laboratory (CLAIR geochronology facility at MIT) during the same year that the abstract was published (Hodges et al., CMP, 1994). These include the decay constant of Steiger and Jager (1977) and the use of the monitor mineral MMhb-1 hornblende with an assumed age of 520.4 Ma (Samson and Alexander, 1987). The ages reported in Saylor and Hodges (1994) were recalculated using the ArAR program (Argon Age Recalculator; Mercer and Hodges, 2016). Ages were recalculated with the decay constant of Renne et al. (2011) and a preferred MMhb-1 age of 523.3 Ma (Spell and McDougall, 2003). We presumed that the initial analyses assumed an atmospheric Ar ratio of 295.5 (Nier, 1950), and we did not adjust this value.

The second data set are $^{40}Ar/^{39}Ar$ ages reported in a master's thesis from Purdue University (Gutenkunst, 2006). These ages are from several measured sections of Cenozoic strata from the eastern Death Valley and Nevada Test Site regions. Contextual and stratigraphic data for these samples are provided in Murray (2001), Gutenkunst

(2006), and Ridgway et al. (2011). Full analytical data for these samples, and discussion of the acquisition parameters, is included in Appendix F of Gutenkunst (2006). This master's thesis is not available through public sources (e.g., ProQuest or similar databases), and a scanned copy was provided to the authors by Ken Ridgway, the principal investigator on the project that generated the data (U. S. Nuclear Regulatory Commission Contract NRC-02-07-006). Permission to include the data in this manuscript and disseminate it to the community was given by K. Ridgway (2020, personal commun.).

The $^{40}Ar/^{39}Ar$ data were acquired at the University of Alaska, Fairbanks, Geochronology laboratory by P. Layer and J. Drake. Analyses were performed on mineral separates (biotite and sanidine) and whole rock chips from ash beds and lavas intercalated in Cenozoic stratigraphic sections. Ages were calculated using the decay constants of Steiger and Jaeger (1977) and the monitor mineral MMhb-1 hornblende with an assumed age of 513.9 Ma (Lanphere and Dalrymple, 2000). Using the original analytical data provided in Gutenkunst (2006), we recalculated integrated, plateau, weighted, and inverse isochron ages for each sample using the program IsoplotR (Vermeesch, 2018). Outlier detection and rejection was undertaken with the standard tools included in the program. The J-factor for the samples presented in Gutenkunst (2006) was re-calculated manually to reflect updated decay constants (Renne et al., 2011) and monitor mineral age (523.3 Ma, Spell and McDougall, 2003). These updated parameters were propagated through the age analysis, although the initial atmospheric Ar ratio was retained at 295.5 for comparison with the recalculated Ar ages from Saylor and Hodges (1994).

New plateau and inverse isochron diagrams are provided for sanidine and biotite $^{40}Ar/^{39}Ar$ ages reported by Gutenkunst (2006) from the eastern Funeral Mountains. As noted in Gutenkunst's original thesis, several samples demonstrate issues with excess Ar. This may derive, as we note in the main manuscript, from mixtures of Cenozoic volcanic materials with Mesozoic plutonic materials that are common in many of the early Cenozoic reworked tuffs in the Death Valley region.

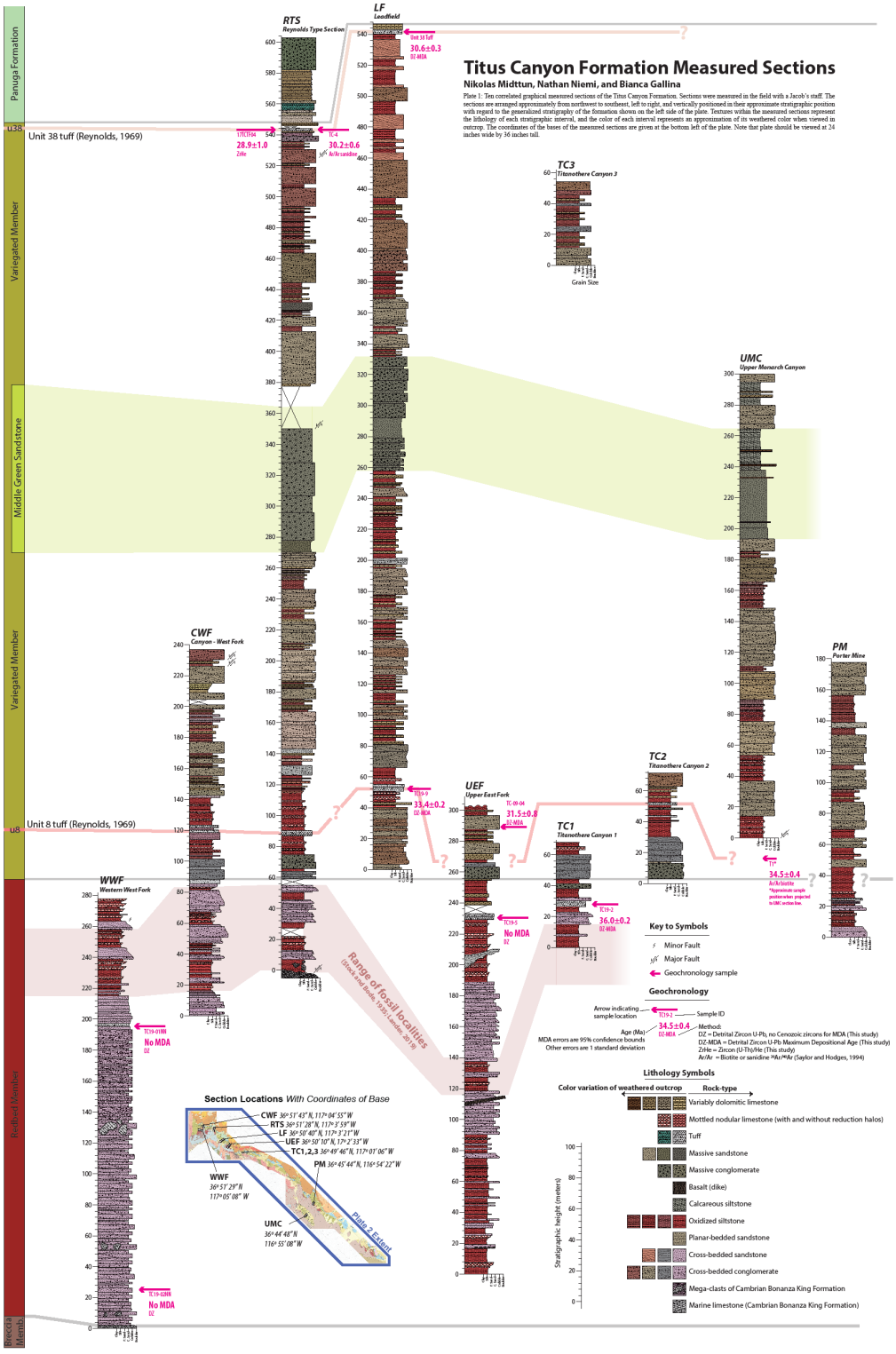


Figure A.1: Measured sections of the Titus Canyon Formation.
Ten correlated graphical measured sections of the Titus Canyon Formation.

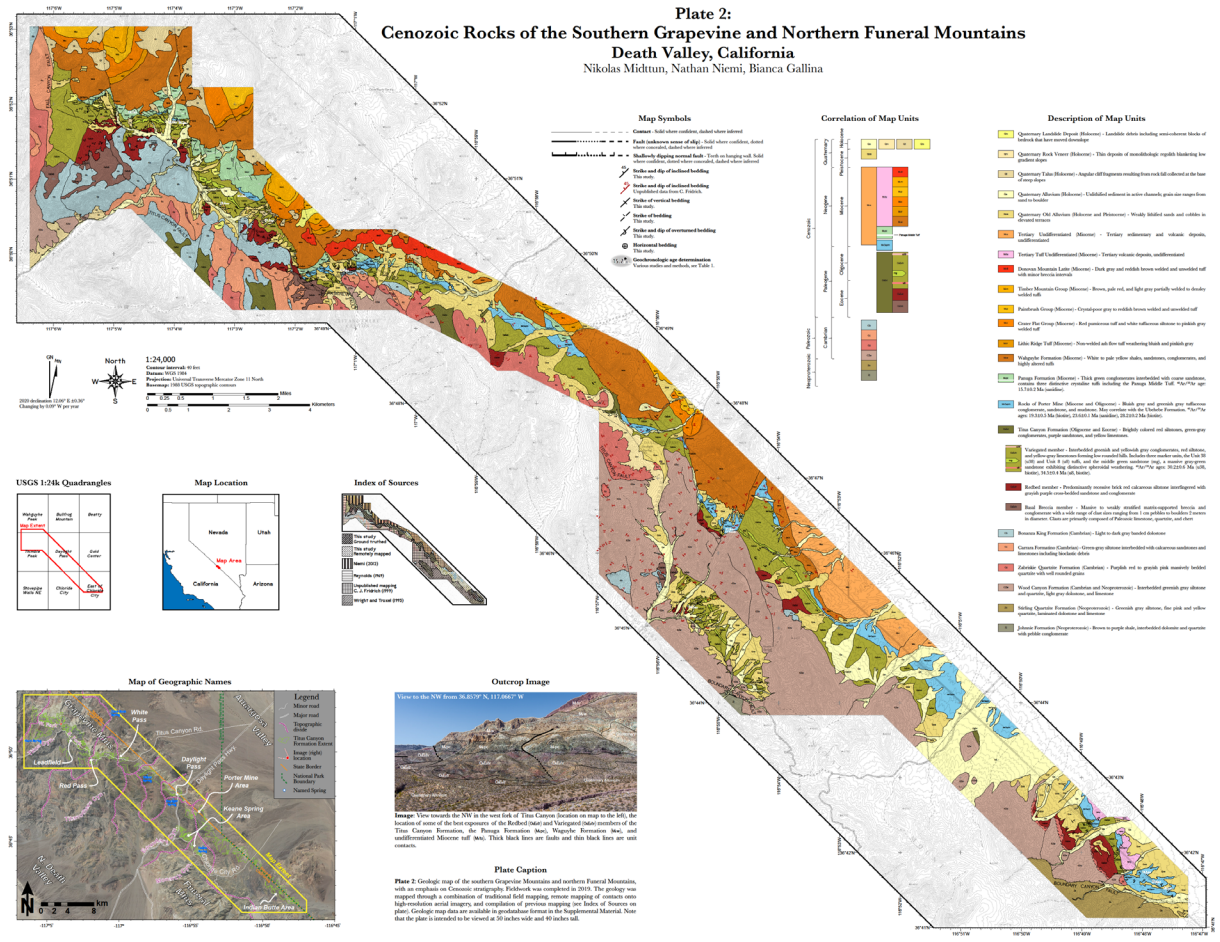


Figure A.2: Geologic map of the southern Grapevine Mountains and northern Funeral Mountains, with an emphasis on Cenozoic stratigraphy.
Geologic map database can be interactively viewed and downloaded at https://arcg.is/1rriKn.

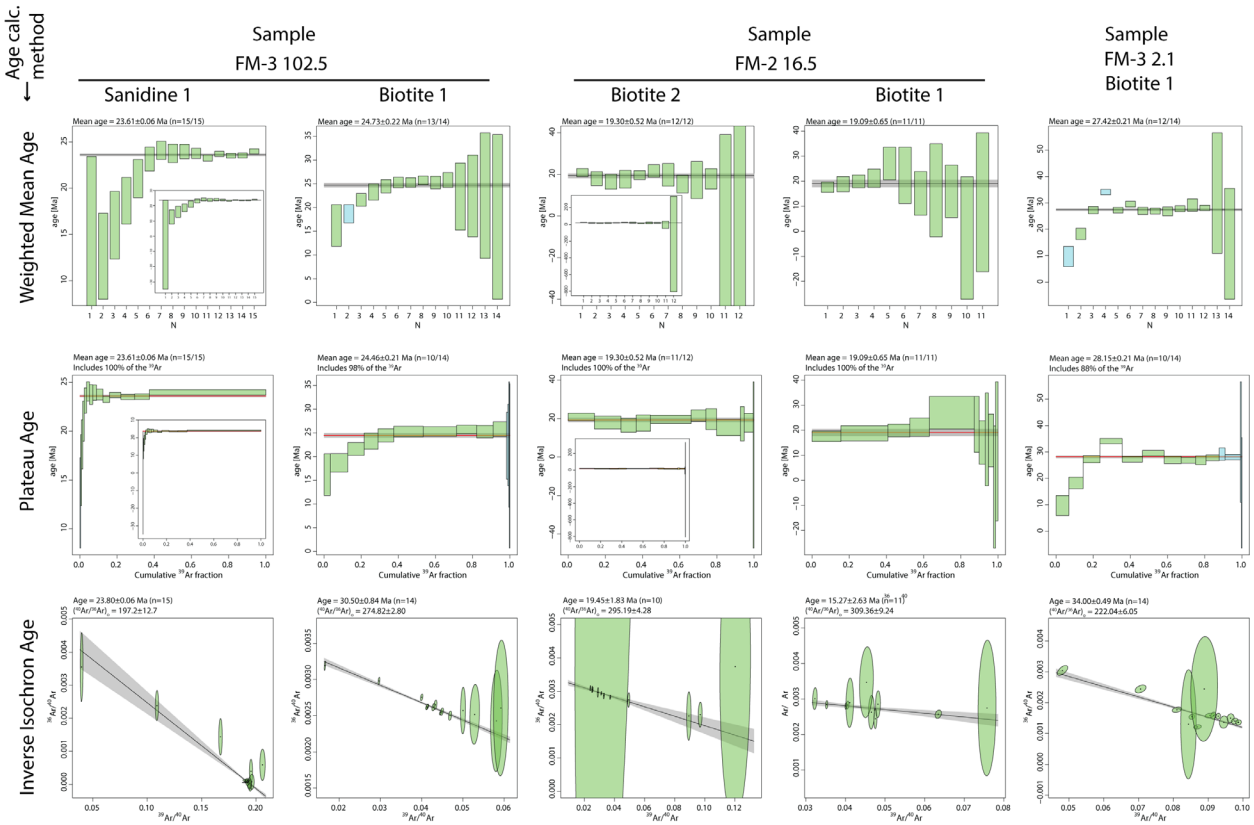


Figure A.3: Supplementary plots of $^{40}Ar/^{39}Ar$ analytical data (Gutenkunst, 2006). *Recalculated $^{40}Ar/^{39}Ar$ analytical plots for data originally from Gutenkunst (2006). Each column represents one of five mineral fractions analyzed from three samples (note: two samples have two mineral fractions analyzed). Each row shows the relevant plot for an age calculation method, including weighted mean (top), plateau (middle), and inverse isochron (bottom). Uncertainties are ±1σ. Insets on some of the plots show the full range of the data while the main plot shows a zoomed in view to better show the behavior of steps near the calculated age.*

Table A.1:Analytical data for Titus Canyon detrital zircon U-Pb analyses.

				Isotopic Ratio						Error	Apparent Age (Ma)						Best Age (Ma)	
Analysis	U (ppm)	206Pb 204Pb	U/Th	206Pb* 207Pb*	± (%)	207Pb* 235U*	± (%)	206Pb* 238U	± (%)		206Pb* 238U*	± (Ma)	207Pb* 235U	± (Ma)	206Pb* 207Pb*	± (Ma)	Best age (Ma)	± (Ma)
TC-09-04-1	380	136901	1.1	5.3178	0.2	13.8279	2.5	0.5333	2.5	1.00	2755.4	56.6	2738.0	24.0	2725.1	2.9	2725.1	2.9
TC-09-04-2	487	3317	1.2	20.8816	9.8	0.1573	10.0	0.0238	1.8	0.18	151.8	2.6	148.3	13.7	93.8	232.6	151.8	2.6
TC-09-04-4	232	3876	0.9	22.3689	12.5	0.1577	12.6	0.0256	0.8	0.07	162.9	1.3	148.7	17.4	-71.7	307.5	162.9	1.3
TC-09-04-5	109	11691	4.0	13.0237	4.1	1.9792	7.7	0.1869	6.6	0.85	1104.8	66.8	1108.4	52.2	1115.5	81.0	1115.5	81.0
TC-09-04-6	712	15432	2.6	20.9698	2.9	0.1656	3.3	0.0252	1.7	0.50	160.4	2.6	155.6	4.8	83.8	68.1	160.4	2.6
TC-09-04-7	497	5845	4.6	21.0278	9.1	0.1054	9.3	0.0161	1.5	0.16	102.8	1.5	101.8	9.0	77.2	217.7	102.8	1.5
TC-09-04-8	742	3237	4.2	26.5953	36.6	0.0270	36.7	0.0052	1.6	0.04	33.5	0.5	27.1	9.8	-513.3	1005.6	33.5	0.5
TC-09-04-9	68	14312	1.0	9.0065	1.2	5.1452	2.2	0.3361	1.8	0.82	1867.8	29.1	1843.6	18.5	1816.3	22.5	1816.3	22.5
TC-09-04-10	133	2357	1.3	18.5666	13.2	0.1777	15.5	0.0239	8.0	0.52	152.5	12.1	166.1	23.7	365.2	299.8	152.5	12.1
TC-09-04-11	28	7986	1.2	7.7794	2.8	6.7586	3.1	0.3813	1.2	0.38	2082.5	21.0	2080.3	27.1	2078.1	49.8	2078.1	49.8
TC-09-04-12	98	14191	1.7	13.2436	3.0	1.8753	3.3	0.1801	1.2	0.38	1067.7	12.1	1072.4	21.7	1082.1	60.8	1082.1	60.8
TC-09-04-13	48	14030	1.2	5.5565	0.8	12.7367	1.2	0.5133	0.9	0.78	2670.6	20.6	2660.4	11.3	2652.6	12.5	2652.6	12.5
TC-09-04-14	228	3315	1.0	23.2180	18.8	0.1444	18.9	0.0243	2.0	0.11	154.9	3.1	137.0	24.2	-163.5	469.9	154.9	3.1
TC-09-04-15	584	2545	1.5	25.9055	27.1	0.0290	27.4	0.0054	3.6	0.13	35.0	1.3	29.0	7.8	-443.7	725.3	35.0	1.3
TC-09-04-16	287	3690	1.6	21.5640	12.3	0.1528	12.4	0.0239	1.7	0.13	152.2	2.5	144.4	16.7	17.1	296.0	152.2	2.5
TC-09-04-17	183	622	0.8	7.2643	328.1	0.0924	328.2	0.0049	6.3	0.02	31.3	2.0	89.7	289.4	2198.0	475.4	2198.0	475.4
TC-09-04-18	128	5554	1.8	19.2504	9.1	0.4854	9.2	0.0678	1.1	0.12	422.7	4.6	401.7	30.4	283.1	208.3	422.7	4.6
TC-09-04-19	87	9938	1.1	14.0192	4.2	1.7754	4.6	0.1805	1.9	0.42	1069.8	19.1	1036.5	30.0	966.9	85.7	966.9	85.7
TC-09-04-20	325	7623	1.8	22.0931	16.4	0.1558	16.5	0.0250	1.6	0.10	159.0	2.5	147.0	22.5	-41.5	400.5	159.0	2.5
TC-09-04-21	186	7218	2.0	18.3018	5.0	0.4773	5.3	0.0634	1.5	0.28	396.0	5.6	396.2	17.2	397.5	113.1	396.0	5.6
TC-09-04-22	324	53922	26.7	8.4187	0.4	5.7392	1.0	0.3504	0.9	0.92	1936.6	15.7	1937.3	8.8	1938.0	7.3	1938.0	7.3
TC-09-04-23	94	17005	2.9	8.7548	0.8	5.2960	1.6	0.3363	1.5	0.89	1868.7	23.8	1868.2	14.1	1867.6	13.7	1867.6	13.7
TC-09-04-24	84	20470	1.4	6.7895	1.0	8.7749	1.4	0.4321	1.1	0.74	2315.2	20.9	2314.9	13.2	2314.6	16.6	2314.6	16.6
TC-09-04-25	1177	21758	1.6	20.3359	3.0	0.1724	3.6	0.0254	2.0	0.55	161.9	3.2	161.5	5.4	156.1	70.3	161.9	3.2
TC-09-04-27	284	788	2.2	30.3709	133.0	0.0218	133.1	0.0048	3.3	0.03	30.9	1.0	21.9	28.9	-881.7	0.0	30.9	1.0

TC-09-04-28	98	23613	1.4	8.6107	1.1	5.5827	1.3	0.3486	0.7	0.52	1928.1	11.1	1913.4	10.9	1897.5	19.5	1897.5	19.5
TC-09-04-29	441	69839	4.0	9.0383	0.4	4.8812	1.2	0.3200	1.1	0.93	1789.6	16.9	1799.0	9.8	1809.9	7.6	1809.9	7.6
TC-09-04-30	5453	13796	5.3	21.5495	2.5	0.0314	3.7	0.0049	2.7	0.73	31.6	0.9	31.4	1.1	18.7	60.4	31.6	0.9
TC-09-04-31	50	13925	3.0	4.8503	0.7	16.5468	2.3	0.5821	2.2	0.96	2957.2	52.2	2908.9	22.0	2875.7	11.0	2875.7	11.0
TC-09-04-32	337	5493	1.0	21.5329	10.6	0.1569	10.6	0.0245	0.7	0.06	156.0	1.0	147.9	14.6	20.5	254.9	156.0	1.0
TC-09-04-33	73	5589	3.3	13.5639	4.2	1.8084	4.7	0.1779	1.9	0.42	1055.5	18.9	1048.5	30.4	1033.9	85.4	1033.9	85.4
TC-09-04-34	426	1302	3.6	43.1809	41.3	0.0167	41.4	0.0052	3.2	0.08	33.6	1.1	16.8	6.9	-2038.6	194.0	33.6	1.1
TC-09-04-35	318	1048	4.0	39.6712	58.4	0.0180	58.7	0.0052	5.1	0.09	33.3	1.7	18.1	10.5	-1729.8	313.6	33.3	1.7
TC-09-04-37	98	29944	2.2	8.7895	1.1	5.1911	2.2	0.3309	1.9	0.87	1842.8	30.0	1851.2	18.3	1860.5	19.3	1860.5	19.3
TC-09-04-38	530	8477	0.9	20.1532	7.5	0.1719	7.7	0.0251	1.6	0.21	159.9	2.6	161.0	11.4	177.2	175.3	159.9	2.6
TC-09-04-39	68	11934	3.0	8.8724	1.4	4.9965	2.6	0.3215	2.2	0.84	1797.1	34.7	1818.7	22.4	1843.5	26.1	1843.5	26.1
TC-09-04-40	102	23911	3.6	9.7850	1.2	4.0396	3.3	0.2867	3.1	0.93	1624.9	44.3	1642.2	27.0	1664.4	22.4	1664.4	22.4
TC-09-04-41	1629	4059	2.1	22.9879	10.5	0.0314	10.6	0.0052	1.2	0.11	33.7	0.4	31.4	3.3	-138.8	260.6	33.7	0.4
TC-09-04-43	496	7417	4.9	20.3564	10.5	0.1760	10.6	0.0260	0.9	0.09	165.3	1.5	164.6	16.0	153.8	246.8	165.3	1.5
TC-09-04-44	547	5843	1.6	21.3648	4.1	0.1595	6.2	0.0247	4.7	0.76	157.4	7.3	150.3	8.7	39.4	97.9	157.4	7.3
TC-09-04-45	954	24185	2.6	20.4219	2.7	0.1634	4.4	0.0242	3.4	0.79	154.1	5.2	153.6	6.2	146.3	62.6	154.1	5.2
TC-09-04-46	180	2786	1.9	19.7771	22.6	0.1703	22.8	0.0244	3.0	0.13	155.6	4.6	159.7	33.7	221.0	529.1	155.6	4.6
TC-09-04-47	231	33571	2.6	11.2425	0.4	2.9538	1.7	0.2408	1.6	0.98	1391.1	20.3	1395.8	12.6	1403.0	7.1	1403.0	7.1
TC-09-04-49	73	17154	1.2	8.8900	1.3	5.0043	2.2	0.3227	1.8	0.81	1802.7	28.6	1820.1	19.0	1839.9	23.9	1839.9	23.9
TC-09-04-50	161	16775	82.7	13.4234	1.8	1.8239	2.5	0.1776	1.7	0.67	1053.7	16.3	1054.1	16.3	1055.0	37.1	1055.0	37.1
TC-09-04-51	144	582	1.2	5.0040	189.4	0.1176	189.4	0.0043	3.0	0.02	27.5	0.8	112.9	205.2	2824.9	450.1	2824.9	450.1
TC-09-04-52	107	10122	2.5	13.4371	2.1	1.8544	2.7	0.1807	1.8	0.65	1070.9	17.3	1065.0	17.8	1052.9	41.4	1052.9	41.4
TC-09-04-53	262	20253	1.9	11.0315	0.8	2.9373	2.1	0.2350	1.9	0.92	1360.7	23.4	1391.6	15.8	1439.2	15.8	1439.2	15.8
TC-09-04-55	211	835	2.0	29.7726	13.7	0.1138	13.8	0.0246	1.6	0.12	156.6	2.5	109.5	14.3	-824.6	392.4	156.6	2.5
TC-09-04-56	84	830	2.0	28.3141	14.4	0.3686	14.4	0.0757	1.1	0.08	470.3	5.0	318.6	39.5	-683.5	399.6	470.3	5.0
TC-09-04-57	267	1469	0.9	26.2256	16.7	0.1282	16.7	0.0244	1.2	0.07	155.3	1.8	122.5	19.3	-476.1	443.8	155.3	1.8
TC-09-04-58	643	3223	2.6	21.5817	4.6	0.1492	4.9	0.0234	1.5	0.31	148.8	2.2	141.2	6.4	15.1	111.2	148.8	2.2
TC-09-04-59	266	506	2.2	34.4379	46.3	0.0208	46.4	0.0052	3.2	0.07	33.5	1.1	20.9	9.6	-1260.2	1520.7	33.5	1.1
TC-09-04-60	313	41838	4.1	9.0439	0.4	4.9138	2.1	0.3223	2.0	0.98	1801.0	31.7	1804.6	17.3	1808.8	6.9	1808.8	6.9

TC-09-04-61	60	6011	1.5	13.3443	4.5	1.7517	4.8	0.1695	1.7	0.36	1009.5	16.1	1027.8	31.1	1066.9	90.3	1066.9	90.3
TC-09-04-62	133	18264	3.2	10.8065	1.4	3.1719	2.6	0.2486	2.2	0.84	1431.3	28.4	1450.3	20.3	1478.4	26.8	1478.4	26.8
TC-09-04-63	1606	5026	4.3	23.1668	9.4	0.0342	9.5	0.0057	1.7	0.18	37.0	0.6	34.2	3.2	-158.1	233.3	37.0	0.6
TC-09-04-64	117	21770	2.7	9.0960	1.0	4.7368	4.3	0.3125	4.1	0.97	1753.0	63.5	1773.8	35.7	1798.4	18.1	1798.4	18.1
TC-09-04-65	448	1651	2.3	34.1019	76.6	0.0214	76.7	0.0053	2.7	0.03	34.0	0.9	21.5	16.3	-1229.5	1018.1	34.0	0.9
TC-09-04-66	427	7036	2.1	21.0694	10.2	0.1853	10.6	0.0283	2.9	0.27	180.0	5.1	172.6	16.8	72.6	242.1	180.0	5.1
TC-09-04-67	503	1497	3.6	37.0710	38.6	0.0203	38.7	0.0055	1.7	0.04	35.2	0.6	20.5	7.8	-1498.3	1322.9	35.2	0.6
TC-09-04-69	837	11994	1.4	20.9746	3.3	0.1647	4.3	0.0250	2.8	0.64	159.5	4.4	154.8	6.2	83.2	79.3	159.5	4.4
TC-09-04-70	3463	8882	6.2	22.5372	6.7	0.0344	7.1	0.0056	2.4	0.34	36.1	0.9	34.3	2.4	-90.0	164.7	36.1	0.9
TC-09-04-72	362	37390	3.2	12.8019	1.3	2.0948	2.1	0.1945	1.7	0.80	1145.7	17.9	1147.1	14.6	1149.8	25.2	1149.8	25.2
TC-09-04-73	115	34506	2.1	6.7980	0.7	8.2495	1.8	0.4067	1.7	0.92	2200.0	31.1	2258.8	16.4	2312.5	11.9	2312.5	11.9
TC-09-04-74	295	2568	1.3	17.0185	26.0	0.2815	26.5	0.0347	5.2	0.20	220.2	11.2	251.8	59.2	558.2	575.9	220.2	11.2
TC-09-04-75	1011	2672	11.3	20.7906	11.4	0.0347	11.5	0.0052	1.4	0.12	33.7	0.5	34.7	3.9	104.1	270.7	33.7	0.5
TC-09-04-76	862	9719	6.8	20.1123	4.9	0.1688	5.2	0.0246	1.8	0.34	156.8	2.7	158.4	7.6	181.9	113.2	156.8	2.7
TC-09-04-78	87	25241	2.2	4.6587	0.4	16.7460	2.5	0.5658	2.5	0.99	2890.6	58.2	2920.4	24.2	2941.0	6.0	2941.0	6.0
TC-09-04-79	134	27778	2.8	8.8810	0.9	5.0120	2.6	0.3228	2.4	0.94	1803.5	38.2	1821.4	21.9	1841.8	16.0	1841.8	16.0
TC-09-04-80	110	15015	0.9	10.8834	1.6	3.1086	2.6	0.2454	2.0	0.78	1414.6	25.7	1434.8	19.8	1465.0	30.4	1465.0	30.4
TC-09-04-81	124	26726	2.4	10.9152	1.8	3.2271	2.3	0.2555	1.4	0.61	1466.6	18.7	1463.7	18.0	1459.4	34.8	1459.4	34.8
TC-09-04-82	284	67527	3.1	8.8443	0.4	5.1723	2.3	0.3318	2.3	0.99	1847.0	36.8	1848.1	19.7	1849.3	6.7	1849.3	6.7
TC-09-04-84	129	25576	0.8	8.9031	0.9	4.9419	2.2	0.3191	2.0	0.91	1785.4	31.4	1809.4	18.8	1837.3	17.1	1837.3	17.1
TC-09-04-85	371	6084	1.9	20.6161	13.8	0.1746	13.9	0.0261	1.6	0.12	166.1	2.7	163.4	21.0	124.0	327.1	166.1	2.7
TC-09-04-86	135	2192	1.1	27.6430	15.9	0.1247	16.1	0.0250	2.2	0.14	159.1	3.5	119.3	18.1	-617.6	436.5	159.1	3.5
TC-09-04-88	1048	668	7.1	27.4020	41.6	0.0275	41.9	0.0055	4.7	0.11	35.1	1.7	27.5	11.4	-593.8	1171.2	35.1	1.7
TC-09-04-89	283	397	0.8	30.7940	31.2	0.0220	31.4	0.0049	3.5	0.11	31.6	1.1	22.1	6.8	-921.9	925.8	31.6	1.1
TC-09-04-90	127	9499	1.0	13.5277	1.8	1.8832	2.9	0.1848	2.3	0.78	1092.9	22.9	1075.2	19.4	1039.3	36.9	1039.3	36.9
TC-09-04-91	162	26823	2.8	9.5916	0.9	4.5094	1.6	0.3137	1.3	0.84	1758.9	20.7	1732.7	13.3	1701.2	15.8	1701.2	15.8
TC-09-04-92	302	1067	1.9	5.1028	559.6	0.1400	559.6	0.0052	4.4	0.01	33.3	1.5	133.1	856.1	2792.9	594.4	2792.9	594.4
TC-09-04-93	270	25538	2.0	13.1498	0.9	1.9587	1.9	0.1868	1.6	0.89	1104.0	16.7	1101.4	12.5	1096.3	17.3	1096.3	17.3
TC-09-04-96	1366	2196	6.1	23.1388	16.0	0.0324	16.1	0.0054	1.8	0.11	35.0	0.6	32.4	5.1	-155.0	399.8	35.0	0.6

TC-09-04-97	307	6213	1.9	22.2882	11.9	0.1463	12.6	0.0236	4.3	0.34	150.6	6.4	138.6	16.4	-62.9	290.9	150.6	6.4
TC-09-04-98	109	148	1.8	-32.2328	118.0	-0.0206	118.2	0.0048	6.9	0.06	30.9	2.1	-21.1	-25.2	0.0	1290.1	30.9	2.1
TC-09-04-99	50	12879	1.6	8.6628	2.5	5.6482	2.8	0.3549	1.4	0.49	1957.8	23.2	1923.5	24.4	1886.7	44.5	1886.7	44.5
TC-09-04-100	1222	4798	5.4	22.6642	8.3	0.0333	8.7	0.0055	2.5	0.29	35.2	0.9	33.3	2.8	-103.8	204.6	35.2	0.9
TC19-01NN-1	560	196695	3.3	20.2421	1.0	0.1873	1.7	0.0276	1.3	0.81	175.2	2.3	174.3	2.7	162.3	23.1	175.2	2.3
TC19-01NN-2	1249	287010	3.4	19.8061	0.9	0.2309	1.4	0.0332	1.1	0.76	210.8	2.2	210.9	2.7	212.6	21.1	210.8	2.2
TC19-01NN-3	932	254312	1.9	20.5270	1.1	0.1099	1.8	0.0164	1.4	0.78	104.9	1.4	105.9	1.8	128.8	25.9	104.9	1.4
TC19-01NN-4	396	53738	2.0	20.2693	1.3	0.1788	1.9	0.0265	1.3	0.71	168.4	2.2	167.0	2.9	147.5	31.3	168.4	2.2
TC19-01NN-5	79	16285	1.3	14.6384	1.8	0.2449	2.2	0.0264	1.2	0.55	167.9	2.0	222.4	4.4	848.3	38.3	167.9	2.0
TC19-01NN-6	345	40310	1.8	20.1366	1.2	0.1871	1.9	0.0276	1.5	0.79	175.4	2.6	174.1	3.1	157.2	27.8	175.4	2.6
TC19-01NN-7	139	27281	1.1	19.9209	1.5	0.1889	2.0	0.0276	1.2	0.63	175.8	2.2	175.7	3.2	174.3	36.2	175.8	2.2
TC19-01NN-8	128	11585	2.1	20.3012	1.3	0.1848	2.2	0.0280	1.2	0.52	178.0	2.0	172.2	3.5	93.8	44.5	178.0	2.0
TC19-01NN-9	238	48626	1.9	19.8295	1.1	0.1870	1.7	0.0271	1.2	0.75	172.4	2.1	174.1	2.6	196.2	25.6	172.4	2.1
TC19-01NN-10	66	13024	3.0	20.2791	1.6	0.1901	2.0	0.0287	1.2	0.59	182.2	2.2	176.7	3.3	103.3	38.7	182.2	2.2
TC19-01NN-11	238	76055	2.0	19.8021	1.2	0.2065	1.8	0.0298	1.4	0.75	189.4	2.5	190.6	3.1	205.4	27.8	189.4	2.5
TC19-01NN-12	358	34595	3.0	20.4203	1.6	0.1126	2.1	0.0168	1.4	0.67	107.7	1.5	108.3	2.2	122.1	36.6	107.7	1.5
TC19-01NN-13	785	254995	1.6	20.0197	0.9	0.1724	1.5	0.0251	1.3	0.82	159.8	2.0	161.5	2.3	186.2	20.4	159.8	2.0
TC19-01NN-14	489	173806	0.9	19.9392	1.3	0.1758	1.9	0.0255	1.4	0.73	162.4	2.2	164.5	2.9	194.4	30.7	162.4	2.2
TC19-01NN-15	187	61366	3.5	20.5939	1.3	0.1630	2.3	0.0245	1.9	0.83	156.0	2.9	153.4	3.2	112.2	30.0	156.0	2.9
TC19-01NN-16	528	95823	1.2	19.8714	1.1	0.2292	1.6	0.0332	1.2	0.74	210.2	2.4	209.5	3.0	201.4	25.1	210.2	2.4
TC19-01NN-17	34	3552	1.5	20.1878	2.8	0.1602	3.7	0.0256	1.0	0.28	163.1	1.7	150.9	5.2	NA	NA	163.1	1.7
TC19-01NN-18	111	51249	2.4	19.4758	1.9	0.1650	2.5	0.0235	1.5	0.61	149.4	2.2	155.1	3.5	242.0	44.9	149.4	2.2
TC19-01NN-19	202	145513	2.7	19.5497	1.5	0.2473	2.1	0.0351	1.4	0.68	222.7	3.1	224.3	4.2	241.7	35.3	222.7	3.1
TC19-01NN-20	411	20609	1.9	20.6089	1.5	0.1142	1.9	0.0173	1.3	0.65	110.7	1.4	109.8	2.0	89.5	34.7	110.7	1.4
TC19-01NN-21	110	18407	3.3	20.1797	1.6	0.1887	2.0	0.0281	1.2	0.59	178.5	2.1	175.5	3.3	135.8	38.6	178.5	2.1
TC19-01NN-22	104	56643	2.6	21.9519	2.5	0.0902	2.7	0.0145	1.2	0.43	92.5	1.1	87.7	2.3	NA	NA	92.5	1.1
TC19-01NN-23	402	17176	5.7	21.2987	1.1	0.0884	1.9	0.0139	1.3	0.66	89.1	1.1	86.0	1.6	2.1	NA	89.1	1.1
TC19-01NN-24	972	105132	1.8	20.7663	1.1	0.1099	1.7	0.0166	1.2	0.74	106.1	1.3	105.9	1.7	99.5	26.1	106.1	1.3

TC19-01NN-25	499	133839	3.3	20.2535	0.9	0.1908	1.6	0.0281	1.3	0.80	178.6	2.2	177.3	2.6	159.1	22.2	178.6	2.2
TC19-01NN-26	273	32297	3.6	19.5019	1.2	0.2483	1.6	0.0355	1.0	0.59	224.6	2.1	225.2	3.3	231.5	30.3	224.6	2.1
TC19-01NN-27	78	27763	1.1	20.3246	2.5	0.1703	2.9	0.0254	1.5	0.53	161.6	2.4	159.7	4.3	130.7	58.1	161.6	2.4
TC19-01NN-28	354	27580	3.1	20.8031	1.0	0.1087	1.7	0.0166	1.4	0.80	106.1	1.5	104.8	1.7	74.9	24.9	106.1	1.5
TC19-01NN-29	232	179945	1.4	20.5123	1.3	0.1831	1.9	0.0273	1.4	0.74	173.6	2.4	170.7	3.0	130.7	30.2	173.6	2.4
TC19-01NN-30	352	62347	2.6	16.3842	1.1	0.2207	1.9	0.0264	1.5	0.80	167.7	2.5	202.5	3.4	629.9	24.3	167.7	2.5
TC19-01NN-31	747	172945	3.0	19.4910	0.7	0.2441	1.4	0.0346	1.2	0.86	219.3	2.5	221.8	2.7	248.2	16.0	219.3	2.5
TC19-01NN-32	190	72160	1.9	20.1686	1.3	0.1736	1.8	0.0255	1.2	0.66	162.5	1.9	162.6	2.6	163.2	30.8	162.5	1.9
TC19-01NN-33	192	38335	4.4	19.7288	1.6	0.1927	1.8	0.0278	0.9	0.51	176.7	1.7	178.9	3.0	208.3	36.7	176.7	1.7
TC19-01NN-34	280	95671	2.5	19.7934	1.2	0.1760	1.5	0.0253	1.0	0.64	161.4	1.5	164.6	2.3	211.5	26.8	161.4	1.5
TC19-01NN-35	103	15668	2.3	20.2433	1.3	0.1847	1.7	0.0277	1.1	0.65	175.9	1.9	172.1	2.7	120.2	30.6	175.9	1.9
TC19-01NN-36	77	8574	1.4	20.1379	1.8	0.1824	2.6	0.0276	1.8	0.69	175.6	3.1	170.1	4.1	94.7	45.0	175.6	3.1
TC19-01NN-37	149	62636	1.5	19.7905	1.6	0.1923	2.1	0.0277	1.3	0.62	176.4	2.2	178.6	3.4	207.3	37.7	176.4	2.2
TC19-01NN-38	173	79315	0.9	19.9063	1.6	0.1685	2.0	0.0244	1.2	0.59	155.6	1.8	158.1	2.9	196.0	36.7	155.6	1.8
TC19-01NN-39	138	52098	1.5	19.0388	2.5	0.1803	2.8	0.0251	1.2	0.42	159.5	1.8	168.3	4.3	293.6	57.0	159.5	1.8
TC19-01NN-40	510	32823	4.7	20.6533	1.1	0.0846	1.9	0.0128	1.5	0.80	82.0	1.2	82.4	1.5	95.3	27.2	82.0	1.2
TC19-01NN-41	873	97024	6.6	19.4831	1.0	0.2441	1.8	0.0346	1.6	0.84	219.4	3.4	221.7	3.7	246.3	22.9	219.4	3.4
TC19-01NN-42	191	100084	2.7	20.1311	1.3	0.1858	1.9	0.0272	1.4	0.73	173.2	2.4	173.1	3.1	170.8	31.0	173.2	2.4
TC19-01NN-43	117	19129	2.0	19.9076	1.5	0.1881	1.9	0.0276	1.2	0.64	175.4	2.1	175.0	3.1	169.3	34.2	175.4	2.1
TC19-01NN-44	167	8319	2.9	20.7119	2.1	0.1007	3.0	0.0157	1.1	0.38	100.5	1.1	97.5	2.8	23.9	NA	100.5	1.1
TC19-01NN-45	282	99209	3.3	20.4611	1.3	0.1124	1.8	0.0167	1.3	0.71	106.9	1.4	108.1	1.8	134.7	29.5	106.9	1.4
TC19-01NN-46	515	156930	2.1	19.7335	0.8	0.2406	1.2	0.0345	0.9	0.77	218.6	2.0	218.9	2.4	222.3	18.1	218.6	2.0
TC19-01NN-47	254	170191	2.1	20.2908	1.0	0.1747	1.8	0.0257	1.5	0.84	163.9	2.5	163.5	2.7	158.3	23.1	163.9	2.5
TC19-01NN-48	601	159464	1.3	20.2683	1.0	0.1753	1.7	0.0258	1.4	0.81	164.3	2.2	164.0	2.6	159.1	23.3	164.3	2.2
TC19-01NN-49	977	70409	2.0	20.6877	0.8	0.1218	1.1	0.0184	0.8	0.66	117.3	0.9	116.7	1.3	105.2	20.3	117.3	0.9
TC19-01NN-50	575	245886	3.2	20.4963	1.2	0.1137	1.7	0.0169	1.2	0.72	108.2	1.3	109.3	1.8	134.4	27.9	108.2	1.3
TC19-01NN-51	808	212512	1.8	20.1764	0.9	0.1128	1.5	0.0165	1.2	0.78	105.7	1.2	108.5	1.5	170.8	21.5	105.7	1.2
TC19-01NN-52	735	102763	1.7	20.4699	1.2	0.1716	1.8	0.0256	1.4	0.76	162.8	2.2	160.8	2.7	131.9	27.3	162.8	2.2
TC19-01NN-53	341	104669	2.9	20.8318	1.4	0.1101	1.8	0.0167	1.2	0.63	106.8	1.2	106.1	1.8	90.9	33.6	106.8	1.2

TC19-01NN-54	215	30188	5.8	19.9726	1.2	0.1970	1.9	0.0288	1.4	0.78	183.2	2.6	182.6	3.1	175.2	27.3	183.2	2.6
TC19-01NN-55	586	243489	1.4	19.3816	0.7	0.2917	1.4	0.0411	1.2	0.85	259.3	3.0	259.9	3.2	264.6	16.7	259.3	3.0
TC19-01NN-56	372	21404	2.3	20.3167	1.4	0.1132	1.8	0.0169	1.1	0.63	108.2	1.2	108.9	1.8	125.1	32.3	108.2	1.2
TC19-01NN-57	192	85155	1.8	20.4976	1.5	0.1826	2.0	0.0272	1.3	0.66	173.3	2.3	170.3	3.2	129.0	36.0	173.3	2.3
TC19-01NN-58	75	14420	0.9	19.7390	1.8	0.1887	2.3	0.0276	1.4	0.62	175.4	2.5	175.6	3.7	178.3	42.2	175.4	2.5
TC19-01NN-59	216	42957	1.9	20.1367	1.3	0.1828	1.8	0.0269	1.2	0.67	171.1	2.0	170.5	2.8	162.1	30.6	171.1	2.0
TC19-01NN-60	147	286795	1.3	19.7115	1.5	0.1867	1.8	0.0267	1.0	0.56	170.0	1.7	173.8	3.0	225.4	35.4	170.0	1.7
TC19-01NN-61	170	16222	2.2	19.4560	1.3	0.1774	2.0	0.0255	1.2	0.62	162.2	2.0	165.8	3.0	216.8	35.8	162.2	2.0
TC19-01NN-62	1934	31965	1.2	16.0960	1.1	0.3161	1.8	0.0372	1.5	0.81	235.4	3.4	278.9	4.5	662.0	23.3	235.4	3.4
TC19-01NN-63	223	63999	2.1	21.3232	1.9	0.0984	2.5	0.0153	1.7	0.67	97.9	1.6	95.3	2.3	31.7	NA	97.9	1.6
TC19-01NN-64	141	77918	1.4	19.7734	1.5	0.1889	1.8	0.0272	1.1	0.59	173.1	1.8	175.7	2.9	210.7	33.9	173.1	1.8
TC19-01NN-65	405	109166	3.2	19.8127	1.2	0.2480	1.6	0.0358	1.2	0.71	226.5	2.6	224.9	3.3	208.6	26.8	226.5	2.6
TC19-01NN-66	736	823865	1.5	20.0351	0.9	0.1898	1.4	0.0276	1.0	0.74	175.6	1.8	176.5	2.2	188.0	21.3	175.6	1.8
TC19-01NN-67	369	54244	2.6	20.0518	1.1	0.2470	1.7	0.0361	1.3	0.77	228.9	2.9	224.1	3.3	174.7	24.9	228.9	2.9
TC19-01NN-68	279	44268	3.3	19.7608	0.9	0.1868	1.5	0.0270	1.1	0.77	171.6	1.9	173.9	2.4	204.6	21.7	171.6	1.9
TC19-01NN-69	382	101004	3.2	20.8070	1.5	0.1124	2.0	0.0170	1.4	0.69	108.8	1.5	108.1	2.1	92.6	35.1	108.8	1.5
TC19-01NN-70	300	35005	3.1	20.6528	1.4	0.1000	1.8	0.0151	1.0	0.58	96.8	1.0	96.8	1.6	96.7	34.3	96.8	1.0
TC19-01NN-71	481	153744	3.9	20.3495	1.1	0.1866	1.9	0.0276	1.5	0.82	175.7	2.6	173.7	3.0	147.6	25.2	175.7	2.6
TC19-01NN-72	343	38256	3.2	19.8924	1.2	0.2481	1.6	0.0361	1.2	0.71	228.7	2.6	225.1	3.3	187.3	26.8	228.7	2.6
TC19-01NN-73	146	20623	2.0	19.9287	1.4	0.1806	1.9	0.0265	1.3	0.67	168.8	2.1	168.6	2.9	165.8	32.6	168.8	2.1
TC19-01NN-74	117	17814	1.6	19.8089	1.6	0.1704	2.2	0.0249	1.3	0.58	158.7	2.0	159.7	3.2	175.1	41.5	158.7	2.0
TC19-01NN-75	62	5908	1.9	19.7556	2.0	0.1720	2.5	0.0260	1.5	0.59	165.2	2.4	161.1	3.8	101.5	48.3	165.2	2.4
TC19-01NN-76	607	68648	1.4	20.5179	1.1	0.1143	1.6	0.0171	1.2	0.75	109.4	1.3	109.9	1.7	121.0	25.4	109.4	1.3
TC19-01NN-77	449	70069	2.8	20.4820	1.0	0.1182	1.6	0.0177	1.3	0.80	112.9	1.5	113.5	1.7	125.0	22.7	112.9	1.5
TC19-01NN-78	59	4906	1.5	20.0815	2.3	0.1618	2.6	0.0251	1.2	0.46	159.8	1.9	152.3	3.7	36.9	NA	159.8	1.9
TC19-01NN-79	1054	227938	1.6	19.9708	1.0	0.2415	1.6	0.0351	1.2	0.77	222.1	2.7	219.6	3.2	193.1	24.3	222.1	2.7
TC19-01NN-80	776	150036	3.3	19.5959	1.0	0.2397	1.7	0.0342	1.3	0.81	216.5	2.9	218.2	3.2	235.6	22.1	216.5	2.9
TC19-01NN-81	583	187752	2.3	19.0381	1.1	0.3055	1.7	0.0423	1.3	0.76	267.0	3.4	270.7	4.0	302.8	25.1	267.0	3.4
TC19-01NN-82	123	234701	1.6	19.6979	1.7	0.1910	2.0	0.0274	1.1	0.54	174.0	1.8	177.5	3.3	223.9	39.0	174.0	1.8

TC19-01NN-83	1919	477015	2.8	20.1697	0.8	0.1814	1.5	0.0266	1.3	0.86	169.2	2.2	169.3	2.4	170.0	18.1	169.2	2.2
TC19-01NN-84	99	22219	2.0	19.9478	1.5	0.1866	2.0	0.0274	1.2	0.61	174.3	2.1	173.7	3.1	166.2	36.2	174.3	2.1
TC19-01NN-85	82	21062	1.9	20.1027	1.6	0.1826	2.0	0.0270	1.2	0.62	172.0	2.1	170.3	3.2	146.2	37.4	172.0	2.1
TC19-01NN-86	89	20113	1.7	19.7694	1.9	0.1689	2.4	0.0246	1.3	0.57	156.8	2.1	158.5	3.5	184.0	45.7	156.8	2.1
TC19-01NN-87	152	30189	1.1	20.3056	1.4	0.1685	2.1	0.0251	1.6	0.75	159.8	2.5	158.1	3.1	132.1	33.1	159.8	2.5
TC19-01NN-88	586	1232980	2.4	20.8198	1.1	0.1140	1.7	0.0172	1.4	0.80	110.1	1.5	109.6	1.8	98.1	24.9	110.1	1.5
TC19-01NN-89	458	135815	2.1	19.6862	1.1	0.2683	1.7	0.0384	1.3	0.77	243.0	3.1	241.3	3.6	224.7	25.0	243.0	3.1
TC19-01NN-90	134	14090	1.4	19.6676	1.4	0.1873	2.0	0.0273	1.4	0.69	173.6	2.3	174.3	3.2	183.7	33.1	173.6	2.3
TC19-01NN-91	170	98754	1.3	20.0098	1.4	0.1919	1.9	0.0280	1.3	0.67	177.8	2.2	178.3	3.1	184.8	32.6	177.8	2.2
TC19-01NN-92	100	13965	4.0	20.1447	1.0	0.1812	1.5	0.0271	1.0	0.70	172.2	1.8	169.1	2.3	126.3	24.6	172.2	1.8
TC19-01NN-93	491	52747	1.8	20.2592	1.0	0.1852	1.4	0.0274	1.0	0.70	174.3	1.7	172.6	2.2	149.1	23.2	174.3	1.7
TC19-01NN-94	148	74378	1.0	19.3873	1.5	0.1982	1.8	0.0280	1.0	0.55	178.0	1.7	183.6	3.0	255.5	33.9	178.0	1.7
TC19-01NN-95	573	120734	2.4	19.6127	1.0	0.2467	1.6	0.0352	1.3	0.80	223.1	2.8	223.9	3.3	232.2	22.6	223.1	2.8
TC19-01NN-96	108	12561	2.4	20.1345	1.7	0.1833	2.2	0.0275	1.4	0.64	174.6	2.4	170.9	3.5	120.1	39.9	174.6	2.4
TC19-01NN-97	288	22899	2.2	20.7602	1.4	0.1135	1.8	0.0173	1.1	0.63	110.9	1.2	109.2	1.8	72.3	32.9	110.9	1.2
TC19-01NN-98	149	21347	2.4	19.6298	1.4	0.2550	1.9	0.0368	1.2	0.62	233.1	2.7	230.6	4.0	205.3	35.3	233.1	2.7
TC19-01NN-99	183	47007	1.3	20.1759	1.4	0.1847	1.8	0.0272	1.1	0.64	173.1	2.0	172.1	2.8	158.3	31.9	173.1	2.0
TC19-01NN-100	190	34324	2.6	17.7529	1.5	0.2661	1.9	0.0345	1.1	0.59	218.9	2.4	239.5	4.0	447.1	33.6	218.9	2.4
TC19-01NN-101	618	50478	2.4	20.6757	1.0	0.1149	1.5	0.0174	1.1	0.74	110.9	1.2	110.5	1.5	101.4	23.1	110.9	1.2
TC19-01NN-102	35	16933	1.5	20.5541	3.1	0.1696	3.4	0.0257	1.3	0.40	163.9	2.2	159.1	5.0	88.6	73.8	163.9	2.2
TC19-01NN-103	486	293832	1.1	20.3187	1.2	0.1771	1.7	0.0261	1.1	0.69	166.2	1.9	165.5	2.5	155.3	28.2	166.2	1.9
Unit 38 tuff-1	314	5856	2.1	13.1791	4.2	0.0530	4.7	0.0052	1.3	0.27	33.7	0.4	52.4	2.4	1026.1	92.3	33.7	0.4
Unit 38 tuff-2	514	14220	2.2	20.1489	1.5	0.0329	2.1	0.0049	1.4	0.68	31.5	0.5	32.8	0.7	130.6	36.0	31.5	0.5
Unit 38 tuff-3	327	29624	2.2	21.1607	2.3	0.0334	2.5	0.0052	1.1	0.42	33.3	0.3	33.4	0.8	39.4	NA	33.3	0.3
Unit 38 tuff-4	409	73081	2.3	20.8546	1.9	0.0330	2.2	0.0050	1.1	0.49	32.2	0.3	33.0	0.7	89.3	45.4	32.2	0.3
Unit 38 tuff-5	332	15400	2.5	22.1799	1.9	0.0311	2.3	0.0051	1.2	0.52	32.8	0.4	31.1	0.7	NA	NA	32.8	0.4
Unit 38 tuff-6	429	198339	1.6	21.2613	1.7	0.0325	2.3	0.0050	1.5	0.66	32.2	0.5	32.5	0.7	52.7	40.8	32.2	0.5
Unit 38 tuff-7	172	22518	1.4	20.3785	2.7	0.0357	2.9	0.0053	1.2	0.40	34.3	0.4	35.7	1.0	130.5	62.5	34.3	0.4

Unit 38 tuff-8	205	179935	3.6	13.2278	0.8	1.9197	1.3	0.1835	1.1	0.81	1086.3	10.6	1088.0	8.8	1091.4	15.4	1091.4	15.4
Unit 38 tuff-9	84	3078	2.1	18.5007	4.8	0.0353	7.0	0.0052	1.3	0.19	33.3	0.4	35.2	2.4	170.9	159.9	33.3	0.4
Unit 38 tuff-10	341	4717	2.4	21.2772	2.2	0.0307	2.6	0.0051	1.2	0.45	32.5	0.4	30.7	0.8	NA	NA	32.5	0.4
Unit 38 tuff-11	1590	179024	2.8	20.6412	1.4	0.0320	1.7	0.0048	1.1	0.62	30.7	0.3	32.0	0.5	127.8	32.2	30.7	0.3
Unit 38 tuff-12	100	74213	6.0	14.2386	1.0	1.5118	1.4	0.1557	0.9	0.67	932.9	8.2	935.2	8.6	940.6	21.3	940.6	21.3
Unit 38 tuff-13	277	6748	2.6	19.3801	3.1	0.0355	3.5	0.0052	1.5	0.42	33.3	0.5	35.4	1.2	180.1	73.1	33.3	0.5
Unit 38 tuff-14	609	12294	1.6	20.5973	1.6	0.0328	2.1	0.0050	1.3	0.59	32.1	0.4	32.7	0.7	79.8	40.9	32.1	0.4
Unit 38 tuff-15	149	7895	1.6	20.9560	3.2	0.0356	4.1	0.0056	1.5	0.38	36.0	0.6	35.5	1.4	2.6	NA	36.0	0.6
Unit 38 tuff-16	423	9378	1.4	21.3829	1.9	0.0319	2.6	0.0051	1.6	0.64	32.8	0.5	31.9	0.8	NA	NA	32.8	0.5
Unit 38 tuff-17	142	383597	2.9	13.9207	0.9	1.6021	1.5	0.1610	1.2	0.79	962.3	10.5	971.0	9.3	990.8	18.5	990.8	18.5
Unit 38 tuff-18	253	3657	2.5	10.6373	11.2	0.0698	11.3	0.0056	1.6	0.14	35.9	0.6	68.5	7.5	1440.9	213.4	35.9	0.6
Unit 38 tuff-19	270	34221	2.5	19.7617	2.4	0.0357	2.8	0.0051	1.5	0.53	33.0	0.5	35.6	1.0	216.8	55.6	33.0	0.5
Unit 38 tuff-20	34	105175	1.1	11.4541	1.1	2.7430	1.6	0.2269	1.1	0.73	1318.0	13.7	1340.2	11.7	1375.8	20.6	1375.8	20.6
Unit 38 tuff-21	76	45218	2.0	10.1484	11.0	0.0730	11.1	0.0054	1.2	0.10	34.4	0.4	71.6	7.7	1602.4	206.3	34.4	0.4
Unit 38 tuff-22	258	6360	2.6	19.9476	2.8	0.0342	3.2	0.0052	1.5	0.47	33.2	0.5	34.2	1.1	104.5	67.8	33.2	0.5
Unit 38 tuff-23	122	3304633	2.6	12.8980	0.8	1.9837	1.4	0.1845	1.2	0.83	1091.3	11.8	1110.0	9.5	1146.7	15.6	1146.7	15.6
Unit 38 tuff-24	115	612220	1.0	9.2119	0.9	4.8760	1.5	0.3239	1.2	0.79	1808.7	19.3	1798.1	13.0	1785.9	17.2	1785.9	17.2
Unit 38 tuff-25	360	220048	1.6	21.6719	2.3	0.0332	2.6	0.0052	1.2	0.46	33.4	0.4	33.2	0.8	16.0	NA	33.4	0.4
Unit 38 tuff-26	327	6430	2.2	20.6785	2.4	0.0327	2.8	0.0051	1.1	0.41	32.9	0.4	32.7	0.9	15.1	NA	32.9	0.4
Unit 38 tuff-27	73	192881	0.5	8.9629	0.8	5.0460	1.2	0.3264	0.9	0.76	1820.9	15.0	1827.1	10.5	1834.1	14.5	1834.1	14.5
Unit 38 tuff-28	445	10290	2.5	18.6241	3.2	0.0375	3.5	0.0052	1.1	0.33	33.3	0.4	37.4	1.3	309.2	74.5	33.3	0.4
Unit 38 tuff-29	255	15624	2.2	20.0511	2.5	0.0359	2.7	0.0053	1.0	0.38	34.0	0.3	35.8	0.9	157.5	57.6	34.0	0.3
Unit 38 tuff-30	370	16396	1.7	21.4193	2.2	0.0323	2.6	0.0051	1.3	0.51	32.8	0.4	32.3	0.8	-0.2	NA	32.8	0.4
Unit 38 tuff-31	363	5797	2.2	21.3651	2.6	0.0307	2.8	0.0050	1.1	0.39	32.2	0.4	30.7	0.9	NA	NA	32.2	0.4
Unit 38 tuff-32	396	7915320	4.4	11.0685	0.7	3.1536	1.5	0.2517	1.3	0.87	1447.5	16.6	1445.9	11.4	1443.5	14.1	1443.5	14.1
Unit 38 tuff-33	580	7132	2.6	19.3974	2.7	0.0358	3.0	0.0052	1.3	0.44	33.5	0.4	35.7	1.1	184.1	63.0	33.5	0.4
Unit 38 tuff-34	1984	24479	1.1	21.2841	0.9	0.0304	1.5	0.0047	1.2	0.82	30.4	0.4	30.4	0.5	32.9	21.0	30.4	0.4
Unit 38 tuff-35	421	98229	2.2	21.1714	2.1	0.0342	2.5	0.0052	1.2	0.49	33.6	0.4	34.1	0.8	68.9	50.9	33.6	0.4
Unit 38 tuff-36	174	320928	2.4	8.9416	0.6	5.1659	0.9	0.3330	0.7	0.76	1852.8	11.3	1847.0	7.8	1840.5	10.8	1840.5	10.8

Unit 38 tuff-37	370	6802	2.8	20.5979	1.9	0.0342	2.3	0.0053	1.3	0.56	34.2	0.4	34.2	0.8	32.6	NA	34.2	0.4
Unit 38 tuff-38	336	4331	2.4	19.2494	3.0	0.0351	3.7	0.0052	1.1	0.31	33.5	0.4	35.0	1.3	140.1	82.0	33.5	0.4
Unit 38 tuff-39	322	6626	2.8	21.4868	2.1	0.0319	2.8	0.0052	1.3	0.47	33.4	0.4	31.9	0.9	NA	NA	33.4	0.4
Unit 38 tuff-40	241	3504	2.2	15.9839	4.1	0.0412	4.3	0.0051	1.5	0.34	32.7	0.5	41.0	1.7	558.4	89.2	32.7	0.5
Unit 38 tuff-41	137	974808	1.1	9.1698	0.6	4.7195	1.2	0.3118	1.0	0.86	1749.8	15.4	1770.7	9.8	1795.4	10.8	1795.4	10.8
Unit 38 tuff-42	907	148330	8.9	21.0118	1.3	0.0350	1.7	0.0053	1.0	0.62	34.1	0.4	34.9	0.6	89.5	30.9	34.1	0.4
Unit 38 tuff-43	113	186570	1.7	11.0292	0.8	3.1582	1.1	0.2512	0.8	0.71	1444.7	10.3	1447.0	8.6	1450.4	14.9	1450.4	14.9
Unit 38 tuff-44	378	17683	2.3	20.6325	2.5	0.0331	3.0	0.0050	1.5	0.51	32.2	0.5	33.1	1.0	96.4	60.0	32.2	0.5
Unit 38 tuff-45	98	299892	1.8	9.2354	0.8	4.6250	1.3	0.3079	1.0	0.76	1730.4	14.5	1753.8	10.5	1781.7	14.7	1781.7	14.7
Unit 38 tuff-46	228	116688	1.8	13.0437	0.7	1.8842	1.1	0.1773	0.9	0.79	1052.4	8.7	1075.5	7.6	1122.7	14.0	1122.7	14.0
Unit 38 tuff-47	323	19772	2.3	19.9645	2.4	0.0352	2.6	0.0051	1.0	0.39	33.1	0.3	35.2	0.9	178.9	56.2	33.1	0.3
Unit 38 tuff-48	98	3091	1.9	16.6338	3.3	0.0407	3.7	0.0053	1.3	0.35	34.0	0.4	40.5	1.5	441.9	76.4	34.0	0.4
Unit 38 tuff-49	364	9941	2.0	21.4533	2.5	0.0323	2.8	0.0052	1.2	0.43	33.2	0.4	32.3	0.9	NA	NA	33.2	0.4
Unit 38 tuff-50	50	113473	2.1	11.7182	0.8	2.7694	1.1	0.2343	0.8	0.71	1357.2	9.7	1347.3	8.3	1331.7	15.1	1331.7	15.1
Unit 38 tuff-51	64	53460	2.3	13.1958	0.9	1.9578	1.4	0.1869	1.0	0.76	1104.7	10.6	1101.1	9.3	1094.0	17.9	1094.0	17.9
Unit 38 tuff-52	421	12102	2.1	20.7445	2.1	0.0327	2.4	0.0050	1.0	0.43	32.3	0.3	32.7	0.8	63.5	51.5	32.3	0.3
Unit 38 tuff-53	287	11825	2.5	19.9727	2.6	0.0356	2.9	0.0053	1.2	0.42	33.8	0.4	35.5	1.0	154.0	60.9	33.8	0.4
Unit 38 tuff-54	135	958872	1.8	13.3980	1.1	1.9071	1.8	0.1842	1.5	0.81	1089.8	15.0	1083.6	12.2	1071.1	21.3	1071.1	21.3
Unit 38 tuff-55	500	154440	2.8	12.4579	0.7	2.1874	1.5	0.1966	1.3	0.87	1157.1	13.8	1177.0	10.4	1213.9	14.3	1213.9	14.3
Unit 38 tuff-56	168	416883	2.6	9.4841	0.8	4.3486	1.2	0.2973	0.9	0.77	1677.7	13.4	1702.6	9.8	1733.4	14.0	1733.4	14.0
Unit 38 tuff-57	59	581651	1.3	9.0429	0.6	5.0488	1.1	0.3292	0.9	0.82	1834.5	14.4	1827.5	9.3	1819.6	11.5	1819.6	11.5
Unit 38 tuff-58	306	14912	2.2	20.8248	2.2	0.0324	2.5	0.0050	1.0	0.40	32.0	0.3	32.4	0.8	65.1	54.7	32.0	0.3
Unit 38 tuff-59	44	60731	1.5	12.1062	1.0	2.3750	1.4	0.2080	1.0	0.69	1218.3	10.5	1235.1	9.9	1264.6	19.7	1264.6	19.7
Unit 38 tuff-60	251	31757	2.1	8.2344	0.9	5.5875	1.4	0.3331	1.1	0.77	1853.4	17.7	1914.2	12.3	1980.6	16.1	1980.6	16.1
Unit 38 tuff-61	181	9084	2.4	19.7813	3.6	0.0353	4.3	0.0052	2.4	0.56	33.5	0.8	35.2	1.5	157.1	84.1	33.5	0.8
Unit 38 tuff-62	381	33517	2.1	21.0002	2.3	0.0331	2.7	0.0051	1.5	0.55	32.5	0.5	33.1	0.9	73.5	54.6	32.5	0.5
Unit 38 tuff-63	315	19747	0.9	20.3549	2.2	0.0338	2.6	0.0050	1.4	0.53	32.3	0.4	33.7	0.9	133.0	51.3	32.3	0.4
Unit 38 tuff-64	121	118096	1.2	19.4722	1.2	0.2675	1.8	0.0376	1.3	0.75	238.1	3.1	240.7	3.8	265.9	27.1	238.1	3.1
Unit 38 tuff-65	182	25029	1.5	20.1960	3.0	0.0342	3.3	0.0050	1.4	0.43	32.4	0.5	34.1	1.1	159.9	70.0	32.4	0.5

Unit 38 tuff-66	354	35976	2.3	20.9896	1.6	0.0341	2.3	0.0052	1.6	0.73	33.5	0.5	34.0	0.8	75.2	37.1	33.5	0.5
Unit 38 tuff-67	199	6033	8.8	22.1343	3.0	0.0296	3.3	0.0050	1.2	0.36	32.2	0.4	29.7	1.0	NA	NA	32.2	0.4
Unit 38 tuff-68	42	57036	1.1	18.4421	1.6	0.4673	1.9	0.0624	1.0	0.53	390.2	3.9	389.3	6.3	383.8	37.0	390.2	3.9
Unit 38 tuff-69	345	15466	1.8	22.1401	2.0	0.0311	2.5	0.0051	1.4	0.55	32.6	0.4	31.1	0.8	NA	NA	32.6	0.4
Unit 38 tuff-70	629	15236	1.3	20.8916	1.6	0.0324	2.2	0.0050	1.3	0.62	32.0	0.4	32.3	0.7	58.4	40.7	32.0	0.4
Unit 38 tuff-71	271	4880	2.4	21.8204	2.5	0.0310	2.9	0.0052	1.1	0.37	33.6	0.4	31.0	0.9	NA	NA	33.6	0.4
Unit 38 tuff-72	358	16775	0.8	20.2988	2.2	0.0332	2.7	0.0049	1.4	0.53	31.8	0.4	33.1	0.9	131.3	53.0	31.8	0.4
Unit 38 tuff-73	172	101670	3.5	13.0777	0.7	1.9228	1.4	0.1817	1.3	0.88	1076.2	12.6	1089.0	9.6	1114.8	13.7	1114.8	13.7
Unit 38 tuff-74	6675	44571	3.6	19.1595	1.8	0.0269	2.3	0.0037	1.4	0.60	24.0	0.3	26.9	0.6	293.2	41.5	24.0	0.3
Unit 38 tuff-75	92	235781	1.7	8.8533	0.6	5.1137	1.1	0.3264	0.8	0.80	1821.1	13.5	1838.4	9.0	1858.0	11.5	1858.0	11.5
Unit 38 tuff-76	88	254984	1.9	6.7301	0.7	8.8488	1.3	0.4293	1.1	0.83	2302.7	21.1	2322.5	11.9	2340.0	12.3	2340.0	12.3
Unit 38 tuff-77	32	73437	1.1	8.5709	0.8	5.2631	1.4	0.3254	1.1	0.80	1816.1	17.5	1862.9	11.7	1915.6	14.8	1915.6	14.8
Unit 38 tuff-78	500	31188	1.6	20.7797	1.6	0.0338	2.0	0.0051	1.3	0.62	32.8	0.4	33.7	0.7	98.6	38.2	32.8	0.4
Unit 38 tuff-79	314	262484	1.9	11.2287	0.8	2.9434	1.3	0.2382	1.0	0.81	1377.1	12.9	1393.1	9.7	1417.7	14.4	1417.7	14.4
Unit 38 tuff-80	468	204695	0.9	19.3838	1.0	0.2470	1.5	0.0345	1.1	0.73	218.9	2.4	224.1	3.0	279.0	23.4	218.9	2.4
Unit 38 tuff-81	434	23290	2.0	21.3201	1.9	0.0324	2.1	0.0050	1.0	0.46	32.4	0.3	32.3	0.7	25.4	NA	32.4	0.3
Unit 38 tuff-82	484	12655	1.8	20.5380	2.2	0.0335	2.5	0.0051	1.2	0.47	32.7	0.4	33.5	0.8	88.0	51.6	32.7	0.4
Unit 38 tuff-83	63	407824	0.5	8.6614	0.9	5.3354	1.3	0.3335	1.0	0.73	1855.4	15.4	1874.6	11.2	1895.8	16.2	1895.8	16.2
Unit 38 tuff-84	337	953105	1.9	21.0252	1.9	0.0344	2.1	0.0052	0.9	0.42	33.6	0.3	34.3	0.7	90.0	45.8	33.6	0.3
Unit 38 tuff-85	497	13388	1.1	19.5604	2.4	0.0371	2.7	0.0053	1.1	0.43	34.4	0.4	37.0	1.0	208.9	56.5	34.4	0.4
Unit 38 tuff-86	204	2843650	1.8	9.1850	0.8	4.7483	1.3	0.3146	1.0	0.79	1763.3	15.6	1775.8	10.7	1790.6	14.1	1790.6	14.1
Unit 38 tuff-87	120	170225	1.4	9.0650	0.8	5.1227	1.4	0.3352	1.1	0.81	1863.5	17.9	1839.9	11.6	1813.3	14.6	1813.3	14.6
Unit 38 tuff-88	78	258016	3.3	13.6133	0.8	1.7426	1.4	0.1712	1.1	0.81	1018.9	10.7	1024.4	9.1	1036.1	16.8	1036.1	16.8
Unit 38 tuff-89	362	17003	2.3	21.4228	2.4	0.0329	2.8	0.0052	1.5	0.52	33.3	0.5	32.9	0.9	0.7	NA	33.3	0.5
Unit 38 tuff-90	491	18182	1.2	20.7453	1.7	0.0349	2.0	0.0053	1.1	0.55	34.1	0.4	34.8	0.7	81.5	39.9	34.1	0.4
Unit 38 tuff-91	311	4016	1.9	22.4087	2.7	0.0301	3.0	0.0053	1.3	0.42	34.1	0.4	30.1	0.9	NA	NA	34.1	0.4
Unit 38 tuff-92	136	102876	4.5	9.0869	0.8	4.7851	1.3	0.3141	1.1	0.81	1760.7	16.6	1782.3	11.2	1807.6	14.1	1807.6	14.1
Unit 38 tuff-93	250	7757	2.2	20.9674	2.2	0.0339	2.7	0.0053	1.4	0.52	34.3	0.5	33.8	0.9	-0.9	NA	34.3	0.5
Unit 38 tuff-94	61	134023	1.2	13.9147	1.2	1.6097	1.6	0.1620	1.1	0.69	968.1	10.2	974.0	10.2	987.3	24.0	987.3	24.0

Unit 38 tuff-95	41	166792	1.3	9.3249	1.1	4.6493	1.7	0.3134	1.3	0.75	1757.5	19.2	1758.2	13.9	1758.9	20.2	1758.9	20.2
Unit 38 tuff-96	49	302231	1.4	8.8550	0.7	5.1157	1.2	0.3273	0.9	0.79	1825.1	15.1	1838.7	10.3	1854.1	13.5	1854.1	13.5
Unit 38 tuff-97	7	12756	2.6	13.3770	4.5	1.6971	6.3	0.1664	4.3	0.69	992.4	40.0	1007.4	40.1	1040.2	91.5	1040.2	91.5
Unit 38 tuff-98	360	9321	2.5	17.1533	3.1	0.0398	3.6	0.0051	1.3	0.37	32.6	0.4	39.7	1.4	490.5	74.3	32.6	0.4
Unit 38 tuff-99	290	89466910	2.0	10.8084	0.8	3.2738	1.1	0.2552	0.7	0.69	1465.3	9.7	1474.9	8.3	1488.5	14.6	1488.5	14.6
Unit 38 tuff-100	445	36930	2.8	21.9455	1.9	0.0320	2.4	0.0051	1.4	0.61	32.9	0.5	32.0	0.7	NA	NA	32.9	0.5
Unit 38 tuff-101	198	835140	2.7	9.1201	0.9	4.8001	1.3	0.3160	1.0	0.76	1770.4	15.4	1784.9	11.0	1801.9	15.6	1801.9	15.6
Unit 38 tuff-102	224	1125859	6.4	13.3228	0.8	1.9083	1.1	0.1835	0.8	0.74	1086.3	8.4	1084.0	7.6	1079.3	15.4	1079.3	15.4
Unit 38 tuff-103	823	34963	1.9	21.6777	1.3	0.0330	1.6	0.0052	0.9	0.57	33.5	0.3	32.9	0.5	NA	NA	33.5	0.3
Unit 38 tuff-104	525	187415	1.9	20.8483	1.6	0.0331	2.0	0.0050	1.2	0.60	32.1	0.4	33.1	0.7	104.9	38.3	32.1	0.4
Unit 38 tuff-105	517	37737	2.0	20.6615	1.8	0.0335	2.3	0.0050	1.4	0.61	32.4	0.5	33.5	0.7	111.2	42.4	32.4	0.5
Unit 38 tuff-106	81	193663	2.1	7.7981	0.9	6.6777	1.4	0.3759	1.1	0.79	2057.0	20.0	2069.7	12.8	2082.3	15.7	2082.3	15.7
TC19-9-1	179	36349	1.1	20.9763	2.9	0.0343	3.2	0.0053	1.4	0.43	33.8	0.5	34.2	1.1	64.0	NA	33.8	0.5
TC19-9-2	250	12500	2.4	20.9670	2.6	0.0363	3.6	0.0057	2.4	0.68	36.4	0.9	36.2	1.3	25.5	NA	36.4	0.9
TC19-9-3	123	10464	1.2	21.6222	3.9	0.0339	4.3	0.0055	1.8	0.42	35.2	0.6	33.9	1.4	NA	NA	35.2	0.6
TC19-9-4	376	25482	1.8	2.9440	13.5	0.2567	13.5	0.0055	1.5	0.11	35.3	0.5	232.0	28.1	3659.6	206.8	35.3	0.5
TC19-9-5	113	4028	1.1	18.9912	3.3	0.0360	4.8	0.0053	1.8	0.38	34.2	0.6	35.9	1.7	149.3	103.5	34.2	0.6
TC19-9-6	245	156550	0.7	20.6778	2.0	0.0354	2.6	0.0053	1.6	0.62	34.2	0.5	35.4	0.9	117.7	47.4	34.2	0.5
TC19-9-7	53	1374	0.8	20.2500	5.4	0.0306	8.3	0.0057	1.8	0.21	36.9	0.7	30.6	2.5	NA	NA	36.9	0.7
TC19-9-8	169	84310	1.0	22.3413	3.2	0.0336	3.6	0.0055	1.6	0.44	35.1	0.5	33.6	1.2	NA	NA	35.1	0.5
TC19-9-9	191	2600	0.6	19.7553	3.9	0.0328	4.4	0.0053	2.0	0.46	34.0	0.7	32.8	1.4	NA	NA	34.0	0.7
TC19-9-10	144	5852	1.1	20.3617	3.5	0.0344	3.9	0.0053	1.6	0.40	34.3	0.5	34.3	1.3	33.2	NA	34.3	0.5
TC19-9-11	137	9913	1.0	21.1951	3.2	0.0339	3.8	0.0054	1.3	0.36	34.5	0.5	33.8	1.2	NA	NA	34.5	0.5
TC19-9-12	140	32605	0.7	20.0126	3.4	0.0379	3.7	0.0055	1.6	0.42	35.6	0.6	37.7	1.4	177.3	78.3	35.6	0.6
TC19-9-13	303	7555	1.9	19.4556	2.8	0.0368	3.1	0.0054	1.1	0.36	34.6	0.4	36.7	1.1	174.1	66.8	34.6	0.4
TC19-9-14	149	2264	0.5	6.0917	3.3	0.1236	5.1	0.0056	3.8	0.76	36.3	1.4	118.4	5.7	2444.0	55.6	36.3	1.4
TC19-9-15	66	3425	1.7	7.0442	15.8	0.1210	15.9	0.0063	2.1	0.13	40.8	0.8	116.0	17.5	2206.9	276.1	40.8	0.8
TC19-9-16	2150	407166	2.6	21.3271	1.1	0.0341	1.4	0.0053	0.8	0.60	33.9	0.3	34.0	0.5	45.6	26.8	33.9	0.3

TC19-9-17	1184	13464	0.9	20.8210	1.8	0.0331	2.1	0.0051	1.1	0.52	32.8	0.4	33.1	0.7	49.6	42.2	32.8	0.4
TC19-9-18	986	677916	1.7	20.6533	1.3	0.0363	1.8	0.0054	1.3	0.71	35.0	0.5	36.2	0.6	121.8	30.1	35.0	0.5
TC19-9-19	210	751993	4.1	8.9208	0.7	4.9485	1.1	0.3196	0.9	0.80	1787.6	13.6	1810.6	9.2	1837.1	12.0	1837.1	12.0
TC19-9-20	261	4091	0.6	19.8781	2.9	0.0350	3.2	0.0054	1.2	0.38	34.9	0.4	35.0	1.1	38.3	NA	34.9	0.4
TC19-9-21	169	9053	3.1	21.5780	2.3	0.0345	2.8	0.0056	1.4	0.52	35.9	0.5	34.5	0.9	NA	NA	35.9	0.5
TC19-9-22	114	4372	1.0	19.8408	4.1	0.0349	5.5	0.0054	1.3	0.23	34.5	0.4	34.8	1.9	53.4	NA	34.5	0.4
TC19-9-23	183	4308	0.8	18.0873	3.0	0.0384	3.4	0.0054	1.5	0.43	34.5	0.5	38.2	1.3	282.2	69.6	34.5	0.5
TC19-9-24	144	14473	1.3	21.6124	2.9	0.0351	3.3	0.0056	1.5	0.46	36.1	0.6	35.0	1.1	NA	NA	36.1	0.6
TC19-9-25	223	2994	0.4	9.6328	2.3	0.0790	2.6	0.0058	1.3	0.48	37.1	0.5	77.2	2.0	1610.9	43.1	37.1	0.5
TC19-9-26	115	19706	0.7	14.0152	7.3	0.0557	7.5	0.0057	1.7	0.23	36.7	0.6	55.0	4.0	949.0	149.0	36.7	0.6
TC19-9-27	95	86120	0.8	21.4937	4.5	0.0348	4.7	0.0054	1.6	0.34	35.0	0.6	34.8	1.6	19.0	NA	35.0	0.6
TC19-9-28	138	2472	0.7	20.2836	3.8	0.0321	4.2	0.0054	1.3	0.31	34.6	0.4	32.1	1.3	NA	NA	34.6	0.4
TC19-9-29	138	16355	0.9	19.8063	3.9	0.0373	4.3	0.0055	1.6	0.38	35.1	0.6	37.2	1.6	177.2	93.7	35.1	0.6
TC19-9-30	1769	965051	3.1	21.2465	1.0	0.0351	1.5	0.0054	1.2	0.76	34.8	0.4	35.1	0.5	53.4	23.8	34.8	0.4
TC19-9-31	156	1750	0.7	17.9711	3.1	0.0347	3.3	0.0053	1.2	0.37	34.3	0.4	34.7	1.1	61.1	NA	34.3	0.4
TC19-9-32	233	216168	0.8	13.0550	4.5	0.0626	4.8	0.0059	1.6	0.34	38.1	0.6	61.7	2.9	1111.4	89.9	38.1	0.6
TC19-9-33	110	3170	1.3	19.3562	3.0	0.0347	6.1	0.0054	1.7	0.28	34.5	0.6	34.7	2.1	50.7	NA	34.5	0.6
TC19-9-34	1273	48958	2.6	19.3197	1.5	0.0370	1.9	0.0052	1.1	0.60	33.5	0.4	36.9	0.7	262.6	34.7	33.5	0.4
TC19-9-35	208	3242	1.1	8.3760	9.2	0.0954	9.3	0.0060	1.2	0.13	38.6	0.5	92.5	8.2	1882.8	167.0	38.6	0.5
TC19-9-36	193	14292	0.7	20.1434	3.1	0.0368	3.5	0.0055	1.6	0.45	35.3	0.6	36.7	1.3	129.1	73.7	35.3	0.6
TC19-9-37	678	315984	0.5	20.5792	1.5	0.0342	1.8	0.0051	0.9	0.53	32.9	0.3	34.2	0.6	125.9	35.8	32.9	0.3
TC19-9-38	63	2049	1.0	17.6253	5.5	0.0376	8.1	0.0055	1.9	0.24	35.3	0.7	37.5	3.0	175.3	NA	35.3	0.7
TC19-9-39	204	16106	3.0	22.2008	2.9	0.0330	3.2	0.0054	1.4	0.43	34.9	0.5	33.0	1.0	NA	NA	34.9	0.5
TC19-9-40	75	8393	0.6	7.7736	4.3	0.1011	4.6	0.0058	1.7	0.37	37.0	0.6	97.8	4.3	2059.1	76.1	37.0	0.6
TC19-9-41	128	2354	1.9	4.5994	7.1	0.2095	7.2	0.0071	1.3	0.17	45.9	0.6	193.1	12.7	2925.9	114.9	45.9	0.6
TC19-9-42	124	2165	0.6	19.3039	4.3	0.0328	4.5	0.0053	1.4	0.32	34.0	0.5	32.8	1.5	NA	NA	34.0	0.5
TC19-9-43	270	12008	0.5	18.3152	2.6	0.0409	2.9	0.0056	1.3	0.43	35.7	0.4	40.7	1.2	346.5	59.9	35.7	0.4
TC19-9-44	244	5084	1.4	19.9292	2.1	0.0350	2.4	0.0054	1.2	0.48	34.5	0.4	35.0	0.8	64.6	50.6	34.5	0.4
TC19-9-45	101	5024	1.6	21.0265	3.7	0.0344	4.7	0.0056	1.5	0.32	36.0	0.5	34.4	1.6	NA	NA	36.0	0.5

TC19-9-46	81	2912	1.0	21.5745	4.5	0.0316	5.1	0.0056	2.2	0.44	35.8	0.8	31.6	1.6	NA	NA	35.8	0.8
TC19-9-47	120	4091	1.7	20.3141	3.2	0.0353	3.7	0.0056	1.5	0.40	36.0	0.5	35.2	1.3	NA	NA	36.0	0.5
TC19-9-48	114	8053	1.4	20.3165	3.1	0.0357	3.4	0.0055	1.2	0.36	35.1	0.4	35.6	1.2	69.3	NA	35.1	0.4
TC19-9-49	51	4320	1.1	19.6384	4.6	0.0371	5.0	0.0057	1.9	0.38	36.4	0.7	36.9	1.8	75.9	NA	36.4	0.7
TC19-9-50	191	2933	0.8	4.9424	1.8	0.1797	2.1	0.0066	1.2	0.55	42.2	0.5	167.8	3.3	2812.9	29.2	42.2	0.5
TC19-9-51	196	12587	2.1	19.7218	2.6	0.0374	3.0	0.0055	1.3	0.43	35.2	0.5	37.3	1.1	173.2	62.7	35.2	0.5
TC19-9-52	638	18735	0.6	21.1361	1.5	0.0354	1.9	0.0055	1.1	0.61	35.5	0.4	35.3	0.6	26.4	NA	35.5	0.4
TC19-9-53	434	78933	0.6	20.0544	1.9	0.0364	2.3	0.0053	1.4	0.60	34.2	0.5	36.3	0.8	181.4	43.6	34.2	0.5
TC19-9-54	215	17135	0.7	19.1487	3.2	0.0397	3.4	0.0056	1.1	0.31	36.0	0.4	39.6	1.3	259.1	73.2	36.0	0.4
TC19-9-55	533	19417	1.9	20.7162	1.7	0.0349	2.2	0.0053	1.2	0.53	34.3	0.4	34.9	0.8	76.4	44.2	34.3	0.4
TC19-9-56	185	249446	0.8	18.8502	2.0	0.0399	2.5	0.0055	1.4	0.56	35.1	0.5	39.7	1.0	329.8	46.2	35.1	0.5
TC19-9-57	178	9109	0.8	20.6434	3.1	0.0357	3.4	0.0055	1.4	0.40	35.6	0.5	35.6	1.2	41.5	NA	35.6	0.5
TC19-9-58	192	29261	1.5	19.8752	2.7	0.0403	3.0	0.0059	1.4	0.45	37.7	0.5	40.1	1.2	185.6	63.0	37.7	0.5
TC19-9-59	231	3888	0.6	4.3000	6.1	0.2221	6.3	0.0070	1.4	0.23	45.1	0.6	203.7	11.6	3049.1	98.0	45.1	0.6
TC19-9-60	208	38173	0.7	16.4220	3.7	0.0464	3.9	0.0056	1.1	0.28	35.8	0.4	46.1	1.7	621.4	79.8	35.8	0.4
TC19-9-61	116	3599	1.3	19.6708	4.1	0.0362	4.4	0.0056	1.3	0.28	36.1	0.5	36.1	1.6	34.0	NA	36.1	0.5
TC19-9-62	199	2397	1.3	21.0857	3.3	0.0297	3.6	0.0052	1.1	0.30	33.7	0.4	29.7	1.0	NA	NA	33.7	0.4
TC19-9-63	82	3469	1.1	25.3657	3.7	0.0279	5.7	0.0058	1.9	0.34	37.1	0.7	28.0	1.6	NA	NA	37.1	0.7
TC19-9-64	233	7053	1.6	20.5721	2.4	0.0349	2.7	0.0055	1.3	0.48	35.1	0.4	34.9	0.9	21.1	NA	35.1	0.4
TC19-9-65	70	180438	2.8	5.0332	0.7	14.6083	1.3	0.5341	1.1	0.82	2758.5	23.9	2790.1	12.3	2813.0	12.0	2813.0	12.0
TC19-9-66	92	1461	1.5	19.2233	4.5	0.0318	4.7	0.0055	1.6	0.33	35.5	0.6	31.8	1.5	NA	NA	35.5	0.6
TC19-9-67	267	53677	1.5	20.8045	2.5	0.0376	2.7	0.0057	1.1	0.41	36.8	0.4	37.5	1.0	85.6	59.2	36.8	0.4
TC19-9-68	102	19266	1.3	19.0315	4.6	0.0399	4.7	0.0056	1.3	0.27	36.0	0.5	39.8	1.8	272.5	104.8	36.0	0.5
TC19-9-69	67	3206	1.0	10.2296	6.3	0.0779	6.4	0.0060	1.4	0.22	38.8	0.6	76.1	4.7	1496.7	119.0	38.8	0.6
TC19-9-70	216	18326	1.0	22.2577	2.3	0.0359	2.7	0.0059	1.4	0.52	37.9	0.5	35.8	1.0	NA	NA	37.9	0.5
TC19-9-71	176	5480	1.0	18.4718	3.6	0.0406	4.2	0.0057	1.0	0.24	36.7	0.4	40.4	1.7	262.7	93.4	36.7	0.4
TC19-9-72	443	125390	0.6	19.9745	1.8	0.0376	2.1	0.0055	1.0	0.50	35.1	0.4	37.5	0.8	194.0	41.9	35.1	0.4
TC19-9-73	118	6255	1.2	16.2812	5.4	0.0438	5.7	0.0054	1.3	0.22	34.6	0.4	43.5	2.4	571.5	121.3	34.6	0.4
TC19-9-74	198	6526	0.7	19.2730	2.6	0.0371	2.9	0.0054	1.1	0.39	34.8	0.4	37.0	1.0	177.7	61.7	34.8	0.4

TC19-9-75	154	4338	1.2	22.4307	3.8	0.0302	4.0	0.0053	1.2	0.31	34.2	0.4	30.2	1.2	NA	NA	34.2	0.4
TC19-9-76	196	3692	0.6	21.8623	2.4	0.0300	3.0	0.0052	1.4	0.48	33.5	0.5	30.0	0.9	NA	NA	33.5	0.5
TC19-9-77	95	18580	1.2	17.8879	4.7	0.0421	6.0	0.0055	3.6	0.61	35.6	1.3	41.9	2.4	418.6	105.7	35.6	1.3
TC19-9-78	404	11701	3.2	13.0006	1.9	0.0606	2.3	0.0058	1.3	0.55	37.3	0.5	59.8	1.3	1087.5	38.3	37.3	0.5
TC19-9-79	299	12591	2.3	20.8427	2.4	0.0359	2.8	0.0056	1.5	0.54	35.8	0.5	35.8	1.0	39.6	NA	35.8	0.5
TC19-9-80	116	4268	1.6	19.8411	3.5	0.0361	5.0	0.0056	1.5	0.31	35.9	0.6	36.1	1.8	47.7	NA	35.9	0.6
TC19-9-81	191	4261	1.3	18.9846	3.3	0.0381	3.7	0.0056	1.4	0.38	36.0	0.5	37.9	1.4	159.9	79.9	36.0	0.5
TC19-9-82	143	9941	0.8	20.6654	3.1	0.0350	3.5	0.0054	1.7	0.48	34.8	0.6	35.0	1.2	45.2	NA	34.8	0.6
TC19-9-83	175	32777	0.9	17.0927	2.6	0.0441	2.8	0.0055	1.1	0.41	35.4	0.4	43.8	1.2	532.3	56.3	35.4	0.4
TC19-9-84	117	4063	1.1	21.1482	3.3	0.0334	3.6	0.0055	1.3	0.36	35.6	0.5	33.3	1.2	NA	NA	35.6	0.5
TC19-9-85	421	17175	3.1	17.3819	5.1	0.0440	5.3	0.0056	1.5	0.28	36.2	0.5	43.7	2.3	477.4	113.0	36.2	0.5
TC19-9-86	301	9630	1.2	19.8351	2.3	0.0367	2.8	0.0054	1.6	0.57	35.0	0.6	36.6	1.0	142.5	53.5	35.0	0.6
TC19-9-87	628	45029	3.2	20.4455	1.2	0.0361	1.7	0.0054	1.2	0.71	34.7	0.4	36.0	0.6	127.7	28.6	34.7	0.4
TC19-9-88	85	5095	1.0	15.6935	5.6	0.0477	5.8	0.0057	1.3	0.23	36.6	0.5	47.3	2.7	634.9	120.8	36.6	0.5
TC19-9-89	60	7627	1.2	23.7106	4.3	0.0311	4.8	0.0056	2.0	0.43	36.1	0.7	31.1	1.5	NA	NA	36.1	0.7
TC19-9-90	142	2182407	1.7	9.9376	0.7	3.8956	1.6	0.2807	1.4	0.90	1595.1	19.9	1612.8	12.7	1635.9	12.8	1635.9	12.8
TC19-9-91	143	37225	1.1	22.1938	2.7	0.0338	3.0	0.0055	1.3	0.42	35.2	0.4	33.7	1.0	NA	NA	35.2	0.4
TC19-9-92	194	27018	0.8	19.6349	3.6	0.0377	3.8	0.0054	1.1	0.30	34.9	0.4	37.6	1.4	213.7	84.0	34.9	0.4
TC19-9-93	299	12026	0.8	21.3046	2.3	0.0359	3.0	0.0057	1.6	0.52	36.6	0.6	35.8	1.1	NA	NA	36.6	0.6
TC19-9-94	851	55395	8.7	20.5036	1.1	0.0597	1.6	0.0089	1.0	0.67	57.3	0.6	58.9	0.9	124.0	27.3	57.3	0.6
TC19-9-95	164	17858	0.6	21.8998	3.1	0.0324	3.6	0.0052	1.8	0.49	33.7	0.6	32.4	1.1	NA	NA	33.7	0.6
TC19-9-96	88	15332	1.1	20.5995	3.8	0.0361	4.1	0.0055	1.7	0.41	35.4	0.6	36.0	1.5	78.1	NA	35.4	0.6
TC19-9-97	103	3285	1.1	23.0840	3.2	0.0289	3.8	0.0054	1.4	0.37	34.7	0.5	28.9	1.1	NA	NA	34.7	0.5
TC19-9-98	156	275456	1.9	8.7731	0.8	5.0511	1.2	0.3216	0.9	0.73	1797.4	14.2	1827.9	10.5	1862.8	15.1	1862.8	15.1
TC19-9-99	714	58023	0.5	21.6070	1.6	0.0343	2.0	0.0054	1.3	0.62	34.7	0.4	34.2	0.7	NA	NA	34.7	0.4
TC19-9-100	156	7091	1.0	20.1786	2.9	0.0350	3.2	0.0054	1.2	0.37	34.4	0.4	35.0	1.1	72.4	70.9	34.4	0.4
TC19-9-101	149	6773	1.0	19.1576	3.2	0.0366	4.1	0.0053	1.3	0.32	34.1	0.4	36.5	1.5	194.0	90.5	34.1	0.4
TC19-9-102	195	11026	1.1	19.8678	2.7	0.0406	3.0	0.0060	1.3	0.42	38.6	0.5	40.4	1.2	148.4	64.2	38.6	0.5
TC19-9-103	157	5102	0.7	14.0209	3.9	0.0539	4.2	0.0057	1.4	0.35	36.7	0.5	53.3	2.2	884.6	81.2	36.7	0.5

TC19-9-104	60	4691	0.9	19.6099	5.0	0.0364	5.5	0.0055	1.8	0.33	35.4	0.6	36.3	1.9	93.9	NA	35.4	0.6
TC19-9-105	321	167022	1.9	21.3585	1.8	0.0368	2.1	0.0057	1.2	0.56	36.6	0.4	36.7	0.8	39.4	NA	36.6	0.4
TC19-02NN-1	55	4469	1.7	20.1984	2.7	0.1744	3.2	0.0274	1.6	0.48	174.5	2.7	163.2	4.8	1.8	NA	174.5	2.7
TC19-02NN-2	243	51793	1.4	19.6038	1.4	0.1928	2.2	0.0276	1.7	0.77	175.6	2.9	179.0	3.6	224.7	32.1	175.6	2.9
TC19-02NN-3	150	32258	1.6	19.3777	2.0	0.1983	2.4	0.0282	1.3	0.56	179.1	2.4	183.7	4.0	243.9	45.9	179.1	2.4
TC19-02NN-4	185	12903	1.0	19.7834	1.6	0.1733	1.9	0.0255	1.0	0.53	162.2	1.7	162.3	2.9	163.4	38.3	162.2	1.7
TC19-02NN-5	730	119512	1.3	19.9172	1.3	0.1787	1.8	0.0259	1.2	0.68	165.0	2.0	167.0	2.8	195.2	30.5	165.0	2.0
TC19-02NN-6	142	27877	2.3	19.3970	1.7	0.1815	2.3	0.0258	1.5	0.66	164.3	2.5	169.4	3.6	241.6	39.8	164.3	2.5
TC19-02NN-7	104	43786	1.3	18.6583	2.7	0.1852	3.1	0.0252	1.4	0.46	160.3	2.3	172.5	4.9	343.2	62.2	160.3	2.3
TC19-02NN-8	90	17960	1.8	19.7221	2.6	0.1963	3.1	0.0285	1.7	0.55	181.1	3.0	182.0	5.1	193.1	59.7	181.1	3.0
TC19-02NN-9	130	22917	1.5	19.9408	1.9	0.1901	2.4	0.0278	1.5	0.60	176.8	2.5	176.7	3.9	175.3	45.4	176.8	2.5
TC19-02NN-10	106	13150	1.7	19.1553	2.0	0.1924	2.3	0.0273	1.0	0.46	173.5	1.8	178.7	3.7	248.9	46.5	173.5	1.8
TC19-02NN-11	343	104164	0.9	19.4948	1.1	0.2106	1.4	0.0298	0.8	0.60	189.6	1.6	194.1	2.5	249.3	26.0	189.6	1.6
TC19-02NN-12	236	139693	0.9	19.9129	1.3	0.1676	1.7	0.0242	1.1	0.64	154.4	1.7	157.3	2.5	201.7	30.2	154.4	1.7
TC19-02NN-13	715	80658	1.5	19.9339	0.9	0.1917	1.4	0.0278	1.1	0.80	176.7	2.0	178.0	2.3	195.7	19.9	176.7	2.0
TC19-02NN-14	181	22388	2.2	19.4012	1.5	0.1916	2.0	0.0273	1.3	0.64	173.5	2.2	178.0	3.2	237.8	34.8	173.5	2.2
TC19-02NN-15	233	32671	0.9	19.7610	1.3	0.1801	2.2	0.0260	1.7	0.77	165.7	2.7	168.1	3.4	202.1	32.7	165.7	2.7
TC19-02NN-16	95	130292	3.8	9.3880	0.9	4.4904	1.4	0.3061	1.1	0.75	1721.3	16.0	1729.2	11.8	1738.8	17.3	1738.8	17.3
TC19-02NN-17	284	13778	1.5	19.8691	1.5	0.1735	1.9	0.0255	1.1	0.59	162.6	1.8	162.5	2.9	160.2	36.2	162.6	1.8
TC19-02NN-18	373	118292	3.0	17.5815	1.9	0.2894	2.3	0.0370	1.2	0.55	233.9	2.9	258.1	5.2	483.2	41.9	233.9	2.9
TC19-02NN-19	604	157402	2.7	19.6335	1.1	0.2438	2.1	0.0348	1.8	0.86	220.6	4.0	221.6	4.2	231.3	24.6	220.6	4.0
TC19-02NN-20	248	32727	1.6	19.5619	1.3	0.1879	1.9	0.0269	1.4	0.71	171.2	2.3	174.8	3.1	223.6	31.6	171.2	2.3
TC19-02NN-21	238	32447	1.5	19.9748	1.4	0.1913	2.1	0.0280	1.5	0.74	178.0	2.7	177.8	3.3	174.4	32.2	178.0	2.7
TC19-02NN-22	49	189243	1.8	13.0253	1.5	1.9360	2.2	0.1833	1.6	0.74	1085.1	15.9	1093.6	14.4	1110.6	29.0	1110.6	29.0
TC19-02NN-23	39	39391	1.6	19.2866	3.3	0.1775	3.7	0.0250	1.7	0.46	159.4	2.7	165.9	5.7	259.8	76.7	159.4	2.7
TC19-02NN-24	436	81822	2.1	19.8564	1.2	0.1934	1.6	0.0280	1.1	0.66	177.9	1.9	179.5	2.7	200.9	28.4	177.9	1.9
TC19-02NN-25	60	4461	2.4	19.2782	3.1	0.1863	3.5	0.0278	1.4	0.42	177.0	2.5	173.4	5.5	124.6	74.2	177.0	2.5
TC19-02NN-26	1260	235630	12.2	20.1290	1.0	0.1897	1.6	0.0278	1.3	0.78	176.5	2.2	176.4	2.6	174.5	23.6	176.5	2.2

TC19-02NN-27	1150	67374	0.7	19.1851	1.1	0.1882	1.7	0.0263	1.3	0.77	167.4	2.1	175.1	2.7	280.4	24.4	167.4	2.1
TC19-02NN-28	93	35072	2.0	20.3882	2.0	0.1836	2.5	0.0274	1.4	0.58	174.3	2.5	171.1	3.9	128.1	47.4	174.3	2.5
TC19-02NN-29	305	121748	0.7	19.7045	1.6	0.1778	2.0	0.0255	1.1	0.58	162.3	1.8	166.2	3.0	222.1	37.5	162.3	1.8
TC19-02NN-30	661	111588	3.5	19.5973	1.2	0.2385	1.9	0.0340	1.5	0.77	215.6	3.2	217.2	3.8	235.1	28.6	215.6	3.2
TC19-02NN-31	123	20709	1.8	19.4342	1.7	0.1759	2.0	0.0252	0.9	0.48	160.1	1.5	164.6	3.0	228.4	40.4	160.1	1.5
TC19-02NN-32	186	34347	0.9	19.6496	1.4	0.1749	1.9	0.0252	1.2	0.65	160.3	1.9	163.7	2.8	212.5	32.9	160.3	1.9
TC19-02NN-33	125	17404	1.3	19.2129	2.3	0.1792	2.7	0.0254	1.5	0.55	161.9	2.4	167.4	4.2	246.2	52.6	161.9	2.4
TC19-02NN-34	249	917779	2.5	19.8290	1.0	0.1925	1.7	0.0277	1.3	0.79	176.4	2.3	178.8	2.8	210.7	24.3	176.4	2.3
TC19-02NN-35	97	45146	1.7	20.3932	2.6	0.1667	3.0	0.0249	1.5	0.49	158.3	2.3	156.5	4.4	129.9	61.7	158.3	2.3
TC19-02NN-36	134	14033	2.1	20.2725	1.6	0.2047	2.4	0.0308	1.6	0.66	195.6	3.1	189.1	4.2	108.5	42.5	195.6	3.1
TC19-02NN-37	577	111614	1.7	20.1431	0.9	0.1758	1.6	0.0258	1.3	0.82	164.2	2.1	164.4	2.4	167.6	21.0	164.2	2.1
TC19-02NN-38	59	261547	2.7	12.6380	1.1	2.1251	1.8	0.1952	1.5	0.80	1149.7	15.4	1157.0	12.6	1170.6	21.8	1170.6	21.8
TC19-02NN-39	247	79506	1.9	19.7595	1.5	0.1908	1.7	0.0275	0.9	0.51	174.8	1.5	177.3	2.8	210.7	34.8	174.8	1.5
TC19-02NN-40	225	41673	1.8	19.3299	1.5	0.1862	1.9	0.0263	1.2	0.62	167.3	2.0	173.4	3.0	257.0	34.5	167.3	2.0
TC19-02NN-41	181	39524	1.7	19.2456	1.5	0.1951	1.9	0.0275	1.3	0.65	174.6	2.2	181.0	3.2	265.2	34.1	174.6	2.2
TC19-02NN-42	274	243223	0.9	19.3298	1.7	0.1917	2.0	0.0269	1.0	0.50	171.3	1.7	178.1	3.2	269.6	39.5	171.3	1.7
TC19-02NN-43	245	4484	1.7	10.7744	8.8	0.3222	9.3	0.0261	2.9	0.31	166.0	4.7	283.6	22.9	1417.4	168.8	166.0	4.7
TC19-02NN-44	499	66168	2.6	19.2488	1.2	0.2439	2.0	0.0342	1.5	0.77	217.1	3.2	221.6	3.9	269.7	28.4	217.1	3.2
TC19-02NN-45	1239	102162	0.7	20.9252	1.0	0.1002	1.5	0.0153	1.1	0.74	97.7	1.0	97.0	1.4	78.2	23.6	97.7	1.0
TC19-02NN-46	565	64050	2.4	19.8253	1.1	0.2390	1.6	0.0346	1.1	0.71	219.1	2.4	217.6	3.1	201.4	26.1	219.1	2.4
TC19-02NN-47	1021	304137	1.9	19.8122	0.9	0.2522	1.4	0.0363	1.1	0.78	230.0	2.5	228.3	2.9	211.5	20.6	230.0	2.5
TC19-02NN-48	635	363676	3.9	19.7509	1.2	0.1770	1.7	0.0254	1.2	0.72	161.8	1.9	165.5	2.6	219.1	26.9	161.8	1.9
TC19-02NN-49	181	17779	1.8	19.6024	1.5	0.1821	2.0	0.0263	1.2	0.61	167.5	2.0	169.9	3.2	202.2	37.1	167.5	2.0
TC19-02NN-50	112	148153	1.4	18.4315	2.8	0.1936	3.1	0.0259	1.3	0.42	165.1	2.1	179.7	5.1	375.9	63.1	165.1	2.1
TC19-02NN-51	412	17885	1.0	19.5459	1.0	0.1739	1.9	0.0251	1.4	0.72	159.5	2.1	162.8	2.9	209.9	30.8	159.5	2.1
TC19-02NN-52	323	65522	1.6	19.6062	1.4	0.1815	2.1	0.0259	1.5	0.73	165.0	2.5	169.3	3.2	230.1	32.5	165.0	2.5
TC19-02NN-53	159	8239	2.1	19.8343	1.7	0.1822	2.1	0.0272	1.2	0.56	172.9	2.0	170.0	3.3	129.9	40.7	172.9	2.0
TC19-02NN-54	1146	5255623	3.1	19.3823	1.0	0.2372	1.8	0.0334	1.6	0.85	211.6	3.3	216.1	3.6	265.1	22.2	211.6	3.3
TC19-02NN-55	151	9470	1.1	20.6222	2.1	0.1640	2.5	0.0254	1.4	0.55	161.5	2.2	154.2	3.5	43.5	NA	161.5	2.2

TC19-02NN-56	201	15655	1.7	19.8785	1.6	0.1715	2.1	0.0252	1.0	0.47	160.7	1.5	160.8	3.1	162.2	43.3	160.7	1.5
TC19-02NN-57	335	173075	1.0	19.6306	1.2	0.1753	1.7	0.0250	1.1	0.68	159.3	1.8	164.0	2.6	231.3	28.6	159.3	1.8
TC19-02NN-58	1018	83335	2.4	19.4017	0.9	0.2486	1.5	0.0351	1.1	0.77	222.6	2.5	225.5	3.0	256.0	21.8	222.6	2.5
TC19-02NN-59	54	24168	1.2	20.3657	3.1	0.1705	3.5	0.0255	1.7	0.47	162.6	2.7	159.9	5.2	120.1	72.9	162.6	2.7
TC19-02NN-60	141	48722189	2.0	9.1752	0.9	4.8435	1.5	0.3229	1.2	0.78	1803.7	18.4	1792.5	12.7	1779.5	17.3	1779.5	17.3
TC19-02NN-61	235	7516	1.9	20.3444	1.6	0.0994	2.9	0.0153	1.4	0.50	97.8	1.4	96.2	2.7	56.3	NA	97.8	1.4
TC19-02NN-62	1266	206055	1.9	19.8341	1.0	0.1913	1.8	0.0276	1.5	0.84	175.3	2.7	177.7	3.0	209.7	22.9	175.3	2.7
TC19-02NN-63	169	24220	1.1	18.6337	2.0	0.1877	2.5	0.0257	1.4	0.57	163.4	2.3	174.7	4.0	329.8	46.4	163.4	2.3
TC19-02NN-64	238	169297	2.4	19.8233	1.6	0.1805	2.2	0.0260	1.5	0.69	165.6	2.5	168.5	3.4	208.9	37.1	165.6	2.5
TC19-02NN-65	1344	225346	2.5	19.6758	1.1	0.2406	1.8	0.0344	1.4	0.78	218.0	3.1	218.9	3.6	229.3	26.4	218.0	3.1
TC19-02NN-66	173	64092	1.1	19.5746	1.7	0.1769	2.2	0.0252	1.5	0.67	160.6	2.4	165.4	3.4	234.5	38.1	160.6	2.4
TC19-02NN-67	128	20581	1.7	20.0023	1.9	0.1886	2.4	0.0277	1.4	0.57	176.4	2.4	175.5	3.9	162.4	46.1	176.4	2.4
TC19-02NN-68	159	456530	1.2	19.4328	1.4	0.1800	1.9	0.0254	1.3	0.69	161.6	2.1	168.1	2.9	261.3	31.4	161.6	2.1
TC19-02NN-69	207	10918	4.0	19.8903	1.5	0.1932	2.0	0.0286	1.3	0.64	181.9	2.3	179.3	3.2	145.2	35.7	181.9	2.3
TC19-02NN-70	247	24403	1.5	19.7003	1.1	0.1767	1.9	0.0255	1.5	0.80	162.5	2.5	165.2	2.9	204.1	26.5	162.5	2.5
TC19-02NN-71	411	149266	2.6	18.3535	2.1	0.1302	2.5	0.0173	1.4	0.54	110.9	1.5	124.3	2.9	388.8	47.2	110.9	1.5
TC19-02NN-72	704	198977	1.7	20.0388	1.1	0.1813	1.4	0.0264	0.8	0.60	167.7	1.4	169.1	2.1	189.3	25.2	167.7	1.4
TC19-02NN-73	154	38608	1.3	19.8788	1.9	0.1909	2.3	0.0277	1.3	0.56	176.3	2.3	177.4	3.8	191.6	44.8	176.3	2.3
TC19-02NN-74	127	14061	1.3	14.3661	3.6	0.2566	3.9	0.0271	1.3	0.34	172.7	2.3	231.9	8.1	885.6	76.3	172.7	2.3
TC19-02NN-75	499	3000946	2.5	21.2943	1.6	0.0958	2.2	0.0148	1.5	0.70	94.7	1.4	92.9	1.9	46.1	37.5	94.7	1.4
TC19-02NN-76	573	87741	2.8	19.0814	1.1	0.2600	1.8	0.0361	1.5	0.82	228.8	3.4	234.7	3.9	294.3	24.0	228.8	3.4
TC19-02NN-77	184	14477	1.1	19.2813	1.1	0.1805	1.9	0.0258	1.5	0.81	164.1	2.5	168.5	2.9	230.0	25.5	164.1	2.5
TC19-02NN-78	163	296310	0.9	19.8027	1.4	0.1779	2.1	0.0256	1.5	0.74	163.1	2.5	166.2	3.2	211.8	32.3	163.1	2.5
TC19-02NN-79	73	6067	1.3	19.6486	2.3	0.1652	3.1	0.0248	1.6	0.52	157.7	2.5	155.3	4.4	117.5	61.4	157.7	2.5
TC19-02NN-80	141	15707	1.5	19.3880	2.1	0.2013	2.6	0.0289	1.4	0.55	183.6	2.6	186.2	4.4	220.1	49.8	183.6	2.6
TC19-02NN-81	106	5956	1.6	19.4088	1.7	0.1831	2.2	0.0271	1.4	0.63	172.6	2.4	170.7	3.5	144.7	40.6	172.6	2.4
TC19-02NN-82	102	40672	1.8	19.5294	1.4	0.1919	2.1	0.0274	1.6	0.75	174.4	2.8	178.2	3.5	228.5	32.4	174.4	2.8
TC19-02NN-83	241	29802	1.4	19.5927	1.9	0.1896	2.4	0.0273	1.3	0.57	173.4	2.3	176.3	3.8	214.9	45.0	173.4	2.3
TC19-02NN-84	268	95860	1.5	19.0048	1.5	0.1988	2.1	0.0276	1.4	0.69	175.3	2.5	184.1	3.5	299.9	33.9	175.3	2.5

TC19-02NN-85	433	108944	2.1	19.1215	1.1	0.2551	1.8	0.0356	1.4	0.79	225.2	3.1	230.7	3.7	287.6	25.1	225.2	3.1
TC19-02NN-86	163	10307	0.9	19.9798	2.1	0.1669	2.7	0.0250	1.7	0.62	158.9	2.6	156.8	3.9	124.5	49.2	158.9	2.6
TC19-02NN-87	317	17747	0.9	19.4220	1.3	0.1766	1.9	0.0254	1.3	0.70	161.4	2.1	165.2	2.8	219.6	30.8	161.4	2.1
TC19-02NN-88	177	56159	1.6	20.4042	1.6	0.1889	2.1	0.0282	1.3	0.63	179.2	2.3	175.7	3.3	129.0	37.5	179.2	2.3
TC19-02NN-89	1199	121789	2.3	19.4511	1.1	0.2691	1.5	0.0382	1.0	0.68	241.4	2.4	242.0	3.2	247.3	25.1	241.4	2.4
TC19-02NN-90	585	76651	2.5	19.3460	1.0	0.2430	1.7	0.0343	1.4	0.82	217.5	3.1	220.9	3.5	257.1	22.9	217.5	3.1
TC19-02NN-91	157	32945	1.4	19.6611	2.0	0.1913	2.5	0.0276	1.4	0.59	175.5	2.5	177.7	4.0	208.0	46.1	175.5	2.5
TC19-02NN-92	275	25027	1.4	20.1966	1.6	0.1747	2.0	0.0260	1.3	0.62	165.3	2.1	163.5	3.0	137.3	37.0	165.3	2.1
TC19-02NN-93	397	36211	1.5	20.0185	1.2	0.1783	1.6	0.0262	1.0	0.66	166.7	1.7	166.6	2.4	165.5	27.2	166.7	1.7
TC19-02NN-94	290	131208	1.4	19.6366	1.1	0.1920	1.7	0.0275	1.3	0.77	174.9	2.3	178.4	2.8	224.1	25.8	174.9	2.3
TC19-02NN-95	185	40597	1.4	19.7478	1.4	0.1760	2.1	0.0255	1.6	0.76	162.2	2.6	164.6	3.3	199.5	32.3	162.2	2.6
TC19-02NN-96	510	28823	1.7	20.0976	1.3	0.1761	2.1	0.0260	1.6	0.78	165.6	2.7	164.7	3.2	151.2	30.8	165.6	2.7
TC19-02NN-97	334	54389	2.4	19.3898	1.2	0.1785	1.6	0.0253	1.1	0.65	161.2	1.7	166.8	2.5	246.1	28.7	161.2	1.7
TC19-02NN-98	185	28101	1.0	19.7204	1.6	0.1765	1.9	0.0256	1.2	0.59	163.1	1.9	165.1	3.0	193.6	36.5	163.1	1.9
TC19-02NN-99	32	52767	3.0	19.7968	3.2	0.2100	3.7	0.0304	1.9	0.51	193.3	3.6	193.5	6.6	195.8	74.7	193.3	3.6
TC19-02NN-100	440	62982	2.5	19.4349	1.1	0.2610	1.5	0.0371	1.1	0.71	234.9	2.5	235.5	3.2	240.8	24.3	234.9	2.5
TC19-02NN-101	735	490695	3.2	19.2548	0.9	0.2451	1.5	0.0344	1.2	0.80	217.8	2.6	222.6	3.0	273.4	21.0	217.8	2.6
TC19-02NN-102	269	174309	1.6	19.9236	1.2	0.1931	1.9	0.0280	1.5	0.78	178.3	2.6	179.3	3.1	192.1	27.6	178.3	2.6
TC19-02NN-103	315	135686	1.1	19.7278	1.2	0.1741	1.6	0.0251	1.1	0.67	159.5	1.7	163.0	2.5	213.5	28.1	159.5	1.7
TC19-02NN-104	340	69891	2.2	19.4506	1.5	0.1824	2.1	0.0259	1.5	0.71	165.0	2.4	170.1	3.2	241.7	33.7	165.0	2.4
TC19-02NN-105	97	23358	1.2	19.8424	1.7	0.1993	2.3	0.0291	1.5	0.66	185.1	2.8	184.5	3.9	177.3	40.2	185.1	2.8
TC19-02NN-106	541	392769	3.7	19.3343	0.8	0.2478	1.4	0.0349	1.2	0.83	220.9	2.6	224.8	2.9	265.5	18.6	220.9	2.6
TC19-02NN-107	329	149471	2.6	20.2965	1.1	0.1764	1.8	0.0261	1.4	0.80	166.0	2.3	165.0	2.7	149.9	25.1	166.0	2.3
TC19-02NN-108	93	24391	1.2	20.1931	2.0	0.1720	2.6	0.0256	1.6	0.61	162.7	2.6	161.2	3.9	137.8	48.9	162.7	2.6
TC19-02NN-109	1181	83546	3.4	19.5261	1.1	0.2374	1.6	0.0339	1.2	0.74	214.7	2.6	216.3	3.2	234.2	25.3	214.7	2.6
TC19-02NN-110	2027	92629	1.0	20.1341	1.0	0.1845	1.7	0.0271	1.4	0.83	172.5	2.4	171.9	2.7	163.4	22.9	172.5	2.4
TC19-5-1	181	12950	0.9	19.9764	1.6	0.1740	2.0	0.0257	1.1	0.54	163.4	1.7	162.9	3.0	155.5	38.7	163.4	1.7
TC19-5-2	251	25104	1.5	20.3566	1.5	0.1681	2.0	0.0250	1.3	0.63	159.1	2.0	157.7	3.0	137.0	37.5	159.1	2.0

TC19-5-3	813	121886	2.0	19.7132	0.8	0.2564	1.3	0.0365	1.0	0.78	231.4	2.4	231.8	2.7	235.6	19.0	231.4	2.4
TC19-5-4	611	4791579	3.6	19.6738	1.1	0.2466	1.8	0.0350	1.4	0.79	221.7	3.2	223.8	3.7	246.6	25.7	221.7	3.2
TC19-5-5	747	115926	2.9	19.4289	0.8	0.2452	1.6	0.0345	1.4	0.87	218.4	2.9	222.7	3.1	268.3	17.9	218.4	2.9
TC19-5-6	510	67018	2.3	20.9476	1.0	0.1129	1.5	0.0171	1.1	0.74	109.6	1.2	108.6	1.5	87.8	24.0	109.6	1.2
TC19-5-7	113	10388	1.9	19.3760	2.4	0.1872	2.6	0.0269	1.2	0.44	171.2	1.9	174.2	4.2	215.5	55.2	171.2	1.9
TC19-5-8	833	186932	2.6	19.5039	0.8	0.1913	1.2	0.0269	0.9	0.75	171.4	1.6	177.7	2.0	262.2	18.9	171.4	1.6
TC19-5-9	184	7269	2.4	20.7325	1.8	0.1054	2.2	0.0165	1.1	0.51	105.2	1.2	101.7	2.1	21.3	NA	105.2	1.2
TC19-5-10	309	20299	2.0	19.8328	1.1	0.1804	1.5	0.0262	1.1	0.70	166.6	1.7	168.4	2.3	193.7	24.6	166.6	1.7
TC19-5-11	664	125437	2.9	19.6397	0.7	0.2526	1.3	0.0359	1.0	0.82	227.1	2.3	228.7	2.6	245.1	16.8	227.1	2.3
TC19-5-12	198	150625	1.4	20.3279	1.3	0.1708	1.5	0.0251	0.8	0.54	159.7	1.3	160.1	2.3	165.2	30.2	159.7	1.3
TC19-5-13	2144	145566	3.4	20.8064	0.9	0.1097	1.7	0.0165	1.4	0.85	105.5	1.5	105.7	1.7	110.3	20.9	105.5	1.5
TC19-5-14	153	177486	1.5	20.2133	1.4	0.1900	1.7	0.0277	0.9	0.54	176.4	1.6	176.6	2.8	179.1	33.3	176.4	1.6
TC19-5-15	426	108281	1.1	20.1405	0.8	0.1731	1.4	0.0252	1.2	0.82	160.5	1.9	162.1	2.2	185.6	19.5	160.5	1.9
TC19-5-16	89	19320	1.5	19.9943	2.6	0.1748	2.8	0.0256	1.0	0.37	162.9	1.7	163.6	4.2	173.9	61.0	162.9	1.7
TC19-5-17	104	6267	1.3	20.5935	1.9	0.1633	2.4	0.0255	1.5	0.62	162.3	2.3	153.6	3.4	22.6	NA	162.3	2.3
TC19-5-18	766	166777	2.7	19.4280	0.8	0.2388	1.2	0.0335	0.9	0.76	212.4	1.9	217.4	2.3	271.9	17.6	212.4	1.9
TC19-5-19	196	20332	0.9	20.3214	1.9	0.1710	2.1	0.0254	0.9	0.43	162.0	1.5	160.3	3.1	135.4	45.1	162.0	1.5
TC19-5-20	76	3415	1.3	18.8836	2.0	0.1810	2.3	0.0269	1.2	0.50	170.8	2.0	168.9	3.6	142.5	47.5	170.8	2.0
TC19-5-21	290	26741	4.8	19.3588	1.1	0.2933	1.4	0.0414	1.0	0.66	261.6	2.4	261.2	3.3	257.2	24.8	261.6	2.4
TC19-5-22	973	654745	3.2	19.9178	0.8	0.2389	1.3	0.0343	1.0	0.76	217.7	2.1	217.5	2.5	215.2	19.3	217.7	2.1
TC19-5-23	86	121476	1.7	20.0663	1.8	0.1718	2.4	0.0249	1.5	0.64	158.8	2.4	161.0	3.6	193.4	42.9	158.8	2.4
TC19-5-24	733	195352	2.2	19.5286	0.8	0.2417	1.4	0.0341	1.2	0.83	216.2	2.5	219.8	2.8	259.5	18.0	216.2	2.5
TC19-5-25	177	51006	1.5	19.8865	1.3	0.1941	1.9	0.0280	1.3	0.72	178.1	2.4	180.1	3.1	206.8	30.4	178.1	2.4
TC19-5-26	230	83434	2.1	19.9745	1.3	0.1866	1.6	0.0270	1.0	0.58	171.6	1.6	173.7	2.6	201.7	31.1	171.6	1.6
TC19-5-27	303	66398	3.5	20.2731	1.1	0.1723	1.5	0.0253	1.0	0.66	161.2	1.5	161.4	2.2	164.8	25.5	161.2	1.5
TC19-5-28	164	38424	1.6	19.8878	1.7	0.1894	2.0	0.0274	1.1	0.54	174.2	1.9	176.1	3.3	201.1	39.4	174.2	1.9
TC19-5-29	87	24404	2.4	20.0217	1.8	0.1892	2.2	0.0277	1.3	0.56	176.0	2.2	176.0	3.6	175.1	43.4	176.0	2.2
TC19-5-30	274	1915555	1.5	20.0620	1.5	0.1748	1.7	0.0253	0.9	0.54	161.2	1.5	163.6	2.6	198.4	34.3	161.2	1.5
TC19-5-31	102	13658	1.4	19.1071	1.8	0.1957	2.2	0.0276	1.2	0.54	175.3	2.1	181.5	3.6	263.3	42.3	175.3	2.1

TC19-5-32	176	9188	1.6	20.3161	1.4	0.1756	1.9	0.0266	1.2	0.64	169.5	2.0	164.3	2.9	89.5	34.1	169.5	2.0
TC19-5-33	864	78603	10.1	20.7461	1.1	0.0928	1.5	0.0140	1.1	0.70	89.3	0.9	90.1	1.3	109.1	25.9	89.3	0.9
TC19-5-34	126	43264	1.5	19.9944	1.4	0.1919	1.8	0.0279	1.1	0.64	177.5	2.0	178.2	2.9	188.8	31.7	177.5	2.0
TC19-5-35	87	14465	2.0	19.4159	2.0	0.1914	2.6	0.0274	1.6	0.59	174.2	2.7	177.8	4.3	227.2	49.4	174.2	2.7
TC19-5-36	774	182058	2.5	19.8149	0.6	0.2469	1.2	0.0354	1.0	0.85	224.5	2.2	224.0	2.4	219.2	14.7	224.5	2.2
TC19-5-37	72	6093	1.7	20.0445	3.1	0.0953	3.5	0.0145	1.6	0.44	92.9	1.5	92.4	3.1	79.3	75.4	92.9	1.5
TC19-5-38	264	33943	2.6	21.0144	1.6	0.1137	1.9	0.0174	1.1	0.54	111.4	1.2	109.3	2.0	63.8	38.8	111.4	1.2
TC19-5-39	532	335132	1.3	20.2834	1.0	0.1746	1.7	0.0256	1.3	0.78	163.1	2.1	163.4	2.5	167.4	24.4	163.1	2.1
TC19-5-40	677	145683	1.6	20.1643	0.9	0.1819	1.5	0.0265	1.2	0.80	168.9	2.0	169.7	2.4	180.7	21.2	168.9	2.0
TC19-5-41	354	43249	2.4	20.6567	1.1	0.1050	1.8	0.0158	1.4	0.79	100.9	1.4	101.4	1.7	113.4	25.6	100.9	1.4
TC19-5-42	945	25714	4.0	18.1915	2.3	0.2703	2.5	0.0359	1.2	0.45	227.2	2.6	242.9	5.5	397.9	50.7	227.2	2.6
TC19-5-43	2408	848174	2.2	19.6051	0.9	0.2634	1.3	0.0373	1.0	0.73	236.1	2.2	237.4	2.8	249.9	20.6	236.1	2.2
TC19-5-44	270	35629	1.6	20.2370	1.4	0.1878	1.9	0.0277	1.3	0.70	176.0	2.3	174.7	3.1	156.8	32.0	176.0	2.3
TC19-5-45	480	76123	2.1	19.5458	1.0	0.2712	1.8	0.0385	1.5	0.83	243.4	3.5	243.6	3.8	246.3	22.9	243.4	3.5
TC19-5-46	71	3246	1.2	19.7436	1.9	0.1738	2.4	0.0273	1.4	0.57	173.5	2.4	162.8	3.7	8.7	NA	173.5	2.4
TC19-5-47	257	32582	1.4	20.0075	1.5	0.1864	1.8	0.0272	1.0	0.54	173.2	1.6	173.5	2.8	178.5	34.2	173.2	1.6
TC19-5-48	1395	197789	4.6	20.5730	0.9	0.1191	1.4	0.0178	1.1	0.75	113.5	1.2	114.3	1.6	130.9	22.3	113.5	1.2
TC19-5-49	566	155232	3.0	19.7535	0.9	0.2480	1.6	0.0355	1.3	0.82	224.9	2.9	224.9	3.2	224.9	21.2	224.9	2.9
TC19-5-50	225	31180	1.9	19.4915	1.3	0.1932	1.6	0.0275	0.9	0.58	174.9	1.6	179.4	2.7	239.1	30.5	174.9	1.6
TC19-5-51	2087	319398	7.0	20.6052	0.7	0.1687	1.3	0.0252	1.1	0.85	160.3	1.7	158.3	1.9	128.9	16.2	160.3	1.7
TC19-5-52	191	46754	1.5	19.8786	1.5	0.1963	1.8	0.0284	1.1	0.60	180.5	2.0	182.0	3.0	201.0	33.7	180.5	2.0
TC19-5-53	973	156730	1.2	20.3306	0.8	0.1686	1.3	0.0248	1.0	0.77	158.2	1.6	158.2	1.9	158.7	19.3	158.2	1.6
TC19-5-54	167	13259	2.2	20.1126	1.3	0.1825	1.9	0.0272	1.3	0.70	172.7	2.2	170.2	2.9	135.5	31.5	172.7	2.2
TC19-5-55	202	52224	1.5	19.9716	1.1	0.2165	1.8	0.0314	1.4	0.77	199.5	2.7	199.0	3.2	192.2	26.4	199.5	2.7
TC19-5-56	89	37595	1.9	20.0982	1.7	0.1845	2.2	0.0270	1.3	0.60	171.9	2.2	171.9	3.4	171.9	40.3	171.9	2.2
TC19-5-57	449	123877	2.6	19.6312	0.9	0.2309	1.4	0.0329	1.1	0.77	208.4	2.2	211.0	2.6	239.4	20.4	208.4	2.2
TC19-5-58	163	30850	1.3	20.0137	1.5	0.1735	1.9	0.0253	1.1	0.58	161.4	1.7	162.4	2.8	177.8	35.3	161.4	1.7
TC19-5-59	1536	130348	3.0	20.2009	0.9	0.1700	1.5	0.0249	1.2	0.81	158.6	1.9	159.4	2.2	171.5	20.8	158.6	1.9
TC19-5-60	82	10272	1.1	20.1618	3.1	0.1109	3.3	0.0167	1.0	0.32	106.5	1.1	106.8	3.3	112.3	73.8	106.5	1.1

TC19-5-61	118	64788	2.0	19.5748	1.8	0.1928	2.3	0.0274	1.4	0.62	174.4	2.4	179.0	3.7	239.3	41.4	174.4	2.4
TC19-5-62	435	108566	1.7	20.2740	1.1	0.1841	1.8	0.0271	1.4	0.77	172.3	2.3	171.6	2.8	161.7	26.5	172.3	2.3
TC19-5-63	399	450027	2.0	20.0524	1.1	0.1770	1.5	0.0257	1.0	0.68	163.6	1.7	165.5	2.3	192.5	25.7	163.6	1.7
TC19-5-64	707	153160	2.3	19.7373	1.1	0.2406	1.6	0.0344	1.2	0.76	218.3	2.6	218.9	3.2	225.6	24.3	218.3	2.6
TC19-5-65	200	28706	1.4	20.0622	1.7	0.1686	2.0	0.0247	1.2	0.57	157.6	1.8	158.2	3.0	168.0	39.4	157.6	1.8
TC19-5-66	90	7998	1.7	20.5790	2.9	0.0943	3.6	0.0146	1.4	0.39	93.5	1.3	91.5	3.2	40.8	NA	93.5	1.3
TC19-5-67	183	17288	1.3	19.7770	1.5	0.1939	2.1	0.0282	1.2	0.57	179.4	2.1	179.9	3.5	186.7	40.0	179.4	2.1
TC19-5-68	144	22736	1.6	20.2137	2.2	0.1142	2.4	0.0169	1.0	0.41	108.2	1.1	109.8	2.5	144.5	50.7	108.2	1.1
TC19-5-69	60	3728	1.4	19.3518	2.5	0.1780	2.9	0.0270	1.3	0.46	171.7	2.2	166.4	4.4	90.6	60.7	171.7	2.2
TC19-5-70	429	95082	2.7	20.7387	1.1	0.1167	1.6	0.0176	1.2	0.74	112.3	1.3	112.1	1.7	107.6	25.2	112.3	1.3
TC19-5-71	124	30628	2.1	20.4367	1.6	0.1714	2.0	0.0256	1.1	0.55	163.0	1.8	160.6	3.0	126.0	39.2	163.0	1.8
TC19-5-72	88	46712	2.6	20.5103	2.2	0.1842	2.5	0.0275	1.2	0.48	175.1	2.1	171.7	4.0	125.4	52.6	175.1	2.1
TC19-5-73	440	51035	1.3	20.8220	0.9	0.1756	1.3	0.0266	1.0	0.74	169.4	1.6	164.3	2.0	90.9	21.2	169.4	1.6
TC19-5-74	598	235289	3.3	20.4551	1.2	0.1139	1.9	0.0169	1.5	0.80	107.9	1.7	109.5	2.0	144.7	27.1	107.9	1.7
TC19-5-75	84	105070	1.9	20.6338	1.8	0.1828	2.2	0.0274	1.1	0.52	174.0	1.9	170.4	3.4	121.9	43.6	174.0	1.9
TC19-5-76	663	78386	1.9	20.4586	1.0	0.1146	1.4	0.0170	1.0	0.73	108.8	1.1	110.1	1.5	139.7	22.7	108.8	1.1
TC19-5-77	136	102104	1.6	19.7077	1.5	0.1789	1.9	0.0256	1.1	0.58	162.8	1.7	167.1	2.9	229.1	35.2	162.8	1.7
TC19-5-78	123	21834	1.1	19.9264	1.6	0.1907	1.9	0.0279	1.1	0.57	177.2	1.9	177.2	3.2	177.7	37.1	177.2	1.9
TC19-5-79	100	84292	1.7	19.5455	2.6	0.1008	2.9	0.0143	1.4	0.48	91.5	1.3	97.5	2.7	247.1	59.4	91.5	1.3
TC19-5-80	125	23857	1.9	19.8849	1.7	0.1868	2.1	0.0272	1.2	0.58	173.0	2.1	173.9	3.4	186.6	40.2	173.0	2.1
TC19-5-81	387	199639	2.8	19.4415	0.8	0.2522	1.3	0.0355	1.0	0.78	225.0	2.2	228.4	2.7	263.6	18.7	225.0	2.2
TC19-5-82	130	89753	3.3	13.6015	0.9	1.7233	1.2	0.1699	0.9	0.70	1011.5	8.1	1017.2	8.0	1029.6	17.9	1029.6	17.9
TC19-5-83	405	1004937	1.7	20.1409	1.3	0.1729	1.6	0.0252	1.0	0.64	160.3	1.7	161.9	2.4	185.2	29.2	160.3	1.7
TC19-5-84	476	147018	7.2	20.2712	1.1	0.1903	1.8	0.0279	1.5	0.81	177.7	2.6	176.9	3.0	165.8	25.0	177.7	2.6
TC19-5-85	225	205166	1.0	19.7795	1.3	0.1750	1.6	0.0251	0.9	0.59	159.6	1.5	163.8	2.4	224.4	29.5	159.6	1.5
TC19-5-86	575	184992	1.4	20.1539	1.1	0.1722	1.7	0.0251	1.3	0.79	160.0	2.1	161.3	2.5	180.5	24.6	160.0	2.1
TC19-5-87	257	36418	1.9	19.9822	1.3	0.1749	1.5	0.0255	0.9	0.56	162.1	1.4	163.7	2.3	185.6	30.0	162.1	1.4
TC19-5-88	351	190055	2.4	20.0702	1.1	0.1878	1.6	0.0273	1.1	0.70	173.6	1.9	174.7	2.6	189.7	26.6	173.6	1.9
TC19-5-89	471	187716	2.1	20.0517	1.1	0.1896	1.5	0.0276	1.0	0.69	175.2	1.8	176.3	2.5	191.3	25.6	175.2	1.8

TC19-5-90	1213	394775	3.6	19.8635	0.9	0.2416	1.4	0.0347	1.1	0.76	220.2	2.3	219.7	2.8	215.0	21.2	220.2	2.3
TC19-5-91	568	283045	2.4	19.4088	1.0	0.2606	1.6	0.0366	1.2	0.75	231.7	2.7	235.1	3.3	269.6	23.8	231.7	2.7
TC19-5-92	294	1064173	2.4	19.3122	1.7	0.1985	2.0	0.0277	1.1	0.56	176.3	2.0	183.9	3.4	282.7	38.5	176.3	2.0
TC19-5-93	874	214045	1.8	20.1421	0.9	0.1882	1.4	0.0274	1.1	0.79	174.5	1.9	175.1	2.3	183.3	20.1	174.5	1.9
TC19-5-94	200	87338	1.8	20.3415	1.3	0.1846	1.6	0.0272	1.0	0.61	173.2	1.7	172.0	2.6	155.5	30.1	173.2	1.7
TC19-5-95	705	96678	3.1	19.6589	0.7	0.2331	1.3	0.0332	1.1	0.85	210.6	2.3	212.7	2.5	236.0	16.2	210.6	2.3
TC19-5-96	89	8492	1.1	20.3935	2.0	0.1676	2.9	0.0256	1.1	0.36	163.0	1.7	157.3	4.3	72.6	64.7	163.0	1.7
TC19-5-97	127	25757	1.5	19.3770	1.6	0.1893	1.9	0.0268	1.1	0.56	170.6	1.8	176.0	3.1	249.8	36.4	170.6	1.8
TC19-5-98	463	72393	1.3	20.0972	1.0	0.1904	1.6	0.0278	1.2	0.75	176.6	2.1	177.0	2.6	181.5	24.4	176.6	2.1
TC19-5-99	221	52862	1.0	20.1463	1.2	0.1844	1.6	0.0270	1.0	0.66	171.8	1.7	171.8	2.5	172.3	27.2	171.8	1.7
TC19-5-100	326	77352	3.6	19.2819	1.1	0.2497	1.5	0.0349	1.1	0.70	221.4	2.3	226.3	3.1	277.8	24.8	221.4	2.3
TC19-5-101	238	17978	1.2	19.7826	1.4	0.1827	1.8	0.0266	1.1	0.59	169.1	1.8	170.4	2.8	188.3	33.7	169.1	1.8
TC19-5-102	176	164901	1.5	19.7692	1.0	0.1954	1.3	0.0280	0.8	0.64	178.0	1.5	181.2	2.2	223.7	23.6	178.0	1.5
TC19-5-103	580	50694	1.7	19.8607	1.0	0.1897	1.5	0.0274	1.1	0.71	174.4	1.8	176.4	2.4	203.7	24.2	174.4	1.8
TC19-5-104	1017	117101	2.8	19.5920	0.8	0.2453	1.5	0.0348	1.3	0.84	220.8	2.8	222.7	3.0	243.8	18.8	220.8	2.8
TC19-5-105	279	17796	0.9	20.0512	1.3	0.1639	1.7	0.0242	1.1	0.65	153.9	1.7	154.1	2.5	157.7	30.5	153.9	1.7
TC19-5-106	120	24702	1.3	19.7010	1.8	0.1869	2.2	0.0269	1.1	0.50	171.3	1.8	174.0	3.5	210.2	43.6	171.3	1.8
TC19-5-107	332	41739	1.1	20.1421	1.3	0.1710	1.7	0.0251	1.1	0.63	159.7	1.7	160.3	2.5	168.2	31.0	159.7	1.7
TC19-5-108	1210	451619	1.9	19.3283	0.9	0.2443	1.6	0.0342	1.3	0.81	216.6	2.7	221.9	3.1	278.6	21.1	216.6	2.7
TC19-5-109	364	95225	1.2	20.2344	1.1	0.1917	1.7	0.0282	1.3	0.76	179.0	2.3	178.1	2.8	166.5	25.8	179.0	2.3
TC19-5-110	110	36209	2.3	20.6114	1.9	0.1826	2.3	0.0275	1.4	0.58	174.6	2.3	170.3	3.7	110.8	45.3	174.6	2.3
TC19-2-1	59	3238	0.9	19.1878	4.5	0.0377	4.9	0.0057	1.6	0.33	36.8	0.6	37.6	1.8	90.2	NA	36.8	0.6
TC19-2-2	93	141446	1.4	9.9902	0.9	4.0251	1.4	0.2903	1.0	0.74	1643.1	15.1	1639.3	11.4	1634.4	17.5	1634.4	17.5
TC19-2-3	162	1630472	1.6	8.5332	0.8	5.6952	1.3	0.3505	1.0	0.79	1937.2	16.9	1930.6	11.1	1923.6	14.2	1923.6	14.2
TC19-2-4	56	208993	1.8	13.1257	1.0	1.9675	1.4	0.1864	1.0	0.70	1102.0	10.2	1104.5	9.7	1109.2	20.6	1109.2	20.6
TC19-2-5	38	38838	0.8	13.4298	1.0	1.8778	1.4	0.1828	0.9	0.66	1082.2	9.1	1073.3	9.1	1055.2	20.8	1055.2	20.8
TC19-2-6	38	295901	2.1	5.2209	0.9	15.1090	1.3	0.5687	1.0	0.75	2902.5	22.8	2822.1	12.4	2765.2	14.1	2765.2	14.1
TC19-2-7	68	96491	1.0	13.2611	1.0	1.9337	1.5	0.1852	1.1	0.76	1095.1	11.3	1092.8	9.8	1088.2	19.1	1088.2	19.1

TC19-2-8	72	21027	1.2	17.6550	1.3	0.6198	1.7	0.0798	1.1	0.65	494.9	5.1	489.7	6.5	465.5	28.1	494.9	5.1
TC19-2-9	78	70041	1.5	13.6453	1.2	1.7519	1.6	0.1727	1.1	0.68	1026.8	10.5	1027.9	10.5	1030.1	24.3	1030.1	24.3
TC19-2-10	104	10209	0.7	20.9538	3.2	0.0360	3.5	0.0056	1.4	0.39	36.1	0.5	35.9	1.2	27.4	NA	36.1	0.5
TC19-2-11	242	524460	2.2	8.4951	0.7	5.7263	1.3	0.3506	1.0	0.82	1937.6	17.5	1935.3	11.0	1932.9	13.1	1932.9	13.1
TC19-2-12	141	3831668	2.9	11.2432	0.8	2.9723	1.5	0.2408	1.3	0.84	1391.0	15.9	1400.6	11.5	1415.1	15.5	1415.1	15.5
TC19-2-13	55	91700	1.3	7.6844	0.7	7.0674	1.4	0.3919	1.2	0.85	2131.6	22.1	2119.9	12.7	2108.6	13.1	2108.6	13.1
TC19-2-14	96	30776475	1.4	7.8412	0.8	6.8951	1.3	0.3897	1.0	0.78	2121.4	18.2	2098.0	11.4	2075.1	14.0	2075.1	14.0
TC19-2-15	74	66021	1.6	13.5190	1.0	1.8967	1.5	0.1854	1.1	0.75	1096.2	11.3	1079.9	10.0	1047.3	20.3	1047.3	20.3
TC19-2-16	589	37411	2.9	20.2966	1.2	0.1071	1.8	0.0158	1.3	0.72	101.0	1.3	103.3	1.7	156.4	28.9	101.0	1.3
TC19-2-17	142	13746	2.3	20.4998	1.7	0.1064	2.2	0.0161	1.4	0.64	102.8	1.4	102.7	2.1	100.0	39.7	102.8	1.4
TC19-2-18	84	650276	3.4	13.7043	0.9	1.7677	1.4	0.1747	1.1	0.76	1037.9	10.3	1033.7	9.1	1024.8	18.5	1024.8	18.5
TC19-2-19	38	340241	1.1	8.9511	0.9	5.1007	1.3	0.3293	1.0	0.76	1834.8	16.0	1836.2	11.2	1837.9	15.6	1837.9	15.6
TC19-2-20	154	114169	1.0	13.5505	0.7	1.7822	1.4	0.1744	1.3	0.88	1036.1	12.1	1039.0	9.4	1045.0	13.9	1045.0	13.9
TC19-2-21	72	2790	1.3	24.2280	3.5	0.0284	6.8	0.0057	1.4	0.20	36.7	0.5	28.5	1.9	NA	NA	36.7	0.5
TC19-2-22	83	118472	1.3	9.1630	0.7	4.7068	1.3	0.3115	1.1	0.86	1748.2	17.2	1768.5	10.9	1792.4	12.1	1792.4	12.1
TC19-2-23	21	27654	0.7	5.5162	0.9	13.2478	1.4	0.5288	1.1	0.76	2736.5	24.1	2697.5	13.4	2668.3	15.3	2668.3	15.3
TC19-2-24	88	107785	1.6	8.7048	0.7	5.5043	1.5	0.3458	1.3	0.89	1914.3	22.0	1901.3	12.8	1887.1	12.2	1887.1	12.2
TC19-2-25	68	49532	1.5	5.4489	0.8	13.5817	1.4	0.5344	1.2	0.82	2759.8	26.5	2721.0	13.7	2692.3	13.8	2692.3	13.8
TC19-2-26	52	134343	2.0	5.2008	0.7	14.1717	1.4	0.5318	1.2	0.88	2749.0	26.9	2761.3	13.0	2770.3	10.8	2770.3	10.8
TC19-2-27	229	12083	1.1	20.2190	1.0	0.1744	1.5	0.0261	0.9	0.59	165.9	1.5	163.2	2.3	124.3	28.3	165.9	1.5
TC19-2-28	575	90604	2.1	19.4279	0.9	0.2685	1.8	0.0377	1.5	0.85	238.7	3.5	241.5	3.8	268.1	21.5	238.7	3.5
TC19-2-29	69	47612	1.4	13.4990	1.2	1.7740	1.7	0.1734	1.2	0.72	1030.9	11.5	1036.0	10.9	1046.7	23.4	1046.7	23.4
TC19-2-30	49	582	1.1	19.2869	5.9	0.0206	9.4	0.0058	1.5	0.16	37.1	0.6	20.8	1.9	NA	NA	37.1	0.6
TC19-2-31	83	461802	2.0	13.6657	0.8	1.7571	1.4	0.1733	1.1	0.81	1030.5	10.6	1029.8	8.9	1028.2	16.3	1028.2	16.3
TC19-2-32	96	51379	1.9	11.5658	0.8	2.6700	1.4	0.2236	1.2	0.83	1300.7	13.8	1320.2	10.5	1351.9	15.5	1351.9	15.5
TC19-2-33	56	16360	3.2	13.1762	0.9	1.8996	1.7	0.1827	1.5	0.85	1081.5	14.5	1080.9	11.4	1079.9	18.4	1079.9	18.4
TC19-2-34	255	8313816	2.5	10.7451	0.8	3.3901	1.4	0.2629	1.1	0.81	1504.7	15.3	1502.1	11.0	1498.5	15.4	1498.5	15.4
TC19-2-35	48	68306	1.8	13.6078	0.8	1.7957	1.5	0.1767	1.2	0.82	1049.1	11.5	1043.9	9.5	1033.1	17.0	1033.1	17.0
TC19-2-36	96	34662	2.4	13.7496	1.2	0.8835	2.1	0.0881	1.7	0.82	544.5	9.0	642.9	10.1	1005.8	24.9	544.5	9.0

TC19-2-37	162	306979	0.5	5.4176	0.9	13.6902	1.2	0.5351	0.8	0.70	2763.1	19.1	2728.5	11.5	2703.0	14.3	2703.0	14.3
TC19-2-38	75	394819	2.1	11.2218	0.8	3.1855	1.3	0.2579	1.0	0.77	1478.9	12.9	1453.7	9.8	1416.9	15.6	1416.9	15.6
TC19-2-39	89	1387	0.8	21.1024	3.7	0.0289	11.8	0.0057	1.5	0.13	36.6	0.5	28.9	3.4	NA	NA	36.6	0.5
TC19-2-40	109	321269	1.7	8.5215	0.7	5.7130	1.5	0.3512	1.3	0.87	1940.3	22.4	1933.3	13.2	1925.9	13.3	1925.9	13.3
TC19-2-41	59	3834	1.5	17.7051	5.3	0.0426	6.1	0.0058	2.2	0.36	37.5	0.8	42.3	2.5	326.9	128.6	37.5	0.8
TC19-2-42	68	31751	1.0	12.2166	0.9	2.3568	1.4	0.2088	1.1	0.76	1222.5	11.9	1229.6	10.0	1242.1	17.8	1242.1	17.8
TC19-2-43	164	919521	1.3	11.3951	0.7	2.8952	1.3	0.2380	1.1	0.85	1376.1	14.0	1380.7	10.0	1387.7	13.2	1387.7	13.2
TC19-2-44	25	47772	0.6	5.3508	0.8	13.9249	1.4	0.5380	1.2	0.84	2775.1	26.2	2744.6	13.2	2722.3	12.6	2722.3	12.6
TC19-2-45	146	115013	3.3	13.0372	1.0	2.0263	1.5	0.1908	1.1	0.75	1125.7	11.3	1124.4	9.9	1121.8	19.2	1121.8	19.2
TC19-2-46	80	51481	1.3	8.8224	0.8	5.0420	1.4	0.3215	1.1	0.80	1797.1	18.0	1826.4	12.1	1860.0	15.3	1860.0	15.3
TC19-2-47	138	124849	1.4	8.9733	0.6	5.1149	1.1	0.3314	0.9	0.85	1845.3	15.1	1838.6	9.4	1831.0	10.8	1831.0	10.8
TC19-2-48	170	2920	2.0	20.8464	3.2	0.0330	3.5	0.0056	1.2	0.35	35.7	0.4	32.9	1.1	NA	NA	35.7	0.4
TC19-2-49	37	43566	1.7	12.9834	1.1	2.0731	1.5	0.1950	0.9	0.64	1148.3	9.8	1139.9	10.0	1124.0	22.4	1124.0	22.4
TC19-2-50	258	495161	2.8	12.9929	0.8	2.0822	1.2	0.1953	1.0	0.79	1149.8	10.4	1143.0	8.6	1129.9	15.3	1129.9	15.3
TC19-2-51	114	38160	1.0	20.9420	3.1	0.0361	3.5	0.0055	1.6	0.46	35.3	0.6	36.0	1.2	80.5	74.2	35.3	0.6
TC19-2-52	32	18759	1.1	10.9285	0.9	3.2644	1.6	0.2596	1.3	0.83	1487.7	17.6	1472.6	12.4	1450.9	17.0	1450.9	17.0
TC19-2-53	133	75571	2.2	13.0411	1.1	1.8669	1.6	0.1762	1.2	0.74	1046.2	11.6	1069.4	10.7	1117.0	21.6	1117.0	21.6
TC19-2-54	274	402798	2.4	13.3929	0.6	1.7912	1.1	0.1733	1.0	0.85	1030.2	9.1	1042.3	7.3	1067.7	12.1	1067.7	12.1
TC19-2-55	136	358932	2.3	11.9685	0.8	2.5579	1.3	0.2211	1.0	0.78	1287.7	11.5	1288.7	9.2	1290.4	15.4	1290.4	15.4
TC19-2-56	67	79918	1.9	4.1031	0.7	21.1109	1.2	0.6256	1.0	0.81	3132.2	24.4	3143.7	11.8	3151.0	11.3	3151.0	11.3
TC19-2-57	170	296218	1.4	8.8393	0.7	5.1890	1.2	0.3312	0.9	0.78	1844.3	15.0	1850.8	10.1	1858.1	13.3	1858.1	13.3
TC19-2-58	134	211245	0.7	5.4647	0.8	13.4686	1.4	0.5314	1.2	0.84	2747.4	27.0	2713.1	13.6	2687.6	12.9	2687.6	12.9
TC19-2-59	185	55595	1.0	8.5307	0.7	4.8066	1.5	0.2966	1.3	0.87	1674.4	18.9	1786.0	12.4	1919.1	13.0	1919.1	13.0
TC19-2-60	55	24857	1.8	9.8030	0.8	4.1697	1.3	0.2966	1.0	0.78	1674.2	15.4	1668.1	11.0	1660.3	15.6	1660.3	15.6
TC19-2-61	121	47630	3.0	12.5813	0.8	2.1864	1.6	0.1992	1.4	0.85	1171.2	15.1	1176.7	11.5	1186.8	16.8	1186.8	16.8
TC19-2-62	131	26681	1.3	12.9976	1.0	1.8945	1.5	0.1790	1.1	0.75	1061.4	10.7	1079.2	9.7	1115.3	19.2	1115.3	19.2
TC19-2-63	50	171790	1.3	6.9960	0.9	8.5159	1.5	0.4301	1.2	0.80	2306.3	23.7	2287.6	13.8	2270.9	15.5	2270.9	15.5
TC19-2-64	50	394291	2.2	4.9792	0.7	15.4918	1.0	0.5571	0.7	0.75	2854.6	17.3	2846.0	9.5	2839.9	10.7	2839.9	10.7
TC19-2-65	171	946111	1.7	8.7782	0.7	5.3946	1.2	0.3421	0.9	0.79	1896.7	15.6	1884.0	10.2	1870.1	13.1	1870.1	13.1

TC19-2-66	156	98298	1.0	18.1284	0.9	0.5057	1.6	0.0664	1.2	0.79	414.1	5.0	415.6	5.3	423.5	21.1	414.1	5.0
TC19-2-67	339	17088	1.7	20.5454	2.6	0.0368	3.0	0.0056	1.3	0.45	35.7	0.5	36.7	1.1	99.1	63.2	35.7	0.5
TC19-2-68	494	15192	2.5	20.6520	2.1	0.0364	2.4	0.0055	1.2	0.50	35.6	0.4	36.3	0.9	81.5	49.5	35.6	0.4
TC19-2-69	74	83996	0.7	8.4810	0.7	5.7416	1.5	0.3523	1.3	0.88	1945.4	21.9	1937.7	12.8	1929.4	12.4	1929.4	12.4
TC19-2-70	172	1091	1.6	15.5303	7.8	0.0394	8.4	0.0056	2.0	0.24	36.0	0.7	39.3	3.2	245.5	188.3	36.0	0.7
TC19-2-71	119	85284	4.6	13.8008	0.9	1.6266	1.4	0.1624	1.1	0.78	970.3	9.8	980.6	8.8	1003.7	17.6	1003.7	17.6
TC19-2-72	163	132519	4.7	13.3417	0.8	1.8314	1.2	0.1766	0.9	0.73	1048.5	8.5	1056.8	7.8	1073.9	16.3	1073.9	16.3
TC19-2-73	145	276253	2.0	8.9700	0.8	5.1935	1.2	0.3365	0.9	0.75	1869.8	14.6	1851.6	10.3	1831.1	14.5	1831.1	14.5
TC19-2-74	89	164400	1.0	11.2149	1.2	3.1834	1.6	0.2579	1.2	0.71	1479.3	15.5	1453.1	12.7	1415.0	22.2	1415.0	22.2
TC19-2-75	224	373023	2.7	9.2898	0.7	4.7485	1.3	0.3184	1.1	0.86	1781.9	17.0	1775.8	10.7	1768.7	12.0	1768.7	12.0
TC19-2-76	83	53404	0.7	8.5081	0.8	5.7418	1.4	0.3535	1.1	0.82	1951.2	18.7	1937.7	11.7	1923.2	13.9	1923.2	13.9
TC19-2-77	76	61180	1.9	8.8788	0.7	5.1603	1.2	0.3316	1.0	0.81	1845.9	15.9	1846.1	10.4	1846.3	13.0	1846.3	13.0
TC19-2-78	180	339618	2.8	13.6706	0.9	1.8042	1.4	0.1783	1.2	0.80	1057.8	11.3	1047.0	9.4	1024.4	17.6	1024.4	17.6
TC19-2-79	168	184547	3.3	9.7512	0.7	4.3073	1.1	0.3036	0.8	0.74	1709.2	12.2	1694.8	9.0	1676.9	13.4	1676.9	13.4
TC19-2-80	92	128814	1.9	13.1856	0.8	1.8995	1.3	0.1814	1.0	0.78	1074.4	10.1	1080.9	8.8	1094.1	16.6	1094.1	16.6
TC19-2-81	93	77772	2.0	13.6914	0.9	1.7151	1.1	0.1702	0.7	0.65	1013.3	6.8	1014.2	7.2	1016.1	17.3	1016.1	17.3
TC19-2-82	200	197460	3.0	13.5270	0.8	1.7480	1.3	0.1711	1.0	0.78	1018.2	9.8	1026.4	8.6	1043.9	16.9	1043.9	16.9
TC19-2-83	143	368133	1.7	12.1701	0.7	2.4167	1.2	0.2127	1.0	0.80	1243.4	11.1	1247.6	8.8	1254.9	14.5	1254.9	14.5
TC19-2-84	441	250805	1.9	13.5767	0.8	1.8018	1.3	0.1772	1.1	0.81	1051.8	10.6	1046.1	8.8	1034.1	15.8	1034.1	15.8
TC19-2-85	132	139520	2.5	13.6971	1.0	1.6882	1.6	0.1676	1.2	0.74	999.1	10.7	1004.1	9.9	1015.0	21.1	1015.0	21.1
TC19-2-86	81	701	1.0	15.4149	5.1	0.0351	5.5	0.0058	1.5	0.28	37.4	0.6	35.1	1.9	NA	NA	37.4	0.6
TC19-2-87	65	106888	1.9	12.7704	1.0	2.0845	1.3	0.1931	0.9	0.67	1138.0	9.0	1143.7	8.9	1154.5	19.2	1154.5	19.2
TC19-2-88	117	231168	2.8	5.3619	0.6	13.6245	1.1	0.5293	0.9	0.83	2738.6	20.5	2724.0	10.5	2713.1	10.3	2713.1	10.3
TC19-2-89	141	112790	1.4	13.1854	0.9	1.8796	1.3	0.1799	0.9	0.73	1066.3	9.1	1073.9	8.4	1089.3	17.3	1089.3	17.3
TC19-2-90	54	134104	1.2	8.8799	0.9	5.2143	1.5	0.3358	1.2	0.81	1866.5	19.7	1854.9	12.7	1842.0	15.7	1842.0	15.7
TC19-2-91	73	30962	1.6	13.5928	0.9	1.7324	1.3	0.1717	1.0	0.71	1021.5	9.0	1020.6	8.6	1018.8	19.2	1018.8	19.2
TC19-2-92	110	133135	2.8	13.2298	0.8	1.9438	1.3	0.1866	1.0	0.77	1103.2	9.8	1096.3	8.5	1082.7	16.2	1082.7	16.2
TC19-2-93	726	9114	0.7	19.9172	1.9	0.0362	2.4	0.0054	1.4	0.60	34.7	0.5	36.1	0.9	129.6	45.4	34.7	0.5
TC19-2-94	82	67723	1.7	8.9650	0.8	5.1040	1.3	0.3319	1.1	0.82	1847.8	17.8	1836.8	11.5	1824.3	13.9	1824.3	13.9

TC19-2-95	140	669739	2.5	10.7417	0.7	3.4041	1.2	0.2648	1.0	0.83	1514.5	13.0	1505.3	9.1	1492.4	12.4	1492.4	12.4
TC19-2-96	17	21752	0.9	12.0949	1.0	2.4104	1.5	0.2129	1.1	0.69	1244.2	12.0	1245.7	11.0	1248.4	21.7	1248.4	21.7
TC19-2-97	45	15947	1.6	13.7151	1.1	1.6545	1.7	0.1664	1.3	0.76	992.0	12.1	991.3	10.9	989.5	22.7	989.5	22.7
TC19-2-98	58	69012	1.6	9.6653	0.8	4.3023	1.7	0.3017	1.5	0.88	1699.8	21.9	1693.8	13.7	1686.4	14.3	1686.4	14.3
TC19-2-99	80	3284	1.3	20.6987	5.2	0.0355	5.7	0.0059	1.6	0.28	37.8	0.6	35.5	2.0	NA	NA	37.8	0.6
TC19-2-100	85	251022	2.6	9.6502	0.8	4.3721	1.3	0.3058	1.1	0.81	1719.9	16.0	1707.1	10.9	1691.4	14.3	1691.4	14.3
TC19-2-101	571	34256	2.5	21.0715	1.4	0.0366	1.9	0.0056	1.3	0.65	36.3	0.5	36.5	0.7	53.6	34.7	36.3	0.5
TC19-2-102	95	869542	0.7	8.8480	0.6	5.2898	1.2	0.3391	1.0	0.84	1882.2	16.0	1867.2	10.0	1850.5	11.4	1850.5	11.4
TC19-2-103	52	114985	2.1	13.8069	1.0	1.6677	1.4	0.1671	1.0	0.70	996.0	8.8	996.3	8.6	997.0	19.6	997.0	19.6
TC19-2-104	90	155168	3.1	5.3265	0.7	14.1959	1.4	0.5481	1.2	0.85	2817.4	27.2	2762.9	13.3	2723.3	12.1	2723.3	12.1
TC19-2-105	132	2019	1.2	19.9523	3.1	0.0326	4.0	0.0055	1.3	0.32	35.5	0.5	32.5	1.3	NA	NA	35.5	0.5

Table A.2: Analytical data for Titus Canyon zircon (U-Th)/He analyses

Sample	U (ppm)	Th (ppm)	He (ncc)	Mass (mg)	Ft*	Radius (μm)	Length (μm)	Uncorr. Age (Ma)	Age Error (Ma)	Corrected Age (Ma)
17CH03 Zra	377.1	196.4	3.4	0.0036	0.76	47.0	202.7	18.4	0.24	24.3
17CH03 Zrb	188.1	156.0	1.6	0.0040	0.73	41.1	292.4	15.2	0.19	20.8
17CH03 Zrc	793.5	502.4	15.8	0.0064	0.80	57.0	245.1	22.4	0.28	28.0
17TCTF01 Zra	200.0	190.0	2.8	0.0086	0.80	57.0	329.9	10.9	0.13	13.6
17TCTF01 Zrb	270.6	286.7	1.4	0.0026	0.72	40.4	197.9	13.0	0.16	18.1
17TCTF01 Zrc	469.5	266.2	1.6	0.0025	0.72	41.1	184.2	10.1	0.13	14.0
17TCTF03 Zra†	1111.6	575.1	10.9	0.0030	0.74	44.0	193.0	24.1	0.31	32.5
17TCTF03 Zrb†	419.5	248.0	8.5	0.0092	0.82	66.7	255.8	16.0	0.21	19.4
17TCTF03 Zrc†	525.8	257.3	5.1	0.0036	0.78	54.8	151.1	19.7	0.25	25.3
17TCTF04 Zra	579.7	342.6	15.4	0.0083	0.81	58.5	302.6	23.1	0.28	28.7
17TCTF04 Zrb	910.2	355.0	27.0	0.0099	0.82	64.5	296.8	22.6	0.30	27.5
17TCTF04 Zrc	1454.2	581.4	46.9	0.0098	0.81	61.0	328.2	24.8	0.33	30.5

* Ft is the alpha-ejection correction after Farley et al. (1996)

† Standard deviation of replicate analyses > 25%

Table A.3: Analytical data for 40Ar/39Ar ages of Gutenkunst (2006)

FM-2 16.5 Biotite #1										Weighted average of J from standards= 0.002536 +/- 0.000013						Original Age		Recalc Age	
Laser	Cum.	40/39	40/39	37/39	37/39	36/39	36/39	% Atm	Ca/K	+/-	Cl/K	+/-	40Ar*/39Ark	+/-		Age	+/-	Age	+/-
(mW)	39Ar	measured	+/-	measured	+/-	measured	+/-	40Ar								(Ma)	(Ma)	(Ma)	(Ma)
200	0.155	15.763	0.081	0.03779	0.00286	0.04051	0.00073	76.1	0.06934	0.00526	0.00446	0.00013	3.767	0.221		17.2	1	17.62	1.065
600	0.4079	24.671	0.086	0.05197	0.00386	0.06978	0.0011	83.7	0.09537	0.00709	0.01024	0.00018	4.026	0.326		18.3	1.5	18.81	1.554
800	0.526	24.924	0.063	0.0428	0.00432	0.06982	0.00093	82.9	0.07853	0.00792	0.01492	0.00015	4.267	0.28		19.4	1.3	19.93	1.302
1000	0.6314	28.365	0.095	0.03022	0.00462	0.08053	0.00133	84	0.05546	0.00847	0.01719	0.0002	4.541	0.392		20.7	1.8	21.2	1.866
1750	0.8725	21.029	0.071	0.09738	0.01042	0.0514	0.00244	72.3	0.17869	0.01913	0.02122	0.00042	5.821	0.722		26.4	3.3	27.06	3.332
2000	0.8988	21.486	0.142	0.16146	0.01984	0.05639	0.00417	77.6	0.29629	0.0364	0.02234	0.00084	4.807	1.229		21.9	5.6	22.38	5.72
2500	0.9316	20.745	0.109	0.20147	0.01755	0.05918	0.00322	84.3	0.36971	0.0322	0.02471	0.00071	3.244	0.95		14.8	4.3	15.14	4.434
3000	0.9488	24.335	0.233	0.11016	0.03738	0.07041	0.00688	85.6	0.20214	0.0686	0.02171	0.00134	3.509	2.025		16	9.2	16.4	9.467
4000	0.9764	30.983	0.225	0.1808	0.02294	0.09323	0.00384	89	0.33178	0.04211	0.02079	0.00076	3.418	1.121		15.6	5.1	15.96	5.353
5000	0.987	22.079	0.347	0.32118	0.05785	0.07665	0.00895	102.6	0.58945	0.10618	0.02467	0.00173	-0.576	2.621		-2.6	12	-2.668	12.47
8000	1	13.202	0.161	0.2302	0.0432	0.03624	0.01032	81.2	0.42244	0.07929	0.01657	0.00223	2.482	3.048		11.3	13.9	11.6	14.17

FM-2 16.5 Biotite #2										Weighted average of J from standards= 0.002536 +/- 0.000013						Original Age		Recalc Age	
Laser	Cum.	40/39	40/39	37/39	37/39	36/39	36/39	% Atm	Ca/K	+/-	Cl/K	+/-	40Ar*/39Ark	+/-		Age	+/-	Age	+/-
(mW)	39Ar	measured	+/-	measured	+/-	measured	+/-	40Ar											
150	0.1413	26.932	0.102	0.10525	0.00407	0.07594	0.00064	83.4	0.19314	0.00746	0.00448	0.0001	4.471	0.205		20.4	0.9	20.85	0.9917
300	0.2841	39.245	0.164	0.20267	0.00405	0.11972	0.00111	90.2	0.37192	0.00743	0.01004	0.00013	3.853	0.327		17.6	1.5	17.97	1.695
450	0.3667	41.863	0.169	0.27249	0.00521	0.12967	0.00122	91.5	0.50006	0.00956	0.01088	0.00028	3.538	0.354		16.1	1.6	16.48	1.842
600	0.443	39.817	0.197	0.14092	0.00475	0.1219	0.00144	90.5	0.2586	0.00871	0.01437	0.00024	3.777	0.408		17.2	1.9	17.63	2.168
900	0.6619	32.081	0.122	0.07896	0.00414	0.0943	0.00068	86.9	0.14489	0.00759	0.0169	0.00022	4.193	0.193		19.1	0.9	19.57	1.086
1200	0.7407	30.386	0.136	0.1245	0.00518	0.08705	0.00102	84.7	0.22845	0.00951	0.02011	0.00025	4.643	0.289		21.1	1.3	21.64	1.525
1500	0.7984	34.549	0.184	0.31956	0.00965	0.10252	0.00193	87.7	0.58646	0.01771	0.02614	0.00033	4.25	0.554		19.4	2.5	19.75	2.767
2500	0.9264	10.31	0.057	0.05677	0.01517	0.02373	0.00158	68.1	0.10418	0.02783	0.01607	0.0006	3.275	0.466		14.9	2.1	15.33	2.177

3000	0.9472	11.182	0.076	0.02704	0.02518	0.02525	0.00332	66.9	0.04962	0.0462	0.0131	0.00094	3.695	0.98	16.8	4.4	17.29	4.55
4000	0.9952	20.235	0.123	0.15956	0.01003	0.05549	0.00178	81.1	0.29279	0.01842	0.01812	0.00057	3.821	0.522	17.4	2.4	17.83	2.497
5000	0.9996	8.314	0.288	-0.14772	0.16107	0.03114	0.01593	111.2	-0.27102	0.29548	0.00563	0.00528	-0.926	4.705	-4.2	21.6	-4.15	22.07
8000	1	29.848	7.239	-0.79523	1.45234	0.26145	0.18429	259.3	-1.45838	2.66208	0.06459	0.04253	-47.475	52.47	-231.5	273	-236.1	292.3

FM-3 102.5
Biotite #1

Weighted average of J from standards= 0.002536 +/- 0.000013

Laser	Cum.	40/39	40/39	37/39	37/39	36/39	36/39	% Atm	Ca/K	+/-	Cl/K	+/-	40Ar*/39Ark	+/-	Age	+/-	Age	+/-
(mW)	39Ar	measured	+/-	measured	+/-	measured	+/-	40Ar							(Ma)	(Ma)	(Ma)	(Ma)
200	0.0339	60.465	0.265	0.07734	0.00407	0.19283	0.00137	94.3	0.14192	0.00746	0.01167	0.00014	3.462	0.399	15.8	1.8	16.1915	2.2388
400	0.1275	33.73	0.102	0.22399	0.00177	0.10054	0.00063	88.1	0.41106	0.00325	0.01306	0.00009	4.008	0.196	18.3	0.9	18.6732	0.9809
600	0.2163	24.996	0.077	0.33597	0.00241	0.06883	0.00043	81.4	0.61659	0.00442	0.01461	0.00013	4.653	0.14	21.2	0.6	21.611	0.6854
800	0.2908	23.081	0.087	0.20444	0.00196	0.06114	0.00057	78.3	0.37517	0.00361	0.01636	0.00009	5	0.171	22.7	0.8	23.2591	0.8738
1000	0.3746	23.324	0.083	0.07852	0.00158	0.06107	0.00044	77.4	0.14409	0.0029	0.01689	0.00011	5.256	0.127	23.9	0.6	24.474	0.7105
1250	0.5338	24.183	0.083	0.03437	0.00075	0.06338	0.00031	77.5	0.06306	0.00138	0.01706	0.00008	5.429	0.097	24.7	0.4	25.2862	0.5691
1500	0.7134	24.211	0.079	0.02822	0.0006	0.06348	0.00027	77.6	0.05178	0.00111	0.01724	0.00007	5.427	0.093	24.7	0.4	25.279	0.5169
1750	0.821	22.382	0.08	0.04954	0.00092	0.05697	0.00021	75.3	0.09091	0.00169	0.01826	0.0001	5.522	0.074	25.1	0.3	25.715	0.466
2000	0.9094	22.266	0.078	0.05649	0.00168	0.05691	0.00042	75.6	0.10365	0.00308	0.01845	0.00013	5.426	0.131	24.7	0.6	25.2628	0.6749
2500	0.9821	21.326	0.071	0.09501	0.0014	0.05333	0.00053	74	0.17434	0.00258	0.01967	0.00013	5.547	0.161	25.2	0.7	25.8054	0.7914
3000	0.989	19.988	0.098	0.16804	0.0133	0.05138	0.00262	76	0.30836	0.02442	0.01977	0.00046	4.789	0.774	21.8	3.5	22.2959	3.5987
4000	0.9937	18.918	0.17	0.36011	0.02527	0.04765	0.00317	74.4	0.6609	0.04638	0.02628	0.00099	4.837	0.933	22	4.2	22.4443	4.3899
5000	0.9973	17.202	0.17	0.56181	0.02664	0.04178	0.00492	71.6	1.03121	0.04892	0.03541	0.00124	4.872	1.451	22.2	6.6	22.53	6.7492
8000	1	16.885	0.208	0.19829	0.02168	0.04401	0.00644	77.1	0.36388	0.03978	0.01864	0.00114	3.866	1.9	17.6	8.6	18.0244	8.8488

FM-3 102.5
Sanidine #1

Weighted average of J from standards= 0.002536 +/- 0.000013

Laser	Cum.	40/39	40/39	37/39	37/39	36/39	36/39	% Atm	Ca/K	+/-	Cl/K	+/-	40Ar*/39Ark	+/-	Age	+/-	Age	+/-
(mW)	39Ar	measured	+/-	measured	+/-	measured	+/-	40Ar							(Ma)	(Ma)	(Ma)	(Ma)
200	0.0007	25.126	0.329	0.08272	0.04909	0.08913	0.01067	104.9	0.15179	0.09009	0.01734	0.00187	-1.234	3.135	-5.7	14.4	-5.667	14.85
400	0.0043	9.179	0.052	0.04416	0.00675	0.02187	0.00172	70.6	0.08102	0.01239	0.0044	0.00032	2.692	0.509	12.3	2.3	12.64	2.369

600	0.0092	5.977	0.024	0.08001	0.00713	0.00858	0.00136	42.5	0.14682	0.01309	0.00187	0.00027	3.419	0.402	15.6	1.8	16	1.863
800	0.0159	4.857	0.024	0.11083	0.00581	0.00285	0.00094	17.3	0.20337	0.01066	0.00093	0.00016	3.994	0.279	18.2	1.3	18.65	1.288
1000	0.024	5.12	0.016	0.12014	0.00342	0.00199	0.00077	11.4	0.22047	0.00627	0.0005	0.00015	4.513	0.227	20.5	1	21.04	1.053
1250	0.0362	5.099	0.023	0.11779	0.00213	0.00037	0.00048	2	0.21614	0.00391	0.00045	0.00013	4.97	0.143	22.6	0.7	23.15	0.6625
1500	0.0515	5.143	0.017	0.09754	0.0023	-0.00017	0.00037	-1.1	0.17899	0.00423	0.00029	0.00009	5.172	0.11	23.5	0.5	24.08	0.5021
1750	0.0698	5.156	0.018	0.09253	0.00161	0.00011	0.00037	0.5	0.16979	0.00295	0.00046	0.00006	5.103	0.109	23.2	0.5	23.76	0.5118
2000	0.0897	5.173	0.015	0.08974	0.00182	0.00002	0.00029	0	0.16467	0.00334	0.00054	0.00007	5.144	0.087	23.4	0.4	23.96	0.4014
2500	0.1247	5.207	0.016	0.06171	0.00118	0.00028	0.0002	1.5	0.11324	0.00217	0.00042	0.00004	5.101	0.061	23.2	0.3	23.77	0.282
3000	0.1597	5.212	0.017	0.06389	0.00102	0.00066	0.00011	3.7	0.11724	0.00187	0.00046	0.00006	4.994	0.037	22.7	0.2	23.27	0.1691
4000	0.2208	5.228	0.02	0.05585	0.00078	0.00039	0.00008	2.2	0.10248	0.00143	0.00045	0.00004	5.087	0.031	23.1	0.1	23.71	0.1427
5000	0.2951	5.235	0.018	0.03734	0.00084	0.00056	0.00008	3.1	0.06851	0.00154	0.00055	0.00003	5.045	0.029	22.9	0.1	23.51	0.137
8000	0.3741	5.262	0.024	0.03826	0.00065	0.00063	0.00007	3.5	0.07021	0.00119	0.00055	0.00003	5.049	0.032	23	0.1	23.54	0.1459
8001	1	5.266	0.031	0.01787	0.00013	0.00032	0.00001	1.8	0.0328	0.00023	0.00046	0.00002	5.145	0.031	23.4	0.1	23.98	0.1435

FM-3 2.1
Biotite #1

Weighted average of J from standards= 0.002536 +/- 0.000013

Laser	Cum.	40/39	40/39	37/39	37/39	36/39	36/39	% Atm	Ca/K	+/-	Cl/K	+/-	40Ar*/39Ark	+/-	Age	+/-	Age	+/-
(mW)	39Ar	measured	+/-	measured	+/-	measured	+/-	40Ar							(Ma)	(Ma)	(Ma)	(Ma)
200	0.0686	20.777	0.264	0.02793	0.00296	0.06328	0.00109	90.1	0.05124	0.00542	0.01168	0.00031	2.051	0.327	9.4	1.5	9.6743	1.9339
400	0.1455	14.171	0.129	0.02227	0.00268	0.03465	0.00068	72.4	0.04086	0.00491	0.01044	0.0002	3.905	0.216	17.8	1	18.2643	1.1036
600	0.2359	12.342	0.086	0.01683	0.00221	0.02186	0.00042	52.4	0.03089	0.00406	0.01142	0.00019	5.855	0.135	26.6	0.6	27.2563	0.6944
800	0.3555	11.505	0.06	0.01414	0.00246	0.01396	0.00032	35.9	0.02595	0.00451	0.01042	0.00015	7.353	0.106	33.3	0.5	34.1296	0.5131
1000	0.4644	11.054	0.069	0.02174	0.00219	0.01752	0.00033	46.9	0.03989	0.00401	0.01142	0.00014	5.849	0.107	26.6	0.5	27.2308	0.5494
1250	0.5813	11.723	0.046	0.02215	0.00174	0.01809	0.00037	45.7	0.04065	0.0032	0.01195	0.00008	6.351	0.117	28.8	0.5	29.5314	0.5448
1500	0.673	10.926	0.038	0.03211	0.00165	0.01727	0.00049	46.8	0.05891	0.00304	0.01168	0.00014	5.797	0.148	26.3	0.7	26.982	0.6885
1750	0.7507	10.767	0.031	0.04359	0.00289	0.01681	0.00041	46.2	0.07998	0.00531	0.01261	0.00016	5.774	0.124	26.2	0.6	26.8758	0.5752
2000	0.8064	10.37	0.045	0.05593	0.00297	0.01552	0.0006	44.3	0.10262	0.00545	0.01378	0.00017	5.76	0.179	26.2	0.8	26.8032	0.8414
2500	0.8774	10.24	0.042	0.02287	0.0025	0.01436	0.00039	41.5	0.04196	0.00459	0.01406	0.00013	5.97	0.12	27.1	0.5	27.7817	0.5639
3000	0.9089	10.583	0.057	0.02019	0.00457	0.01448	0.00086	40.5	0.03705	0.00838	0.01253	0.00023	6.276	0.256	28.5	1.2	29.195	1.1965
4000	0.9917	10.13	0.034	0.02812	0.00233	0.01378	0.00036	40.3	0.0516	0.00428	0.01271	0.00013	6.032	0.109	27.4	0.5	28.0638	0.5134

5000	0.9966	11.858	0.128	-0.00749	0.02997	0.01544	0.00859	38.6	-0.01374	0.05499	0.01388	0.00154	7.266	2.54	33	11.4	33.7433	11.6464
8000	1	11.254	0.2	-0.05981	0.04695	0.02753	0.00779	72.5	-0.10973	0.08614	0.01497	0.00235	3.085	2.3	14.1	10.4	14.5027	10.7013

Appendix A References

Gutenkunst, M., 2006, Stratigraphic and geochronologic analysis of Eocene-Miocene synextensional strata in the Grapevine and Funeral mountains of southwestern Nevada and southeastern California: Implications for regional correlation of "pre-basin and range" stratigraphy [M.S. thesis]: Purdue University, 265 p.

Hodges, K.V., Hames, W.E., Olszewski, W., Burchfiel, B.C., Royden, L.H., and Chen, Z., 1994, Thermobarometric and $^{40}Ar/^{39}Ar$ geochronologic constraints on Eohimalayan metamorphism in the Dinggye area, southern Tibet: Contributions to Mineralogy and Petrology, v. 117, p. 151–163.

Mercer, C.M., and Hodges, K.V., 2016, ArAR — A software tool to promote the robust comparison of K–Ar and $^{40}Ar/^{39}Ar$ dates published using different decay, isotopic, and monitor-age parameters: Chemical Geology, v. 440, p. 148–163, doi:10.1016/j.chemgeo.2016.06.020.

Nier, A.O., 1950, A redetermination of the relative abundances of the isotopes of carbon, nitrogen, oxygen, argon, and potassium: Physical Review, v. 77, p. 789–793, doi:10.1103/PhysRev.77.789.

Renne, P.R., Balco, G., Ludwig, K.R., Mundil, R., and Min, K., 2011, Response to the comment by W.H. Schwarz et al. on "Joint determination of ^{40}K decay constants and $^{40}Ar^*/^{40}K$ for the Fish Canyon sanidine standard, and improved accuracy for $^{40}Ar/^{39}Ar$ geochronology" by P.R. Renne et al. (2010): Geochimica et Cosmochimica Acta, v. 75, p. 5097–5100, doi:10.1016/j.gca.2011.06.021.

Ridgway, K., Stamatakos, J., Gutenkunst, M., and Dubreuilh, P., 2011, Stratigraphic analysis and regional correlation of Oligocene and Early Miocene strata in the Yucca Mountain area: U.S. Nuclear Regulatory Commission Contract NRC-02-07-006, 60 p.

Samson, S.D., and Alexander, E.C., 1987, Calibration of the interlaboratory ^{40}Ar- ^{39}Ar dating standard, MMhb-7: Chemical Geology, v. 66, p. 27–34.

Saylor, B.Z., 1991, The Titus Canyon Formation: Evidence for early Oligocene extension in the Death Valley area, CA [M.S. thesis]: Massachusetts Institute of Technology, 65 p.

Saylor, B.Z., and Hodges, K.V., 1994, $^{40}Ar/^{39}Ar$ age constraints on the depositional history of the Oligocene Titus Canyon Formation, Death Valley, CA: Geological Society of America Abstracts with Programs.

Spell, T.L., and McDougall, I., 2003, Characterization and calibration of $^{40}Ar/^{39}Ar$ dating standards: Chemical Geology, v. 198, p. 189–211, doi:10.1016/S0009-2541(03)00005-6.

Steiger, R.H., and Jäger, E., 1977, Subcommission on geochronology: Convention on the use of decay constants in geo- and cosmochronology: Earth and Planetary Science Letters, v. 36, p. 359–362, doi:10.1016/0012-821X(77)90060-7.

Tummers, B., 2006, DataThief III, https://datathief.org/.

Vermeesch, P., 2018, IsoplotR: A free and open toolbox for geochronology: Geoscience Frontiers, v. 9, p. 1479–1493, doi:10.1016/j.gsf.2018.04.001.

Appendix B
Analytical Data for Chapter 3

Table B.1: Apatite fission-track analytical data.

Sample	No. of	Track Counts			Track Density (x10^6 tracks/cm^2)			Chi Squared Prob.	Dpar	Analyst	Central Age	Track Lengths	No. Track
	grains	N_s	N_i	N_d	ρ_s	ρ_i	ρ_d	$P\chi^2$	(µm)		(Ma) (±1se)	(µm)	Lengths
NBR18-C1	20	798	2620	5756	1.357	4.455	1.799	99.67%	2.01	SNT	95.7±4.2	13.55±0.11	100
NBR18-CP1	19	570	2719	7627	0.565	2.696	2.383	71.79%	1.52	NCM	64.16±3.37	13.4±0.22	39
NBR18-DB1	20	521	1257	5669	1.451	3.501	1.772	99.75%	1.94	SNT	127.95±7.02	13.09±0.12	100
NBR18-GH1	10	310	6281	7482	0.651	13.19	2.338	78.72%	1.66	NCM	14.88±1.05	13.78±0.2	34
NBR18-PR1	10	33	550	7338	0.094	1.563	2.293	99.04%	1.58	NCM	17.73±3.26	14.77±0.87	3
NBR18-SI1	20	617	2687	7265	0.555	2.416	2.27	59.85%	1.59	NCM	66.93±4.03	12.07±0.22	84
NBR18-T1	20	162	2096	7193	0.195	2.517	2.248	94.20%	1.66	NCM	22.38±2.04	13.94±0.35	16
NBR18-WH1	20	295	2372	7121	0.288	2.316	2.225	91.91%	1.65	NCM	35.61±2.63	12.7±0.31	24
NBR19-NM1	20	483	1728	7410	0.579	2.071	2.316	92.17%	1.59	NCM	82.99±4.76	13.25±0.14	84
GP102605-3	18	224	6516	7048	0.268	7.796	2.203	92.23%	1.56	NCM	9.76±0.77	13.77±0.16	50
95BR009*	25	450	1170	5982	1.325	3.179	1.598	0.13	-	DFS	112.8±10.5	13.13±0.12	100
95BR011*	25	150	1830	5982	0.337	2.679	1.598	0.76	-	DFS	46.4±4.1	12.89±0.18	100
95BR014*	25	412	3247	5982	1.421	9.978	1.611	0.87	-	DFS	32.4±2.9	12.31±0.18	150

*Analsyes from Stockli (1999)

Area of Graticule Square = 6.4e-07 cm^2

SNT = Stuart N Thomson (Zeta = 351.9±3.8)

NCM = Nikolas C Midttun (Zeta = 258.1±10.0)

DFS = Daniel F Stockli (Zeta = 356±5; Stockli, 1999)

Table B.2: Apatite (U-Th)/He analytical data.

Sample	U	Th	Sm	He	Mass	Ft*	Termina-tions	Radius	Length	Uncorr. Age	Age Error	Corrected Age	Notes	Mean Age	S.E. (Ma)
	(ppm)	(ppm)	(ppm)	(ncc)	(mg)		**	(μm)	(μm)	(Ma)	(Ma)	(Ma)		(Ma)	S.E. as % of age
NBR18-C1a	31.1	60.3	178.4	0.8945	0.0030	0.75	EE	45.5	178.3	54.3	0.58	72.8		70.5	1.0
NBR18-C1b	33.9	64.6	139.3	0.5978	0.0020	0.71	EE	40.4	150.7	50.2	0.55	70.3			1%
NBR18-C1c	34.2	50.1	149.5	0.9165	0.0031	0.75	EE	47.7	166.5	53.4	0.61	70.8			
NBR18-C1d	22.5	72.0	205.5	0.3676	0.0016	0.71	EB	41.7	111.3	48.5	0.51	68.1			
NBR18-CP1a	16.5	27.9	104.0	0.3401	0.0027	0.75	EE	46.4	155.5	44.5	0.52	59.6	Excluded at p<2% (Dixon Q test)	43.7	5.3
NBR18-CP1b	13.8	21.7	100.2	0.2127	0.0031	0.75	EB	45.5	185.5	29.5	0.34	39.6			12%
NBR18-CP1c	17.9	29.8	120.2	0.2748	0.0032	0.75	EE	45.7	193.0	27.7	0.31	37.0			
NBR18-CP1d	15.6	25.6	145.3	0.4214	0.0054	0.77	EE	47.9	289.3	29.7	0.34	38.7			
NBR18-DB1a	41.3	69.1	282.5	0.9133	0.0030	0.78	BB	56.1	120.1	42.6	0.47	54.9		61.8	23.3
NBR18-DB1b	20.6	41.0	184.5	1.6899	0.0034	0.75	EB	46.4	197.9	132.1	1.34	175.5	Excluded at p<1% (2 outlier Grubb's test)		38%
NBR18-DB1c	45.2	114.1	487.7	0.8479	0.0031	0.77	BB	53.9	132.1	31.1	0.32	40.3			
NBR18-DB1e	35.2	52.8	311.3	0.3799	0.0048	0.80	BB	63.2	150.6	13.4	0.15	16.7	Excluded at p<1% (2 outlier Grubb's test)		
NBR18-DB1f	37.4	90.8	408.7	0.8362	0.0037	0.76	EB	47.9	202.3	31.0	0.33	40.8			
NBR18-DB1g	41.6	58.3	297.4	0.4736	0.0022	0.74	EB	47.0	123.2	31.8	0.37	42.8			
NBR18-DV1a	101.6	168.5	223.2	0.1949	0.0025	0.75	BB	48.6	129.0	4.6	0.05	6.1		3.2	0.6
NBR18-DV1b	10.8	16.1	97.0	0.0218	0.0028	0.76	EB	49.5	140.5	4.0	0.07	5.3			20%
NBR18-DV1c	30.1	159.5	341.9	0.1451	0.0028	0.75	EB	47.9	151.9	6.2	0.06	8.2			
NBR18-DV1d	129.2	360.1	456.4	0.2917	0.0025	0.75	EB	48.8	129.4	4.5	0.05	6.0			

NBR18-GH1a	74.7	89.3	120.7	0.3133	0.0025	0.76	BB	52.6	112.2	10.7	0.13	14.1		14.1	1.9
NBR18-GH1b	104.9	170.6	239.6	0.4440	0.0031	0.77	EB	51.7	145.8	8.0	0.09	10.5			13%
NBR18-GH1c	43.0	37.5	78.2	0.2599	0.0028	0.76	EB	49.5	141.8	14.7	0.18	19.4			
NBR18-GH1d	105.8	113.6	209.3	0.4524	0.0030	0.74	EE	43.3	201.0	9.2	0.11	12.5			
NBR18-MC1a §	3.6	13.2	155.2	0.1326	0.0033	0.76	EE	47.3	184.2	46.8	0.52	62.0		55.6	5.3
NBR18-MC1b §	4.8	15.9	151.2	0.1336	0.0037	0.78	EB	56.8	141.8	33.6	0.36	42.8			10%
NBR18-MC1c	23.6	32.3	179.6	0.7383	0.0037	0.75	BB	46.4	211.1	52.8	0.61	70.0			
NBR18-MC1d §	1.7	4.4	62.8	0.0671	0.0035	0.79	EB	60.7	117.5	54.6	0.64	69.3			
NBR18-MC1e §	4.7	17.9	232.0	0.0766	0.0021	0.73	EE	44.2	135.2	31.5	0.38	43.1			
NBR18-MC1f §	4.5	15.3	228.3	0.2210	0.0058	0.80	EE	57.6	217.3	37.0	0.39	46.4			
NBR18-PR1a	9.1	23.6	229.2	0.0709	0.0040	0.77	EE	50.4	197.9	9.4	0.11	12.2		12.0	0.4
NBR18-PR1b	9.4	18.9	208.5	0.1014	0.0058	0.81	BB	63.8	176.3	10.0	0.12	12.4			3%
NBR18-PR1c	7.2	22.5	214.1	0.0392	0.0028	0.75	BB	46.4	164.3	8.4	0.12	11.3			
NBR18-PR1d	11.8	29.7	273.5	0.1557	0.0035	0.78	BB	55.7	140.0	18.9	0.21	24.3	Excluded at p<2% (Dixon Q test)		
NBR18-Sl1a	16.6	32.3	119.3	0.3349	0.0068	0.82	BB	68.5	180.8	16.6	0.18	20.2		22.1	1.0
NBR18-Sl1c	18.6	35.6	123.2	0.2341	0.0039	0.78	BB	54.1	165.6	18.1	0.20	23.2			4%
NBR18-Sl1d	19.1	31.8	124.2	0.1471	0.0026	0.75	EB	46.4	151.9	17.0	0.19	22.8			
NBR18-T1a	12.6	26.2	81.6	0.0773	0.0032	0.77	BB	51.7	147.5	10.4	0.12	13.5		14.6	1.1
NBR18-T1b	10.6	29.6	140.1	0.0832	0.0032	0.74	EE	44.2	200.5	11.9	0.13	16.1			7%
NBR18-T1c	22.4	8.4	35.0	0.1079	0.0028	0.76	BB	51.0	133.8	12.8	0.18	16.8			
NBR18-T1d	13.7	26.5	95.1	0.0570	0.0025	0.73	BB	42.6	173.6	8.9	0.11	12.2			

NBR18-WH1b	19.8	7.5	54.5	0.3591	0.0043	0.78	BB	53.0	188.6	31.9	0.44	41.0	Excluded at p<1% (2 outlier Grubb's test)	26.1	0.8
NBR18-WH1c	19.4	59.6	221.6	0.2417	0.0029	0.74	EB	45.1	179.3	20.0	0.21	26.9			3%
NBR18-WH1d	19.5	59.8	246.3	0.8618	0.0042	0.79	EB	60.1	143.1	50.3	0.53	63.3	Excluded at p<1% (2 outlier Grubb's test)		
NBR18-WH1e	24.0	82.1	245.9	0.4261	0.0039	0.77	BB	51.0	186.8	20.5	0.21	26.6			
NBR18-WH1f	17.4	49.7	228.5	0.2358	0.0032	0.75	BB	47.3	177.6	20.5	0.21	27.2			
NBR18-WH1g	17.3	51.3	185.5	0.2065	0.0032	0.76	EB	48.6	167.4	17.9	0.19	23.6			
NBR19-NM1a	13.1	45.9	96.5	0.3423	0.0029	0.77	BB	56.3	112.6	40.6	0.43	52.4		59.2	2.5
NBR19-NM1b	14.9	49.4	103.7	0.5105	0.0034	0.76	EB	47.9	182.4	46.5	0.48	61.4			4%
NBR19-NM1c	14.5	51.1	140.4	0.9108	0.0060	0.79	EB	56.3	235.0	46.7	0.48	58.8			
NBR19-NM1d	15.4	45.3	98.8	0.2679	0.0018	0.72	BB	43.3	119.7	46.3	0.49	64.0			
GP102605-3a	61.1	69.3	104.3	0.3468	0.0056	0.79	BB	54.8	232.8	6.5	0.08	8.3		8.0	0.1
GP102605-3b	45.2	45.1	95.3	0.0674	0.0017	0.72	BB	42.4	118.4	5.6	0.07	7.8			1%
GP102605-3c	197.1	189.7	200.1	0.6494	0.0035	0.78	EB	57.9	130.7	6.3	0.08	8.0			
GP102605-3d	63.5	45.0	87.6	0.3304	0.0059	0.80	EB	57.2	224.8	6.2	0.08	7.8			
NPQM1612a	28.4	94.7	376.8	0.3722	0.0040	0.80	EB	63.2	123.3	15.1	0.15	18.9		16.3	1.4
NPQM1612b	25.9	77.5	210.5	0.1509	0.0026	0.73	EB	41.8	181.5	10.9	0.11	14.9			8%
NPQM1612c	28.6	60.8	145.9	0.1680	0.0024	0.74	BB	45.1	144.5	13.5	0.15	18.2			
NPQM1612d	33.8	52.5	172.5	0.1193	0.0021	0.75	EB	48.6	112.6	9.8	0.11	13.1			
NPQM 1800a	26.4	92.9	213.0	0.6568	0.0036	0.78	BB	53.9	152.0	31.3	0.32	40.3		35.1	3.1
NPQM 1800b	14.1	43.7	118.2	0.1666	0.0026	0.74	EB	45.7	156.4	21.0	0.22	28.2			9%

NPQM 1800c	21.9	83.7	200.3	0.2651	0.0022	0.75	BB	50.8	105.2	23.7	0.26	31.5			
NPQM 1800d	24.0	62.2	120.1	0.2118	0.0015	0.73	BB	47.1	85.2	29.3	0.31	40.4			
NPQM 2000a	24.0	77.1	156.3	1.0239	0.0064	0.78	BB	52.6	287.5	31.0	0.33	39.5		39.5	2.8
NPQM 2000b	16.7	37.3	81.1	0.2991	0.0035	0.79	BB	63.9	106.5	27.4	0.30	34.6			7%
NPQM 2000c	22.1	73.8	148.1	0.3244	0.0025	0.74	EB	46.4	141.8	27.3	0.28	36.6			
NPQM 2000d	25.8	78.4	197.0	1.2187	0.0059	0.80	BB	60.8	199.2	38.0	0.39	47.3			
NPQM 2200a	25.7	80.8	156.0	1.3731	0.0045	0.77	BB	48.6	239.0	55.3	0.57	72.2		64.9	9.4
NPQM 2200b	25.4	60.0	123.9	0.5910	0.0027	0.77	BB	53.2	120.1	44.6	0.47	58.2			14%
NPQM 2200c	28.1	70.3	170.7	1.3737	0.0038	0.77	EB	52.6	168.7	67.0	0.69	86.5			
NPQM 2200d	14.0	35.8	101.4	0.2189	0.0025	0.74	BB	44.8	155.0	31.6	0.33	42.7			
NPQM 2600a	19.9	51.8	114.8	1.1366	0.0043	0.77	BB	51.0	207.2	66.8	0.68	86.3		92.0	2.7
NPQM 2600b	25.1	97.3	203.7	1.7446	0.0042	0.79	BB	57.9	155.1	71.0	0.71	90.0			3%
NPQM 2600c	26.3	59.1	119.5	1.0538	0.0031	0.75	BB	45.5	185.5	69.2	0.74	92.6			
NPQM 2600d	25.5	75.1	114.8	1.2347	0.0031	0.75	BB	46.4	181.1	74.5	0.76	99.2			
NPQM 2800a	31.0	79.3	157.9	0.8542	0.0021	0.73	EB	43.5	138.7	66.4	0.70	91.1		141.3	56.0
NPQM 2800b	19.5	67.5	162.0	1.6211	0.0057	0.79	EB	54.8	234.1	66.2	0.67	83.9			40%
NPQM 2800c	27.5	63.7	128.2	0.7841	0.0025	0.76	BB	51.7	114.0	61.4	0.65	81.0			
NPQM 2800d	24.1	59.9	119.0	2.8883	0.0026	0.76	BB	53.0	114.4	236.2	2.42	309.3	Excluded at p<1% (Dixon Q test)		

* Ft is the alpha-ejection correction after Farley et al. (1996)

§ Uranium < 5 ppm

** Coded grain terminations: E = Euhedral, B = Broken

Table B.3: Zircon (U-Th)/He analytical data.

Sample	U (ppm)	Th (ppm)	He (ncc)	Mass (mg)	Ft*	Radius (μm)	Length (μm)	Uncorr. Age (Ma)	Age Error (Ma)	Corrected Age (Ma)	Notes
NBR18-DV1 Zra	3362.47	1367.54	14.8426	0.0022	0.73	44	144.4	14.8	0.2	20.24	
NBR18-DV1 Zrb	774.93	589.68	9.0174	0.0042	0.76	46.4	241.6	19.5	0.25	25.74	
NBR18-DV1 Zrc	811.13	498.82	5.9751	0.0035	0.76	47	194.8	15.3	0.2	20.29	
NBR18-WH1 Zra	1041.16	501.69	109.6318	0.0092	0.82	64.7	272.1	84.7	1.09	103.28	
NBR18-WH1 Zrb	1717.71	870.3	54.5975	0.0031	0.73	41.7	222.6	74.8	0.96	102.26	
NBR18-WH1 Zrc	1750.16	891.74	85.9436	0.0042	0.76	46.4	243.4	85.5	1.1	112.97	
NBR18-GH1 Zra	1029.78	1627.53	9.9165	0.0048	0.76	47.9	260.2	12	0.14	15.75	
NBR18-GH1 Zrb	1008.97	665.4	11.5075	0.0048	0.76	47.9	258.8	17	0.21	22.28	
NBR18-GH1 Zrc	2422.31	2479.32	34.0932	0.006	0.79	55.4	243.8	15.5	0.19	19.61	
NBR18-CP1 Zra	1172.1	271.82	67.1005	0.0067	0.81	61.4	222.2	66.3	0.9	82	
NBR18-CP1 Zrb	1489.65	306.27	111.1373	0.0098	0.82	62.3	313.2	59.9	0.82	73.38	
NBR18-CP1 Zrc	1416.63	377.84	28.892	0.0026	0.72	40.4	196.2	61.2	0.85	84.96	
NBR18-C1 Zra	1040.98	471.67	64.4454	0.0051	0.79	57.2	193.5	90.2	1.18	113.68	
NBR18-C1 Zrb	632.42	357.46	33.3969	0.0037	0.76	47.9	199.2	103.8	1.33	136.64	
NBR18-C1 Zrc	735.82	400.46	41.0672	0.0043	0.79	58.7	153.9	95	1.21	119.91	
NBR18-T1 Zra†	563.02	200.21	24.1394	0.0064	0.81	63.2	199.2	51	0.69	62.86	Rejected at 90% (Dixon q)
NBR18-T1 Zrb†	546.79	251.2	7.5487	0.0068	0.79	54.8	281.4	15.2	0.2	19.13	
NBR18-T1 Zrc†	498.27	223.07	2.5757	0.0031	0.75	45.7	184.2	12.5	0.17	16.67	
NBR18-PR1 Zra	331.09	187.48	1.5047	0.0038	0.77	50.4	186.9	8.7	0.12	11.3	
NBR18-PR1 Zrb	2285.81	459.29	6.6233	0.0028	0.75	46.4	162.5	8.1	0.11	10.86	
NBR18-PR1 Zrc	611.25	320.17	3.0916	0.0037	0.75	44.2	233.7	10.1	0.13	13.6	

NBR18-SI1 Zra	2287.28	827.38	78.3786	0.0031	0.74	43.5	203.6	83.6	1.14	113.12
NBR18-SI1 Zrb	2181.4	838.16	120.9934	0.0046	0.76	47.3	254	91.5	1.2	120.12
NBR18-SI1 Zrc	2163.33	765.05	218.8708	0.0078	0.79	53.2	343.6	97.8	1.47	123.75
NBR18-MC1 Zra	729.68	466.33	14.6492	0.0044	0.77	50.1	217.3	32.8	0.41	42.49
NBR18-MC1 Zrb	874.36	458.03	29.1448	0.0067	0.81	62.5	211.6	36.8	0.48	45.41
NBR18-MC1 Zrc	1012.89	560.23	15.0983	0.0032	0.75	46.4	182.4	34.4	0.62	45.88
NBR18-DB1 Zra	1164.2	737.35	41.1061	0.0023	0.72	40.4	173.6	110.4	1.38	153.7
NBR18-DB1 Zrb	770.02	561.28	49.1665	0.0037	0.77	50.8	176.2	121.9	1.45	158.57
NBR18-DB1 Zrc	486.45	385.07	35.9368	0.0041	0.76	46.4	237.2	124.1	1.52	164.11
NBR19-NM1 Zra	1929.97	1073.71	96.3519	0.0037	0.76	47.3	208	96.8	1.25	127.68
NBR19-NM1 Zrb	1582.35	781.46	106.5937	0.0044	0.76	46.4	255.7	111.7	1.45	147.42
NBR19-NM1 Zrc	1235.53	877.28	87.7805	0.0047	0.76	45.7	276.5	107.3	1.37	141.96
GP102605-3 Zra	913.35	506.97	2.5708	0.0031	0.74	44.8	190.4	6.7	0.09	8.97
GP102605-3 Zrb	1464.73	618.72	4.5261	0.0034	0.74	44	219.1	6.8	0.09	9.17
GP102605-3 Zrc	1123.33	484.21	3.9728	0.0037	0.75	44.8	226.6	7.2	0.1	9.68
NPQM 1800 Zra	2436.4	1082	107.8923	0.0048	0.77	50.8	230.1	69	1.16	89.1
NPQM 1800 Zrb	3237.7	1597.4	113.8005	0.0036	0.74	43.3	239	71.9	1	97
NPQM 1800 Zrc	2306.9	1080.8	128.9187	0.0061	0.8	57	232.8	68.1	0.92	85.5
NPQM 2800 Zra	4083.6	2479.5	171.3847	0.0031	0.75	45.5	186.9	96.8	1.4	129.5
NPQM 2800 Zrb	3301.8	2300.9	173.6433	0.0043	0.77	49.5	217.3	86.7	1.23	112.9
NPQM 2800 Zrc	2824.1	1857.6	278.7684	0.0075	0.79	54.2	318	93.2	1.31	117.6

* Ft is the alpha-ejection correction after Farley et al. (1996)

† Standard deviation of replicate analyses > 25% of mean age.

Appendix C
Analytical Data for Chapter 4

Table C.1: Zircon and apatite (U-Th)/He analytical data.

Sample	U (ppm)	Th (ppm)	Sm (ppm)	eU (ppm)	He (ncc)	Mass (mg)	Ft*	Terminations **	Radius (μm)	Length (μm)	Uncorr. Age (Ma)	Age Error (Ma)	Corrected Age (Ma)
Apatite													
AZ0623a §	2.8	13.0	239.3	7.7	0.0746	0.0016	0.72	EE	43.3	107.8	60.0	0.63	83.41
AZ0623b §	3.8	13.0	243.6	8.8	0.0505	0.0017	0.72	BB	42.0	118.4	33.2	0.36	46.43
AZ0623c §	3.2	17.6	277.2	9.6	0.0851	0.0016	0.70	EE	39.3	125.0	56.9	0.61	81.13
AZ0623d §	2.8	15.2	264.7	8.5	0.0434	0.0013	0.70	BB	40.2	98.9	39.6	0.50	56.65
AZ0623e §	1.3	7.0	144.5	4.1	0.0214	0.0016	0.74	BB	49.7	82.2	31.1	0.50	42.18
AZ0625a §	4.5	15.6	106.2	9.0	0.0377	0.0013	0.71	EB	43.5	83.5	28.0	0.34	39.49
AZ0625b §	4.6	16.1	132.5	9.4	0.0695	0.0021	0.73	EE	42.6	145.9	30.5	0.36	41.97
AZ0625c	5.1	21.3	144.0	11.2	0.0606	0.0015	0.73	EB	47.9	79.1	32.1	0.39	44.18
AZ0625d §	3.6	13.6	112.1	7.7	0.0272	0.0012	0.70	EB	41.7	86.1	24.5	0.32	35.02
AZ0625e	6.6	17.9	96.8	11.5	0.1243	0.0020	0.73	EE	43.9	130.7	45.4	0.50	62.29
ARM17-TI-Ca	11.0	17.5	194.1	16.7	0.0324	0.0023	0.74	EB	47.0	130.7	7.0	0.10	9.40
ARM17-TI-Cb	22.6	21.5	166.8	29.0	0.1349	0.0045	0.78	BB	52.3	202.8	8.8	0.11	11.34
ARM17-TI-Cc	9.6	15.7	217.9	15.0	0.0401	0.0031	0.76	EB	48.8	162.6	7.4	0.09	9.80
ARM17-TI-Cd	11.4	15.7	313.1	17.6	0.0358	0.0022	0.74	EB	45.1	132.1	8.3	0.10	11.31
ARM17-T1-Da	11.5	24.7	120.1	18.3	0.0712	0.0031	0.75	EB	46.4	179.3	10.5	0.12	13.99
ARM17-T1-Db	9.0	22.7	143.0	15.5	0.0491	0.0033	0.76	BB	49.5	165.6	8.2	0.10	10.71
ARM17-T1-Dc	9.6	15.8	89.9	14.0	0.0374	0.0024	0.75	BB	47.7	129.0	9.2	0.11	12.27
ARM17-T1-Dd	7.6	21.5	128.5	13.7	0.0399	0.0025	0.76	BB	52.6	111.3	9.8	0.12	12.89
ARM17-T1-Ea	12.9	17.8	130.9	18.1	0.0441	0.0040	0.79	EB	57.0	153.7	5.0	0.06	6.36
ARM17-T1-Eb	21.0	28.1	188.1	29.1	0.0646	0.0031	0.78	BB	55.7	124.6	6.0	0.08	7.71
ARM17-T1-Ed	24.3	32.2	184.9	33.4	0.0980	0.0027	0.75	BB	47.1	149.3	9.3	0.11	12.36

ARM17-TI-Fa	5.3	13.5	73.9	9.0	0.0259	0.0043	0.80	BB	61.6	140.5	5.3	0.07	6.71
ARM17-TI-Fb	9.9	22.8	121.5	16.2	0.0580	0.0043	0.79	BB	57.6	161.7	6.9	0.08	8.77
ARM17-TI-Fc	12.8	28.1	151.7	20.6	0.0390	0.0026	0.75	EB	47.7	140.5	6.1	0.07	8.07
ARM17-TI-Fd	8.3	19.7	71.7	13.5	0.0465	0.0042	0.80	EB	61.0	140.0	6.7	0.07	8.44
ARM17-T2-Ca	35.3	35.9	182.1	45.2	0.0993	0.0028	0.77	BB	53.2	121.5	6.6	0.08	8.60
ARM17-T2-Cb	11.0	21.2	205.0	17.6	0.0925	0.0054	0.81	BB	65.4	155.9	8.6	0.10	10.62
ARM17-T2-Cc	34.9	30.3	137.6	43.1	0.1180	0.0030	0.77	EB	52.3	136.9	7.5	0.09	9.79
ARM17-T2-Cd	36.4	41.8	221.5	48.0	0.2166	0.0056	0.80	EB	59.4	196.6	6.8	0.08	8.52
ARM17-T5-Ba §	0.6	3.6	175.4	2.8	0.0114	0.0035	0.79	BB	61.4	115.7	13.3	0.30	16.89
ARM17-T5-Bb §	0.6	5.7	163.4	3.2	0.0121	0.0024	0.75	BB	47.9	130.7	16.1	0.33	21.48
ARM17-T5-Bc §	0.3	4.7	113.6	2.3	0.0158	0.0023	0.74	EB	46.4	132.1	32.5	0.67	43.82
ARM17-T5-Bf §	0.4	2.6	125.1	2.1	0.0293	0.0044	0.78	EE	53.9	188.6	42.1	0.76	53.91
ARM17-R-8a	10.0	31.5	252.9	19.4	0.0543	0.0016	0.71	BB	42.0	115.8	14.8	0.18	20.73
ARM17-R-8b §	1.1	3.4	172.8	3.3	0.0125	0.0016	0.71	EB	40.4	118.8	25.5	0.58	36.14
ARM17-R-10a §	3.8	8.2	19.1	5.9	0.0254	0.0015	0.72	BB	44.0	93.2	23.1	0.37	32.18
ARM17-R-10b §	2.4	13.6	184.5	7.1	0.0119	0.0024	0.75	BB	48.6	127.7	5.7	0.10	7.56
ARM17-R-10c §	3.6	10.1	20.8	6.2	0.0385	0.0020	0.73	EB	43.3	132.5	24.8	2.56	34.11
ARM17-R-10d	11.9	22.4	24.8	17.4	0.0710	0.0020	0.72	EE	41.1	150.6	16.1	0.18	22.46
ARM17-R-11b	12.8	14.1	215.8	17.8	0.0355	0.0019	0.73	EB	44.8	118.8	8.8	0.12	12.01
ARM17-R-11e §	2.6	11.0	238.6	7.1	0.0667	0.0023	0.73	BB	43.3	152.0	42.1	0.48	57.62
ARM17-R-11f §	4.1	8.4	165.8	7.4	0.0208	0.0019	0.72	EB	41.1	143.1	12.7	0.19	17.69
ARM17-R-11h §	4.1	12.6	277.2	9.2	0.0200	0.0017	0.71	EE	40.2	129.4	11.9	0.18	16.83
ARM17-R-12a	32.0	35.8	51.5	40.8	0.2592	0.0026	0.76	EE	51.0	121.9	20.5	0.23	27.06
ARM17-R-12b §	1.4	8.5	60.3	3.9	0.0201	0.0017	0.70	EB	38.9	135.7	26.0	0.41	37.05

ARM17-R-12c	5.8	15.3	131.1	10.5	0.0630	0.0034	0.73	EB	41.7	243.4	15.3	0.17	20.92
ARM17-R-12d §	1.1	4.9	50.2	2.7	0.0268	0.0031	0.77	EB	52.3	142.7	27.7	0.42	36.06
ARM17-R-14a §	1.1	6.7	93.0	3.4	0.0255	0.0028	0.76	EB	51.9	129.9	24.3	0.36	31.84
ARM17-R-14b §	2.2	10.4	151.0	5.9	0.1138	0.0057	0.80	EB	58.5	208.0	32.9	0.36	41.18
ARM17-R-14c §	1.9	9.8	128.2	5.2	0.0407	0.0030	0.78	EB	59.2	106.4	24.4	0.28	31.24
ARM17-R-14d §	2.0	10.8	164.5	5.9	0.0738	0.0060	0.80	BB	57.9	222.2	20.6	0.22	25.75
PONT-ID-01a §	4.1	9.5	267.6	8.5	0.0362	0.0019	0.73	BB	44.8	119.7	21.7	0.252	29.69
PONT-ID-01b §	3.1	5.4	295.5	6.7	0.0239	0.0031	0.77	BB	53.9	130.8	12.5	0.440	16.18
PONT-ID-01d §	3.5	6.8	312.6	7.6	0.0273	0.0046	0.80	EB	60.1	159.9	8.2	0.095	10.32
PONT-ID-01e §	3.3	5.5	250.2	6.6	0.0177	0.0026	0.76	EB	50.1	129.4	10.0	0.155	13.21
PONT-ID-03aa §	1.8	5.0	395.5	6.1	0.0144	0.0014	0.70	EB	40.0	112.2	20.4	0.309	29.08
PONT-ID-03ab §	3.1	12.2	618.8	10.9	0.0544	0.0018	0.71	EB	41.1	132.5	35.7	0.388	49.96
PONT-ID-03ac §	2.2	5.7	424.7	6.9	0.0566	0.0034	0.77	EE	53.2	147.6	32.8	0.348	42.44
PONT-ID-03ad	7.1	12.5	480.1	13.9	0.0460	0.0015	0.70	EB	39.5	121.5	22.3	0.284	31.80
PONT-ID-06a	35.4	24.1	287.3	43.3	0.1790	0.0025	0.76	EB	52.6	114.4	13.9	0.185	18.21
PONT-ID-06b	17.5	33.8	348.2	28.3	0.1084	0.0026	0.75	BB	47.9	143.1	12.8	0.139	17.03
PONT-ID-06c	21.5	53.9	344.8	36.9	0.1870	0.0029	0.77	EB	52.6	129.4	15.3	0.167	19.99
PONT-ID-06d	19.9	46.8	353.2	33.7	0.0774	0.0026	0.74	EB	45.7	153.7	7.7	0.137	10.33
PONT-ID-07a	13.4	40.6	120.4	23.9	0.0884	0.0036	0.77	EB	50.8	171.4	8.7	0.094	11.28
PONT-ID-07b	14.0	31.0	110.1	22.2	0.3453	0.0018	0.72	EE	43.3	117.0	74.5	0.809	103.10
PONT-ID-07c	18.2	58.2	135.5	32.9	0.1966	0.0039	0.78	EB	54.1	165.6	12.8	0.136	16.44
PONT-ID-07d	19.3	63.5	159.3	35.5	0.1092	0.0027	0.73	EB	42.0	190.4	9.5	0.102	13.01
PONT-ID-09a	7.7	13.5	106.4	11.8	0.0358	0.0027	0.76	EB	49.5	136.9	9.3	0.115	12.33
PONT-ID-09b	11.5	14.5	144.4	16.1	0.0152	0.0015	0.71	EE	41.7	109.6	4.7	0.070	6.56
PONT-ID-09c	8.1	15.0	113.8	12.6	0.0398	0.0032	0.74	EE	44.2	205.4	8.2	0.105	11.01

PONT-ID-09d	12.9	17.8	142.4	18.2	0.0340	0.0020	0.73	EE	43.5	132.5	7.6	0.092	10.39
PONT-ID-11a	25.7	70.4	150.7	43.4	0.5186	0.0055	0.79	BB	56.1	216.4	18.3	0.180	23.09
PONT-ID-11b	29.5	52.1	138.2	42.8	0.3337	0.0043	0.80	EE	63.8	131.2	15.2	0.170	18.95
PONT-ID-11c §	4.2	7.8	23.5	6.2	0.0399	0.0040	0.79	EB	57.9	147.8	13.0	0.165	16.43
PONT-ID-11e	33.4	53.7	118.1	47.0	0.4526	0.0048	0.79	EE	56.3	188.6	16.7	0.185	21.15
PONT-ID-13a	14.8	19.7	60.7	19.9	0.2789	0.0065	0.83	BB	76.0	139.6	18.1	0.214	21.82
PONT-ID-13b	30.0	49.5	179.4	43.0	0.3579	0.0039	0.78	BB	56.3	151.9	18.1	0.201	23.07
PONT-ID-13c	55.0	47.6	138.9	67.3	0.9620	0.0050	0.82	BB	73.9	112.6	24.1	0.301	29.53
PONT-ID-13d	33.1	33.4	96.8	41.7	0.5532	0.0046	0.80	EB	60.1	158.1	24.1	0.288	30.30
PONT-ID-14a	5.3	20.5	80.7	10.7	0.1103	0.0047	0.79	EE	56.3	182.7	18.7	0.199	23.75
PONT-ID-14b	44.5	121.5	435.5	76.5	0.9932	0.0063	0.81	BB	65.4	182.9	17.6	0.186	21.68
PONT-ID-14c	38.0	41.1	94.3	48.4	1.0539	0.0076	0.84	EB	84.4	132.5	23.9	0.289	28.47
PONT-ID-14d	30.0	66.2	132.6	46.7	0.3955	0.0052	0.80	BB	58.7	187.3	13.6	0.147	17.09
PONT-AY-01a	14.1	30.4	63.4	21.7	0.0387	0.0020	0.71	BB	39.5	158.1	7.1	0.082	10.06
PONT-AY-01b	52.1	89.6	180.7	74.6	0.2765	0.0030	0.75	BB	46.2	173.1	10.4	0.114	13.88
PONT-AY-01c	31.3	82.0	280.6	52.8	0.0865	0.0016	0.71	BB	40.2	121.9	8.6	0.097	12.20
PONT-AY-01d	24.4	54.3	116.9	38.1	0.0823	0.0018	0.73	BB	45.5	110.9	9.6	0.109	13.11
PONT-AY-02a	12.0	15.0	78.1	16.1	0.0842	0.0045	0.80	EB	60.1	155.5	9.6	0.12	12.10
PONT-AY-02b	15.8	15.0	138.4	20.4	0.0572	0.0032	0.77	EB	53.2	141.3	7.3	0.09	9.41
PONT-AY-02c	47.0	59.5	214.5	62.7	0.1147	0.0022	0.73	EE	44.2	137.0	7.1	0.09	9.64
PONT-AY-02d	20.8	29.7	210.8	29.4	0.0962	0.0035	0.77	EB	53.2	151.9	8.0	0.10	10.34
PONT-AY-03a §	4.8	3.7	24.3	5.8	0.0130	0.0037	0.77	EB	51.7	172.3	4.3	0.155	5.55
PONT-AY-03b	65.5	34.1	27.1	73.7	0.0749	0.0022	0.74	EB	45.5	133.8	3.7	0.051	4.97
PONT-AY-03c	14.0	35.0	131.2	23.2	0.0113	0.0029	0.75	BB	47.0	164.3	1.2	0.016	1.54
PONT-AY-03d	12.74	35.89	169.32	22.5	0.0243	0.0030	0.77	EB	51.7	140.0	2.8	0.042	3.71

PONT-AY-5-1a	32.91	36.87	160.42	42.9	0.4136	0.0073	0.82	EE	68.5	193.0	11.2	0.135	13.58
PONT-AY-5-1b	30.44	80.21	199.29	50.9	0.4451	0.0069	0.82	EB	68.2	184.2	10.7	0.107	13.01
PONT-AY-5-1c	38.21	26.71	216.01	46.2	0.2002	0.0035	0.79	BB	58.5	126.3	10.5	0.134	13.38
PONT-AY-5-1d	31.99	141.59	290.09	67.6	0.2007	0.0029	0.75	EE	46.6	163.9	8.7	0.088	11.61
PONT-AY-07a	41.66	78.02	118.58	60.9	0.1930	0.0025	0.75	EB	48.4	135.2	10.3	0.118	13.69
PONT-AY-07b	56.45	116.82	107.64	84.8	0.2303	0.0025	0.75	BB	49.5	128.1	8.9	0.095	11.77
PONT-AY-07c	37.03	107.78	105.35	63.2	0.3116	0.0039	0.79	EB	58.5	142.7	10.4	0.110	13.15
PONT-AY-07e	38.81	111.30	146.75	66.1	0.1873	0.0025	0.75	BB	49.5	128.5	9.3	0.096	12.26
PONT-AY-09a	84.60	96.83	53.11	107.8	0.5702	0.0037	0.79	BB	62.3	117.1	11.9	0.137	15.07
PONT-AY-09b	43.77	86.48	61.99	64.6	0.2641	0.0038	0.77	EE	52.3	170.5	9.0	0.099	11.58
PONT-AY-09c	75.22	132.61	88.60	107.1	0.7433	0.0036	0.78	EB	56.3	140.0	16.1	0.179	20.54
PONT-AY-09d	100.67	142.78	83.91	134.9	0.6265	0.0046	0.77	EE	50.8	220.4	8.4	0.095	10.83
PONT-AY-10a	29.37	60.05	45.41	43.8	0.2415	0.0044	0.78	EE	51.7	205.4	10.3	0.110	13.24
PONT-AY-10b	53.95	69.89	60.26	70.9	0.7857	0.0056	0.80	EE	59.4	197.0	16.4	0.184	20.50
PONT-AY-10d	62.35	87.32	49.49	83.3	0.2933	0.0029	0.75	EB	46.4	165.6	10.1	0.116	13.50
PONT-AY-10e	46.25	113.91	98.79	73.8	0.1794	0.0022	0.72	EB	40.9	164.3	9.1	0.098	12.58
Zircons													
PONT-AY-01 Zra	703.37	314.30	-	777.2	9.2792	0.0034	0.77	EE	52.3	155.5	28.7	0.38	37.27
PONT-AY-01 Zrb	1305.26	953.57	-	1529.3	8.9529	0.0018	0.73	EE	44.8	111.3	26.8	0.35	36.82
PONT-AY-01 Zrc	581.35	604.80	-	723.5	14.3707	0.0056	0.81	EE	64.7	167.0	29.1	0.38	35.93
PONT-AY-02 Zra	615.32	407.38	-	711.1	17.1410	0.0040	0.76	EE	47.0	224.0	49.8	0.64	65.65
PONT-AY-02 Zrb	624.08	224.96	-	676.9	14.1945	0.0073	0.78	EE	51.9	337.4	23.7	0.32	30.17
PONT-AY-02 Zrc	366.90	182.86	-	409.9	10.4021	0.0034	0.74	EE	42.6	232.3	61.5	0.82	83.40
PONT-AY-07 Zra	2160.41	1432.55	-	2497.1	47.6739	0.0058	0.81	EE	62.3	184.3	27.4	0.35	33.91

PONT-AY-07 Zrb	1183.86	692.83	-	1346.7	22.8439	0.0052	0.79	EE	55.4	211.1	26.8	0.35	33.97
PONT-AY-07 Zrc	1578.80	892.97	-	1788.7	17.6176	0.0028	0.74	EE	44.8	173.7	28.9	0.38	38.97
PONT-AY-09 Zra	813.28	632.98	-	962.0	24.1534	0.0073	0.81	EE	60.7	244.7	28.5	0.35	35.28
PONT-AY-09 Zrb	1370.42	914.73	-	1585.4	52.7742	0.0037	0.75	EE	45.7	219.1	74.3	0.94	98.79
PONT-AY-09 Zrc	2218.75	1357.17	-	2537.7	30.0353	0.0033	0.74	EE	44.2	212.9	29.2	0.38	39.30
PONT-AY-10 Zra	1137.88	1098.12	-	1395.9	17.6171	0.0037	0.75	EE	44.2	232.8	28.5	0.42	38.20
PONT-AY-10 Zrb	816.96	520.34	-	939.2	12.9954	0.0040	0.76	EE	47.3	222.2	28.6	0.36	37.65
PONT-AY-10 Zrc	643.08	708.60	-	809.6	10.4177	0.0038	0.74	EE	43.3	249.1	28.2	0.34	38.06

* Ft is the alpha-ejection correction after Farley et al. (1996)

§ Uranium < 5 ppm

** Coded grain terminations: E = Euhedral, B = Broken

Red grain ages were excluded as outliers based on the Dean and Dixon Q-test (Dean and Dixon, 1951)